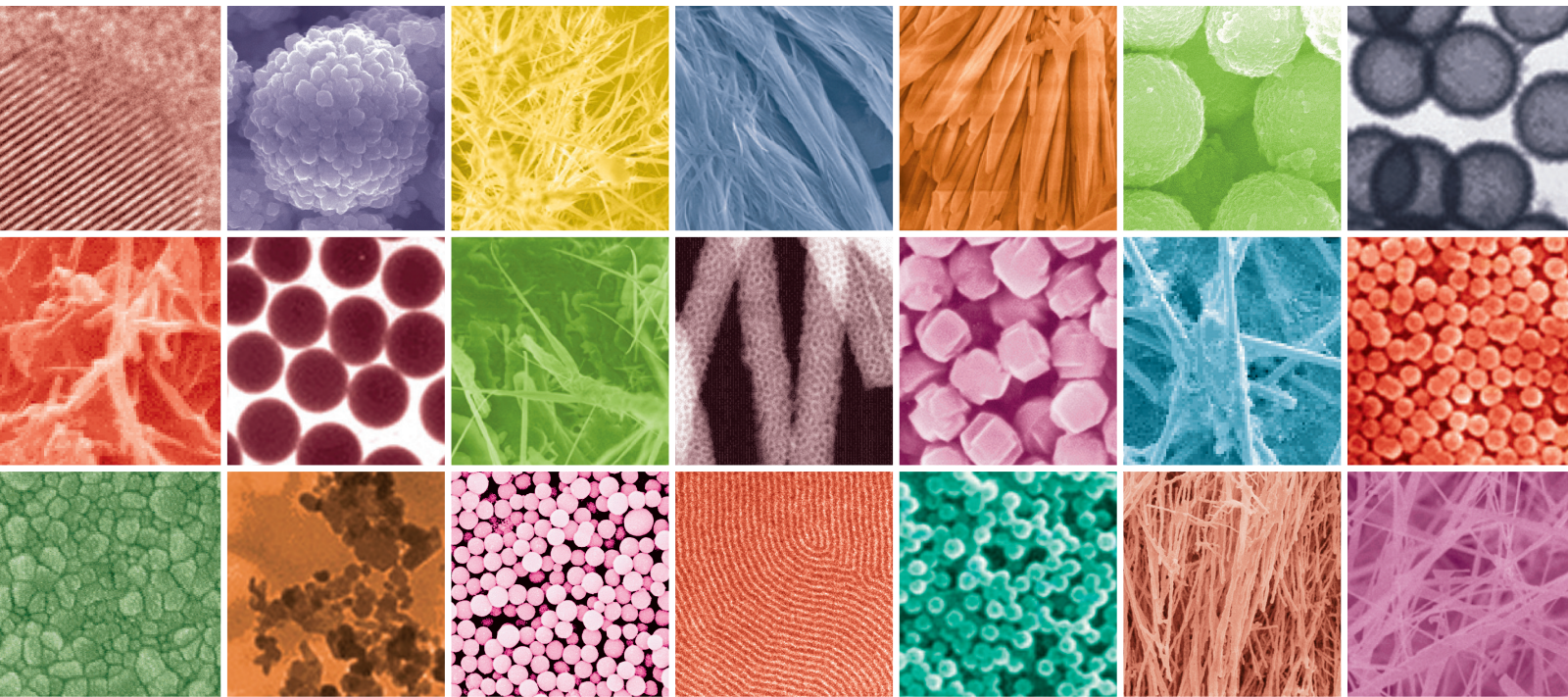


Low-Dimensional Carbon Nanomaterials 2013

Guest Editors: Teng Li, Sulin Zhang, and Nadya Mason





**Low-Dimensional Carbon
Nanomaterials 2013**

Journal of Nanomaterials

**Low-Dimensional Carbon
Nanomaterials 2013**

Guest Editors: Teng Li, Sulin Zhang, and Nadya Mason



Copyright © 2014 Hindawi Publishing Corporation. All rights reserved.

This is a special issue published in "Journal of Nanomaterials." All articles are open access articles distributed under the Creative Commons Attribution License, which permits unrestricted use, distribution, and reproduction in any medium, provided the original work is properly cited.

Editorial Board

- Katerina E. Aifantis, Greece
Nageh K. Allam, USA
Margarida Amaral, Portugal
Xuedong Bai, China
Lavinia Balan, France
Enrico Bergamaschi, Italy
Theodorian Borca-Tasciuc, USA
C. Jeffrey Brinker, USA
Christian Brosseau, France
Xuebo Cao, China
Shafiq Chowdhury, USA
Kwang-Leong Choy, UK
Cui ChunXiang, China
M. A. Correa-Duarte, Spain
Shadi A. Dayeh, USA
Claude Estourns, France
Alan Fuchs, USA
Lian Gao, China
Russell E. Gorga, USA
Hongchen Chen Gu, China
Mustafa O. Guler, Turkey
John Zhanhu Guo, USA
Smrati Gupta, Germany
Michael Harris, USA
Zhongkui Hong, China
Michael Hu, USA
David Hui, USA
Y.-K. Jeong, Republic of Korea
Sheng-Rui Jian, Taiwan
Wanqin Jin, China
Rakesh K. Joshi, UK
Zhenhui Kang, China
Fathallah Karimzadeh, Iran
Alireza Khataee, Iran
Do Kyung Kim, Republic of Korea
Alan K. T. Lau, Hong Kong
Burtrand Lee, USA
Benxia Li, China
Jun Li, Singapore
Xing-Jie Liang, China
Shijun Liao, China
Gong Ru Lin, Taiwan
J. -Y. Liu, USA
Tianxi Liu, China
Songwei Lu, USA
Daniel Lu, China
Jue Lu, USA
Ed Ma, USA
Gaurav Mago, USA
Santanu K. Maiti, India
Sanjay R. Mathur, Germany
Vikas Mittal, United Arab Emirates
Weihai Ni, Germany
Sherine Obare, USA
Atsuto Okamoto, Japan
Abdelwahab Omri, Canada
Edward Andrew Payzant, USA
Kui-Qing Peng, China
Anukorn Phuruangrat, Thailand
Mahendra Rai, India
Suprakas Sinha Ray, South Africa
Ugur Serincan, Turkey
Huaiyu Shao, Japan
Donglu Shi, USA
Vladimir Sivakov, Germany
Marinella Striccoli, Italy
Bohua Sun, South Africa
Saikat Talapatra, USA
Nairong Tao, China
Titipun Thongtem, Thailand
Somchai Thongtem, Thailand
Alexander Tolmachev, Ukraine
Valeri P. Tolstoy, Russia
Tsung-Yen Tsai, Taiwan
Takuya Tsuzuki, Australia
Raquel Verdejo, Spain
Mat U. Wahit, Malaysia
Shiren Wang, USA
Yong Wang, USA
Ruibing Wang, Canada
Cheng Wang, China
Zhenbo Wang, China
Jinquan Wei, China
Ching-Ping Wong, Hong Kong
Xingcai Wu, China
Guodong Xia, Hong Kong
Zhi Li Xiao, USA
Ping Xiao, UK
Shuangxi Xing, China
Yangchuan Xing, USA
N. Xu, China
Doron Yadlovker, Israel
Yingkui Yang, China
Khaled Youssef, USA
Kui Yu, Canada
William W. Yu, USA
Haibo Zeng, China
Tianyou Zhai, Japan
Renyun Zhang, Sweden
Bin Zhang, China
Yanbao Zhao, China
Lianxi Zheng, Singapore
Chunyi Zhi, Hong Kong

Contents

Fabrication of Metal Alloy-Deposited Flexible MWCNT Buckypaper for Thermoelectric Applications, Jih-Hsin Liu, Hsin-Yuan Miao, Saravanan Lakshmanan, Li-Chih Wang, and Ren-Hui Tsai
Volume 2013, Article ID 635647, 6 pages

The Analytical Transmission Electron Microscopy: A Powerful Tool for the Investigation of Low-Dimensional Carbon Nanomaterials, Stefano Casciardi, Renata Sisto, and Marco Diociaiuti
Volume 2013, Article ID 506815, 15 pages

Catalyst Design Using Nanoporous Iron for the Chemical Vapor Deposition Synthesis of Single-Walled Carbon Nanotubes, Tarek M. Abdel-Fattah, Phillip A. Williams, Russell A. Wincheski, and Qamar A. Shams
Volume 2013, Article ID 421503, 7 pages

Functionalization of Graphene with Nitrile Groups by Cycloaddition of Tetracyanoethylene Oxide, Xiaojun Peng, Yang Li, Guoliang Zhang, Fengbao Zhang, and Xiaobin Fan
Volume 2013, Article ID 841789, 5 pages

Highly Conductive, Transparent Flexible Films Based on Metal Nanoparticle-Carbon Nanotube Composites, Wen-Yin Ko and Kuan-Jiuh Lin
Volume 2013, Article ID 505292, 16 pages

Graphene Supported Pt/Ni Nanoparticles as Magnetically Separable Nanocatalysts, Ru Liu, Qingshan Zhao, Yang Li, Guoliang Zhang, Fengbao Zhang, and Xiaobin Fan
Volume 2013, Article ID 602602, 7 pages

Effect of Modified and Nonmodified Carbon Nanotubes on the Rheological Behavior of High Density Polyethylene Nanocomposite, Adewunmi A. Ahmad, Abdulhadi A. Al-Juhani, Selvin Thomas, S. K. De, and Muataz A. Atieh
Volume 2013, Article ID 731860, 12 pages

Enhanced Strain-Dependent Electrical Resistance of Polyurethane Composites with Embedded Oxidized Multiwalled Carbon Nanotube Networks, R. Benlikaya, P. Slobodian, and P. Riha
Volume 2013, Article ID 327597, 10 pages

Methanol Adsorption on Graphene, Elsebeth Schröder
Volume 2013, Article ID 871706, 6 pages

Energy Dissipation and the High-Strain Rate Dynamic Response of Vertically Aligned Carbon Nanotube Ensembles Grown on Silicon Wafer Substrate, P. Raju Mantena, Tezeswi Tadepalli, Brahmananda Pramanik, Veera M. Boddu, Matthew W. Brenner, L. David Stephenson, and Ashok Kumar
Volume 2013, Article ID 259458, 7 pages

Thin, Flexible Supercapacitors Made from Carbon Nanofiber Electrodes Decorated at Room Temperature with Manganese Oxide Nanosheets, S. K. Nataraj, Q. Song, S. A. Al-Muhtaseb, S. E. Dutton, Q. Zhang, and E. Sivaniah
Volume 2013, Article ID 272093, 6 pages

Carbon Micronymphaea: Graphene on Vertically Aligned Carbon Nanotubes, Jong Won Choi, Seoul Ki Youn, and Hyung Gyu Park
Volume 2013, Article ID 734686, 7 pages

Effect of Catalyst Morphology on the Quality of CVD Grown Graphene, Ya-Ping Hsieh, Yi-Wen Wang, Chu-Chi Ting, Hsiang-Chen Wang, Kuang-Yao Chen, and Chang-Chung Yang
Volume 2013, Article ID 393724, 6 pages

Effects of Increasing Electrodes on CNTs Yield Synthesized by Using Arc-Discharge Technique, Samy Yousef, A. Khattab, T. A. Osman, and M. Zaki
Volume 2013, Article ID 392126, 9 pages

On the Phononic Bandgap of Carbon Nanotubes, Kohei Yamamoto, Hiroyuki Ishii, Nobuhiko Kobayashi, and Kenji Hirose
Volume 2013, Article ID 525070, 4 pages

Heat Transfer between an Individual Carbon Nanotube and Gas Environment in a Wide Knudsen Number Regime, Hai-Dong Wang, Jin-Hui Liu, Xing Zhang, Tian-Yi Li, Ru-Fan Zhang, and Fei Wei
Volume 2013, Article ID 181543, 7 pages

Embedding Effect on the Mechanical Stability of Pressurised Carbon Nanotubes, Motohiro Sato, Hisao Taira, Tetsuro Ikeda, and Hiroyuki Shima
Volume 2013, Article ID 767249, 9 pages

Classic and Quantum Capacitances in Bernal Bilayer and Trilayer Graphene Field Effect Transistor, Hatef Sadeghi, Daniel T. H. Lai, Jean-Michel Redoute, and Aladin Zayegh
Volume 2013, Article ID 127690, 7 pages

Research Article

Fabrication of Metal Alloy-Deposited Flexible MWCNT Bucky Paper for Thermoelectric Applications

Jih-Hsin Liu,^{1,2} Hsin-Yuan Miao,^{1,2} Saravanan Lakshmanan,²
Li-Chih Wang,^{2,3} and Ren-Hui Tsai¹

¹ Department of Electrical Engineering, Tunghai University, 181 Taichung Harbor Road, Section 3, Taichung 40704, Taiwan

² Tunghai Green Energy Development and Management Institute, Tunghai University, 181 Taichung Harbor Road, Section 3, Taichung 40704, Taiwan

³ Department of Industrial Engineering and Enterprise Information, Tunghai University, 181 Taichung Harbor Road, Section 3, Taichung 40704, Taiwan

Correspondence should be addressed to Hsin-Yuan Miao; kenymiao@thu.edu.tw

Received 31 March 2013; Revised 10 September 2013; Accepted 27 September 2013

Academic Editor: Sulin Zhang

Copyright © 2013 Jih-Hsin Liu et al. This is an open access article distributed under the Creative Commons Attribution License, which permits unrestricted use, distribution, and reproduction in any medium, provided the original work is properly cited.

We report the fabrication of a flexible network of multiwall carbon nanotubes (MWCNTs) known as buckypaper (BP) for thermoelectric (TE) applications. A thermal evaporation method was used to deposit TE metal alloys onto the BP. The TE properties were improved primarily by increasing the Seebeck coefficient values (50 and 75 $\mu\text{V}/\text{K}$) and the electrical conductivity by approximately 10 000 S/m. High-temperature resistivity studies were performed to confirm the semiconductivity of buckypaper. Variations in resistivity were observed to be the result of the metal alloys coated on the BP surface. We also demonstrated that a substantial increase in the Seebeck coefficient values can be obtained by connecting 3 and 5 layers of metal-deposited BP in series, thereby enhancing the TE efficiency of MWCNT-based BP for application in thermoelectric devices.

1. Introduction

Recently, a considerable amount of effort has been devoted to developing thermoelectric (TE) devices that are capable of generating electricity from heat. TE devices that conserve heat energy should be cost-efficient and possess a high thermoelectric figure of merit [1]. Good TE materials must have a high Seebeck coefficient, which enhances thermoelectricity, low electrical resistivity, which minimizes Joule heating, and low thermal conductivity, which sustains a large temperature gradient [2]. The performance of a TE material is determined by its dimensionless figure of merit $ZT = S^2T/\rho\kappa$, where S , ρ , and κ are the Seebeck coefficient, electrical resistivity, and thermal conductivity of the materials, respectively.

Previous studies have focused on semimetallic nanomaterials such as Bi, Sb, Te, and Bi-Sb alloys because of their promising thermoelectric properties [3–5]. Bi_2Te_3 -based alloys are known to be a state-of-the-art material currently available for TE applications [6]. Recently, Zhang et al. [7]

reported that the Seebeck coefficient of Bi_2Te_3 can be improved by incorporating single wall carbon nanotubes (SWCNTs) into the matrix. Furthermore, highly doped SWCNTs can be used to tune Bi_2Te_3 from n - to p -type. Despite their excellent thermoelectric properties, these materials exhibit poor mechanical property, which complicates the fabrication process, and can cause reliability problems in their application, especially in miniature TE modules.

Recently, there has been considerable focus on macroscopic assemblies of various carbon nanotubes (CNTs) such as buckypaper (BP), fibers, pellets, and thin films because the characteristics of a single CNT can be used on a macroscopic scale to fabricate reliable, high-performance devices [8, 9]. BP is a macroscopic assembly of nanotubes that are formed through filtration after their dispersion in organic solvents. BP typically has a laminar structure with a random orientation of the bundles of tubes in the plane of the sheet [10]. High structural integrity in this MWCNT BP is thought to be derived primarily from their long lengths (up

to micrometer scale), because the longer the tubes, the greater the mechanical robustness of the intermingled bundle. There has been a considerable level of interest in developing novel BP-based composite materials with improved mechanical properties and electrical conductivity for numerous potential applications. It has been established that SWCNTs exhibit considerably high electrical conductivity at room temperature because the charge carrier in the nanotubes exhibits substantial mobility [11]. CNTs exhibit excellent TE properties because of their nanoscale, low-dimensional, and porous structures [12]. Several studies have reported that the values of Seebeck coefficients for individual types of SWCNTs and MWCNTs are approximately $42 \mu\text{V/K}$ [13] and $82 \mu\text{V/K}$ [14], respectively, and for SWCNT and MWCNT films range from 20 to $25 \mu\text{V/K}$ [15, 16]. Zhan et al. [17] showed that the TE efficiency of SWCNTs could be improved by fabricating SWCNT/ceramic nanocomposites with metal oxides such as Al_2O_3 and nanocrystalline Y_2O_3 -stabilized tetragonal ZrO_2 polycrystals.

A review of the extant literature shows that few reports have focused on improving the thermoelectric properties of MWCNT-based BP and there is no report on the effect of the deposition of metal alloy nanoparticles on MWCNT BP. The purpose of this study was to elucidate the TE performance of MWCNT BP by depositing Bi, Te, and Sb alloys on the surface of BP and to measure the corresponding electrical resistivity and Seebeck coefficients. A thermal evaporation method was used because it guarantees high degree of homogeneity and uniform coverage. This report provides a simple and convenient method for fabricating high-quality and flexible MWCNT BP that exhibits promising electrical properties.

2. Materials and Methods

2.1. Fabrication of MWCNT Bucky paper. The BP used in this study was fabricated using MWCNTs through vacuum filtration. The modified procedure used for fabricating the MWCNT BP was adopted from previous reports [18, 19]. The MWCNTs were dispersed in distilled water and stabilized using Triton-X-100, a nonionic surfactant. The aqueous suspension of MWCNTs was produced using ultrasonication (Misonic, 20 kHz, 63 W). Following the filtration and drying processes, the paper was peeled carefully and washed in an isopropyl alcohol bath to completely remove the surfactant, thereby producing a thin sheet (approx. $110 \mu\text{m}$) of random network MWCNT BP (RBP). Compared with aligned membranes, the fabricated RBP exhibited a broader distribution of larger pores, which offers several advantages. For example, it can be rolled or bent without cracking, which is a unique mechanical property that is superior to that of the conventional inorganic TE materials applied in flexible energy conversion systems.

2.2. Deposition of Metal Alloys. A thermal evaporation technique was used to deposit the TE metal alloy on the RBP surface. The metal films (approx. $80 \mu\text{m}$) were deposited onto the BP by Bi, Sb, and Te granules (99.99%) as a vapor source. The BP substrate was fixed on a ceramic holder and

TABLE 1: EDX-weight percentage of the elements present in the BP samples.

| Elements* | BiTe-RBP | SbBi-RBP | SbTe-RBP | SbBiTe-RBP |
|-----------|----------|----------|----------|------------|
| C | 58.26 | 55.22 | 54.40 | 48.12 |
| O | 6.15 | 5.35 | 4.77 | 3.20 |
| Bi | 7.18 | 10.30 | — | 10.22 |
| Sb | — | 14.58 | 18.07 | 17.67 |
| Te | 16.45 | — | 6.65 | 12.15 |

*Fe, Ti, and Al are the impurities present in the sample due to the ultrasonication tip.

inserted into a deposition chamber that was subsequently evacuated under a relative pressure of 10^{-5} torr. The distance from source to the substrate was approximately 30 cm. The total deposition time varied from 1 to 2 min in a vacuum. The ratio of the metal source was 1:1 (0.06 g each). The samples after deposition of alloy of Bi + Te, Sb + Bi, Sb + Te, and Sb + Bi + Te onto the RBP, surface were referred as BiTe-RBP, SbBi-RBP, SbTe-RBP and SbBiTe-RBP, respectively.

2.3. Characterizations. The surface morphology and composition analyses of the BP were examined using field emission scanning electron microscopy (FESEM) with energy dispersive X-ray (EDX) JEOL JSM-7000F. The temperature-dependent electrical resistivity (ρ) measurements of the BP samples were conducted using a standard programmable DC voltage/current detector four-point probe method in a temperature range from 300 to 550 K. Direct thermal conductivity of the pristine RBP at 300 K was measured using a hot disk analyzer TPS 2500. The Seebeck coefficient (S) was determined by applying a temperature gradient along the sample and measuring the thermoelectric voltage. For all the samples, electrical resistivity (ρ) and Seebeck coefficient (S) were measured as a function of temperature, and $S(T)$ was measured for 3 and 5 sheets of the metal-deposited BP samples which were connected in series.

3. Results and Discussion

3.1. Morphological and Compositional Analysis. Figures 1(a)–1(e) show the FESEM images of the RBP, BiTe-RBP, SbBi-RBP, SbTe-RBP, and SbBiTe-RBP, respectively. The microstructures of all samples illustrate the random entanglement, and the network structures of CNTs were formed. Figure 1(a) shows the porous structure of RBP, indicating the complete removal of surfactants between the tubes [20], whereas Figures 1(b)–1(d) show an increase in the tube diameter of metal alloy/MWCNT composites. It reveals that the deposition of metal nanoparticles on the surface caused a densely packed network structure of CNTs in the buckypaper. Furthermore, the network structures of the MWCNT BP were unaltered by the deposition of the metal particles. The insets in Figures 1(a)–1(e) are images of the pure and metal-deposited BP samples. Table 1 shows the elemental composition of the metal-deposited BP samples observed using EDX.

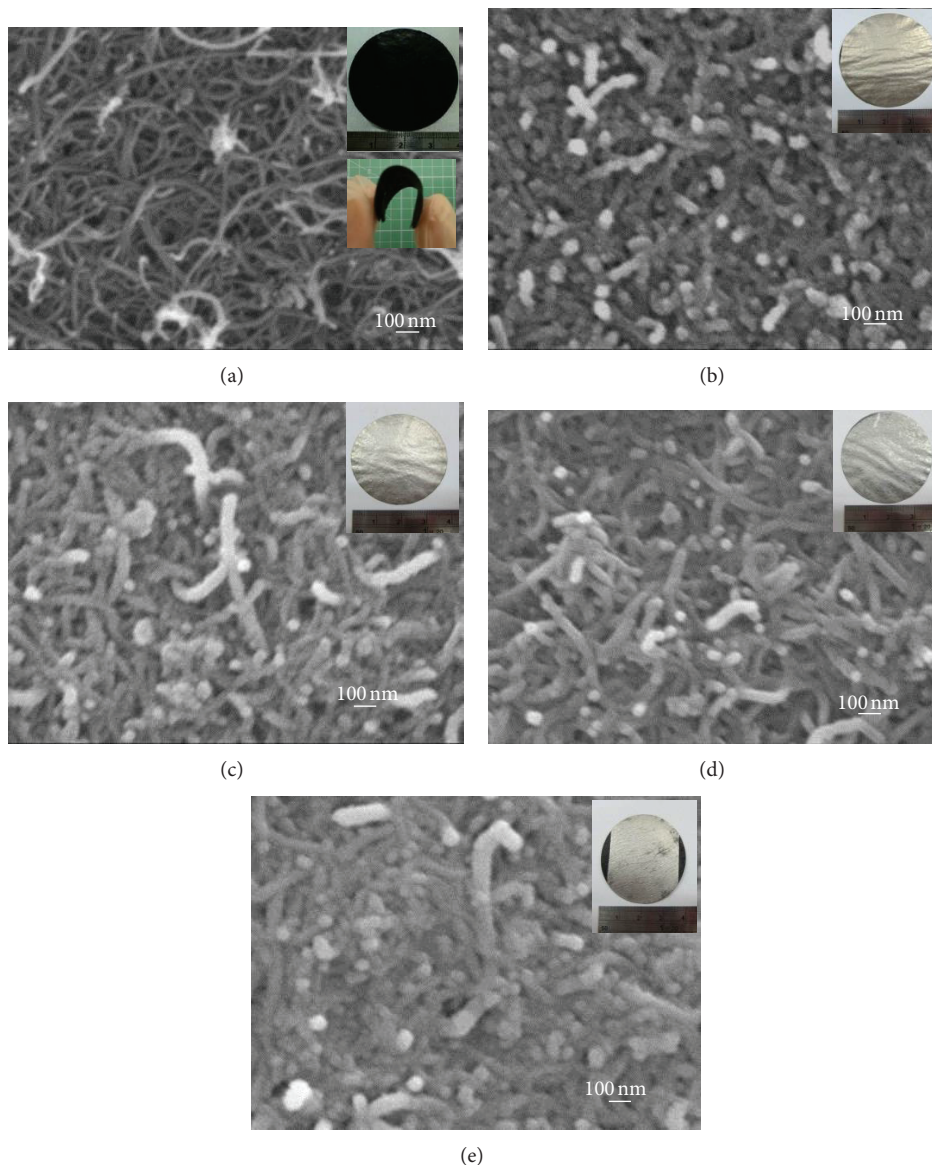


FIGURE 1: FE-SEM images of buckypaper samples for (a) RBP, (b) BiTe-RBP, (c) SbBi-RBP, (d) SbTe-RBP, and (e) SbBiTe-RBP. Insets in (a)–(e) are the photo images of buckypaper samples, respectively.

3.2. Electrical Resistivity Studies. Figure 2 shows the high-temperature electrical resistivity (ρ) plots for the pure and metal-deposited MWCNT-BP samples. The room temperature (RT) resistivity for all samples ranged from approximately 0.01 to 0.06 Ω -cm, which is comparatively low and decreases as the temperature increased, indicating that all the BP samples exhibited strong semiconducting behavior. The difference in the observed resistivity among the various metal alloy-deposited BP were attributed to the oxidation of nanotubes on the surface of buckypaper [17]. The increased slope indicated that the localization length decreased as the barriers between the intertube contacts increased and the oxidation is due to absorption of moisture on the surface of the BP during the measurement process [20]. These results show that the temperature dependence of the resistivity for all the samples was mostly dominated by the transportation

of carriers between the tube junctions through hopping or tunneling, thereby resulting in semiconducting behavior [21, 22].

Based on the observed semiconducting behavior, the variable-range hopping (VRH) model appears to be the predominant conduction mechanism [23]. It could be considered that the BP is a 3-dimensional network of dispersed bundle-bundle junctions that allow the carriers to move within a sheet. Therefore, the electrical conduction occurs either in the tube-tube, within the nanotube bundles or between neighbour bundles through their contacts. The resistivity is primarily dominated by the electric field gradient across the material because the electrons must hop between different bundles of CNTs [23]. The essential part is that the electrons hopped between conducting entities (NTs) were separated by the metallic particles which leads to

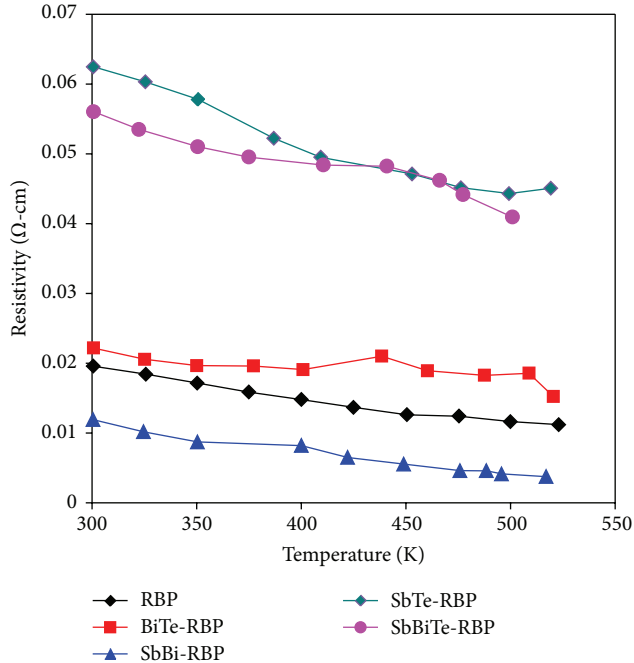


FIGURE 2: High-temperature-dependent electrical resistivity measurements for pure and metal alloy-deposited RBP samples.

a nonmetallic dependence of $\rho(T)$. The hopping conduction was probably the characteristic electric transport behavior between the nanotubes and bundles.

Compared with the pure samples, the metal-deposited RBP samples exhibited an increased resistivity value, indicating that the particles deposited onto the surface of the nanotubes might have caused a slight blockage at the intertube junctions and thereby forming a barrier for the hopping and tunneling of electrons. Kim et al. [24] also reported that the presence of metal content within the CNTs can affect the RT resistivity. Previous research indicated that the electrical conductivity of fully connected CNT networks can be limited by tube-tube contact resistance [25].

3.3. Seebeck Coefficient Measurement. Figure 3(a) shows the temperature-dependent Seebeck coefficient $S(T)$ for a single sheet of metal-deposited MWCNT buckypaper. Figures 3(b) and 3(c) show the Seebeck coefficients for 3 and 5 sheets of metal-deposited BP connected in series, respectively. The Seebeck coefficient is related to the transport of energetic charged particles, whereas the electrical conductivity is related to the transport of all mobile charges [26]. In this study, the observed $S(T)$ values were negative, indicating that the majority of carriers were electrons. For all samples, the strongly curved T-dependence of “S”, which exhibited a nonlinear behavior, shows the semiconducting nature of the CNT networks, which also supports the resistivity results [27].

Table 2 shows the maximum $S(T)$ values obtained for the single layer as well as for the 3 and 5 sheets in series. The $S(T)$ value for the single layer of pristine MWCNT BP was $-13.49 \mu\text{V/K}$ ($\kappa = 0.1824 \text{ W/mK}$ at 300 K) is comparable [15, 23, 28], and in our case it increases to approximately

TABLE 2: Measured Seebeck coefficient S ($-\mu\text{V/K}$) for metal alloy-deposited RBP samples.

| Samples | Single | 3 sheets | 5 sheets |
|------------|--------|----------|----------|
| BiTe-RBP | 20.66 | 49.44 | 67.22 |
| SbBi-RBP | 22.15 | 45.22 | 77.98 |
| SbTe-RBP | 20.17 | 41.31 | 65.28 |
| SbBiTe-RBP | 19.90 | 47.14 | 74.89 |

$22 (\pm 1) \mu\text{V/K}$ after the deposition of TE metal alloys. The variation in the Seebeck coefficient originated from the change in the doping of metal alloys and its composition on MWCNTs and the amount of charges transferred to the BP. It was also stated that the Seebeck coefficient for CNT mats is independent of the CNT type, and high energetic charges are transported regardless of the junction types [28]. This unique relationship between the Seebeck coefficient (S) and high electric conductivity (σ) implies that it is possible to balance the metal alloy films on the surface of BP to increase the carrier mobility and attain the maximum power factor ($S^2\sigma$). We also demonstrated that 3 and 5 layers of metal-deposited BP can be used to attain a high Seebeck coefficient of approximately $50 (\pm 4)$ and $75 (\pm 6) \mu\text{V/K}$, respectively. This shows that an array of metal-deposited BP connected in series can achieve high “ σ ” and $S^2\sigma$, thereby enhancing the thermoelectric efficiency.

We determined that increasing the thickness of the metal alloys on the BP surface weakens the quantum confinement effects and reduces the interaction between the metal particles and CNTs. This reduces the carrier density in the BP, which increases the resistivity of the sample. Furthermore, the intertube junctions in the BP are essential factors for improving the electrical transport and mechanical strength. This work demonstrates the fundamental challenges associated with employing the TE nanoparticles within BP to increase the surface properties as well as the inter-particle contacts, which was primarily considered in order to maximize the TE efficiency. We are further involved in controlling various parameters such as composition and thickness to achieve higher electrical and low thermal conductivity for processing the MWCNT-based BP as efficient thermoelectric (TE) material into a functional device.

4. Conclusion

In summary, the alloy of Bi, Sb, and Te nanoparticles was deposited on the surface of the buckypaper by employing a thermal evaporation method. The electrical measurements of the pure and metal alloy-deposited MWCNT buckypapers have been performed. The RT electrical resistivity was observed in the range from 0.01 to 0.06 $\Omega\text{-cm}$, which also demonstrated the semiconductivity of the CNT networks. The observed $S(T)$ values are comparable to those of BPs synthesized using various methods. An increase in the value was observed for the Seebeck coefficient to approximately 50 and 75 $\mu\text{V/K}$ by connecting the metal alloy-deposited BP sheets in series. The results show the potential of these TE NPs to be further refined and maximized to increase the efficiency

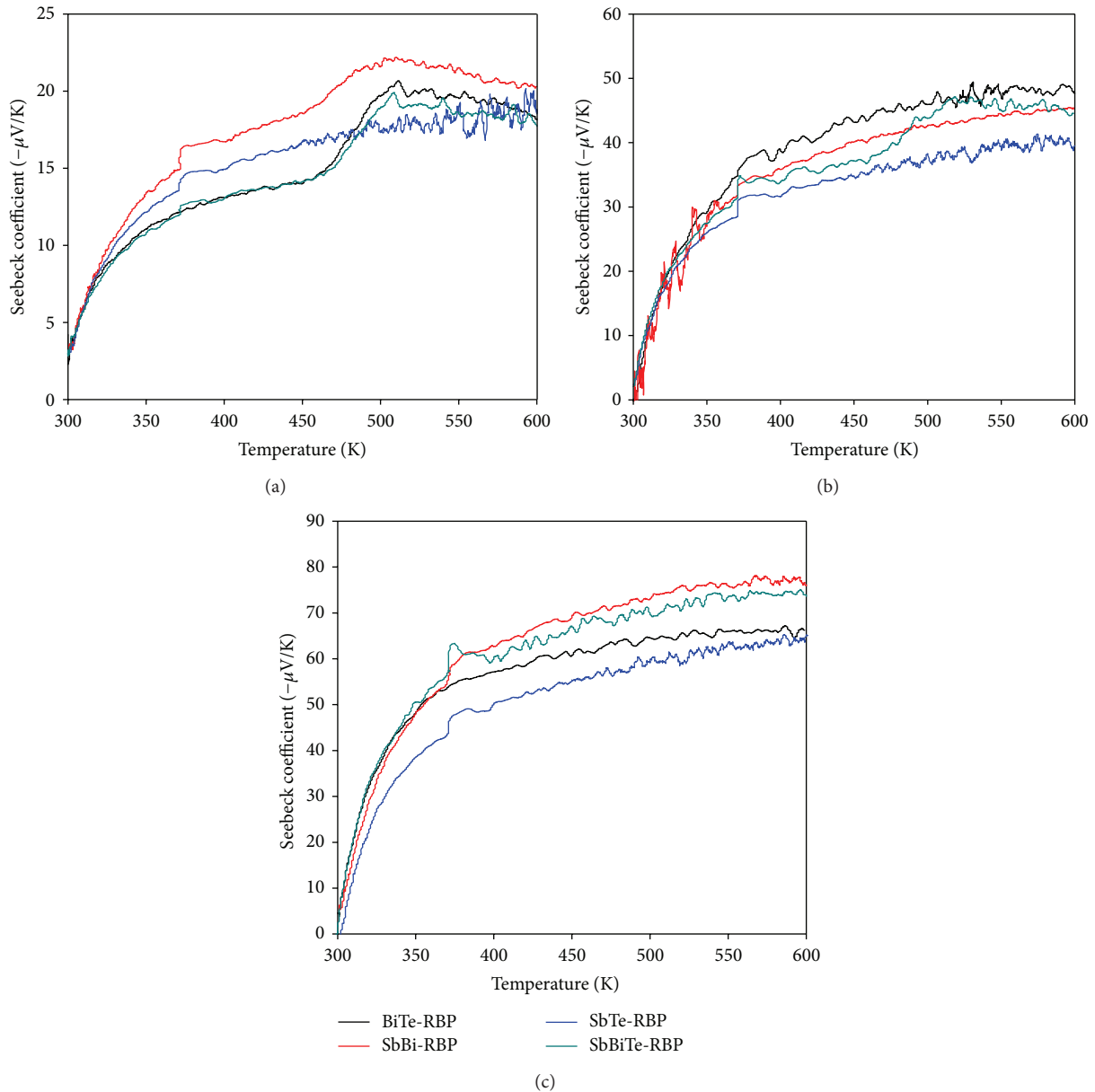


FIGURE 3: Seebeck coefficient $S(T)$ for metal alloy-deposited RBP samples. (a) Single layer, (b) 3 sheets connected in series, and (c) 5 sheets connected in series.

of BP-based thermoelectric materials. Further study on the inclusion of these TE particles in BP by controlling their size and composition to maximize the inter-tube contacts and improve surface properties through sample processing, to increase the electrical conductivity and enhance the thermoelectric efficiency, is part of our ongoing studies in this field.

Acknowledgments

This work was supported by the Global Research and Education on Environment and Society (GREENS) program, Tung-hai University, Taiwan, and the National Science Council, Taiwan (NSC101-2221-E-029-006 and NSC101-2221-E-029-010).

References

- [1] W. Liu, X. Yan, G. Chen, and Z. Ren, "Recent advances in thermoelectric nanocomposites," *Nano Energy*, vol. 1, no. 1, pp. 42–56, 2012.
- [2] M. S. Dresselhaus, G. Chen, M. Y. Tang et al., "New directions for low-dimensional thermoelectric materials," *Advanced Materials*, vol. 19, no. 8, pp. 1043–1053, 2007.
- [3] A. L. Prieto, M. Martín-González, J. Keyani, R. Gronsky, T. Sands, and A. M. Stacy, "The electrodeposition of high-density, ordered arrays of $\text{Bi}_{1-x}\text{Sb}_x$ nanowires," *Journal of the American Chemical Society*, vol. 125, no. 9, pp. 2388–2389, 2003.
- [4] D. Mott, N. T. Mai, N. T. B. Thuy et al., "Bismuth, antimony and tellurium alloy nanoparticles with controllable shape and

- composition for efficient thermoelectric devices," *Physica Status Solidi (A)*, vol. 208, no. 1, pp. 52–58, 2011.
- [5] H. J. Goldsmid, *Semiconductors and Semimetals*, vol. 69, chapter 1, Academic Press, New York, NY, USA, 2000.
 - [6] W. J. Xie, X. F. Tang, Y. G. Yan, Q. J. Zhang, and T. M. Tritt, "High thermoelectric performance BiSbTe alloy with unique low-dimensional structure," *Journal of Applied Physics*, vol. 105, no. 11, Article ID 113713, 2009.
 - [7] Y. Zhang, X. L. Wang, W. K. Yeoh, R. K. Zeng, and C. Zhang, "Electrical and thermoelectric properties of single-wall carbon nanotube doped Bi₂Te₃," *Applied Physics Letters*, vol. 101, no. 3, Article ID 031909, 4 pages, 2012.
 - [8] J. Liu, J. Sun, and L. Gao, "Flexible single-walled carbon nanotubes/polyaniline composite films and their enhanced thermoelectric properties," *Nanoscale*, vol. 3, no. 9, pp. 3616–3619, 2011.
 - [9] W. Zhao, S. Fan, N. Xiao et al., "Flexible carbon nanotube papers with improved thermoelectric properties," *Energy and Environmental Science*, vol. 5, no. 1, pp. 5364–5369, 2012.
 - [10] L. Berhan, Y. B. Yi, A. M. Sastry, E. Munoz, M. Selvidge, and R. Baughman, "Mechanical properties of nanotube sheets: alterations in joint morphology and achievable moduli in manufacturable materials," *Journal of Applied Physics*, vol. 95, no. 8, pp. 4335–4345, 2004.
 - [11] T. W. Ebbesen, H. J. Lezec, H. Hiura, J. W. Bennett, H. F. Ghaemi, and T. Thio, "Electrical conductivity of individual carbon nanotubes," *Nature*, vol. 382, no. 6586, pp. 54–56, 1996.
 - [12] I. Kunadian, R. Andrews, M. P. Mengüç, and D. Qian, "Thermoelectric power generation using doped MWCNTs," *Carbon*, vol. 47, no. 3, pp. 589–601, 2009.
 - [13] C. H. Yu, L. Shi, Z. Yao, D. Li, and A. Majumdar, "Thermal conductance and thermopower of an individual single-wall carbon nanotube," *Nano Letters*, vol. 5, no. 9, pp. 1842–1846, 2005.
 - [14] P. Kim, L. Shi, A. Majumdar, and P. L. McEuen, "Thermal transport measurements of individual multiwalled nanotubes," *Physical Review Letters*, vol. 87, no. 21, Article ID 215502, 4 pages, 2001.
 - [15] C. Meng, C. Liu, and S. Fan, "A promising approach to enhanced thermoelectric properties using carbon nanotube networks," *Advanced Materials*, vol. 22, no. 4, pp. 535–539, 2010.
 - [16] M. T. Byrne and Y. K. Guin'Ko, "Recent advances in research on carbon nanotube—polymer composites," *Advanced Materials*, vol. 22, no. 15, pp. 1672–1688, 2010.
 - [17] G. D. Zhan, J. D. Kuntz, A. K. Mukherjee, P. Zhu, and K. Koumoto, "Thermoelectric properties of carbon nanotube/ceramic nanocomposites," *Scripta Materialia*, vol. 54, no. 1, pp. 77–82, 2006.
 - [18] Z. Wang, Z. Liang, B. Wang, C. Zhang, and L. Kramer, "Processing and property investigation of single-walled carbon nanotube (SWNT) buckypaper/epoxy resin matrix nanocomposites," *Composites A*, vol. 35, no. 10, pp. 1225–1232, 2004.
 - [19] Y. W. Chen, H. Y. Miao, M. Zhang, R. Liang, C. Zhang, and B. Wang, "Analysis of a laser post-process on a buckypaper field emitter for high and uniform electron emission," *Nanotechnology*, vol. 20, no. 32, Article ID 325302, 2009.
 - [20] J. G. Park, J. Smithyman, C. Y. Lin et al., "Effects of surfactants and alignment on the physical properties of single-walled carbon nanotube buckypaper," *Journal of Applied Physics*, vol. 106, no. 10, Article ID 104310, 6 pages, 2009.
 - [21] A. B. Kaiser, G. Düsberg, and S. Roth, "Heterogeneous model for conduction in carbon nanotubes," *Physical Review B*, vol. 57, no. 3, pp. 1418–1421, 1998.
 - [22] J. C. Charlier, "Defects in carbon nanotubes," *Accounts of Chemical Research*, vol. 35, no. 12, pp. 1063–1069, 2002.
 - [23] A. M. Díez-Pascual, J. Guan, B. Simard, and M. A. Gómez-Fatou, "Poly(phenylene sulphide) and poly(ether ether ketone) composites reinforced with single-walled carbon nanotube buckypaper: II—mechanical properties, electrical and thermal conductivity," *Composites A*, vol. 43, no. 6, pp. 1007–1015, 2012.
 - [24] H. M. Kim, K. Kim, C. Y. Lee et al., "Electrical conductivity and electromagnetic interference shielding of multiwalled carbon nanotube composites containing Fe catalyst," *Applied Physics Letters*, vol. 84, no. 4, pp. 589–591, 2004.
 - [25] A. Buldum and J. P. Lu, "Contact resistance between carbon nanotubes," *Physical Review B*, vol. 63, no. 16, Article ID 161403(R), 4 pages, 2001.
 - [26] C. Yu, Y. S. Kim, D. Kim, and J. C. Grunlan, "Thermoelectric behavior of segregated-network polymer nanocomposites," *Nano Letters*, vol. 8, no. 12, pp. 4428–4432, 2008.
 - [27] J. Hone, I. Ellwood, M. Muno et al., "Thermoelectric power of single-walled carbon nanotubes," *Physical Review Letters*, vol. 80, no. 5, pp. 1042–1045, 1998.
 - [28] Y. J. Choi, Y. Kim, S. G. Park et al., "Effect of the carbon nanotube type on the thermoelectric properties of CNT/Nafion nanocomposites," *Organic Electronics*, vol. 12, no. 12, pp. 2120–2125, 2011.

Research Article

The Analytical Transmission Electron Microscopy: A Powerful Tool for the Investigation of Low-Dimensional Carbon Nanomaterials

Stefano Casciardi,¹ Renata Sisto,¹ and Marco Diociaiuti²

¹ Department of Occupational Hygiene, National Institution for Insurance against Accidents at Work (INAIL Research), Monte Porzio Catone, Rome, Italy

² Department of Technologies and Health, Italian National Institute of Health (ISS), Rome, Italy

Correspondence should be addressed to Stefano Casciardi; s.casciardi@inail.it

Received 15 April 2013; Accepted 14 October 2013

Academic Editor: Nadya Mason

Copyright © 2013 Stefano Casciardi et al. This is an open access article distributed under the Creative Commons Attribution License, which permits unrestricted use, distribution, and reproduction in any medium, provided the original work is properly cited.

Chemical and physical characterization of nanomaterials is essential to improve synthesis processes, for new technological and commercial applications, and to assess their toxicity through *in vitro* and *in vivo* studies. New nanomaterials and new synthesis processes are continuously tested and updated to exploit their innovative properties. In this paper, low-dimensional carbon nanostructure characterization was performed using analytical transmission electron microscopy. Conventional and advanced microscopy techniques, such as acquisition of high resolution images, nanobeam electron diffraction patterns, X-ray energy dispersion, and electron energy loss spectra, were used to determine the main physical and chemical properties of single wall and multiwall carbon nanotubes, graphene flakes, and amorphous carbon films. Through the resulting micrographs, diffraction patterns, and spectra, the main low-dimensional carbon nanostructures properties were determined in terms of structural defects and/or the presence of metallic or heavy elements, such as those used as catalyst or to decorate nanotubes. The obtained information is of crucial importance to investigate low-dimension nanomaterial biological activity.

1. Introduction

Among low-dimensional carbon nanostructures, nanotubes play the main role up to now. They were discovered by chance in 1991 by the physicist Sumio Iijima (NEC Corporation, Tsukuba, Ibaraki, Japan), in the analysis of the products obtained in the growth of fullerenes, the third allotropic species of carbon [1]. Actually, in the late 1950s, researchers, Roger Bacon (Union Carbide Corporation, Cleveland, OH, USA) and then in the 1970s and 1980s (Morinobu Endo), had unknowingly observed nanotubes but had not recognized them as such [2, 3].

As for all materials of nanometric dimension, nanotubes have technical characteristics making them especially attractive in a wide range of applications [4–16]. There are numerous sectors in which the specific properties of carbon nanotubes can be used, and there are many other potential sectors where applied research is investing considerable

resources. For example, these materials are very resistant to traction. Indeed, it can be said that carbon nanotubes, without structural defects, are the most resistant organic material. Nanotubes are likewise very light and highly flexible and can be folded repeatedly up to 90° without being damaged. All these properties make them the best materials available today for reinforcing fibres in high performance composite materials, replacing and having definitely superior properties than the natural or artificial fibres used up to now, for example, carbon fibres, Kevlar, or glass wool, to mention but a few.

Although the basic element of carbon nanotubes is the graphitic sheet, the good electrical conducting properties of graphite appear only partially in nanotubes, which are electronic hybrids. This fact suggests the use of nanotubes for manufacturing much smaller electronic devices and with much higher performance levels compared to the ones that are currently based on silicon physics. Carbon nanotubes can

be used to make diodes, transistors, LEDs, ultraviolet lasers, photovoltaic cells, electronic cannons for producing ultra-high-definition plasma screens, and much more [17, 18].

Another property of nanotubes is their capillarity due to the tubular shape and high surface area/weight ratio. This characteristic makes nanotubes ideal for the adsorption of gas and their application in producing fuel cells. Nanotubes also react to the presence of electrical fields by bending and thus modifying their resonance frequency. This characteristic could lead to applications in the field of nanotechnologies, with the manufacturing of nanoscales and nanometric electromechanical switches. Since nanotubes have all these properties and more, it is not surprising that many commercial products already contain them, and many more are currently being studied, designed, and marketed.

Nowadays, the unzipping of single and multiwalled nanotubes offers a viable route for large-scale synthesis of graphene flakes [19]. Recently, carbon structures with sp^2 hybridization, such as bilayer, few-layer graphene, and graphene nanoribbons, have entered the flat nanocarbon world [20]. Each of these systems exhibits peculiar properties which are different from both graphene and graphite [21–23]. However, most properties of graphene films and graphene nanoribbons remain unexplained and, therefore, cannot be controlled without a knowledge of the structural defects such as spontaneous warping of the sheets [24–26].

The mechanical, electrical, optical, chemical, and thermoelectric properties of carbon materials are strongly influenced by the proportion of sp^3 carbon atoms in the material. Due to their chemical inertness, high hardness, and low friction, amorphous carbon finds applications in coating for magnetic storage devices, razor blades, optical devices, field emitting devices, and biocompatible coating for human implants [27].

In spite of this wide use of nanomaterials, which will likely further increase, their negative effects on health are not well known. The nanometric size enables these materials to go through any biological barrier. While on the one hand this characteristic can be exploited in biomedical applications, such as drug delivery to target organs [28, 29], on the other hand there are considerable concerns that there is a risk that these potentially harmful agents are highly pervasive. *In vitro* and *in vivo* studies on cytotoxicity and genotoxicity, together with epidemiological studies on the correlation between concentrations of ultrafine particles and cardiorespiratory diseases, are starting to provide information on the biological effects of nanomaterials [30–38].

The studies on nanomaterials, conducted on cell cultures and laboratory animals, are providing evidence on cytotoxicity and genotoxicity effects, on oxidation stress and on damages of the respiratory, cardiocirculatory, neurological, and immune systems. Sometimes, however, the conclusions drawn by various authors are contrasting. This can partly be attributed to the fact that there are different experimental conditions applied in the tests (e.g., the cell types and animals exposed, the nanomaterials used for exposure, and dosage values). For some of these parameters, control

was not easy. An example can be seen in the nanotube samples. If different types are used in the various experiments (single-walled, multiwalled, pristine, purified, functionalized, decorated), there will be different responses from the biological systems. Even if the same type of nanotube is used, there may also be considerable differences between one sample and another. This is all the more so if the nanotubes are bought commercially, in this case one lot might be completely different from another one even if purchased from the same seller. This obviously makes it more difficult to compare the results obtained not only by different laboratories, but also within the same research group, if there has not been highly accurate control of the experimental conditions. The technical characteristics and the biological effects are heavily dependent on the chemical and physical properties of the nanomaterials in general, and therefore, in the specific case, also of nanotubes. It is thus essential, both for their technological application and for evaluating any negative effects on health, to characterize as far as possible the nanostructures from a chemical and physical point of view.

This paper illustrates the characterization by analytical transmission electron microscopy of low-dimensional carbon nanostructures, such as nanotubes for 1D carbon nanostructures, and amorphous and graphene flakes for 2D ones.

We applied, in a transmission electron microscope, high resolution imaging, electron diffraction, energy dispersion X-ray spectroscopy (EDXS), and electron energy loss spectroscopy (EELS). The main drawback of these techniques is related to the possible local damage of the sample by the highly focused energetic electron beam (the energy is deposited in a volume of only few nm^3). Electron induced damages can take a variety of forms, including dissociation, desorption, oxidation, reduction, polymerization, carbonization, and diffusion depending on the specimen material and the gases present in the ultrahigh vacuum system [39, 40]. Therefore, particular care must be devoted to the investigation of nanostructures, so as to minimize electron beam damaging. This can be obtained using the nanobeam where the electron damage is minimized due to the low beam intensity.

Unconventional nanobeam electron diffraction (NED) and EELS (NEELS) measurements were made using a nanometer-sized coherent parallel beam of electrons [41, 42]. In particular, by reducing the size of the incident electron beam to a few nanometers with the condenser aperture and the spot size condenser lens, EELS spectra and diffraction patterns were acquired on single low-dimensional nanostructures. Unlike conventional selected area electron diffraction (SAED), the diffraction volume is defined directly by the electron probe [43]. Finally, TEM images of the nanostructure under investigation should be taken before and after acquisition to ensure the quality of the measurements.

The purpose was to measure the main size parameters of the nanostructures and to identify the presence of structural defects and of contaminants like the catalyst used to synthesize the nanostructures.

2. Materials and Methods

2.1. Sample Preparation. For observation with TEM microscopy, the nanotubes, the graphene, and the highly oriented pyrolytic graphite (HOPG) flakes were dispersed in isopropyl alcohol. The suspension was placed in an ultrasound bath for about 5 minutes. A few drops of the suspension were deposited on standard size (diameter 3.05 mm) 1,000 mesh gold grids. If we had analyzed the length of the nanotubes, we would have placed a few drops of the suspension on a 400 mesh copper grid on which a layer of amorphous carbon has previously been placed. Since the information about the measurement of the length of the nanotubes is of little use, the extremely high ratio between the length and diameter can, for practical purposes, lead to consider the nanotubes as 1 dimensional structures, that is, with an infinite length with respect to the diameter, copper grids with amorphous carbon film were not used. Only the gold grids without any film were used. The nanotubes remain suspended between the bars of the grid, and the absence of a support film enables optimal observation.

Standard Cu grids covered with amorphous carbon film were used to investigate thin amorphous layers [44].

2.2. Transmission Electron Microscopy. The microscope used (model Tecnai 12 G2 Twin, FEI Company, Hillsboro, OR, USA) was equipped with a thermionic gun (single-crystal lanthanum hexaboride), with an energy dispersive X-ray spectrometer (model Genesis 4000, EDAX Inc., Mahwah, NY, USA) and a “post-column” electron energy filter (Bio filter, GATAN Inc., Pleasanton, CA, USA). The energy-filtered images and EELS spectra were acquired by the use of a slow-scan CCD camera (model 794 IF, GATAN Inc., Pleasanton, CA, USA).

Conventional imaging was performed in energy filtered image mode configuration, at electron energy of 120 keV, with a collection angle of about 20 mrad. To enhance image contrast and resolution, chromatic aberrations were reduced by collecting only elastic electrons ($\Delta E = 0$). All the high resolution images were collected at the “Scherzer defocus”, in order to optimize the transfer function of the optical system balancing the effect of spherical aberration ($C_s = 2.2$ mm) against a particular negative value of Δf (about 103 nm). In this case the image contrast in the Weak Phase Object (WPO) approximation represents the two dimensional projection of the crystal potential [45].

All the NEELS and NED experiments were performed on individual nanostructures by using a nanometer-sized (up to about 20 nm) coherent parallel electron beam [43]. Actually, these joint measurements allowed us to directly visualize the area of the specimen (about 50 nm in diameter) from which spectra and diffractions were acquired.

Qualitative elemental analysis was performed by means of EDXS [45].

2.3. Statistical Analysis. To measure dimensional carbon nanotube (CNT) characteristics, conventional TEM images must contain a sufficient number of nanotubes to produce

significant statistics, but also sufficiently dispersed and untangled in order to easily obtain the measurement of the diameters, and follow the path of the nanotube so as not to use it again in subsequent measurements. From 4 to 10 TEM images were used to analyse the dimensions, by which it was possible to acquire the values of the diameters of between 60 and 80 nanotubes.

2.4. Electron Energy Loss Spectroscopy. Spectra used to perform EELS microanalysis were acquired in image mode (convergence and collection angle of 0.1 and 20 mrad, resp.) and the obtained information was relative to the zone defined by the superposition of the circular spectrometer aperture (2 mm of diameter) and the image. Using this configuration, the size of the analyzed zone depends on the magnification and can be easily varied.

The sample thickness t_r can be determined by EELS measurements (low loss region of Figure 11) by calculating the integrated intensity of the elastic peak, I_0 , and that of the first order plasmon features, I_p , through the following relation:

$$t_r = \lambda \ln \left(\frac{I_p}{I_0} \right), \quad (1)$$

where λ is the electron mean free path (about 174 nm in our case) [46].

For EELS microanalysis, ionization edges of the investigated species were analysed. The edge detection was defined by the minimum permissible signal/noise (S/N) ratio as 3, corresponding to 98% certainty for detection of the element [47].

Spectral processing for the estimation of the atomic ratios was performed according to the Egerton procedure [48]. In order to calculate the atomic ratio, the following relation was used:

$$\frac{N_x}{N_y} = \frac{S_x(\alpha, \Delta) \sigma_y(\alpha, \Delta)}{S_y(\alpha, \Delta) \sigma_x(\alpha, \Delta)}, \quad (2)$$

where S_x is the integrated core edge intensity for element x in an energy window Δ , with a collecting angle α and σ_x, σ_y are the ionization cross-sections calculated from the hydrogenic model [49, 50] using the same energy and angle values. In general, a power law [47, 51] describes the background under the edge:

$$B(E) = AE^{-r}, \quad (3)$$

where the two parameters A and r are obtained by the least-square minimization in a limited energy region δ before the edge and extrapolated above the edge region to be integrated. The correlation coefficient between the experimental points in the energy window δ and the points relative to the chosen background was used as test of fit. For both the C-K edge and the O-K edge the widths of the fitting ranges (δ) were 10 eV and 190 eV, respectively, and the width of energy window used to calculate the element relative quantification (Δ) was 25 eV for both elements.

Error sources in EELS microanalysis have been extensively discussed [47, 52]. Statistical limitation, approximate

calculation of the appropriate cross-sections, and, mainly, uncertainty in the background subtraction are the principal sources. The error bar relative to EELS measurements was estimated to be about 20% when particular problems in the background interpolation are absent, that is; when correlation coefficients between experimental points and background are higher than 0.9 (corresponding to a probability that the two curves are not correlated less than 0.001).

Elemental composition was analyzed by means of Digital Micrograph software (version 3.9.5, Gatan Inc., Pleasanton, CA, USA).

3. Results and Discussion

3.1. One-Dimensional Nanomaterials. We intend CNTs as 1-dimensional carbon nanomaterials and several kinds of CNTs were analyzed. Conventional TEM images and high resolution images were acquired at different magnifications values. The quality of the medium-sized magnifications of the conventional images already makes it possible to measure the external and inner diameters of nanotubes and thus to calculate the number of walls of the nanotubes. The high-resolution images make it possible to directly measure the number of and the distance between the walls, to evaluate the presence of structural defects and the presence of amorphous carbon on the external walls of nanotubes.

The chemical composition of the nanotubes, of the catalyst nanoparticles, and of those used for decoration was analyzed by EDXS and EELS. Analyzing the fine structure of the EELS spectrum near the carbon K edge (energy-loss near-edge-structure, ELNES), information on the nature of the chemical bonds of the carbon in the nanotubes can be obtained, whereas it is possible to obtain structural information on the nanomaterial by studying the oscillations in the carbon spectrum following the carbon peak (extended energy-loss fine structure, EXELFS) [53, 54].

Conventional TEM images with sufficiently high magnifications were acquired to facilitate the measurement of the nanotubes' outer diameters and inner channels. Figure 1 shows TEM images acquired to measure the nanotube diameters: (a) for a sample of undecorated nanotubes; (b) for nanotubes decorated with copper nanoparticles, clearly observed as being attached to the external surfaces. The images clearly show the essential geometric characteristics of the tubes, with darker external walls and the lighter internal channels. All this information cannot be obtained with scanning electron microscopy, which only provides images of the tubular surfaces of the samples, without details on their internal structure (in practice, it is not possible to establish whether the tubes are full or hollow). We remind that decoration with copper nanoparticles enhances the photocurrent response of CNT [55–57].

In Figure 1 a sample of “bamboo-like” nanotubes is also shown. In (c) how it is not correct to talk of 1-dimensional structure because the length of these type of nanotubes can be very short is clearly shown: the nanotube can easily break in a node point. In (d) a detail of a nanotube is shown, with the absence of the inner channel and the axial symmetry.

TABLE 1: Statistics regarding the measurement of external diameters, the inner channel, and the number of walls for undecorated and decorated nanotube samples.

| Sample | Outer diameter (nm) | Inner channel (nm) | Wall number |
|-----------------------|----------------------|---------------------|------------------|
| Undecorated nanotubes | 7.6 ± 1.7 (50%) | 4.0 ± 1.0 (37%) | 5 ± 1 (23%) |
| | 10.8 ± 3.0 (44%) | 4.9 ± 3.3 (63%) | 7 ± 1 (35%) |
| | 15.4 ± 1.5 (6%) | | 9 ± 4 (42%) |
| Decorated nanotubes | 7.9 ± 2.2 (33%) | | 5 ± 1 (9%) |
| | 11.5 ± 2.2 (37%) | 4.0 ± 2.3 (74%) | 8 ± 1 (29%) |
| | 14.5 ± 1.7 (23%) | 7.1 ± 2.4 (26%) | 9 ± 2 (41%) |
| | 17.2 ± 4.1 (7%) | | 13 ± 2 (21%) |

The errors associated with the value of the diameters and walls are equal to a standard deviation.

Unlike the others, the micrographs shown in (c) and (d) were acquired using a 400 mesh copper grid coated with a carbon film, due to their limited length.

Table 1 shows statistical data on the measurement of the outer diameters, inner channels, and the number of walls for both samples, undecorated and decorated. The data were obtained by showing a histogram of the number of times the value of the outer diameter of the nanotubes has been counted, for example, as shown in Figure 2; this number must be in 1 nm intervals and fit with a suitable Gaussian number. The values shown in Table 1 are equal to the maximum of the Gaussian curve, with the associate errors equal to one sigma and the percentages in parentheses being obtained in such a way that the sum of the areas included in the Gaussian curves is equal to 100.

Using high resolution images, we can directly count the number of nanotube walls, measure the distance between the walls, and verify the presence of structural defects in the nanotube, such as the closing of the inner channel, the breakage of one or more walls, the presence of amorphous or crystalline carbon on the external walls, and the presence of nanoparticles of the catalyst and of materials used for internal and external decoration of the nanotubes. To perform both high resolution TEM (HRTEM) images and spectroscopic analysis we chose to self-support CNTs on mesh grids, without any additional support films. In this way we avoid the interferences due to any substrate on images and spectra. The presence of a carbon film, however, thin it may be, could worsen the contrast obtainable for the photographs and interfere with the nanotubes' EELS analysis.

Figure 3 shows some examples of HRTEM images of nanotubes with different numbers of carbon walls. In (a) a bundle of single-wall nanotubes, in (b) a three-wall nanotube (as an example of few-wall nanotube), and in (c) a nanotube with more than ten walls (as an example of many-wall nanotube) are shown. All the nanotubes have very few defects. In (b) and (c) it is possible to directly observe pieces of single graphene sheets onto the external surface of the nanotubes [24].

By HRTEM it is possible to accurately study CNTs defects at the atomic scale. Some very common nanotube defects can be observed in Figure 4(a). The inner channel is not well defined and is characterized by variable diameter. In

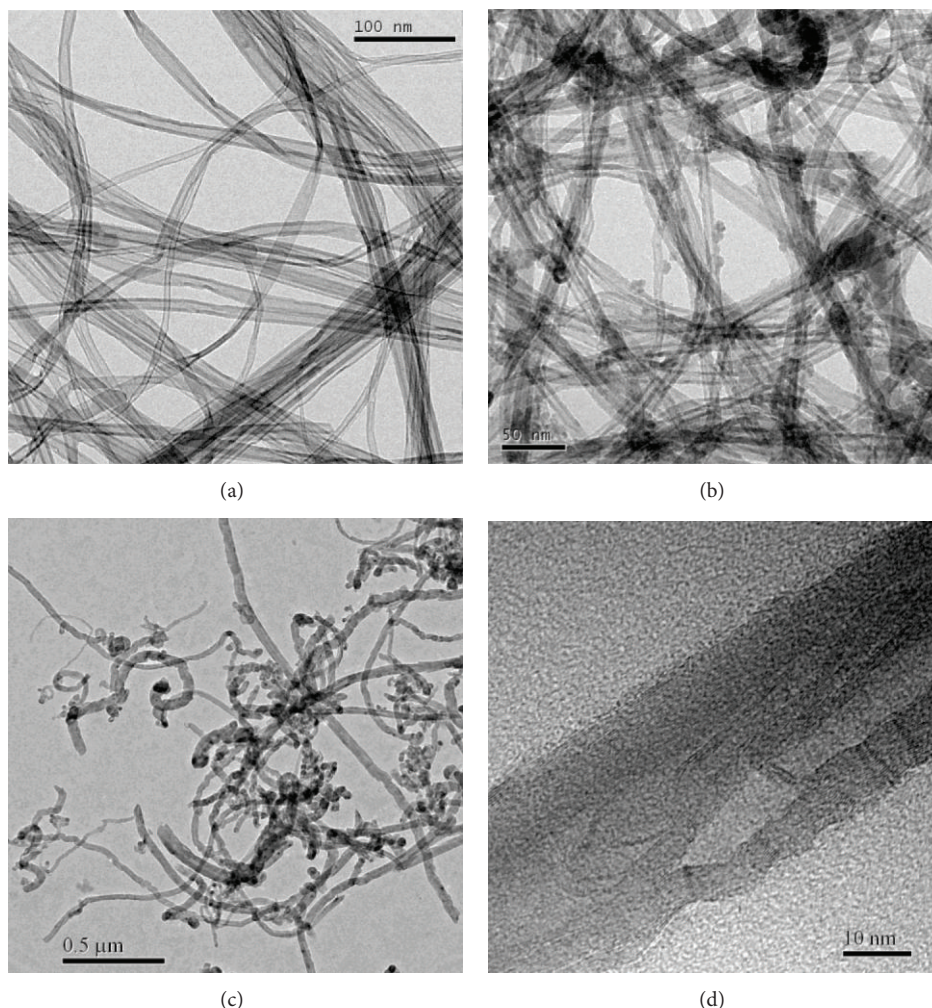


FIGURE 1: TEM images of (a) nondecorated nanotubes; (b) decorated nanotubes; (c) “bamboo-like” commercial nanotubes; (d) high resolution image of a bamboo-like nanotube.

many points the channel is broken by the carbon walls and onto the external nanotube surface numerous pieces of single graphene sheets crumpled up can be directly visualized. By HRTEM less common defects can also be visualized. Figure 4(b) shows a rupture of the carbon sheets is normal to the nanotube axis. Figure 4(c) shows a particular nanostructure where the internal channel was not created at all and the nanomaterial resembles a stack of “nanocups.”

Finally, a special mention for Figure 4(d) showing a very particular form of a spiral structure, in a way that we could speak of a carbon “nano-spring”: the number of carbon atoms linked in hexagonal rings with respect to that linked in pentagonal rings is such that the nanotube assumes the spiral configuration.

The composition of the elements of the nanotubes and nanoparticles can be analysed by EDX spectroscopy in a wide sample zone (of about 500 nm) including several CNTs and nanoparticles. Figure 5(a) shows an EDXS spectrum of carbon nanotubes while Figure 5(b) shows that of catalyst nanoparticles (Fe) and decoration material (Cu). The Au peak

is due to the grid and though it is very intense, it does not interfere with the sample peaks.

EELS spectroscopy allowed us to select single nanostructures and acquire C-K edge spectra as reported in Figure 6(a). One of the greatest potentials of EELS spectroscopy is the exact spatial localization of the acquired data. Indeed, with special apertures, it is possible to acquire the spectra coming only from a selected portion of the sample, around 50 nm. As an example, in Figure 6(a) (inset) the portion of the nanotube, from which the spectra were acquired, is shown.

Figure 6(a) shows the C-K edge, where the near edge fine peaks are clearly visible located at 284 eV and 290 eV that can be ascribed to the carbon molecular orbitals π^* and σ^* , respectively. This C-K edge resulted to be well structured, indicating the highly ordered carbon atomic arrangement of the CNT.

Figure 6(b) shows an EELS spectrum with the C-K, O-K, and Fe-L_{2,3} edges. It is important to detect the presence of O to assess whether the sample has undergone an oxidation process, and if so, how much. Even the occurrence of

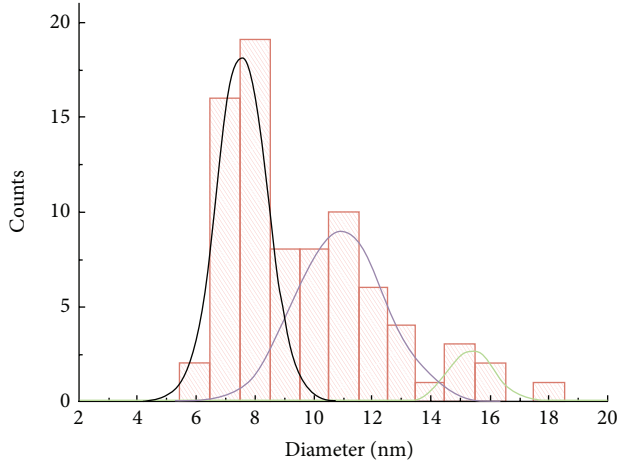


FIGURE 2: Histogram of the measurements of the outer diameter of the undecorated nanotube sample.

nanoparticles on the CNTs surface can be monitored by EELS spectroscopy that can furnish the nanoparticle chemical composition (Figure 6(b)). In this case, the percentage of C, O, and Fe atoms, obtained by the analysis of the C-K, O-K, and Fe-L_{2,3} edge electron energy loss spectrum, are N_C (at%) = 94 ± 13 , N_O (at%) = 5 ± 1 , and N_{Fe} (at%) = 1.0 ± 0.5 .

EELS spectra contain not only compositional information but even important structural information. In particular, EXELFS spectroscopy is a very powerful technique because with suitable Fourier analysis it is possible to obtain information on the spatial distribution of the first-neighbour atoms with respect to the excited atom, just like the data obtained by spectroscopy using X-rays (extended X-ray absorption fine structure, EXAFS); however, in order to use the last one, a synchrotron is required, and in any case it provides information mediated over the entire sample [58, 59]. Moreover, EXELFS spectroscopy gives structural information along the direction defined by the transferred momentum vector \mathbf{q} which is defined by the acquisition geometry. This is important in the case of anisotropic materials such as graphite or low-dimensional carbon materials. In our experiments we acquired spectra with a wide collection angle (20 mrad), giving rise to a \mathbf{q} vector mainly oriented normal to the electron beam [60].

Figure 7(a) shows the EXELFS and EXAFS oscillations obtained from C-K spectra of the type shown in Figure 6, but for a sample of HOPG. These spectra were compared with the oscillations obtained from a theoretical simulation of the structure of the graphite, using a FEFF v. 8.2 software program [61]. The HOPG is used because it is a material especially suited for comparison with multiwalled carbon nanotubes (MWCNT). In Figure 7(a), it can be clearly observed that the two different techniques—the other using electrons (EXELFS) and the one using X-rays (EXAFS) for exciting the carbon atom in the graphite—reproduce in the same way the energy position of the spectral structures, although the intensities are slightly different. These spectral structures, regardless of the way they were generated, are

closely correlated to the structural parameters of the graphite. It can also be noted that the experimental data, which are very similar to each other, are in agreement with the theoretical simulation calculated with FEFF, considering a sphere of graphite with a radius of about 8 Å. The corresponding Fourier transforms, Figure 7(b), allow tracing the graphite in terms of distances between atoms. Indeed, if considering that the excited atom corresponds to zero ($R = 0$), the positions of the neighbouring atoms correspond to peaks in the radial distribution function $F(R)$ in the direction defined by \mathbf{q} .

The radial distribution of the graphite plane, both for EXAFS and EXELFS, is very well reproduced. Except for any phase factors, it can be concluded that

- (i) the first peak represents the first neighbours at 1.42 Å,
- (ii) the second peak represents the ones at 2.46 Å and 2.83 Å,
- (iii) the third one includes all the atoms at a distance from the excited atom between 3.35 Å and 4 Å.

This result is confirmed by the theoretical simulation performed by FEFF (blue curve).

Figure 8 shows our experimental C-K spectrum concerning a MWCNT. The EXELFS extraction can only be performed with the absence of an O peak, since this would interfere with the extended oscillations of the carbon, making it virtually impossible to process the data. It can be observed that it is very difficult to detect the oscillations in the part of the curve with the highest energies by sight inspection only.

In particular, Figure 8(b) shows the comparison between the EXELFS oscillations of the HOPG and of the MWCNT. With regard to the latter, it is important to note that EXELFS spectrum of MWCNT shows no traces of oxygen (530 eV) and nitrogen (410 eV); this characteristic leads to believe that they are well-graphitized tubes, since nitrogen and oxygen can create structural defects in the walls of the tube. It can also be deduced that in this sample of multiwalled nanotubes there are no metallic precursors such as iron (720 eV), utilized in the synthesis process. The Fourier transforms in Figure 8(c), calculated on the basis of the spectrum in Figure 8(a), highlight that the two structures of the graphite and multiwalled nanotubes are quite similar but not identical [53, 62]. The results reported here are relative to the atomic structure along the CNT axis, due to the \mathbf{q} orientation in our experimental conditions. What has been described up to now shows in particular the enormous potentials of this technique for the study of the structure in terms of inter-atomic distances around an excited atom.

Figure 9 shows the results concerning the NED experiment on two MWCNTs: a 7-wall versus a 14-wall nanotube. Insets report the relative diffractograms, obtained by the same technique and published by Zuo et al. for a 2 walls nanotube [63]. As it can be observed in the insets, when the number of walls decreases the diffraction spots that lose their circular symmetry and become undefined smears. This feature is in good agreement with the case of 2 walls where Zuo et al. observed wide lines organized in hexagonal symmetry [63]. In our case, we observe the same behaviour, coming from

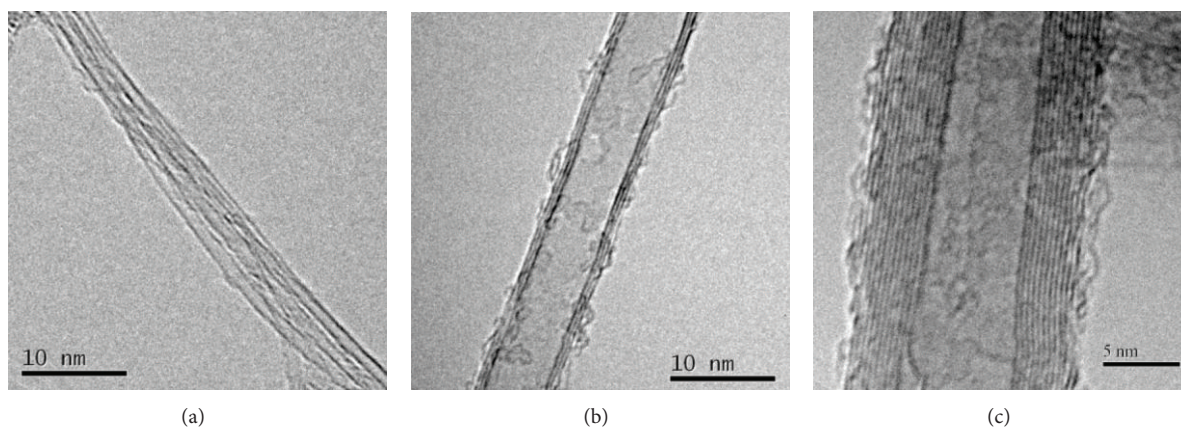


FIGURE 3: Examples of high resolution TEM images of carbon nanotubes with different numbers of walls: (a) bundle of single-wall nanotubes; (b) three-wall nanotube; (c) multiwall nanotube.

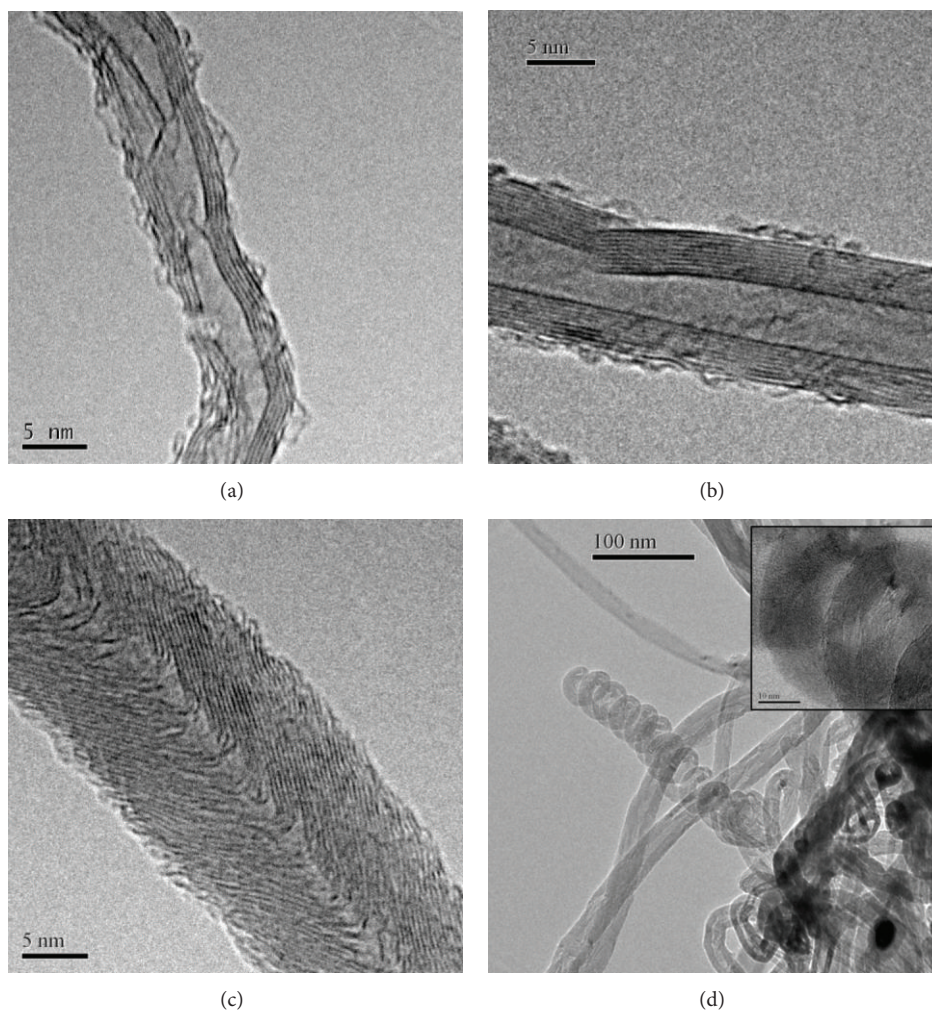


FIGURE 4: Examples of carbon nanotubes defects: ((a) and (b)) nanotube wall breaks and presence of amorphous carbon and graphene pieces onto the nanotube external surface; (c) a “nano-cup”; (d) a “nano-spring” (the inset shows the high resolution spring coils).

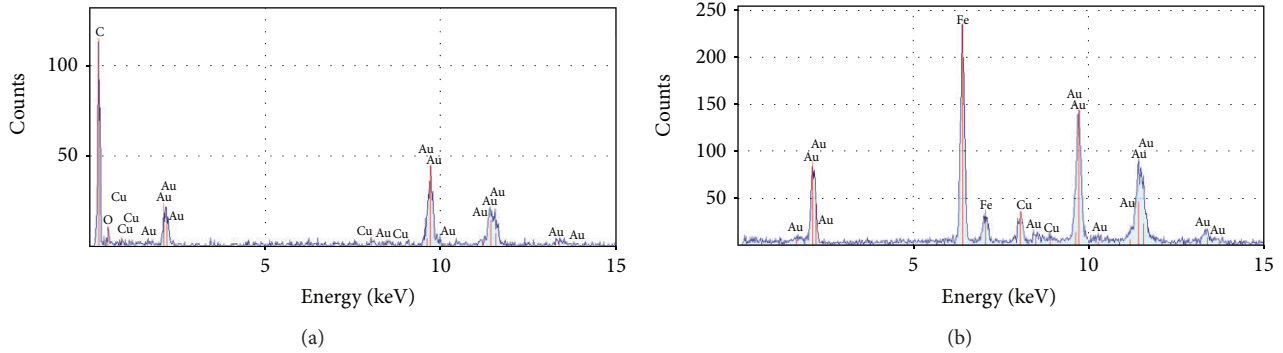


FIGURE 5: EDX spectra of: (a) carbon nanotubes; (b) nanoparticles of catalyst (Fe) and decoration material (Cu).

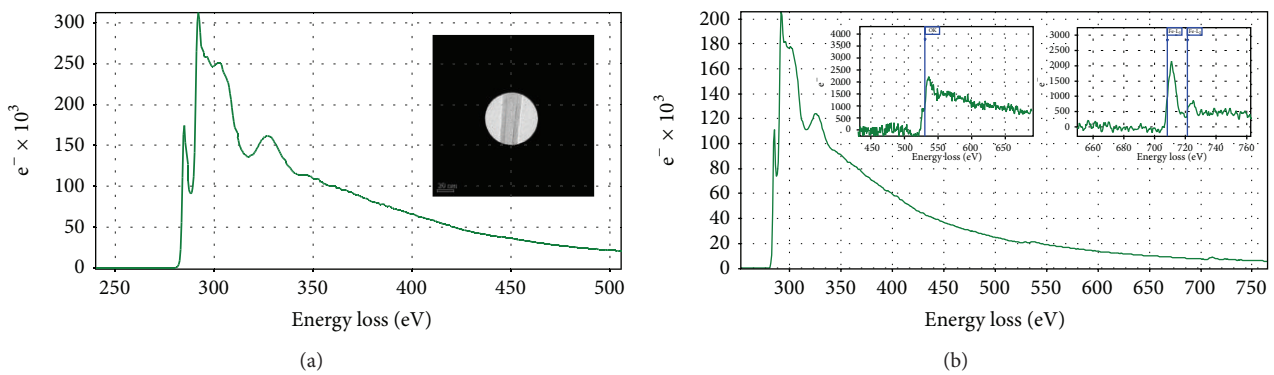


FIGURE 6: ELNES (a) and EXELFS (b) spectra for the carbon K edge of the undecorated sample. In the inset the portion of nanotube from which ELNES spectrum was acquired is shown. Spectra evidence of the carbon K edge (284 eV), the oxygen K edge (532 eV), and the iron $L_{2,3}$ edge (708 eV).

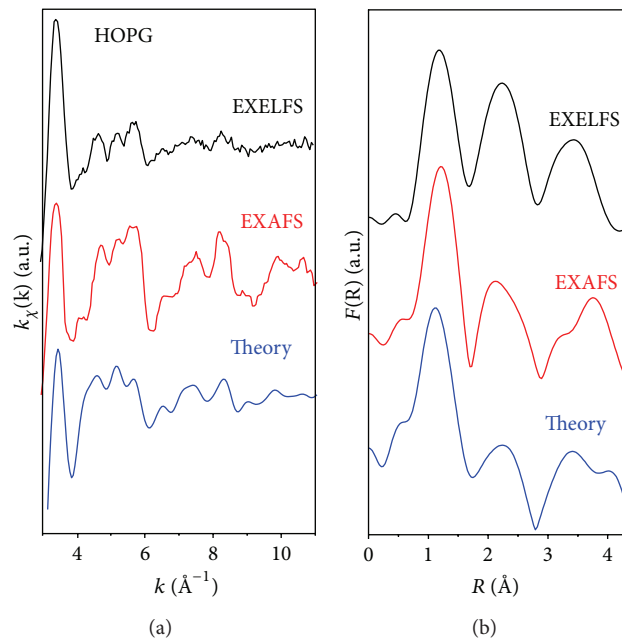


FIGURE 7: (a) Comparison of the oscillations of the EXELFS and EXAFS spectra and of the theoretical curve, for HOPG (a) and (b) the corresponding Fourier transforms.

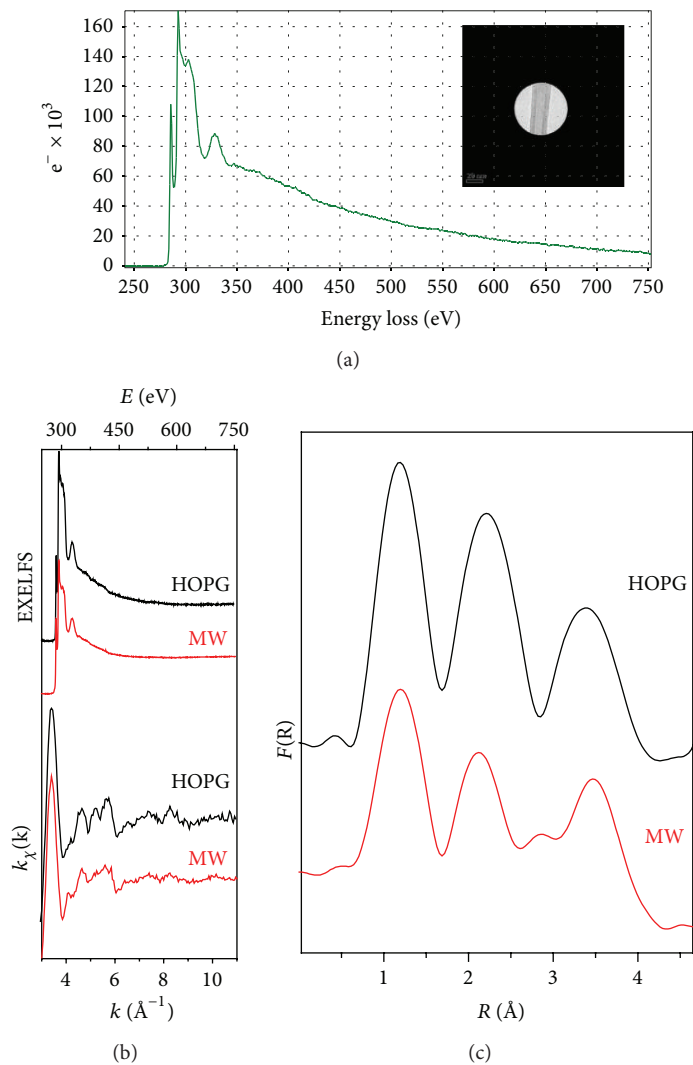


FIGURE 8: EXELFS of an undecorated MWCNT (a), comparison of HOPG and the MWCNT of the EXELFS spectra and their processing to highlight the oscillations (b), and of the corresponding Fourier transforms (c).

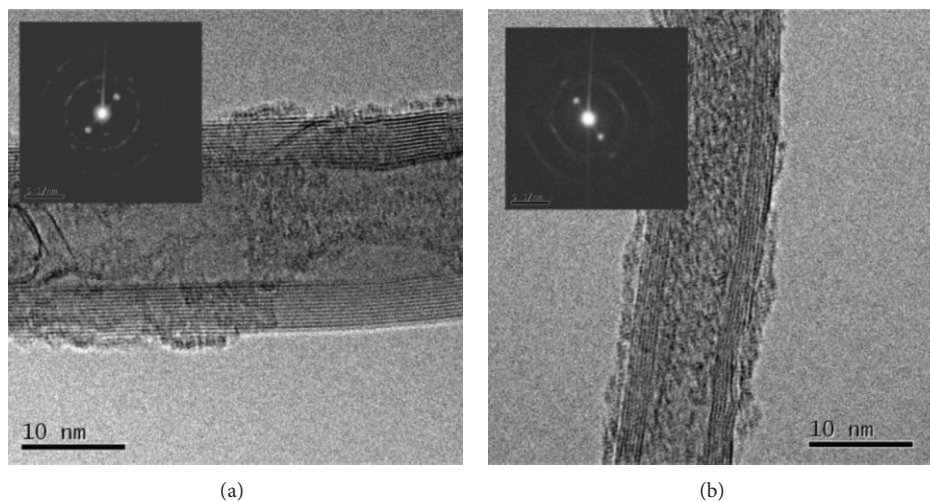


FIGURE 9: HRTEM images of a 14-wall CNT (a) and a 7-wall CNT (b). The insets show the relative NED patterns.

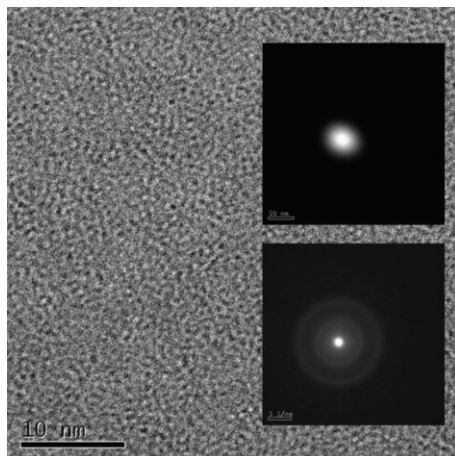


FIGURE 10: TEM image of a thin amorphous carbon film. The upper inset shows the electron beam spot size employed to obtain the nanodiffraction shown in the lower inset.

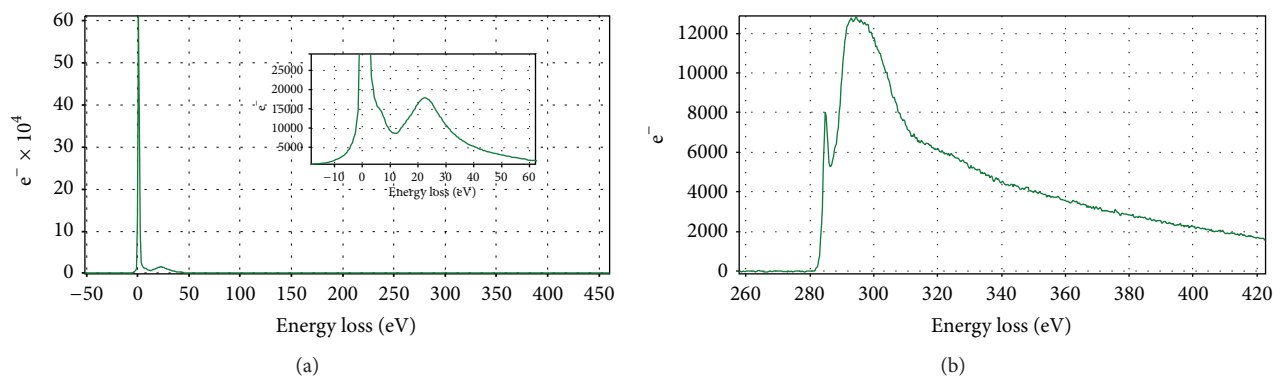


FIGURE 11: EELS spectra of the amorphous carbon film: (a) zero-loss and low-energy peaks employed to calculate the film thickness; ELNES carbon K edge obtained in imaging mode (b).

a circular diffraction pattern with spots for 14 walls CNT to an hexagonal pattern with undefined lines for 7 walls CNT.

We stress that only the combined application of EXELFS and NED techniques can give unique structural information about nanomaterials made of few carbon atoms not disposed in ordered symmetries as in a perfect crystal.

3.2. Two-Dimensional Nanomaterials. Self-sustaining, very thin flakes of amorphous carbon and graphene were investigated up to the formation of the graphite structure. With the aim to gain information about their thickness, morphology, defects, elemental composition, and atomic structure we performed both conventional and HRTEM imaging, X-ray and EELS microanalysis, and NED and NEELS experiments.

Figure 10 shows the flat morphology of a thin amorphous film. HRTEM was unable to visualize any structure and only a fine grain can be observed. This is the reason why this kind of carbon material is generally used as substrate in conventional transmission electron microscopy. The fine grain is due to the local order existing in the C atomic distribution that renders the sample not ideally amorphous. This fact is also observed in the NED pattern reported in the inset, where two

very wide and fair Debye rings are visible. Microanalytical results obtained by both EDXS and EELS did not show any contamination or oxidation (data not shown). In the case of Figure 11, we obtained a thickness value of $T = 15$ nm. Figure 11(b) shows the C-K edge from this amorphous carbon flake where, contrary to the case of CNT of Figure 6, only the peak located at 284 eV, ascribed to the C molecular orbital π^* , is clearly visible. Also the NES resulted to be less structured, in agreement with the quasiamorphous atomic arrangement.

In Figure 12 crumpled graphene flakes, obtained by open single wall nanotubes and imaged at low magnification, are reported.

In Figure 13(a), we report a HRTEM image of a graphene flake, compared to the area illuminated by the electron nanobeam (the bright area in the dark background shown in panel (b)). The diffraction pattern was recorded from exactly the same area as the HRTEM image in panel (b) and under identical illumination conditions. The small beam size makes it possible to probe small volumes of the specimen and, hence, to observe features induced by defects with high spatial resolution. For instance, in region 1 (circled) of Figure 13(a), the diffraction pattern shows twin sixfold symmetric spots (Figure 13(c)) corresponding to a couple of flat layers with

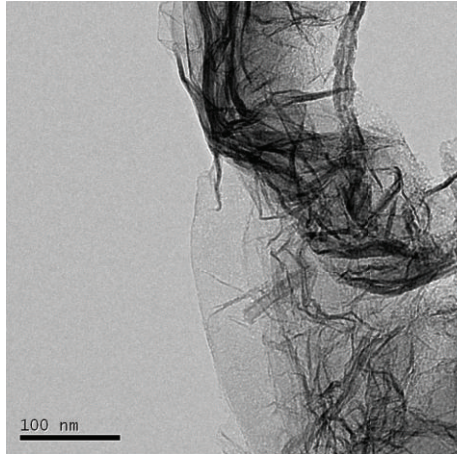


FIGURE 12: TEM image of graphene flakes.

different stacking. The inner spots correspond to (10) lattice planes and the outer spots to (11) planes [24]. The spot separation indicates the good crystalline structure of the layers [64]. In region 2 of Figure 13(a) in which extensive folding of sheets is present, the diffraction pattern is markedly changed. Here, the c -axis is locally tilted from the incident beam direction and the sequence of layers along the c -axis is imaged. The sheet periodicity induces two closely spaced peaks in Figure 13(d) from which an interlayer spacing, d_c , is estimated [64]. Moreover, Debye rings due to the lack of crystallographic orientation among the sheets are also present.

Depending on the degree of folding, some diffraction patterns have intermediate features between those of Figures 13(c) and 13(d). An example is given in Figure 13(e) in which the sixfold symmetry of (10) and (11) spots indicates a higher degree of ordering than panel (d). We stress that the observed changes are completely averaged out using conventional SAED, due to the lack of spatial resolution. Since the thinnest flakes are just a few tens of nanometers wide, the beam intensity in SAED is too low to record a diffraction pattern from them.

Figure 14 shows low-loss spectra recorded by the nanobeam technique from the same area of the NED reported before. In this region the energy loss is mainly due to the plasmon excitation occurring in the material. Collective excitation of the free electrons strongly depends on the geometry of the samples and, in the case of 2D nanomaterials, the shape and intensity of the plasmon can give useful information about the sample thickness.

The position of plasmon modes indicates a double layer, as found with diffraction. Moreover, for the two thinnest spectra, the plasmon resonance shows a plateau-like shape (Figure 14(a)), as expected for systems with less than 5 layers [65].

By probing areas of increasing thickness, we observe a continuous shift of the plasmon peaks towards the graphite values and a progressive increase of their intensity. The correlation between the shift and the relative thickness t_r is shown in Figure 14(b) in which the position of

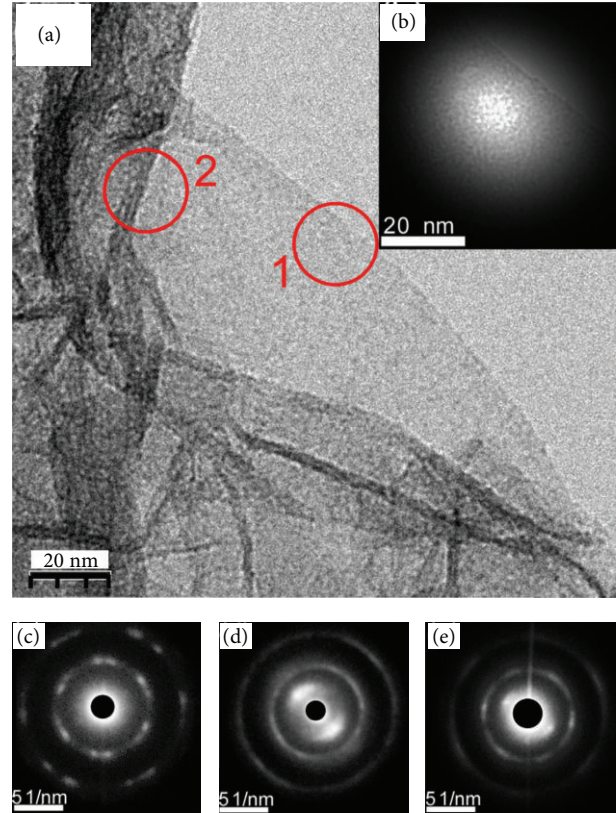


FIGURE 13: (a) High resolution TEM image of a graphene flake compared to the area illuminated by the electron nanobeam shown in panel (b). (c)–(e) NED patterns of different regions of the flakes. Panel (c) is recorded from the area labeled as 1 in panel (a), while panel (d) from the region 2. Panel (e) corresponds to an area of the sample (not shown) having intermediate folding. Reprinted with permission from [64].

the π -resonance is plotted as a function of t_r . If we assume, in accordance with electron diffraction data, that the thinnest sample is a double layer of graphene, the absolute thickness can be estimated by the calibration curve of Figure 14(b). It is worth noting that conventional analysis, based on EELS data only, would have overestimated t_r in this range of thickness, as it generally occurs for very thin films [47].

Finally, in Figure 15(a) a well-formed HOPG flake is reported, together with the relative nanobeam diffraction pattern and C-K edge spectrum. In this case, the thickness is 84 nm. In Figure 15(a), at low magnification, the superposition of multiple layers is indicated by the different gray levels. The inset shows the NED hexagonal pattern, demonstrating that the flake c -axis is parallel to the beam. In Figure 15(b), the C-K edge is reported. At this stage, the material cannot be considered bidimensional, but it is now a perfect tridimensional crystal.

4. Conclusions

The data obtained confirm that transmission electron microscopy is a suitable technique for the characterization

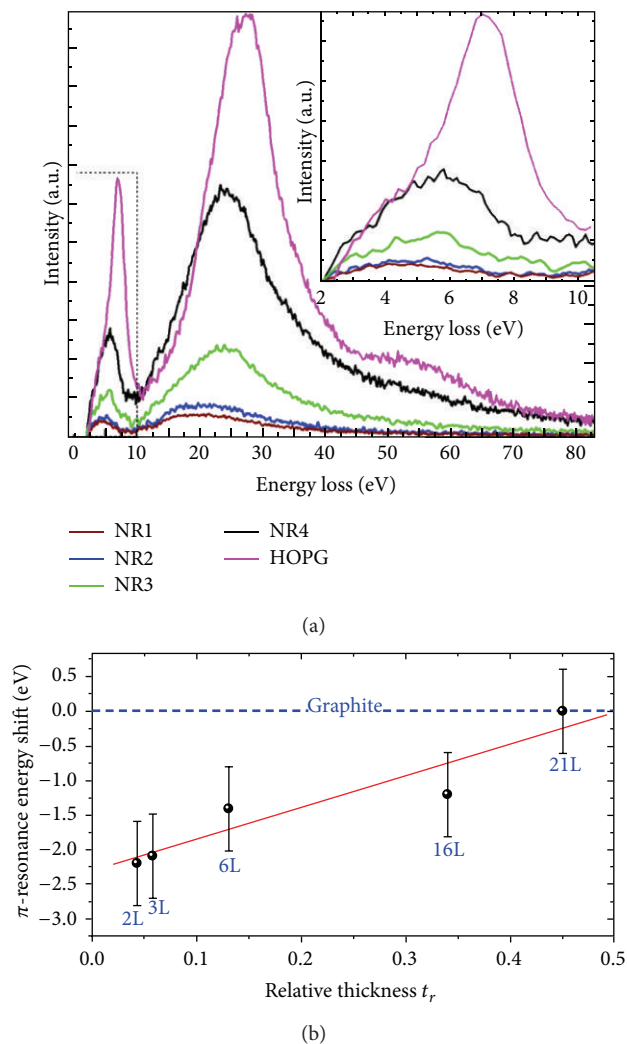
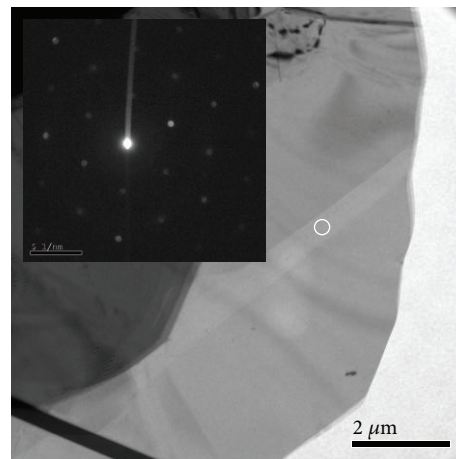


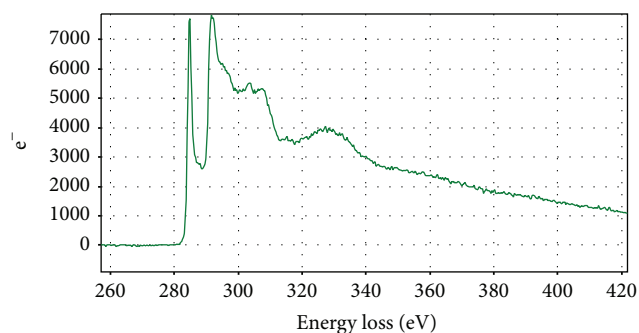
FIGURE 14: (a) EELS spectra obtained from graphene flakes of different thicknesses and from graphite. In the inset, the π -resonance peaks are blown up. (b) Energy shift of π -resonance as a function of the relative thickness t_r , obtained from the EELS spectra with the log-ratio method. The number of layers (L) is estimated by calibrating the EELS thickness data to the results of electron diffraction, assuming a linear dependence of t_r on the number of layers. Reprinted with permission from [64].

of low-dimensional carbon nanostructures, due to the possibility of providing morphological, structural, and elemental composition information. Likewise, with respect to the other techniques for the characterization of nanostructures that are also highly useful, for example, Raman spectroscopy, electron microscopy enables to obtain data with accurate spatial localization on limited zones of nanostructures (few nanometers), and not just on massive samples of micrometric or larger sizes, in which the information inevitably comes from a large number of objects, in which there may be unwanted contaminants that may generate signals that irretrievably alter the data coming from the sample under analysis.

The use of EELS allows to obtain highly localized spectroscopic and structural information, but it is somewhat



(a)



(b)

FIGURE 15: TEM image of a HOPG flake (a). The white circle shows the point from where the NED (inset) and the C-K edge spectrum (b) are taken.

limited by the low detection efficiency for heavy elements, the intrinsic difficulty of the technique in supplying quantitative information on the amount of elements contained in the sample, and by the highly specialized skills required for performing ELNES and EXELFS analysis.

The importance of being able to correctly characterize low-dimensional carbon nanostructures will undoubtedly increase due to the increasing use and dissemination of these materials. Characterization is a necessary step also for developing synthesis processes. As far as accurate the checking of the parameters may be (e.g., in the case of chemical vapour deposition, the substrate temperature, the vacuum level, the pressure of the gaseous precursor, and the sizes of the catalyst), the nanotubes synthesized in different processes will necessarily have differing characteristics. This is an aspect familiar to those who, for example, purchase commercial nanotubes which, though bought from the same supplier, are completely different from one lot to the next.

Indeed, in various cases, because of the analyses conducted with TEM microscopy, it has been ascertained that the synthesis process of the commercial nanotubes had not been properly performed, with the consequent production of nanotubes full of structural defects, often of the bamboo-like type, with a different configuration with respect to the typical

ones of a nanotube, that is, without a defined number of walls, a uniform outer diameter, and an inner channel. Characterization is likewise fundamental for correctly assessing the influence that nanomaterials can have on biological systems, since the presence of any negative effects is closely related to the type of nanostructure involved.

Finally, the analysis of the airborne particulate is increasingly affected by the presence of nanostructural materials intentionally produced by man, which are dispersed in working and living environments. Electron microscopy, with its powerful analytical instruments, proves particularly useful in the characterization of ultrafine particles in which there is a wide variety of structures, differing in composition, size, state of aggregation, and origin. These investigations are fundamental both to correlate the presence of biological effects on man with real harmful agent and to identify man-made and other sources most responsible for the production of nanometric airborne particulate.

Conflict of Interests

The authors report no conflict of interests.

References

- [1] S. Iijima, "Helical microtubules of graphitic carbon," *Nature*, vol. 354, no. 6348, pp. 56–58, 1991.
- [2] A. Oberlin, M. Endo, and T. Koyama, "High resolution electron microscope observations of graphitized carbon fibers," *Carbon*, vol. 14, no. 2, pp. 133–135, 1976.
- [3] A. Oberlin, M. Endo, and T. Koyama, "Filamentous growth of carbon through benzene decomposition," *Journal of Crystal Growth*, vol. 32, no. 3, pp. 335–349, 1976.
- [4] P. Avouris, T. Hertel, R. Martel, T. Schmidt, H. R. Shea, and R. E. Walkup, "Carbon nanotubes: nanomechanics, manipulation, and electronic devices," *Applied Surface Science*, vol. 141, no. 3–4, pp. 201–209, 1999.
- [5] C. Dekker, "Carbon nanotubes as molecular quantum wires," *Physics Today*, vol. 52, no. 5, pp. 22–28, 1999.
- [6] A. D. Maynard, P. A. Baron, M. Foley, A. A. Shvedova, E. R. Kisin, and V. Castranova, "Exposure to carbon nanotube material: aerosol release during the handling of unrefined single-walled carbon nanotube material," *Journal of Toxicology and Environmental Health A*, vol. 67, no. 1, pp. 87–107, 2004.
- [7] O. V. Salata, "Applications of nanoparticles in biology and medicine," *Journal of Nanobiotechnology*, vol. 2, article 3, 2004.
- [8] R. Beckman, E. Johnston-Halperin, Y. Luo, J. E. Green, and J. R. Heath, "Bridging dimensions: demultiplexing ultrahigh-density nanowire circuits," *Science*, vol. 310, no. 5747, pp. 465–468, 2005.
- [9] J. Y. Chen, A. Kutana, C. P. Collier, and K. P. Giapis, "Materials science: electrowetting in carbon nanotubes," *Science*, vol. 310, no. 5753, pp. 1480–1483, 2005.
- [10] J. Chen, V. Perebeinos, M. Freitag et al., "Applied physics: bright infrared emission from electrically induced excitons in carbon nanotubes," *Science*, vol. 310, no. 5751, pp. 1171–1174, 2005.
- [11] J.-P. Salvetat, J.-M. Bonard, N. B. Thomson et al., "Mechanical properties of carbon nanotubes," *Applied Physics A*, vol. 69, no. 3, pp. 255–260, 1999.
- [12] D. Jariwala, V. K. Sangwan, L. J. Lauhon, T. J. Marks, and M. C. Hersam, "Carbon nanomaterials for electronics, optoelectronics, photovoltaics, and sensing," *Chemical Society Reviews*, vol. 42, no. 7, pp. 2824–2860, 2013.
- [13] V. Shanov, W. Cho, R. Malik et al., "CVD growth, characterization and applications of carbon nanostructured materials," *Surface and Coatings Technology*, vol. 230, pp. 77–86, 2013.
- [14] M. S. Arnold, J. L. Blackburn, J. J. Crochet et al., "Recent developments in the photophysics of single-walled carbon nanotubes for their use as active and passive material elements in thin film photovoltaics," *Physical Chemistry Chemical Physics*, vol. 15, no. 36, pp. 14896–14918, 2013.
- [15] S. Parveen, S. Rana, and R. Figueiro, "A review on nanomaterial dispersion, microstructure, and mechanical properties of carbon nanotube and nanofiber reinforced cementitious composites," *Journal of Nanomaterials*, vol. 2013, Article ID 710175, 19 pages, 2013.
- [16] J. Zhao and J. Zhu, "Electron microscopy and in situ testing of mechanical deformation of carbon nanotubes," *Micron*, vol. 42, no. 7, pp. 663–679, 2011.
- [17] C. Wang, K. Takei, T. Takahashi, and A. Javey, "Carbon nanotube electronics-moving forward," *Chemical Society Reviews*, vol. 42, no. 7, pp. 2592–2609, 2013.
- [18] Y. Wu, X. Lin, and M. Zhang, "Carbon nanotubes for thin film transistor: fabrication, properties, and applications," *Journal of Nanomaterials*, vol. 2013, Article ID 627215, 16 pages, 2013.
- [19] M. Terrones, "Sharpening the chemical scissors to unzip carbon nanotubes: crystalline graphene nanoribbons," *ACS Nano*, vol. 4, no. 4, pp. 1775–1781, 2010.
- [20] M. Terrones, A. R. Botello-Méndez, J. Campos-Delgado et al., "Graphene and graphite nanoribbons: morphology, properties, synthesis, defects and applications," *Nano Today*, vol. 5, no. 4, pp. 351–372, 2010.
- [21] S. Dutta and S. K. Pati, "Novel properties of graphene nanoribbons: a review," *Journal of Materials Chemistry*, vol. 20, no. 38, pp. 8207–8223, 2010.
- [22] Y. Zhu, S. Murali, W. Cai et al., "Graphene and graphene oxide: synthesis, properties, and applications," *Advanced Materials*, vol. 22, no. 35, pp. 3906–3924, 2010.
- [23] Y. H. Wu, T. Yu, and Z. X. Shen, "Two-dimensional carbon nanostructures: fundamental properties, synthesis, characterization, and potential applications," *Journal of Applied Physics*, vol. 108, no. 7, Article ID 071301, 2010.
- [24] J. C. Meyer, A. K. Geim, M. I. Katsnelson, K. S. Novoselov, T. J. Booth, and S. Roth, "The structure of suspended graphene sheets," *Nature*, vol. 446, no. 7131, pp. 60–63, 2007.
- [25] U. Bangert, M. H. Gass, A. L. Bleloch, R. R. Nair, and A. K. Geim, "Manifestation of ripples in free-standing graphene in lattice images obtained in an aberration-corrected scanning transmission electron microscope," *Physica Status Solidi A*, vol. 206, no. 6, pp. 1117–1122, 2009.
- [26] A. Fasolino, J. H. Los, and M. I. Katsnelson, "Intrinsic ripples in graphene," *Nature Materials*, vol. 6, no. 11, pp. 858–861, 2007.
- [27] A. Grill, "Diamond-like carbon: state of the art," *Diamond and Related Materials*, vol. 8, no. 2–5, pp. 428–434, 1999.
- [28] A. K. Bhaskar, V. N. Deshmukh, and L. Prajapati, "Carbon nanotube as a drug delivery system: a review," *International Journal of Pharmacy and Technology*, vol. 5, no. 2, pp. 2695–2711, 2013.
- [29] M. Roldo and D. G. Fatouros, "Biomedical applications of carbon nanotubes," *Annual Reports on the Progress of Chemistry C*, vol. 109, pp. 10–35, 2013.

- [30] World Health Organization, *Health Aspects of Air Pollution Results From the WHO Project "Systematic Review of Health Aspects of Air Pollution in Europe"*, WHO Regional Office for Europe, Copenhagen, Denmark, 2004.
- [31] G. Oberdörster, E. Oberdörster, and J. Oberdörster, "Nanotoxicology: an emerging discipline evolving from studies of ultrafine particles," *Environmental Health Perspectives*, vol. 113, no. 7, pp. 823–839, 2005.
- [32] C.-W. Lam, J. T. James, R. McCluskey, S. Arepalli, and R. L. Hunter, "A review of carbon nanotube toxicity and assessment of potential occupational and environmental health risks," *Critical Reviews in Toxicology*, vol. 36, no. 3, pp. 189–217, 2006.
- [33] Department of Employment and Workplace Relations, Australian Safety and Compensation Council, "A review of the potential occupational health and safety implication of nanotechnology," Final Report, 2006.
- [34] National Institute for Occupational Safety and Health, *Approaches to Safe Nanotechnology: An Information exchange with NIOSH*, Department of Health and Human Services, Centers for Disease Control and Prevention, 2007.
- [35] C. L. Ursini, D. Cavallo, A. M. Fresegna et al., "Study of cytotoxic and genotoxic effects of hydroxyl-functionalized multiwalled carbon nanotubes on human pulmonary cells," *Journal of Nanomaterials*, vol. 2012, Article ID 815979, 9 pages, 2012.
- [36] Y.-Y. Guo, J. Zhang, Y.-F. Zheng, J. Yang, and X.-Q. Zhu, "Cytotoxic and genotoxic effects of multi-wall carbon nanotubes on human umbilical vein endothelial cells in vitro," *Mutation Research*, vol. 721, no. 2, pp. 184–191, 2011.
- [37] K. Yang and Z. Liu, "In vivo biodistribution, pharmacokinetics, and toxicology of carbon nanotubes," *Current Drug Metabolism*, vol. 13, no. 8, pp. 1057–1067, 2012.
- [38] S. Sharifi, S. Behzadi, S. Laurent, M. Laird Forrest, P. Stroeve, and M. Mahmoudi, "Toxicity of nanomaterials," *Chemical Society Reviews*, vol. 41, no. 6, pp. 2323–2343, 2012.
- [39] C. J. Humphreys, "Radiation effects," *Ultramicroscopy*, vol. 28, no. 1–4, pp. 357–358, 1989.
- [40] R. F. Egerton, P. Li, and M. Malac, "Radiation damage in the TEM and SEM," *Micron*, vol. 35, no. 6, pp. 399–409, 2004.
- [41] Z. Liu, Q. Zhang, and L.-C. Qin, "Accurate determination of atomic structure of multiwalled carbon nanotubes by non-destructive nanobeam electron diffraction," *Applied Physics Letters*, vol. 86, no. 19, Article ID 191903, pp. 1–3, 2005.
- [42] A. Béché, J. L. Rouvière, J. P. Barnes, and D. Cooper, "Strain measurement at the nanoscale: comparison between convergent beam electron diffraction, nanobeam electron diffraction, high resolution imaging and dark field electron holography," *Ultramicroscopy*, vol. 131, pp. 10–23, 2013.
- [43] J. M. Zuo, M. Gao, J. Tao, B. Q. Li, R. Twesten, and I. Petrov, "Coherent nano-area electron diffraction," *Microscopy Research and Technique*, vol. 64, no. 5–6, pp. 347–355, 2004.
- [44] W. Robards and A. J. Wilson, *Procedures in Electron Microscopy*, John Wiley & Sons, New York, NY, USA, 1998.
- [45] D. B. Williams and C. B. Carter, *Transmission Electron Microscopy: A Textbook For Materials Science*, Springer, New York, NY, USA, 1996.
- [46] R. F. Egerton, "Electron energy-loss spectroscopy in the TEM," *Reports on Progress in Physics*, vol. 72, no. 1, Article ID 016502, 2009.
- [47] R. F. Egerton, *Electron Energy Loss Spectroscopy in the Electron Microscope*, Plenum Press, New York, NY, USA, 1996.
- [48] R. F. Egerton, "Formulae for light-element microanalysis by electron energy-loss spectrometry," *Ultramicroscopy*, vol. 3, no. 2, pp. 243–251, 1978.
- [49] R. F. Egerton, "K-shell ionization cross-sections for use in microanalysis," *Ultramicroscopy*, vol. 4, no. 2, pp. 169–179, 1979.
- [50] R. D. Leapman, P. Rez, and D. F. Mayers, "K, L, and M shell generalized oscillator strengths and ionization cross sections for fast electron collisions," *The Journal of Chemical Physics*, vol. 72, no. 2, pp. 1232–1243, 1980.
- [51] D. R. Liu and L. M. Brown, "Influence of some practical factors on background extrapolation in EELS quantification," *Journal of Microscopy*, vol. 147, no. 1, pp. 37–49, 1987.
- [52] C. Colliex, "Electron energy loss in the electron microscope," in *Advances in Optical and Electron Microscopy*, R. Barer and V. E. Cosslet, Eds., vol. 9, Academic Press, New York, NY, USA, 1984.
- [53] P. Castrucci, F. Tombolini, M. Scarselli et al., "Anharmonicity in single-wall carbon nanotubes as evidenced by means of extended energy loss fine structure spectroscopy analysis," *Physical Review B*, vol. 75, no. 3, Article ID 035420, 2007.
- [54] J. J. Ritsko, N. O. Lipari, P. C. Gibbons, and S. E. Schnatterly, "Core excitons in tetrathiafulvalene-tetracyanoquinodimethane (TTF-TCNQ)," *Physical Review Letters*, vol. 37, no. 16, pp. 1068–1071, 1976.
- [55] M. de Crescenzi, F. Tombolini, M. Scarselli et al., "Visible and near ultraviolet photocurrent generation in carbon nanotubes," *Surface Science*, vol. 601, no. 13, pp. 2810–2813, 2007.
- [56] M. Scarselli, C. Scilletta, F. Tombolini et al., "Photon harvesting with multi wall carbon nanotubes," *Superlattices and Microstructures*, vol. 46, no. 1–2, pp. 340–346, 2009.
- [57] M. Scarselli, C. Scilletta, F. Tombolini et al., "Multiwall carbon nanotubes decorated with copper nanoparticles: effect on the photocurrent response," *Journal of Physical Chemistry C*, vol. 113, no. 14, pp. 5860–5864, 2009.
- [58] B. K. Teo and D. C. Joy, *EXAFS Spectroscopy, Techniques, and Applications*, Plenum Press, New York, NY, USA, 1981.
- [59] B. K. Teo, *EXAFS: Basic Principles and Data Analysis*, vol. 9 of *Inorganic Chemistry Concepts*, Springer, Heidelberg, Germany, 1986.
- [60] M. Diociaiuti, L. Lozzi, M. Passacantando, S. Santucci, P. Picozzi, and M. de Crescenzi, "Influence of non-dipolar terms on the Cu $L_{2,3}$ and $M_{2,3}$ electron energy loss fine structure (EELFS) spectra in transmission and reflection mode," *Journal of Electron Spectroscopy and Related Phenomena*, vol. 82, no. 1–2, pp. 1–12, 1996.
- [61] P. Castrucci, F. Tombolini, M. Scarselli et al., "Comparison of the local order in highly oriented pyrolytic graphite and bundles of single-wall carbon nanotubes by nanoscale extended energy loss spectra," *Journal of Physical Chemistry C*, vol. 113, no. 12, pp. 4848–4855, 2009.
- [62] P. Castrucci, M. Scarselli, M. de Crescenzi et al., "Packing-induced electronic structure changes in bundled single-wall carbon nanotubes," *Applied Physics Letters*, vol. 87, no. 10, Article ID 103106, 2005.
- [63] J. M. Zuo, I. Vartanyants, M. Gao, R. Zhang, and L. A. Nagahara, "Atomic resolution imaging of a carbon nanotube from diffraction intensities," *Science*, vol. 300, no. 5624, pp. 1419–1421, 2003.
- [64] L. Persichetti, F. Tombolini, S. Casciardi et al., "Folding and stacking defects of graphene flakes probed by electron nanobeam," *Applied Physics Letters*, vol. 99, no. 4, Article ID 041904, 2011.

- [65] T. Eberlein, U. Bangert, R. R. Nair et al., "Plasmon spectroscopy of free-standing graphene films," *Physical Review B*, vol. 77, no. 23, Article ID 233406, 2008.

Research Article

Catalyst Design Using Nanoporous Iron for the Chemical Vapor Deposition Synthesis of Single-Walled Carbon Nanotubes

Tarek M. Abdel-Fattah,¹ Phillip A. Williams,² Russell A. Wincheski,² and Qamar A. Shams³

¹ Applied Research Center, Thomas Jefferson National Accelerator Facility and Department of Molecular Biology and Chemistry, Christopher Newport University, Newport News, VA 23606, USA

² Nondestructive Evaluation Sciences Branch, NASA Langley Research Center, Hampton, VA 23681, USA

³ Aeronautics Systems Engineering Branch, NASA Langley Research Center, Hampton, VA 23681, USA

Correspondence should be addressed to Tarek M. Abdel-Fattah; fattah@cnu.edu

Received 15 March 2013; Accepted 18 September 2013

Academic Editor: Nadya Mason

Copyright © 2013 Tarek M. Abdel-Fattah et al. This is an open access article distributed under the Creative Commons Attribution License, which permits unrestricted use, distribution, and reproduction in any medium, provided the original work is properly cited.

Single-walled carbon nanotubes (SWNTs) have been synthesized via a novel chemical vapor deposition (CVD) approach utilizing nanoporous, iron-supported catalysts. Stable aqueous dispersions of the CVD-grown nanotubes using an anionic surfactant were also obtained. The properties of the as-produced SWNTs were characterized through atomic force microscopy and Raman spectroscopy and compared with purified SWNTs produced via the high-pressure CO (HiPCO) method as a reference, and the nanotubes were observed with greater lengths than those of similarly processed HiPCO SWNTs.

1. Introduction

Of vital importance to the next generation of aerospace vehicles are structurally resilient, lightweight, and space durable materials and structural health monitoring sensors that can withstand environmental rigors. Carbon nanotubes (CNTs) have shown significant potential in these and a wide variety of other applications on the basis of their remarkable mechanical and electronic properties [1, 2]. CNTs, however, can be produced by several synthesis methods, with some methods better suited for particular applications. Single-walled carbon nanotubes (SWNTs) grown between suspended pillars, for example, have been studied as potential nanoscale power lines [3]. A dominant approach for the synthesis of SWNTs is chemical vapor deposition (CVD), including the high-pressure carbon monoxide (HiPCO) technique [4]. In this paper, we present an alternative CVD method of synthesis of SWNTs for use in composites and aerospace sensor applications. Specifically, we describe the novel incorporation of iron catalysts within a mesoporous material for CNT production.

Mesoporous materials (MPMs) are a class of inorganic molecular sieves [5]. Pores in the nanoscale range of 2 to 100 nm make these materials very attractive as shape selective

adsorbents or catalysts. Generally, the MPM is prepared in solution by supramolecular assembly of organic molecules as templates with an inorganic precursor. In the original synthesis of MPMs is the formation of rod-like micelles using charged surfactants such as alkyltrimethylammonium surrounded by inorganic species followed by the polymerization of silicates to form the framework of MPMs. The pore size of MPMs can be tuned in the nanosize range based on the number of carbon atoms in the alkyl chain length of surfactants from about 1.6 nm for eight carbon atoms to 3.8 nm for 16 carbon atoms. The pores are separated by silicate walls whose thickness is in the range of 0.8 to 1.6 nm. As-synthesized MPMs have specific crystalline phases that can be controlled by varying the ratio of surfactants to silicates. For example, MCM-41 has independent channels; MCM-48 has cubic and interconnected channels, whereas MCM-50 has a layered structure. Organic templates can be removed by heating as-synthesized MPM without significant structural changes except for MCM-50, in which the structure collapses. After calcination, MCM-41 and MCM-48 materials have large surface area per gram ratios making them excellent candidates for pollutant remediation and catalysts for large molecules. For example, Abdel-Fattah et al. have synthesized

close-ended multiwalled carbon nanotubes (MWNTs), in the absence of metal catalysts, from sucrose using mesoporous MCM-41 silicate as templates [6].

Varying the templates from charged surfactants to neutral surfactants such as primary amines produces hexagonal mesoporous silica materials (HMS) with thicker walls in the range of 2-3 nm [5, 7]. Introducing active metal centers in the framework makes HMS very appealing as catalysts for SWNT synthesis. In a previous study, Abdel-Fattah and Pinnavaia had demonstrated the introduction of different active centers, such as Sn and Fe, into the framework of HMS for ring opening polymerization of lactic acid [8]. Later on, other research studies had studied also the synthesis and the catalytic properties of Fe-HMS materials such as phenol hydroxylation [9, 10].

In this paper, we report the use of iron modified HMS (Fe-HMS) as catalysts for the synthesis of high-quality SWNTs by chemical vapor deposition. The as-produced nanotubes exhibit the ability for dispersion in aqueous surfactant solutions and for selective deposition on surfaces via dielectrophoresis. Material characterization is documented with atomic force microscopy and Raman spectroscopy and compared with HiPCO SWNTs as a reference.

2. Experimental Details

2.1. Catalyst Design and Preparation. Fe-HMS samples with Fe 2% were prepared with dodecylamine as a directing agent, as described in our previous work [8]. Briefly, the synthesis comprised the mixture of two solutions: one containing tetraethyl orthosilicate, iron (III) ethoxide, and another containing dodecylamine in water/ethanol mixture. After mixing, this solution was then stirred at room temperature for 24 h. The solid, denoted Fe-HMS, was recovered by filtration, washed with hot water, and air-dried. Amines occluded in the mesopores were removed by calcination in air at 773 K for 4 h.

2.2. CNT Growth. Carbon nanotubes were formed by CVD of methane at 1193 K on the 2% Fe-HMS (2% Fe), as catalysts. For a methane CVD experiment, 10 mg of 2% Fe-HMS was placed in a quartz tube mounted in a tube furnace. An argon flow was passed through the quartz tube as the furnace was heated to reach 1193 K. The Ar flow was then replaced by methane (99% purity) at a flow rate of 1500 cm³/min under 1.25 atm head pressure. The methane flow lasted for 10 min and subsequently was replaced by argon, and the furnace was cooled to room temperature.

2.3. CNT Aqueous Surfactant Suspension and Dielectrophoresis. As-produced, raw CNT material was suspended in deionized water containing 0.5 wt% sodium dodecylbenzene sulfonate (NaDDBS), an anionic surfactant [9]. The aqueous suspension was subjected to a protocol, similar to that described by Paredes and Burghard [10], consisting of centrifugation followed by agitation in an ultrasonic bath to disperse the CNTs uniformly in the suspension. Immediately before deposition onto a substrate, the suspension was sonicated again for 25 minutes. As a reference, separate, aqueous NaDDBS suspensions of purified HiPCO SWNTs were also

processed via the aforementioned protocol for comparison with CNTs synthesized via the Fe-HMS CVD method.

Substrates consisted of oxidized Si samples with metal electrodes first patterned via photolithography for large scale contacts and then followed by electron beam lithography for submicron features and contacts to the CNTs. Thin metal films of electrode pairs with 1.5 μm spacing, patterned via electron beam lithography, were deposited via thermal evaporation of Cr as an adhesion layer followed by Au onto the substrates. CNTs were then deposited and aligned to the electrode pair locations through use of dielectrophoresis (DEP) [11, 12]. For the dielectrophoretic deposition, an AC voltage of 10.0 V peak to peak with a frequency of 2.0 MHz was applied between the 1.5 μm gaps of the electrode pairs for 10 minutes as a droplet of the CNT suspension was placed on the samples.

2.4. Material Characterization and Analysis. 2% Fe-HMS catalyst samples were characterized by X-ray diffraction (XRD) using a Philips PW 1710 diffractometer (Cu K α radiation). The nitrogen adsorption and desorption isotherms at 77.4 K were measured using a Coulter Omnisorp 360 CX sorptometer or ASAP 2010 sorptometer via a continuous adsorption procedure. Before the measurements, samples were evacuated overnight at 423 K and 10⁻⁶ Torr. The BET surface area was calculated from the linear part of the BET plot. The pore size distributions were calculated from adsorption branches of N₂ adsorption/desorption isotherms based on the BJH model. Transmission electron microscopy (TEM) was performed to characterize the structure and morphology of the Fe-HMS catalysts material. Also, scanning electron microscopy (SEM) equipped with energy dispersive spectroscopy (EDS) was used to determine chemical composition of the Fe-HMS catalyst materials.

The physical and morphological properties of the CNTs were characterized via Raman spectroscopy and atomic force microscopy (AFM). Raman spectra were acquired with a Kaiser dispersive Raman spectrometer operating with an excitation laser of 785 nm wavelength. Topographic images from atomic force microscopy were obtained using a Digital Instruments-Veeco Metrology Group Nanoscope IIIa Multimode AFM in tapping mode. AFM analysis software was used for CNT diameter and length measurements within instrumental resolutions of 0.1 nm and 50 nm, respectively. AFM image quality for samples of CNTs deposited from aqueous surfactant suspension onto patterned substrates was improved through the removal of excess surfactant on the samples by washing the samples with methanol and then heating them to 180°C in air for 2.5 hours, as has also been reported previously in other studies [9, 10].

3. Results and Discussion

The results of the preparation of the Fe-HMS catalysts were investigated via several techniques. Figure 1 shows the structure and morphology of a 2% Fe-HMS sample analyzed by TEM. The TEM image qualitatively reveals the uniform periodic, porous wormhole structure of the 2% Fe-HMS and the range of 25 nm similar to that already reported for pure silica HMS [7]. Quantitative analysis of the XRD data

TABLE I: Chemical composition of 2% Fe-HMS catalyst via EDS.

| Element | Normalized weight % | Atom % |
|---------|---------------------|------------------|
| C | 51.18 ± 0.30 | 60.84 ± 0.36 |
| O | 37.58 ± 0.33 | 33.53 ± 0.29 |
| Al | 0.22 ± 0.01 | 0.12 ± 0.01 |
| Si | 10.68 ± 0.06 | 5.43 ± 0.03 |
| Fe | 0.34 ± 0.06 | 0.09 ± 0.01 |

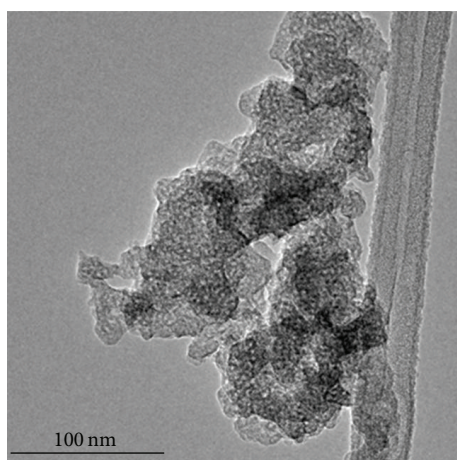


FIGURE 1: TEM image of 2% Fe-HMS catalysts.

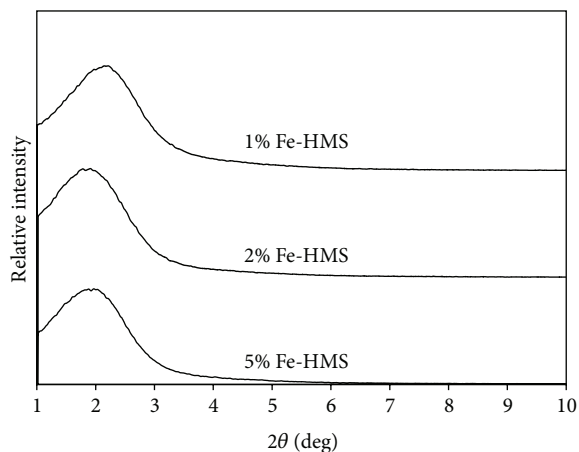
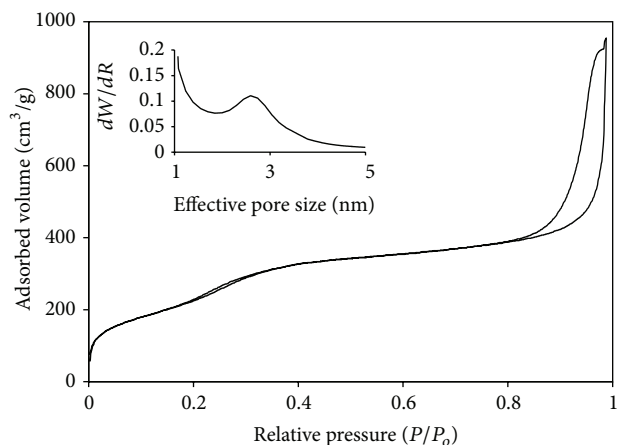


FIGURE 2: Powder XRD pattern of Fe-HMS samples with varying concentrations of Fe.

for the Fe-HMS materials, as shown in Figure 2, indicates an XRD pattern composed of a unique broad peak at 2.0° , similar to that already reported for pure silica HMS [7]. The N_2 adsorption/desorption isotherms in Figure 3 show that the solids contain regular pores of ca. 2.7 nm diameter. Comparison with the X-ray powder data gives an average wall thickness of ca. 1.8 nm, in agreement with previous determinations. Further, calculations of the BET surface area of the 2% Fe-HMS catalysts yield an average surface area of $980 \text{ m}^2/\text{g}$.

FIGURE 3: The nitrogen adsorption and desorption isotherms for 2% Fe-HMS, measured at 77.4 K. The inset presents the Horvath-Kawazoe pore size distribution curve for the Fe-HMS catalysts, where dW/dR is the derivative of the normalized N_2 volume adsorbed with respect to the pore size (diameter) of the adsorbent.

To characterize the elemental chemical composition of the 2% Fe-HMS catalysts, energy dispersive spectroscopy (EDS) via X-ray analysis was performed on the samples in the SEM. Table 1 lists a summary of the quantitative EDS results. The EDS results indicate that the ratio of Fe (0.34%) to Si (10.68%) is 3.2% (Ratio = $(0.34\%/10.68\%) \times 100$.) that is close to the synthetic ratio, 2%.

Raman spectroscopy was performed on the CNTs synthesized via CVD incorporating the Fe-HMS catalysts. Analysis of Raman spectra, in Figure 4(a), of the CNTs in aqueous surfactant suspension deposited on an oxidized silicon substrate shows the presence of G- ($\sim 1590 \text{ cm}^{-1}$) and D- ($\sim 1300 \text{ cm}^{-1}$) bands, indicating the graphitic structure of the synthesized nanotubes. The D- and G-bands are understood to be due to the sp^3 and sp^2 carbon bonding, respectively [13]. The intensity and shape of these peaks give information on the electrical properties of the CNTs. The low D-to-G-band intensity ratio suggests the presence of high-quality, low-defect CNTs. Also, as can be seen in Figure 4(b), the Raman spectra reveal the presence of several low ($200\text{--}350 \text{ cm}^{-1}$) Raman-shift peaks. These peaks are understood to be exhibited by the SWNTs due to their radial breathing vibrational modes (RBM) [13]. Using the empirical relationship between the Raman RBM peak frequency ω_{RBM} and the SWNT diameter d_{SWNT} for HiPCO SWNTs, $\omega_{\text{RBM}} = 239 (\text{cm}^{-1} \text{ nm})/d_{\text{SWNT}}$

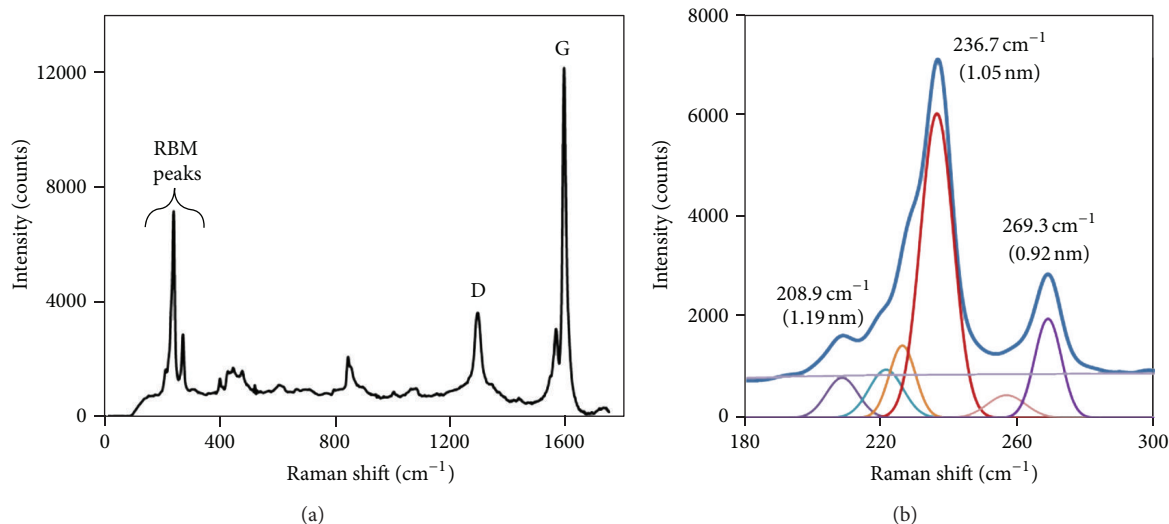


FIGURE 4: (a) Raman spectrum from carbon nanotubes grown by the novel CVD method incorporating Fe-HMS. (b) The presence of the radial breathing mode (RBM) peaks indicates the presence of single-walled carbon nanotubes (SWNTs).

(nm) + 8.5 cm^{-1} , one can estimate the diameters of the CVD SWNTs exhibiting the RBM spectral peaks [14, 15]. For example, the RBM peak at 236.7 cm^{-1} in Figure 4(b) corresponds to an individual nanotube of 1.05 nm in diameter. Also, from the so-called Kataura plot and the relationship between diameter and chirality, we estimate that the RBM peak originated from the presence of a semiconducting SWNT [16, 17]. Thus, the Raman spectra characteristics (i.e., the presence of RBM, D-band, and G-band peaks) of the material produced by this novel method are clear evidence not only for the synthesis of carbon nanotubes but also for the specific synthesis of single-walled carbon nanotubes.

Physical characteristics of the CVD-grown SWNT material were also evaluated by spin-coating an aliquot of the aqueous NaDDBS surfactant suspension of the as-produced SWNTs onto oxidized Si substrates and acquiring topographic images via AFM. AFM observations show that the as-produced CVD SWNT material displayed less surface debris and contaminants compared to depositions of purified HiPCO SWNTs. Since the CVD SWNT material was not subjected to any purification process, the observation indicates that the raw CVD SWNT material has a lower percentage of amorphous carbon and residual catalyst after synthesis than its HiPCO SWNT counterpart. Another possible explanation is that the residue and byproducts of the raw CVD SWNT material are easily dissolved or are not soluble at all in the aqueous surfactant solution used in this study. This property of the as-produced CVD SWNTs minimizes prior processing to purify the nanotube material and reduces the potential damage that can be incurred on CNTs subjected to various purification and chemical processing techniques [18–20].

AFM images also show the presence of small bundles of SWNTs, and typical diameters (as determined from measurements of the height of the bundles) are 3.0–15.0 nm with measured lengths from 2.0 to $10.0 \mu\text{m}$. In contrast, typical lengths of bundles of similarly processed (in terms of suspension in solvents), purified HiPCO SWNTs are

measured in the range of 500 nm to $3.0 \mu\text{m}$. The longest SWNT bundle observed in one scan is over $20.0 \mu\text{m}$ long with a measured average diameter of $2.0 \pm 0.4 \text{ nm}$. This single nanotube or bundle of nanotubes spans the entire length of the image scan and is shown in Figures 5(b) and 5(c).

Controlling the parameters and the materials used in CVD process can explain the observed long SWNTs. First, choosing methane as the hydrocarbon source in CVD process is one of the key factors because methane is known to be the most kinetically stable hydrocarbon that undergoes the least pyrolytic decomposition at high temperatures. Therefore, the carbon atoms needed for nanotube growth are supplied by the catalytic decomposition of methane on supported iron surfaces. This is one of the primary reasons that the synthesized nanotubes are nearly free of amorphous carbon coatings caused by self-pyrolysis of methane. A second parameter is the CVD reaction time. Limiting the CVD reaction times to only 10 min at a high methane flow rate prevented the formation of amorphous carbon, producing longer SWNTs, rather than the buildup of carbon as an overcoating to form multiwalled nanotubes (MWCNTs). Thirdly, we find that Fe-HMS as a catalyst produces longer SWNTs due to large domain size (wall thickness) and active nanosize iron centers.

Controlling the deposition and alignment of CNTs onto substrates is often required for precise fabrication of nanotube sensor devices for various applications (strain, temperature, chemical sensing, etc.), and the use of dielectrophoretic assembly of CNTs (both MWNTs and SWNTs) has been investigated previously as a means to accomplish this task [21–25]. To explore the suitability of the CVD SWNTs grown in this study for device fabrication, dielectrophoresis (DEP) is used to attempt controlled deposition of the SWNTs. Briefly, a droplet of the SWNT NaDDBS suspension is placed on the lithographically patterned oxidized silicon substrate containing regions of metal thin film electrodes for concentrated assembly of the CNTs for 10 minutes while an electric field is

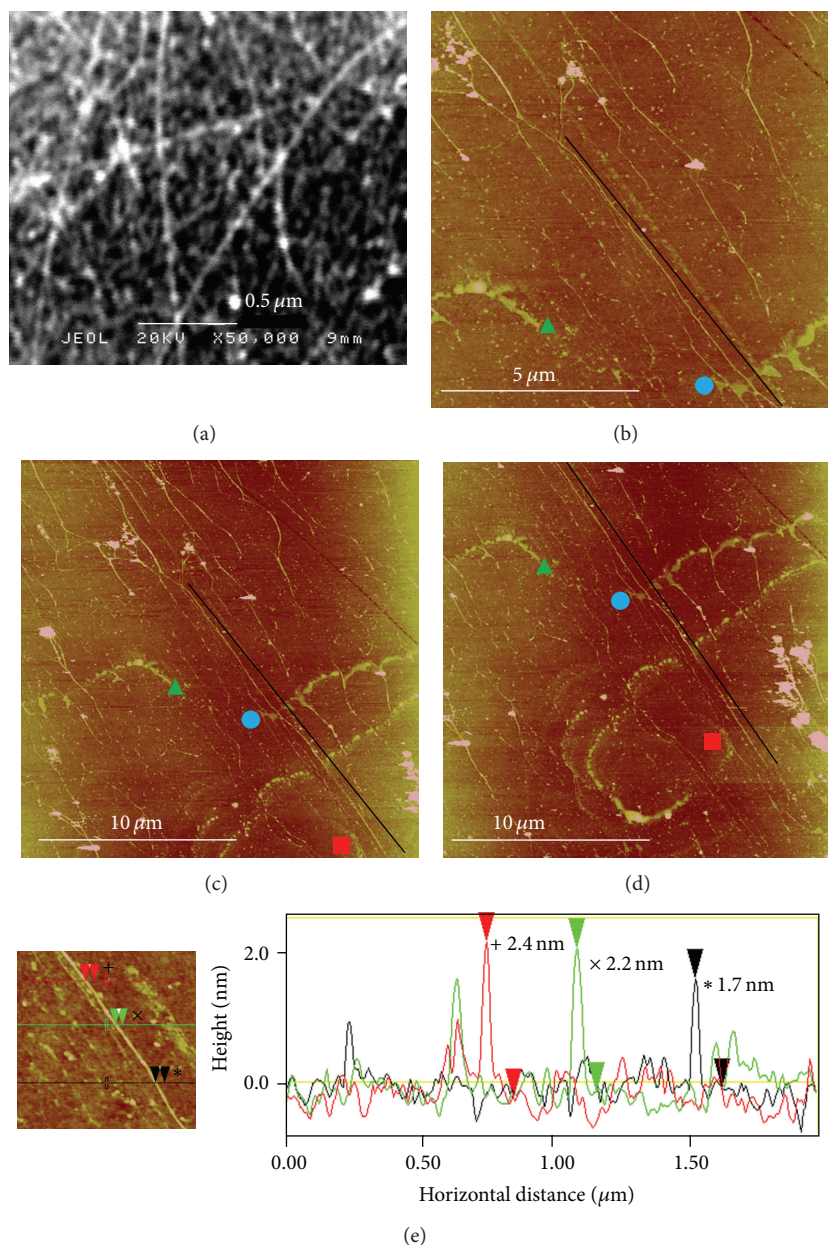


FIGURE 5: (a) SEM image of as-grown SWNTs on a silicon wafer using the CVD method incorporating Fe-HMS as catalyst. ((b)–(d)) AFM topographic images of as-grown SWNTs in aqueous NaDDBS solution spin-cast onto an oxidized silicon substrate; color range (height scale) in all AFM images is 10 nm. The images show minimal residual catalyst, small-diameter (3–15 nm) SWNT bundles, and a long ($>20 \mu\text{m}$) SWNT bundle. The long SWNT bundle is tracked in each image, shown beside the black line as a visual aid. The three markers (triangle, circle, and square) indicate corresponding locations in each image. (e) To determine the diameter of the long SWNT bundle, the height of the bundle was measured at several different positions along the length, yielding an average diameter of $2.0 \pm 0.4 \text{ nm}$.

applied between the electrodes. After the deposition, SWNTs are adhered successfully to the electrodes as observed via AFM. Figure 6 shows an AFM image of the lithographically patterned surface after the CNT deposition. The length of the as-grown CVD SWNTs, combined with their ability to be deposited controllably via DEP, facilitates the insertion of the CVD SWNTs into the design and fabrication of various sensor architectures, similar to previous studies by the authors for CNT strain sensors using HiPCO SWNTs [26, 27].

4. Conclusion

We have demonstrated a novel approach using Fe-HMS as catalyst in the CVD synthesis of CNTs. Fe-HMS has an ordered nanopore structure in the range of 25 nm and highly dispersed active iron sites. By combining the Fe-HMS structural properties and controlling the CVD parameters, they produced bundles and individual SWCNTs with observed lengths on the order of several microns. The raw, as-produced SWNT material was able to be dispersed in an aqueous

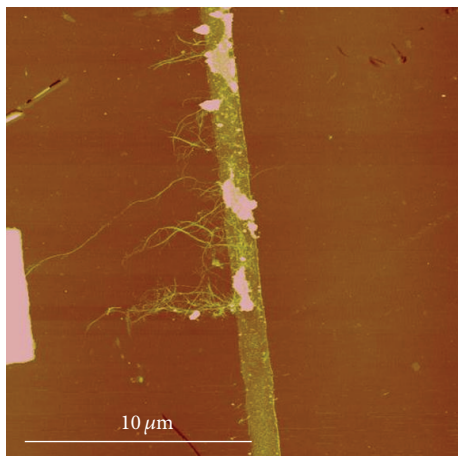


FIGURE 6: AFM image of as-produced SWNTs dispersed in aqueous surfactant solution and deposited via dielectrophoresis (DEP) onto an oxidized Si substrate patterned with metal electrodes; color range (height scale) is 50 nm.

surfactant suspension without any prior purification or processing, and SWNTs deposited from suspension showed minimal surface debris or contamination from residual catalysts. These features make SWNTs synthesized with this CVD method promising candidates for efficient incorporation into polymer composites and for aerospace applications as sensor devices.

Acknowledgments

The authors would like to thank C. Burkett and B. DeBono for helpful technical contributions to the experiments in this work. This work was partially performed when Dr. Phillip A. Williams held a National Research Council postdoctoral associate appointment at NASA Langley Research Center and Dr. Tarek M. Abdel-Fattah was a NASA Summer Faculty Research Fellow.

References

- [1] M. Meyyappan, *Carbon Nanotubes: Science and Applications*, Boca Raton, Mass, USA, CRC Press, 2004.
- [2] C. Hierold, *Carbon Nanotube Devices: Properties, Modeling, Integration and Applications*, Wiley-VCH, Weinheim, Germany, 2008.
- [3] E. Pop, D. Mann, J. Cao, Q. Wang, K. Goodson, and H. Dai, "Negative differential conductance and hot phonons in suspended nanotube molecular wires," *Physical Review Letters*, vol. 95, no. 15, Article ID 155505, 2005.
- [4] P. Nikolaev, M. J. Bronikowski, R. K. Bradley et al., "Gas-phase catalytic growth of single-walled carbon nanotubes from carbon monoxide," *Chemical Physics Letters*, vol. 313, no. 1-2, pp. 91-97, 1999.
- [5] P. T. Tanev and T. J. Pinnavaia, "Mesoporous silica molecular sieves prepared by ionic and neutral surfactant templating: a comparison of physical properties," *Chemistry of Materials*, vol. 8, no. 8, pp. 2068-2079, 1996.
- [6] T. M. Abdel-Fattah, E. J. Siochi, and R. E. Crooks, "Pyrolytic synthesis of carbon nanotubes from sucrose on a mesoporous silicate," *Fullerenes Nanotubes and Carbon Nanostructures*, vol. 14, no. 4, pp. 585-594, 2006.
- [7] P. T. Tanev and T. J. Pinnavaia, "A neutral templating route to Mesoporous molecular sieves," *Science*, vol. 267, no. 5199, pp. 865-867, 1995.
- [8] T. M. Abdel-Fattah and T. J. Pinnavaia, "Tin-substituted mesoporous silica molecular sieve (Sn-HMS): synthesis and properties as a heterogeneous catalyst for lactide ring-opening polymerization," *Chemical Communications*, no. 5, pp. 665-666, 1996.
- [9] M. F. Islam, E. Rojas, D. M. Bergey, A. T. Johnson, and A. G. Yodh, "High weight fraction surfactant solubilization of single-wall carbon nanotubes in water," *Nano Letters*, vol. 3, no. 2, pp. 269-273, 2003.
- [10] J. I. Paredes and M. Burghard, "Dispersions of individual single-walled carbon nanotubes of high length," *Langmuir*, vol. 20, no. 12, pp. 5149-5152, 2004.
- [11] H. A. Pohl, *Dielectrophoresis, the Behavior of Neutral Matter in Nonuniform Electric Fields*, Cambridge University Press, Cambridge, Mass, USA, 1978.
- [12] M. Dimaki and P. Bøggild, "Frequency dependence of the structure and electrical behaviour of carbon nanotube networks assembled by dielectrophoresis," *Nanotechnology*, vol. 16, no. 6, pp. 759-763, 2005.
- [13] S. Reich, C. Thomsen, and J. Maultzsch, *Carbon Nanotubes: Basic Concepts and Physical Properties*, Wiley-VCH, Weinheim, Germany, 2004.
- [14] H. Kuzmany, W. Plank, M. Hulman et al., "Determination of SWCNT diameters from the Raman response of the radial breathing mode," *European Physical Journal B*, vol. 22, no. 3, pp. 307-320, 2001.
- [15] M. J. O'Connell, *Carbon Nanotubes: Properties and Applications*, Taylor and Francis, Boca Raton, Mass, USA, 2006.
- [16] H. Kataura, Y. Kumazawa, Y. Maniwa et al., "Optical properties of single-wall carbon nanotubes," *Synthetic Metals*, vol. 103, no. 1-3, pp. 2555-2558, 1999.
- [17] J. Maultzsch, H. Telg, S. Reich, and C. Thomsen, "Radial breathing mode of single-walled carbon nanotubes: optical transition energies and chiral-index assignment," *Physical Review B*, vol. 72, no. 20, Article ID 205438, 2005.
- [18] C. A. Furtado, U. J. Kim, H. R. Gutierrez, L. Pan, E. C. Dickey, and P. C. Eklund, "Debundling and dissolution of single-walled carbon nanotubes in amide solvents," *Journal of the American Chemical Society*, vol. 126, no. 19, pp. 6095-6105, 2004.
- [19] M. Monthieux, B. W. Smith, B. Bouteaux, A. Claye, J. E. Fischer, and D. E. Luzzi, "Sensitivity of single-wall carbon nanotubes to chemical processing: an electron microscopy investigation," *Carbon*, vol. 39, no. 8, pp. 1251-1272, 2001.
- [20] J. G. Wiltshire, A. N. Khlobystov, L. J. Li, S. G. Lyapin, G. A. D. Briggs, and R. J. Nicholas, "Comparative studies on acid and thermal based selective purification of HiPCO produced single-walled carbon nanotubes," *Chemical Physics Letters*, vol. 386, no. 4-6, pp. 239-243, 2004.
- [21] M. Dimaki and P. Bøggild, "Waferscale assembly of Field-Aligned nanotube Networks (FANs)," *Physica Status Solidi A*, vol. 203, no. 6, pp. 1088-1093, 2006.
- [22] A. H. Monica, S. J. Papadakis, R. Oslander, and M. Paranjape, "Wafer-level assembly of carbon nanotube networks using dielectrophoresis," *Nanotechnology*, vol. 19, no. 8, Article ID 085303, 2008.

- [23] D. Sickert, S. Taeger, I. Kühne, M. Mertig, W. Pompe, and G. Eckstein, "Strain sensing with carbon nanotube devices," *Physica Status Solidi B*, vol. 243, no. 13, pp. 3542–3545, 2006.
- [24] D. Xu, A. Subramanian, L. Dong, and B. J. Nelson, "Shaping nanoelectrodes for high-precision dielectrophoretic assembly of carbon nanotubes," *IEEE Transactions on Nanotechnology*, vol. 8, no. 4, pp. 449–456, 2009.
- [25] J. Chung and J. Lee, "Nanoscale gap fabrication and integration of carbon nanotubes by micromachining," *Sensors and Actuators A*, vol. 104, no. 3, pp. 229–235, 2003.
- [26] B. Wincheski, M. Namkung, J. Smits, P. Williams, and R. Harvey, "Effect of alignment on transport properties of carbon nanotube/metallic junctions," in *Proceedings of the Materials Research Society Symposium Proceedings*, pp. 209–214, April 2003.
- [27] A. N. Watkins, J. L. Ingram, J. D. Jordan, R. A. Wincheski, J. M. Smits, and P. A. Williams, "Single wall carbon nanotube-based structural health sensing materials," in *Proceedings of the NSTI Nanotechnology Conference and Trade Show (NSTI Nanotech '04)*, vol. 3, pp. 149–152, March 2004.

Research Article

Functionalization of Graphene with Nitrile Groups by Cycloaddition of Tetracyanoethylene Oxide

Xiaojun Peng, Yang Li, Guoliang Zhang, Fengbao Zhang, and Xiaobin Fan

State Key Laboratory of Chemical Engineering, Key Laboratory for Green Chemical Technology, School of Chemical Engineering & Technology, Tianjin University, Tianjin 300072, China

Correspondence should be addressed to Xiaobin Fan; xiaobinfan@tju.edu.cn

Received 12 March 2013; Accepted 16 September 2013

Academic Editor: Sulin Zhang

Copyright © 2013 Xiaojun Peng et al. This is an open access article distributed under the Creative Commons Attribution License, which permits unrestricted use, distribution, and reproduction in any medium, provided the original work is properly cited.

Graphene has got considerable attention in both experimental and theoretical fields for its extraordinary properties. Covalent functionalization is an efficient strategy to render graphene additional properties and overcome its shortcomings such as zero band gap and nondispersibility in solvents. This study reports the synthesis and characterizations of a new kind of functionalized graphene, graphene-TCNEO, obtained by 1,3-dipolar cycloaddition. The graphene-TCNEO was systematically characterized by FTIR, Raman, XPS, SEM, TEM, and EDS mapping, and the covalent linkage between graphene and tetracyanoethylene oxide was firmly verified. Considering the great diversity of nitrile chemistry, the obtained graphene-TCNEO could be further transformed into other graphene-based derivatives with interesting properties.

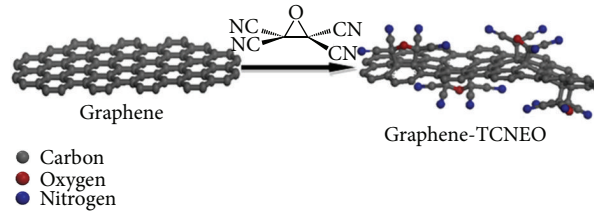
1. Introduction

Graphene has got considerable attention from both experimental and theoretical fields for its extraordinary properties, such as large surface area, unique mechanical, thermal, optical, and electronic transport properties [1–3]. Although these properties endow graphene great potential in many practical applications, its inertness nature, zero band gap, and nondispersibility in solvents [4] weaken its competitive strength in the synthesis of composites, semiconductors, sensors, and so forth [5–8]. Therefore, functionalization of graphene [9] has attracted widespread attention in the past few years. Covalent functionalization [10–12] of graphene with organic atoms or molecules is of particular interest, as it can combine the unique properties of each component while overcoming the shortcomings of graphene as mentioned above. Through direct attachment of organic atoms or molecules to the C=C bonds of graphene [13, 14] and the rich covalent reactions of oxygen-containing groups in graphene oxide [15–17], a variety of strategies to functionalize graphene for different application purposes have been demonstrated. In this study, we report a method to introduce abundant nitrile groups to pristine graphene by cycloaddition reaction of graphene with tetracyanoethylene oxide [18–20] (TCNEO) (Scheme 1).

2. Experimental Details

The process for the functionalized graphene material is shown in Scheme 1. The mixture of desired 10 mg graphene prepared by the methods of high temperature expansion [21], 60 mg TCNEO, and 200 mL solution of 1,2-dibromoethane were added into a 250 mL round-bottomed flask and stirred and heated at 140°C to reflux for 24 h under N₂ atmosphere. After the reaction completed, the reaction mixture was filtered through nylon membrane. The obtained filter cake was washed several times by anhydrous ethanol and deionized water, respectively. The final product was suspended in deionized water through sonication and dried under vacuum freeze-drying to obtain the desired graphene-TCNEO.

The graphene and functionalized graphene were characterized by infrared spectrum (FTIR) (Thermo-Nicolet 380), X-ray photoelectron spectroscopy (XPS) (PerkinElmer, PHI 1600 spectrometer), Raman spectroscopy (NT-MDT NTEGRA Spectra), scanning electron microscopy (SEM) (Hitachi S4800), high-resolution transmission electron microscopy (HRTEM) (Philips Tecnai G2 F20), and energy dispersive spectroscopy (EDS) (Hitachi S4800).



SCHEME 1: Synthesis of graphene-TCNEO hybrid materials.

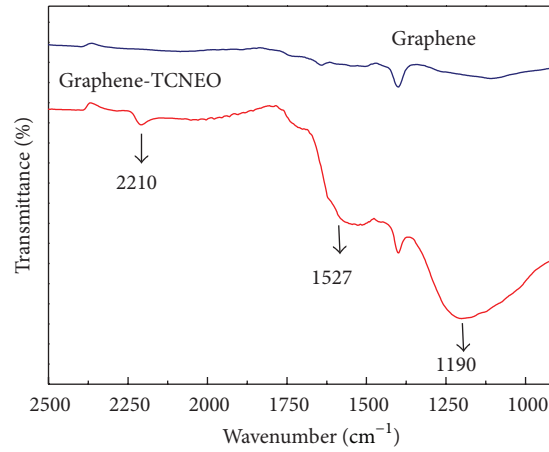
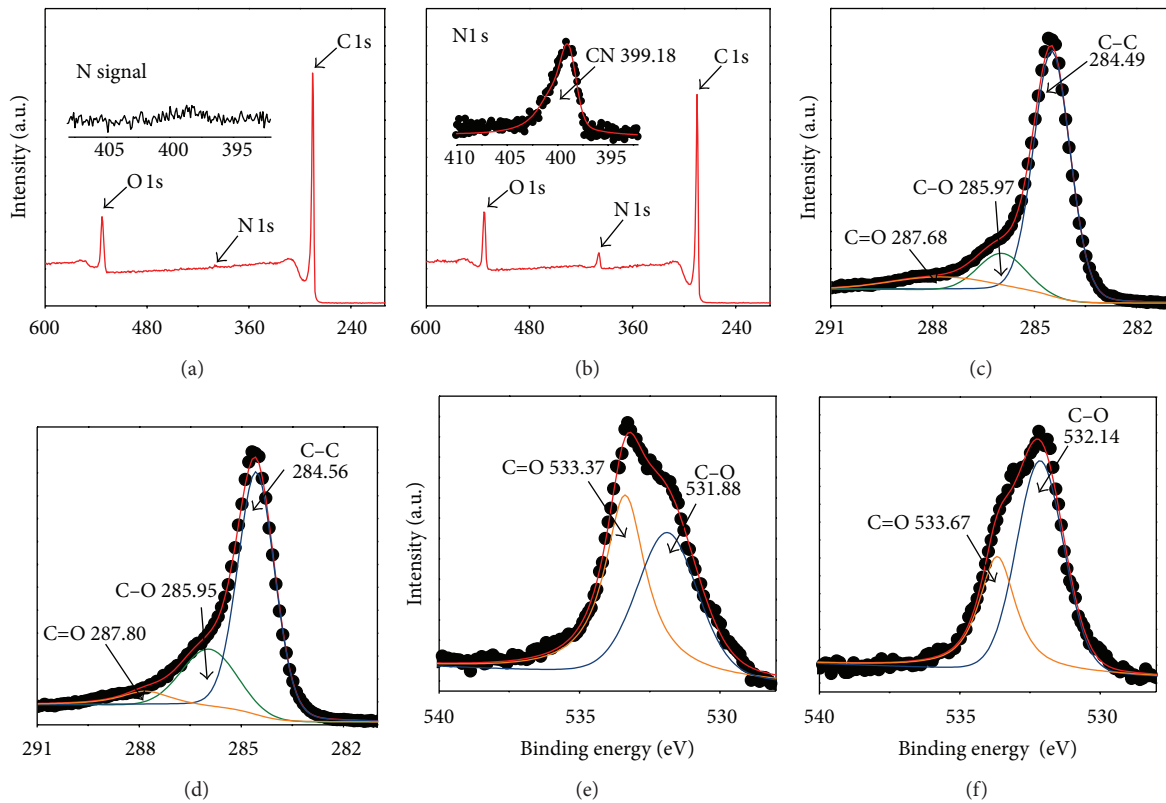
FIGURE 1: FTIR spectra of graphene and graphene-TCNEO, the peaks located at the 1399 cm^{-1} by the residual of solvent in the purge process.

FIGURE 2: XPS general spectra and curve fit of N 1s core-level spectra for graphene (a) and functionalized graphene (b), C 1s core level for graphene (c) and functionalized graphene (d), and O 1s core level for graphene (e) and functionalized graphene (f).

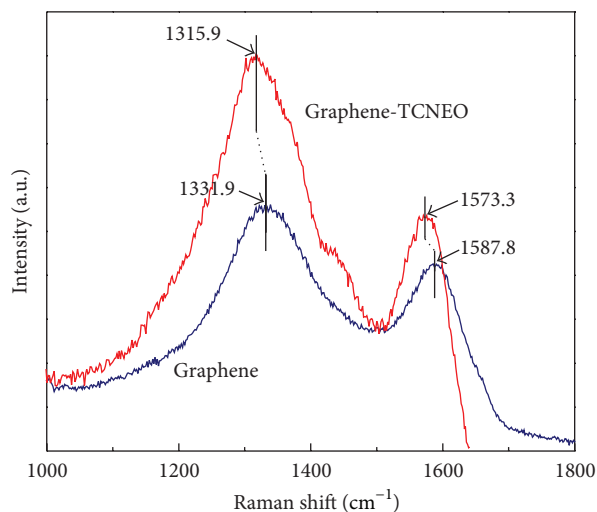


FIGURE 3: The Raman spectrum of graphene and grapheme-TCNEO.

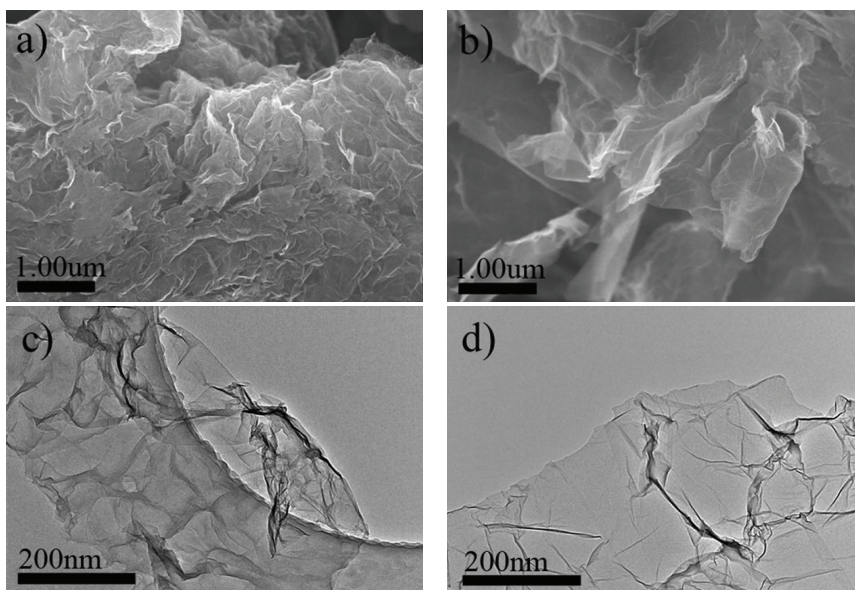


FIGURE 4: SEM images of graphene (a) and functionalized graphene (b), TEM images of graphene (c) and functionalized graphene (d).

3. Results and Discussions

Graphene and tetracyanoethylene oxide were mixed and dispersed in 1,2-dibromoethane, followed by continuous reactions at 140°C for 12 h in the N_2 atmosphere. After being purified by repeated filtration and redispersion, the final product was obtained. As can be seen from Figure 1, the obtained grapheme-TCNEO shows the characteristic vibration of nitrile groups from TCNEO at 2210 cm^{-1} . Because of the conjugation effect caused by the conjugated structure of the attached graphene sheets, the vibration of the nitrile groups shifts to relatively lower wavenumber [22, 23]. In addition, two new peaks at 1527 cm^{-1} and 1190 cm^{-1} are also readily observed in grapheme-TCNEO, respectively and represent the skeletal vibration of the generated polysubstituted

homocyclic ring and the stretching vibration of the introduced C–O. These results will be further supported by later X-ray photoelectron spectroscopy (XPS) and Raman analysis.

Compared with the graphene (Figure 2(a)), a new peak at about 399 eV corresponding to the binding energy of N 1s is clearly observed in the obtained grapheme-TCNEO, attributed to the introduced nitrile groups (Figure 2(b)). In the corresponding high-resolution N 1s spectrum, there is a single peak binding in 399.18 eV that suggests the presence of nitrile groups [24]. Based on the elemental ratios, the degree of functionalization is calculated to be approximately 1 TCNEO group in 85 carbon atoms. Additional evidence for the introduction of TCNEO to graphene comes from the obvious increase of C–O bonds in the C 1s and O 1s spectra of the obtained grapheme-TCNEO (Figures 2(c)–2(f)).

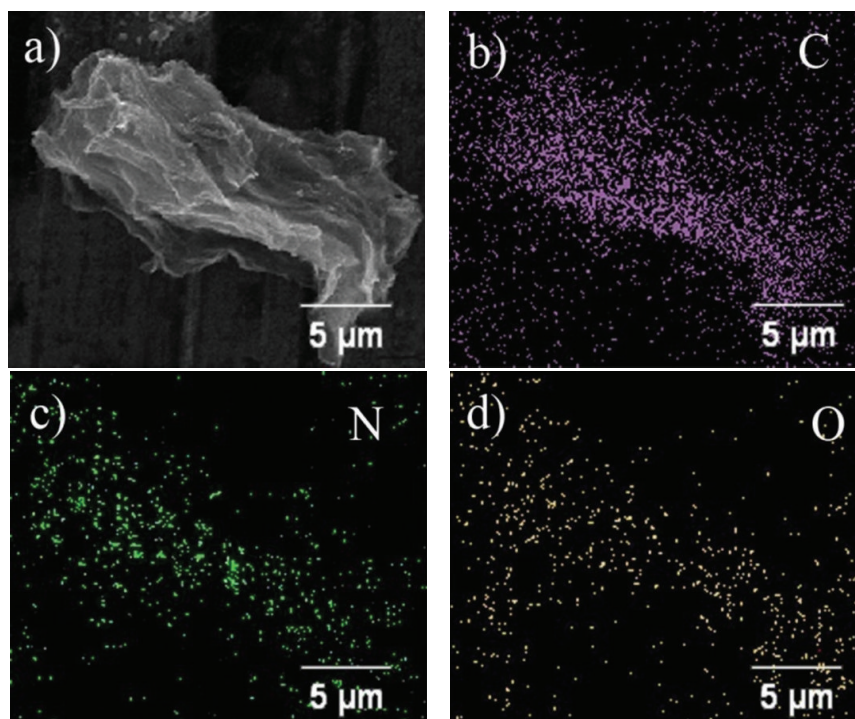


FIGURE 5: The SEM image of the grapheme-TCNEO (a) and corresponding quantitative EDS element mapping of C (b), N (c), and O (d).

Raman spectra analysis [25] reveals a significant increase in the intensity ratio (I_D/I_G) of graphene after functionalization (Figure 3). Considering the G band and D band that represent the sp^2 C atoms and defects, respectively, it can be anticipated that the destructions of the sp^2 hybridization structure are raised from the successful cycloaddition reactions. This result matches up with the results of FTIR and XPS discussed above. Moreover, the noticeable red shifts (15 cm^{-1}) of the G band and D band are observed after the reaction, probably due to the introduced conjugated nitrile groups that alter the conjugate structure of the graphene basal plane.

The structural change of graphene before and after functionalizations was further investigated by scanning electron microscope (SEM) and transmission electron microscope (TEM). As can be seen from Figures 4(a) and 4(b), the obtained grapheme-TCNEO shows a wrinkled structure similar to the pristine graphene sheets. TEM images (Figures 4(c) and 4(d)) demonstrate that both the grapheme-TCNEO and graphene are semitransparent due to their thin natures and have the dark veins that simply resulted from overlapped regions of the graphene sheets. The corresponding quantitative energy dispersive X-ray spectroscopy (EDS) mappings (Figure 5) confirm that elements C, N, and O are homogeneously distributed on the surfaces of the obtained grapheme-TCNEO, providing visualized evidence for the successful functionalization of graphene with nitrile groups.

4. Conclusions

In summary, we report an efficient strategy to functionalize graphene with nitrile groups. Systematic characterizations

demonstrated that the nitrile groups were homogeneously introduced to the surfaces of graphene via the cycloaddition reaction with tetracyanoethylene oxide (TCNEO). Considering the diversity of nitrile chemistry, the obtained grapheme-TCNEO may be further transformed into other graphene-based derivatives with interesting properties.

Acknowledgments

This study was supported by the National Natural Science Funds for Excellent Young Scholars (no. 21222608), Research Fund of the National Natural Science Foundation of China (no. 21106099), Foundation for the Author of National Excellent Doctoral Dissertation of China (no. 201251), the Tianjin Natural Science Foundation (no. 11JCYBJC01700), and the Programme of Introducing Talents of Discipline to Universities (no. B06006).

References

- [1] A. Peigney, C. Laurent, E. Flahaut, R. R. Bacsá, and A. Rousset, "Specific surface area of carbon nanotubes and bundles of carbon nanotubes," *Carbon*, vol. 39, no. 4, pp. 507–514, 2001.
- [2] C. Lee, X. Wei, J. W. Kysar, and J. Hone, "Measurement of the elastic properties and intrinsic strength of monolayer graphene," *Science*, vol. 321, no. 5887, pp. 385–388, 2008.
- [3] K. S. Novoselov, A. K. Geim, S. V. Morozov et al., "Electric field in atomically thin carbon films," *Science*, vol. 306, no. 5696, pp. 666–669, 2004.
- [4] J. C. Meyer, A. K. Geim, M. I. Katsnelson, K. S. Novoselov, T. J. Booth, and S. Roth, "The structure of suspended graphene sheets," *Nature*, vol. 446, no. 7131, pp. 60–63, 2007.

- [5] H. Bai, C. Li, and G. Q. Shi, "Functional composite materials based on chemically converted graphene," *Advanced Materials*, vol. 23, no. 9, pp. 1089–1115, 2011.
- [6] P. K. Santra and P. V. Kamat, "Mn-doped quantum dot sensitized solar cells: a strategy to boost efficiency over 5%," *Journal of the American Chemical Society*, vol. 134, no. 5, pp. 2508–2511, 2012.
- [7] O. Akhavan, E. Ghaderi, and R. Rahighi, "Toward single-DNA electrochemical biosensing by graphene nanowalls," *ACS Nano*, vol. 6, no. 4, pp. 2904–2916, 2012.
- [8] J. G. Yu, M. Jaroniec, H. G. Yu, and W. H. Fan, "Synthesis, characterization, properties, and applications of nanosized photocatalytic materials," *Journal of Nanomaterials*, vol. 2012, Article ID 783686, 3 pages, 2012.
- [9] N. Gorjizadeh and Y. Kawazoe, "Chemical functionalization of graphene nanoribbons," *Journal of Nanomaterials*, vol. 2010, Article ID 513501, 7 pages, 2010.
- [10] H. F. Yang, C. S. Shan, F. Li, D. X. Han, Q. X. Zhang, and L. Niu, "Covalent functionalization of polydisperse chemically-converted graphene sheets with amine-terminated ionic liquid," *Chemical Communications*, vol. 26, pp. 3880–3882, 2009.
- [11] J. R. Lomeda, C. D. Doyle, D. V. Kosynkin, W. F. Hwang, and J. M. Tour, "Diazonium functionalization of surfactant-wrapped chemically converted graphene sheets," *Journal of the American Chemical Society*, vol. 130, no. 48, pp. 16201–16206, 2008.
- [12] J. Y. Ji, G. H. Zhang, H. Y. Chen et al., "A general strategy to prepare graphene-metal/metal oxide nanohybrids," *Journal of Materials Chemistry*, vol. 21, no. 38, pp. 14498–14501, 2011.
- [13] L. H. Liu, M. M. Lerner, and M. D. Yan, "Derivatization of pristine graphene with well-defined chemical functionalities," *Nano Letters*, vol. 10, no. 9, pp. 3754–3756, 2010.
- [14] X. Y. Zhang, L. L. Hou, A. Cnossen et al., "One-pot functionalization of graphene with porphyrin through cycloaddition reactions," *Chemistry—A European Journal*, vol. 17, no. 32, pp. 8957–8964, 2011.
- [15] Y. Li, H. Y. Chen, L. Y. Voo et al., "Synthesis of partially hydrogenated graphene and brominated graphene," *Journal of Materials Chemistry*, vol. 22, no. 30, pp. 15021–15024, 2012.
- [16] S. Stankovich, R. D. Piner, S. T. Nguyen, and R. S. Ruoff, "Synthesis and exfoliation of isocyanate-treated graphene oxide nanoplatelets," *Carbon*, vol. 44, no. 15, pp. 3342–3347, 2006.
- [17] Y. W. Zhu, S. Murali, W. W. Cai et al., "Graphene and graphene oxide: synthesis, properties, and applications," *Advanced Materials*, vol. 22, no. 35, pp. 3906–3924, 2010.
- [18] W. J. Linn and R. E. Benson, "Tetracyanoethylene oxide. II. Addition to olefins, acetylenes, and aromatics," *Journal of the American Chemical Society*, vol. 87, no. 16, pp. 3657–3665, 1965.
- [19] W. J. Linn, "Tetracyanoethylene oxide. III. Mechanism of the addition to olefins," *Journal of the American Chemical Society*, vol. 87, no. 16, pp. 3665–3672, 1965.
- [20] K. C. Nicolaou, S. A. Snyder, T. Montagnon, and G. Vassilikogiannakis, "The diels—alder reaction in total synthesis," *Angewandte Chemie*, vol. 41, no. 10, pp. 1668–1698, 2001.
- [21] P. Guo, H. H. Song, and X. H. Chen, "Electrochemical performance of graphene nanosheets as anode material for lithium-ion batteries," *Electrochemistry Communications*, vol. 11, no. 6, pp. 1320–1324, 2009.
- [22] R. E. del Sesto, J. S. Miller, P. Lafuente, and J. J. Novoa, "Exceptionally Long (> or =2.9 Å) CC bonding interactions in pi-[TCNE]2(2-) dimers: two-electron four-center cation-mediated CC bonding interactions involving pi* electrons," *Chemistry—A European Journal*, vol. 8, no. 21, pp. 4894–4908, 2002.
- [23] B. A. Lindquist and S. A. Corcelli, "Nitrile groups as vibrational probes: calculations of the C≡N infrared absorption line shape of acetonitrile in water and tetrahydrofuran," *Journal of Physical Chemistry B*, vol. 112, no. 20, pp. 6301–6303, 2008.
- [24] D. Cagniant, R. Gruber, J. P. Boudou, C. Bilem, J. Bimer, and P. D. Salbut, "Structural characterization of nitrogen-enriched coals," *Energy and Fuels*, vol. 12, no. 4, pp. 672–681, 1998.
- [25] S. Niyogi, E. Bekyarova, M. E. Itkis et al., "Spectroscopy of covalently functionalized graphene," *Nano Letters*, vol. 10, no. 10, pp. 4061–4066, 2010.

Review Article

Highly Conductive, Transparent Flexible Films Based on Metal Nanoparticle-Carbon Nanotube Composites

Wen-Yin Ko and Kuan-Jiuh Lin

Department of Chemistry, National Chung-Hsing University, Taichung 40227, Taiwan

Correspondence should be addressed to Kuan-Jiuh Lin; kjlin@dragon.nchu.edu.tw

Received 28 February 2013; Revised 13 July 2013; Accepted 15 July 2013

Academic Editor: Sulin Zhang

Copyright © 2013 W.-Y. Ko and K.-J. Lin. This is an open access article distributed under the Creative Commons Attribution License, which permits unrestricted use, distribution, and reproduction in any medium, provided the original work is properly cited.

Metallic nanoparticles decorated on MWCNTs based transparent conducting thin films (TCFs) show a cheap and efficient option for the applications in touch screens and the replacement of the ITO film because of their interesting properties of electrical conductivity, mechanical property, chemical inertness, and other unique properties, which may not be accessible by their individual components. However, a great challenge that always remains is to develop effective ways to prepare junctions between metallic nanoparticles and MWCNTs for the improvement of high-energy barriers, high contact resistances, and weak interactions which could lead to the formation of poor conducting pathways and result in the CNT-based devices with low mechanical flexibility. Herein, we not only discuss recent progress in the preparation of MNP-CNT flexible TCFs but also describe our research studies in the relevant areas. Our result demonstrated that the MNP-CNT flexible TCFs we prepared could achieve a highly electrical conductivity with the sheet resistance of ~ 100 ohm/sq with $\sim 80\%$ transmittance at 550 nm even after being bent 500 times. This electrical conductivity is much superior to the performances of other MWCNT-based transparent flexible films, making it favorable for next-generation flexible touch screens and optoelectronic devices.

1. Introduction

Flexible transparent conducting films (TCFs) with low electrical resistance and high optical transmittance have received considerable attention for niche applications in flexible or foldable displays, touch screens, solar cells, transistors, and transparent electrodes for liquid-crystal displays [1–3]. Deposition of indium-tin oxide (ITO) on plastic substrates for the preparation of flexible TCFs has been an attractive strategy owing to its transparency, conductivity, and wide usability [4, 5]. Nevertheless, ITO is costly and brittle, and the film transparency is poor in the near-infrared range. Therefore, a substitute for ITO is necessary.

The high flexibility, high specific surface area, low density, and excellent electrical, optical, and mechanical properties of carbon nanotubes (CNTs) have made them ideal candidates for next-generation flexible TCFs [3, 6, 7]. Among various CNT-based flexible TCFs, composites of zero-dimensional metallic nanoparticles (MNPs) decorated on one-dimensional CNTs (MNP-CNTs) have received

most of attention because of their electrical conductivity, mechanical properties, chemical inertness, and other unique characteristics, which may not be shown by their individual components [8–10]. In practice, however, high-energy barriers, high contact resistances, and weak interactions between the CNTs and MNPs led to the formation of high-resistance (10^4 – 10^9 Ω) electrical contacts and poor conducting pathways [11], resulting in the development of MNP-CNT-based devices with low mechanical flexibility (without taking into account their intrinsic electronic properties) and leading to limitations on their application in flexible TCFs. Thus, methods to fabricate junctions for improving the adhesion between the MNPs and CNTs for the seamless connection of two CNTs have been explored. This chapter will discuss recent progress in the preparation of MNP-CNT flexible TCFs, organized as follows. First, we will introduce the synthesis methods for preparation of MNP-CNT nanocomposites. Next, selected approaches for the formation of MNP-CNT flexible TCFs will be discussed. Finally, we will review techniques of postmodification treatment for MNP-CNTs to

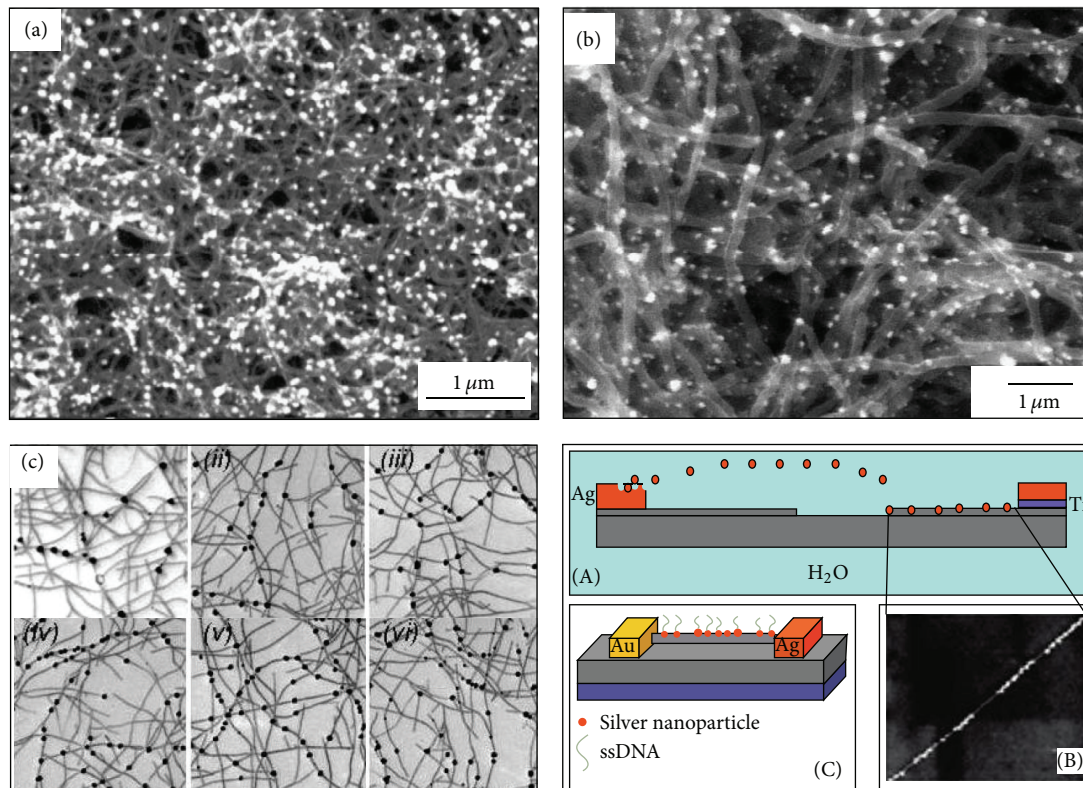


FIGURE 1: SEM images of various MNP-CNT nanocomposites prepared by the electrochemical deposition method. (a) Pt-CNT-graphite nanocomposite and (b) PtRu-CNT-graphite nanocomposite (reproduced with permission from [17, 18], Copyright ©2004 Elsevier). (c) FESEM images of Pd NPs decorated on the sidewalls of SWCNTs at different applied potentials between -0.1 and -0.35 V versus Ag/AgCl (reproduced with permission from [19], Copyright ©2011 American Chemical Society). (d) Decoration of Ag NPs along SWCNTs to form two-terminal electrical devices (reproduced with permission from [10], Copyright ©2011 American Chemical Society).

improve junctions between CNTs. In each section, after a brief introduction to recent results reported in the literature, we will describe our research studies in the relevant areas. In the final section, important results of electrical, optical, and mechanical performances in the MNP-CNT flexible TCFs we designed will be presented.

2. Synthesis Methods for MNP-CNT Nanocomposites

CNTs, which do not react with metal salts, have been widely used as supports for building MNP-CNT nanocomposites by depositing MNPs on the sidewalls of CNTs. Numerous methods that have been developed to synthesize MNP-CNT nanocomposites can be divided into physical, chemical, and electrochemical categories [12]. Among them, the liquid-phase synthesis route in the chemical and electrochemical categories, such as electrochemical deposition, the microwave-assisted approach, dispersion of MNPs onto the functionalized CNTs, and the polyol process, has been proven as a powerful tool for the fabrication of MNP-CNT nanocomposites (Table 1).

2.1. Electrochemical Deposition Method. The electrochemical deposition method involves simple reduction of metal ions on selected substrates from an electrolyte solution and enabling effective control on nucleation and growth procedure of material synthesis [13–15]. It is an excellent synthetic approach for preparing inorganic NPs and their relative CNT-metal nanocomposites because of the following advantages: (1) easy control of size distributions and densities of MNPs on CNTs by tuning the concentration of metal precursors and the electrochemical-deposition parameters of applied potential and deposition time; (2) large-scale synthesis; (3) short-term formation [16]. By using CNTs grown directly on substrates and electrochemically deposited high-purity MNPs, decoration of Pt or bimetallic Pt-Ru NPs with sizes of 60–80 nm on multiwalled carbon nanotubes (MWCNTs) was successfully carried out by He et al. [17, 18]. The process was utilized in the pregrowth of MWCNTs on a graphite disc by chemical vapor deposition and subsequent electrodeposition of Pt or bimetallic Pt-Ru NPs on the CNT-graphite electrode by the potentiostatic method at a saturated calomel electrode (SCE) deposition potential of -0.25 V (Figures 1(a) and 1(b)). Using a similar process, Day and coworkers electrodeposited Pd and Pt NPs on single-walled carbon nanotube (SWCNT)

TABLE 1: Methods for the synthesis of MNP-CNT nanocomposites.

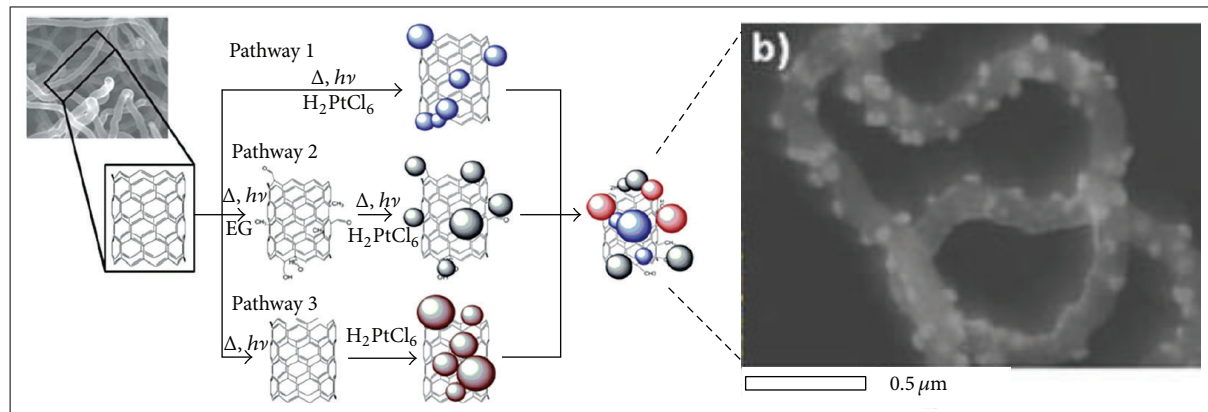
| Synthesis method | Metal | Particle size (nm) | CNT type | Ref. |
|---|-------|--------------------|-----------------------------------|------|
| Electrochemical deposition | Pt | 60–80 | MWCNT on graphite disc | [18] |
| | Ag | ~100 | SWCNT on Si/SiO ₂ | [10] |
| | Ni | hundreds | Functionalized MWCNTs | [16] |
| | Pd | 20–40 | SWCNT on Si/SiO ₂ | [19] |
| | PtRu | 60–80 | MWCNT on graphite disc | [17] |
| Microwave-assisted reduction | Pt | ~5.0 | Bulk 3-D MWCNTs | [21] |
| | Ru | 1.8–2.6 | MWCNTs | [22] |
| | Au | 3.0 | Functionalized SWCNTs | [23] |
| | Pt | 2.5 | Functionalized SWCNTs | [23] |
| | Pd | 24.6 | Sulfonated MWCNTs | [24] |
| | Ni | 16.1 | Sulfonated MWCNTs | [24] |
| Dispersion of MNPs on functionalized CNTs | Sn | 25.1 | Sulfonated MWCNTs | [24] |
| | Pt | ~4.0 | Acid oxidation-MWCNTs | [29] |
| | Au | 3.0–7.0 | Dendrimer-modified MWCNTs | [30] |
| | Pd | 2.0 | Thiol group-functionalized MWCNTs | [26] |
| | PtPd | 2.0–4.0 | Polypyrrole-functionalized MWCNTs | [25] |
| | Pt | 33.8 | PSS-functionalized MWCNTs | [31] |
| Polyol process | Pt | 1.8 | PVP-functionalized MWCNTs | [32] |
| | Pt | 2.0–3.0 | Purified CNTs | [35] |
| | Pd | 5.4 | Acid oxidation-MWCNTs | [36] |
| | Pt | ~2.3 | Purified MWCNTs | [39] |
| | Sn | 3–5 | Acid-treated MWCNTs | [38] |
| | Au | <10 | Purified MWCNTs | [39] |
| | PtPd | 2.4–5.4 | Acid oxidation-MWCNTs | [36] |
| | PtRu | 3.0 | Acid oxidation-MWCNTs | [37] |
| PtAg | ~3.8 | Purified MWCNTs | [39] | |

networks pregrown on the surface of a SiO₂ layer on a Si substrate (Si/SiO₂), using a microcapillary electrochemical cell at an applied potential in the range of –0.1 to –0.4 V (Ag/AgCl); in addition, they discovered that the density, distribution, and size of the MNPs could be controlled through the deposition potential and time (Figure 1(c)) [19]. Sahoo et al. further demonstrated that the Ag NPs could be synthesized and decorated along CNTs and the coverage densities of Ag NPs could be changed under the control of deposition time, applied voltage, and location of CNTs with respect to the anode (Figure 1(d)) [10]. However, large or random particle size of MNPs in MNP-CNT nanocomposites was always obtained through electrochemical deposition owing to the contradiction between a larger driving force for nuclei formation and an inhibitive mechanism for crystal growth.

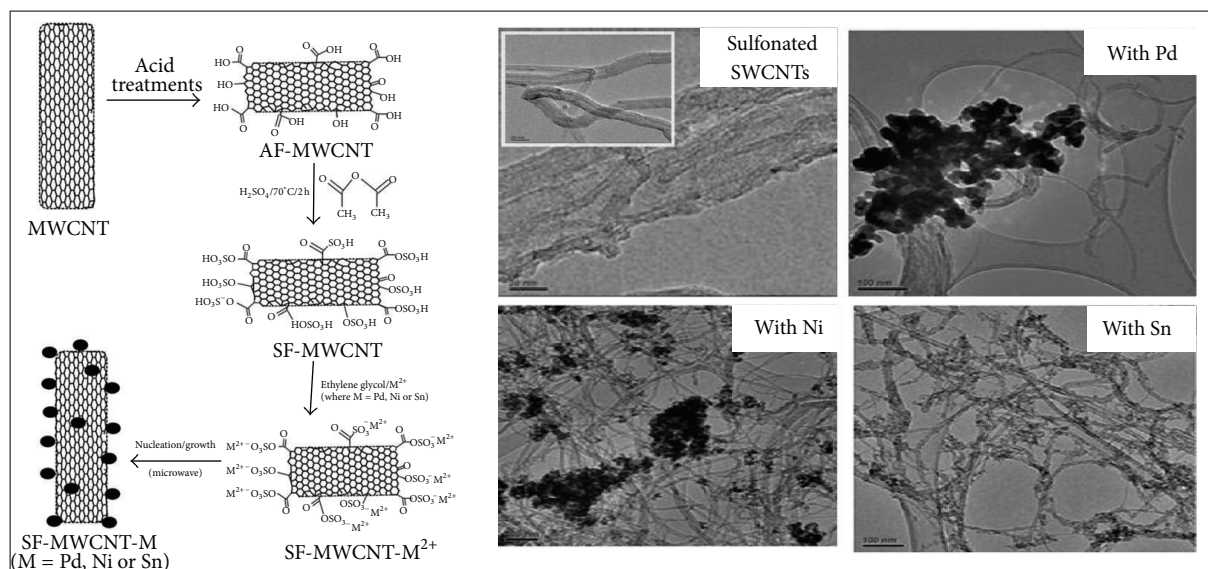
2.2. Microwave-Assisted Reduction. Microwave-assisted reduction, providing direct energy for effective heating of a reaction mixture by transferring electromagnetic energy into thermal energy, has been considered a convenient and rapid heating technique in the synthesis of MNP-CNT nanocomposites [20]. Minett's group successfully took advantage of bulk three-dimensional (3D) MWCNT architecture as the support and decorated Pt NPs measuring

~5 nm in size on CNTs by microwave-assisted reduction performed on an H₂PtCl₆ precursor and ethylene glycol mixture (Figure 2(a)) [21]. Zhang et al. further demonstrated that the twinned Ru NP-CNT nanocomposites could be fabricated by microwave treatment of a mixture of Ru₃(CO)₁₂ and CNTs pretreated in an Ar flow for 2 h in a quartz-tube reactor; the structure of Ru NPs could be rearranged into single crystals as the microwave heating proceeded [22]. Furthermore, microwave-assisted hydrothermal synthesis, a kind of improved microwave-assisted method, has also been developed for the preparation of MNP-CNT nanocomposites [23]. One of the representative works in microwave-assisted hydrothermal synthesis was reported by Ramulifho and coworkers, who prepared Pd, Ni, and Sn NPs decorated on the surface of sulfonated MWCNTs (Figure 2(b)) [24].

2.3. Dispersion of MNPs onto Functionalized CNTs. Introducing more binding sites and surface anchor groups to CNTs to benefit MNP decoration has been considered an effective tool for MNP-CNT nanocomposites synthesis [25], for which chemical functionalization of the CNT surface is essential. Among various techniques to modify the surface of CNTs, covalent attachment of functional groups such as carbonyl-, carboxyl-, and amine-groupson to the surface of CNTs is one of the most promising routes because of its capability



(a)



(b)

FIGURE 2: (a) Schematic illustration of microwave-assisted reduction for the preparation of Pt NP-MWCNT nanocomposites and image of the resulting product (reproduced with permission from [21], Copyright ©2010 The Royal Society of Chemistry). (b) Synthesis procedure and relevant TEM images of the prepared MNPs supported on sulfonated MWCNTs by using the microwave-assisted hydrothermal method (reproduced with permission from [24], Copyright ©2012 Elsevier).

to result in strong metal-CNT interactions, thereby giving stable MNP-CNT nanocomposites with heavily loaded MNPs [12, 26]. The addition of carbonyl and carboxyl groups on the surface of CNT is the most common covalent functionalization process for the modification of the CNT surface. By this process, CNTs are functionalized with $-C=O$, $-COO-$, and $-COOH$ groups through pretreatment of CNTs in acidic aqueous solutions such as those of O_3 and H_2O_2 , which provide nucleation sites for the deposition of MNPs [27, 28]. Hull et al. successfully used the sonochemical treatment method to functionalize the CNT surface with $-C=O$, $-C-O-C-$, $-COO-$, and $-C-OH$ groups in an HNO_3 - H_2SO_4 aqueous solution, allowing them to deposit Pt NPs with diameters of ~ 4 nm (Figure 3(a)) [29]. In another representative

work reported by Lu and Imae, an MNP-CNT nanocomposite was created from MWCNTs modified with fourth-generation NH_2 -terminated poly(amido amine) dendrimers (CNT-DEN) and controllable Au NPs (Figure 3(b)). Besides, several MNPs with controllable size of Ag, Cu, Pt, and Ag@Au supported on the surface of CNT/DEN were successfully obtained [30]. Polymers, wrapping around CNTs to introduce surface functional groups on the CNTs, have also been used to anchor MNPs supported on CNT surface to form MNP-CNT nanocomposites. For example, Pt nanoflowers could be immobilized on the surface of MWCNTs wrapped by poly(sodium 4-styrenesulfonate) (PSS-MWCNTs); Au and Pd NPs could also be decorated on the surface of PSS-MWCNTs (Figure 3(c)) [31]. Another representative work on

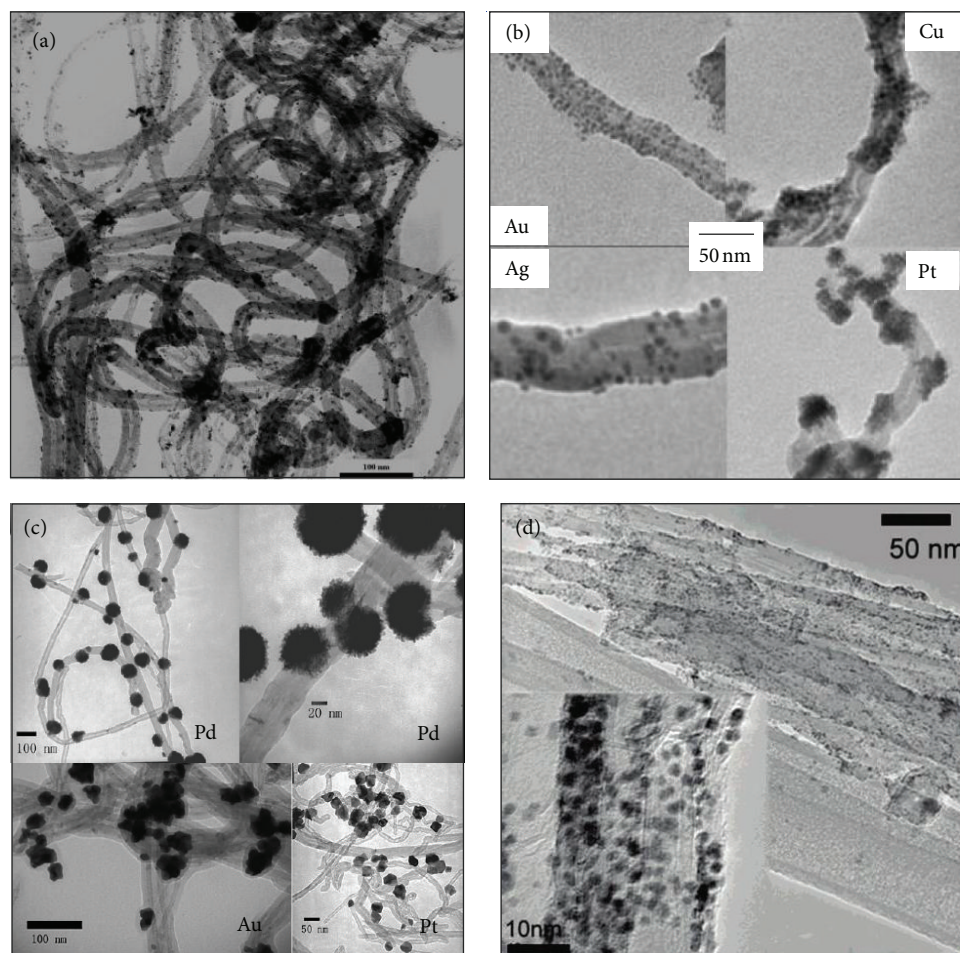


FIGURE 3: (a) TEM image of functionalized CNTs with $-C=O$, $-C-O-C-$, $-COO-$, and $-C-OH$ groups by sonochemical treatment, followed by deposition of Pt NPs (reproduced with permission from [29], Copyright ©2006 American Chemical Society). (b) TEM images of CNT-DEM-NPs (reproduced with permission from [30], Copyright ©2007 American Chemical Society). (c) TEM images of Pd/PSS-MWCNTs, Au/PSS-MWCNTs, and Pt/PSS-MWCNTs (reproduced with permission from [31], Copyright ©2010 The Royal Society of Chemistry), (d) TEM image of Pt/PVP-MWCNTs (reproduced with permission from [32], Copyright ©2007 American Chemical Society).

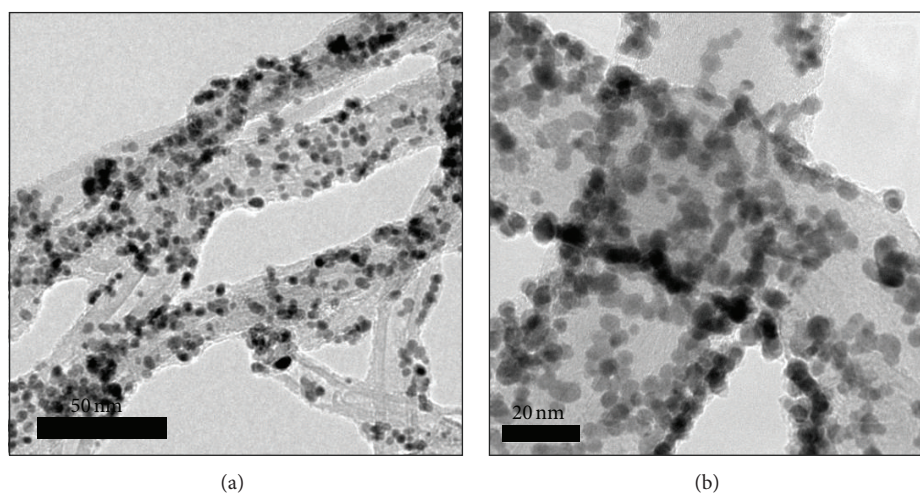


FIGURE 4: Representative HRTEM images of (a) Pt NPs and (b) bimetallic AgPt NPs attached on MWCNTs by using the polyol process in our work.

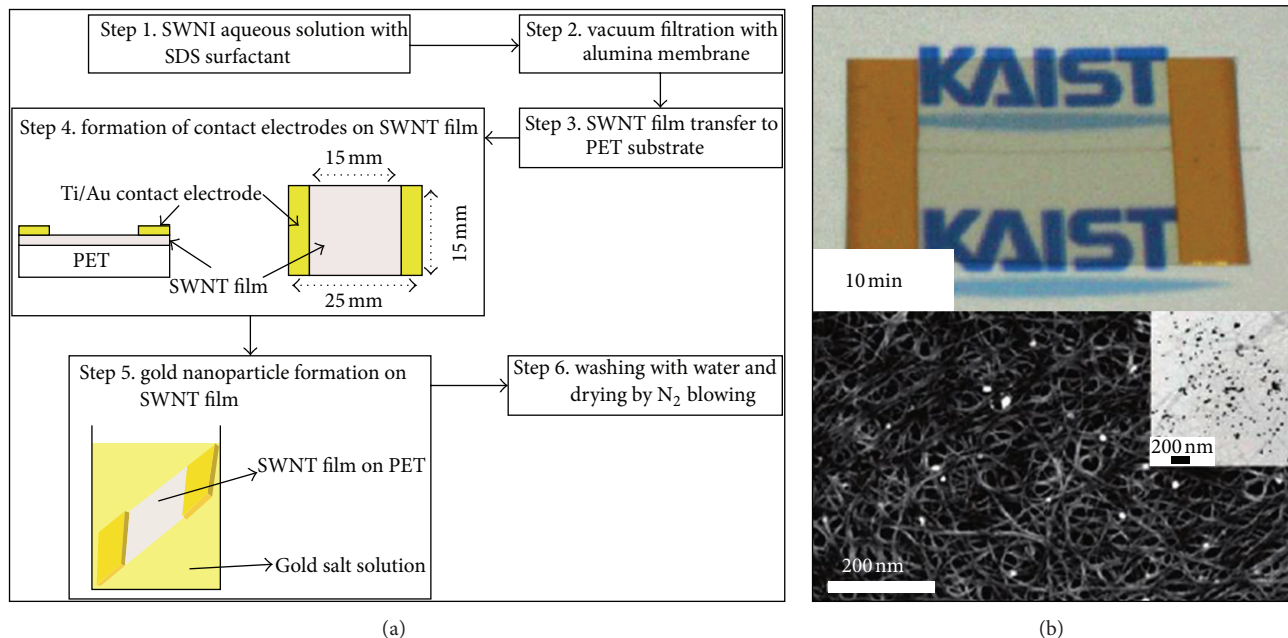


FIGURE 5: (a) Schematic illustration of the fabrication of Au-SWCNT films by the vacuum filtration method followed by electroless reduction of Au ions on the SWCNT networks. (b) Optical image and TEM image of Au-SWCNT flexible TCFs (reproduced with permission from [43], Copyright ©2007 American Chemical Society).

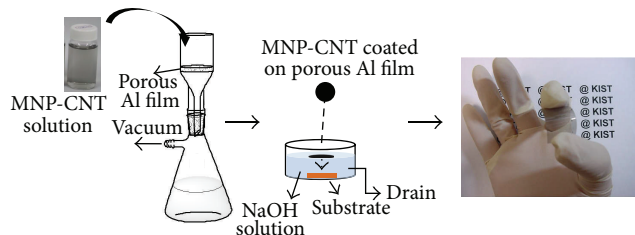


FIGURE 6: Schematic illustration of the vacuum filtration technique with subsequent process of Al membrane transfer for the formation of MNP-CNT flexible TCFs (reproduced with permission from [40], Copyright ©2010 Elsevier).

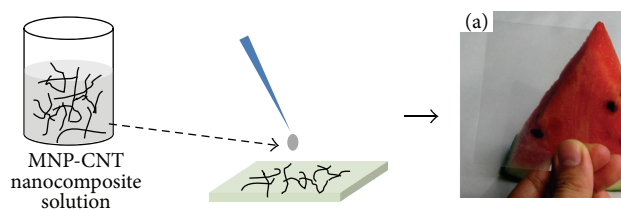


FIGURE 7: Schematic illustration of the drop-coating process for the formation of MNP-CNT flexible TCFs (reproduced with permission from [45], Copyright ©2012 Springer-Verlag).

the synthesis of Pt-MWCNT and PtRu-MWCNT nanocomposites using poly(vinyl pyrrolidone) (PVP) was carried out by Hsin and coworkers, where PVP not only helped form a homogenous CNT-dispersed aqueous solution but also

served as the functional group binding the metal ions and MNPs (Figure 3(d)) [32].

2.4. Polyol Process. The polyol process, which involves the reduction of a metal salt precursor in a polyol, a compound containing multiple hydroxyl groups that serves as the solvent for the metal precursor and its reducing agent, has been widely used to synthesize inorganic nanostructures and their relative nanohybrids [33, 34]. Recently, preparation of MNP-CNT nanocomposites through the polyol process attracted much interest because of the advantages of homogeneous reduction and nucleation, leading to narrow, small, and monodispersed MNPs supported on the surfaces of CNTs. Based on this method, several kinds of MNPs deposited on CNTs, such as Pt, Pd, and bimetallic PtPd and PtRu, were successfully obtained [35–38]. In our work, we also demonstrated the successful preparation of Au (<10 nm), Pt (~2.3 nm), and bimetallic AgPt NPs (~3.8 nm) supported on MWCNTs by using a simple polyol process with surfactant-assisted sonication (Figure 4) [39]. In brief, a known quantity of metallic precursor and a predetermined quantity of purified MWCNTs were mixed in ethylene glycol to obtain a homogeneous solution under a nitrogen atmosphere using a probe-type sonicator. The mixture solution was then heated to 160°C at a heating rate of 2°C/min and was maintained at this temperature for 2 h. More importantly, the size of the MNPs, the composition ratio of bimetals, and their loading amount and distribution on the sidewalls of CNTs could be controlled by the reaction time, formation temperature, and weight ratio of the precursors to CNTs.

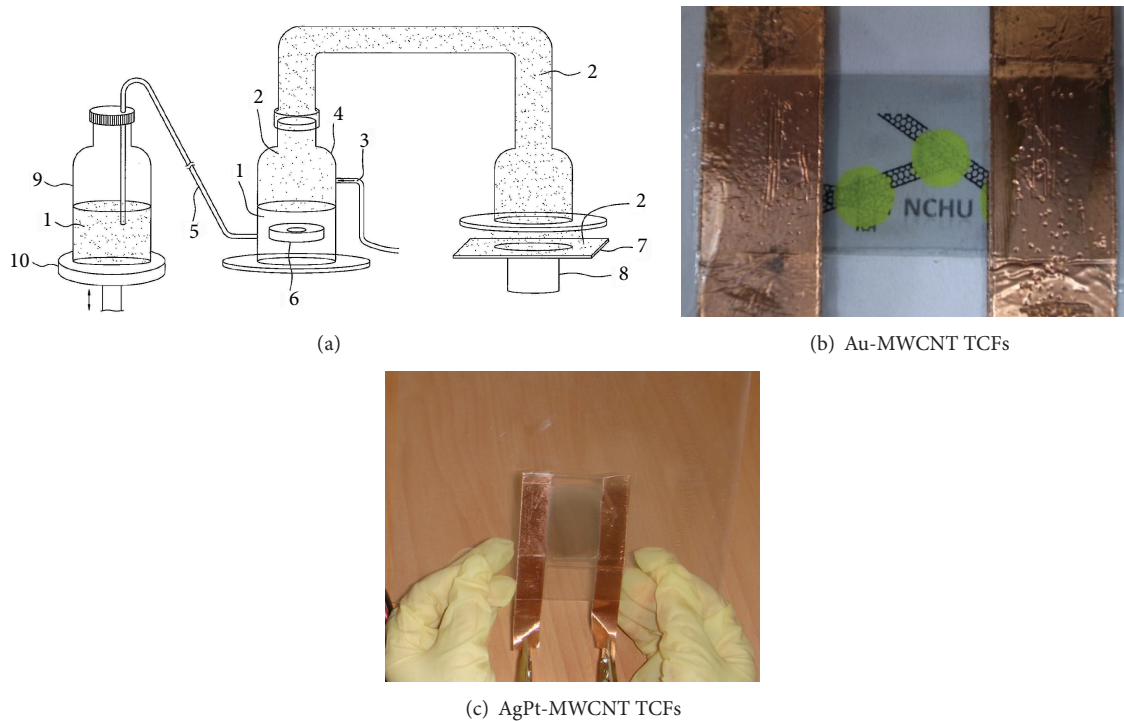


FIGURE 8: (a) Schematic view of equipment we designed that combines an ultrasonic atomizer with a spin-coating apparatus for fabricating MNP-CNT TCFs. The CNT solution 1 is atomized at a supersonic atomizing frequency to form atomized particles 2 of various sizes, including the CNTs. Specifically, 1 is contained in an atomizing container 4 and is maintained at a constant level using a siphon 5 that connects 4 with a reservoir 9. Thus, a supersonic atomizing member 6 that generates the supersonic atomizing frequency is maintained at a constant depth below the level of 1 to produce the atomized particles 2 of desirable particle size. 9 is placed on an elevating device 10. The levels 1 in 4 can be controlled by adjusting the height of 10. Preferably, 9 can be provided with a probe-type sonicator (not shown) to maintain a homogeneous dispersion of 1 in 9. A carrier gas 3 is provided to carry 2 to a substrate 7 placed on a spin-coating equipment 8 for the formation of conductive, thin CNT films. (b) Au-MWCNT TCFs and (c) AgPt-MWCNT TCFs prepared from ultrasonic atomization with the spin-coating method.

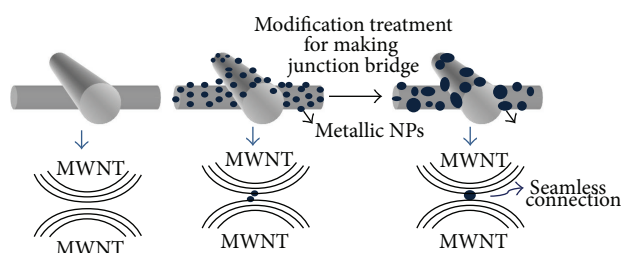


FIGURE 9: Schematic illustration of MNPs adhered to CNTs for making a junction bridge to connect CNTs seamlessly with the aid of modification treatments.

3. Methods for Fabricating MNP-CNT Flexible TCFs

Several approaches have been used to build MNP-CNT flexible TCFs through physical, chemical, and electrochemical processes. Among them, the solution-based deposition processes of vacuum filtration, drop coating, and ultrasonic atomization with the spin-coating method, followed by thermal treatment, have been widely applied to fabricate MNP-CNT flexible TCFs because of their competitive advantages

of low cost, use without high vacuum requirements, low-temperature process, suitability for various substrates, and easy adaptability to mass production.

3.1. Vacuum Filtration. The vacuum filtration technique is a simple and cheap approach, which involves vacuum filtration of homogeneous suspensions with desired products under a low vacuum to create a relevant nanonetwork film on the surface of a filter. The technique uses a porous Al membrane and the subsequent transfer of resulting MNP-CNT film onto a desired substrate by dissolving the membrane [40–43]. By employing vacuum filtration to form SWCNT films and subsequent electroless reduction of Au ions (Au^{3+}) on the SWCNT networks, Kong and coworkers obtained Au-SWCNT flexible TCFs with highly conductive, high-density properties, as shown in Figure 5 [43]. Park et al. further demonstrated that Au-MWCNT hybrid films with improved flexible, transparent, and conducting properties could be synthesized by depositing an Au-NP-decorated MWCNT hybrid solution on poly(ethylene terephthalate) (PET) films by vacuum filtration followed by removal of the Al-membrane filtration filter (Figure 6) [40]. This method can offer uniform films with precise control of the MNP-CNT framework; it is not suitable for mass production, however.

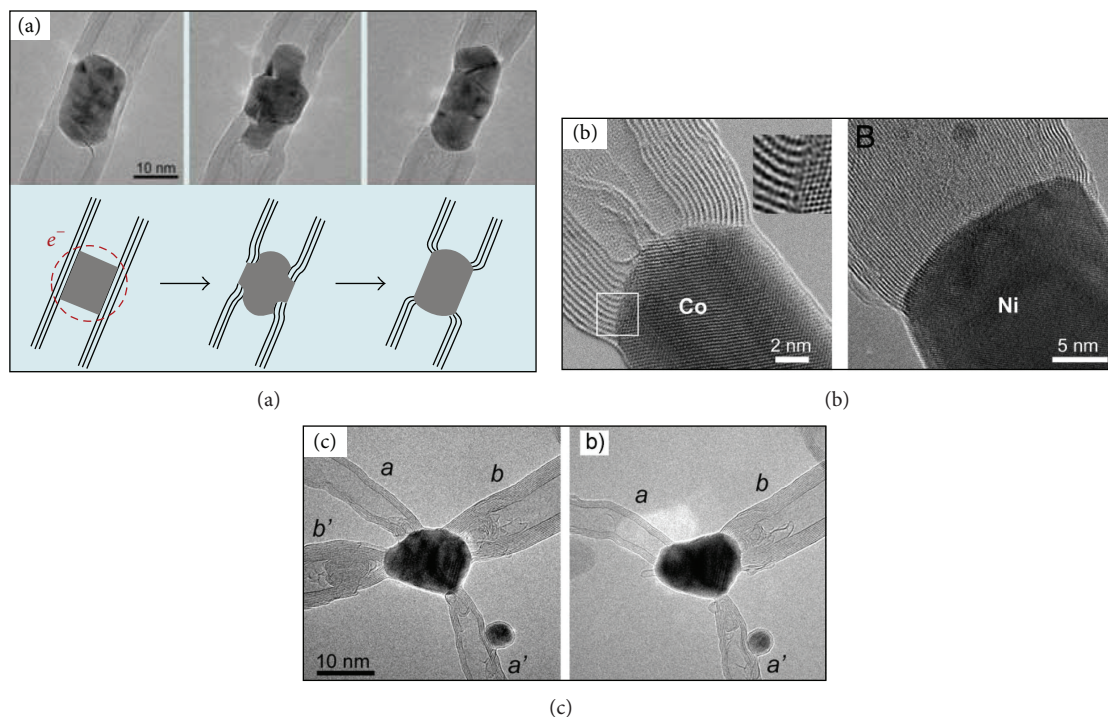


FIGURE 10: Formation of CNT-MNP-CNT heterojunctions with different metal nanoparticles through intense electron-beam irradiation at temperatures of 450–700 °C (reproduced with permission from [50] Copyright ©2009 National Academy of Sciences and [51], Copyright ©2009 Wiley).

3.2. Drop-Coating. The drop-coating procedure, used to release droplets of a colloidal solution of MNP-CNT nanocomposites on a substrate, has been considered a good candidate for fabrication of MNP-CNT flexible TCFs because of its coffee-ring effect during the evaporation process, which can form a film of high conductivity and transparency [44]. Recently, flexible, hybrid transparent electrodes of Ag nanowires and single-walled CNTs with excellent conductivity and transmittance as well as long stability have been produced by Tokuno et al. through this method (Figure 7) [45]. Nevertheless, disadvantages of this method remain, such as low density and nonuniform thickness of films, limiting their suitability for scaling up to broader applications.

3.3. Ultrasonic Atomization with Dip Coating. Ultrasonic atomization, a technique of producing a fine spray from a liquid, is a relatively inexpensive technique for the continuous production of micron- and nanometer-sized materials to assist the production of large-scale films by spin coating [46]. It involves the generation and subsequent deposition of a mist of micron-sized droplets from a humidifier on the surface of a substrate. The water drops then evaporate, and the solute precipitates to form products. For the fabrication of MNP-CNT flexible TCFs, first, isolation of the MNP-CNT nanocomposites is necessary to form atomized particles from the homogeneous MNP-CNT solution with the desired viscosity. These atomized particles are subsequently transferred to spin-coating equipment with a carrier gas stream of nitrogen and then spin-coated on flexible substrates

and rinsed with water several times to remove the remaining surfactants. The resulting films possess not only good mechanical flexibility but also excellent conductivity owing to its dense, compact frameworks. Recently, we have successfully prepared MNP-CNT flexible TCFs composed of Au and AgPt NPs supported on MWCNTs from a homogeneous MNP-MWCNT composite solution using our design of an ultrasonic atomization-spin coating tool (Figure 8(a)) [39]. The resulting Au-MWCNT and AgPt-MWCNT thin films exhibit good electrical conductivity (sheet resistance of 100–200 ohm/sq) and high transparency (transmittance of 80–85% at 550 nm), which are competitive with those of most other CNT-based films (Figures 8(b) and 8(c)). In addition, the optical transmittance and electrical conductivity of MNP-MWCNT films can be controlled by the deposition time of ultrasonic atomization [39].

4. Modification of MNP-CNT Nanocomposites

The disadvantages of high-energy barriers, high contact resistances, and weak interactions between the CNTs and MNPs make it difficult for them to form MNP-CNT TCFs because of the poor conducting pathways and low mechanical flexibility. It is well known that the electrical conductivity and mechanical stability of the CNT thin films are strongly dependent on the CNT network connections and densities. Therefore, junction fabrication for CNTs by cross-linked materials of MNPs to obtain well-defined electrical contacts and firmly attached CNTs have been explored (Figure 9).

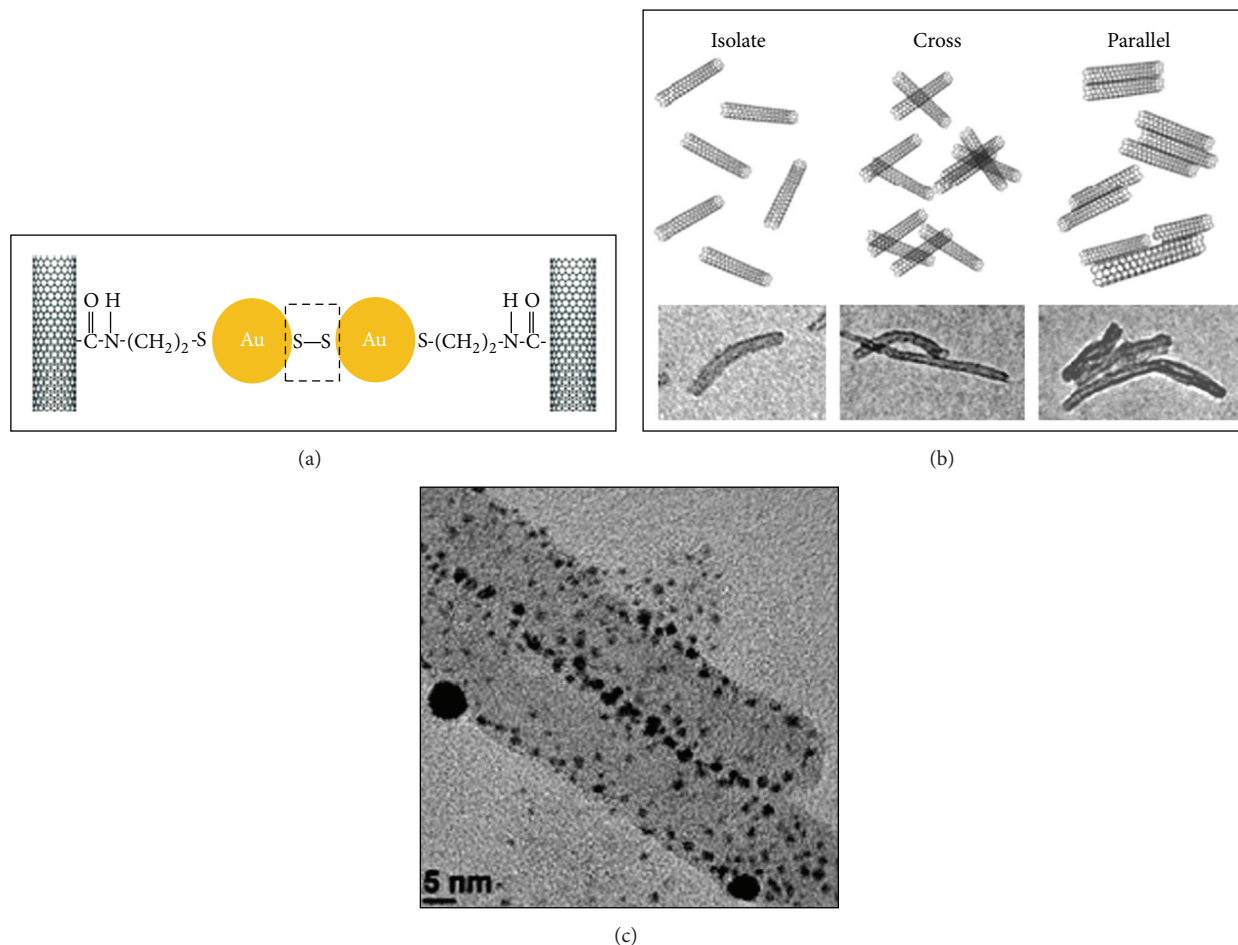


FIGURE 11: (a) Schematic illustration for cross-linking two CNTs by creating chemical bonding between thiol groups immobilized on the surface of AuNPs of different AuNP-CNTs. (b-c) TEM images of the assembly of AuNP-CNTs strands (reproduced with permission from [54], Copyright ©2011 American Chemical Society).

Postmodification treatment such as electron-beam welding, incorporation of polymers and surfactants, and microwave (MW) plasma irradiation, which can improve adhesion between the MNPs and CNTs to form junctions, have been used for the connection of two CNTs.

4.1. Electron-Beam Welding. Electron-beam welding, used to weld the CNTs and create contacts between them for the formation of interconnected CNTs through electron-beam irradiation [47–49], has been employed recently in welding of CNTs to metal NPs to form heterojunctions. This method can offer robust junctions between CNTs and metal NPs because of the formation of covalent metal-carbon bonds, allowing CNTs to firmly attach to the surface of metal NPs. Using this approach with intense electron-beam irradiation at temperatures of 450–700°C, Rodriguez-Manzo et al. successfully obtained strong MNP-CNT nanocomposites, composed of Fe, Co, Ni, and FeCo, with robust CNT and MNPs heterojunctions in which all the CNT layers were strongly bonded to the surface of MNPs (Figures 10(a) and 10(b)) [50]. Two-, three-, and four-terminal junctions of CNTs with a Co

NP as the central node were also successfully prepared by further tailoring of the junction with a focused electron beam (Figure 10(c)) [51]. To effectively employ this method, it is essential to use a transmission electron microscope as well as maintain both ultrahigh energetic electron irradiation and high-temperature annealing.

4.2. Creating Chemical-Bonding Bridges. Creating chemical bonding between functional groups immobilized on the surface of MNPs of different MNP-CNTs to cross-link two CNTs has been demonstrated to reduce contact resistance between them, thus improving the electrical and mechanical performances of the CNT-based films [52, 53]. Recently, assembly of AuNP-CNTs into strands in an interconnected, parallel arrangement and cross-arrangement by cross-linking of the thiol groups attached on AuNPs have been carried out in Rhee's group. Their work involved the synthesis of AuNP-CNT nanocomposites by combining thiolated MWCNTs and Au NPs through sonication at 60°C for 1 h and subsequent interaction of the AuNP-MWCNTs with alkanedithiols through stirring at room temperature (Figure 11) [54]. It is a

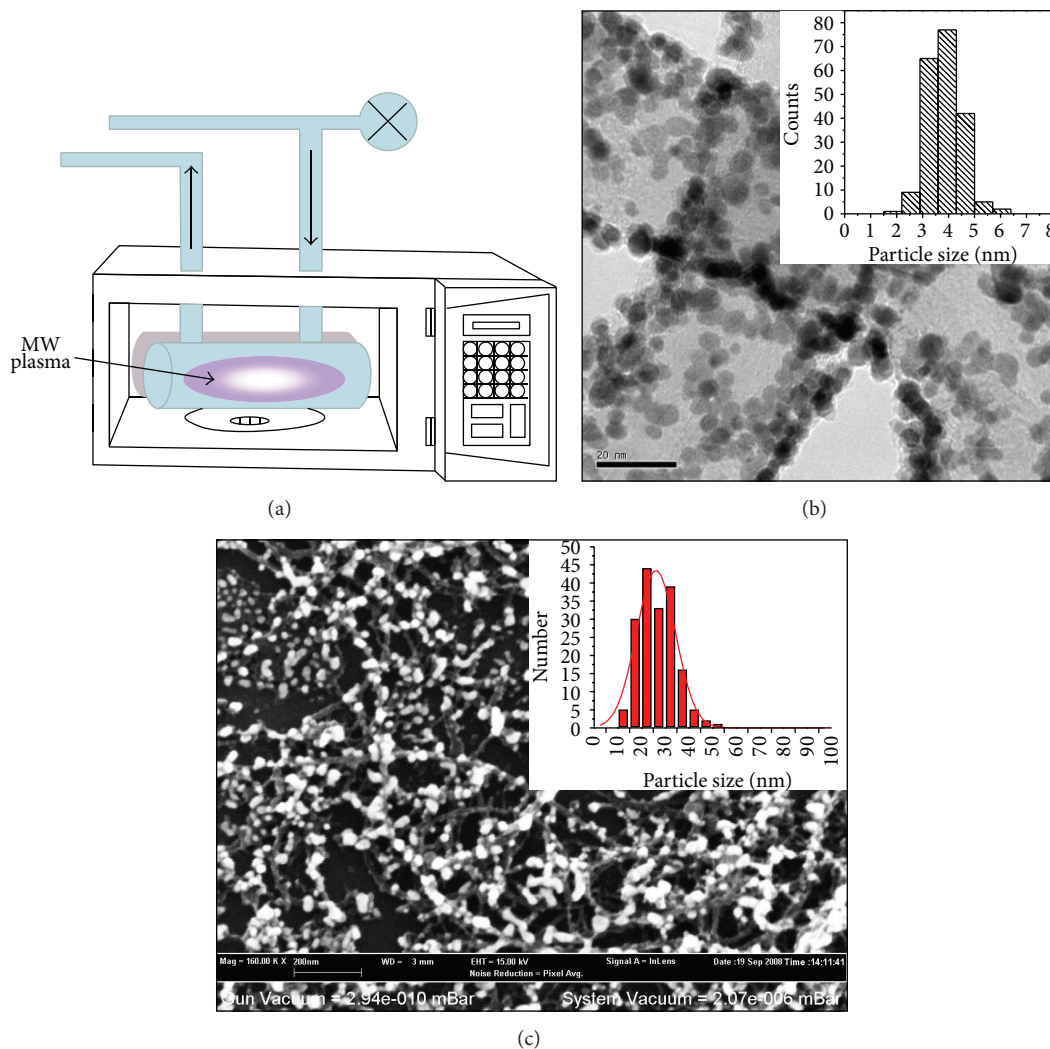


FIGURE 12: (a) Scheme of the MW plasma irradiation oven that we designed for postmodification treatment of MNP-MWCNT thin films. Morphology and size distribution of AgPt nanoalloys attached to AgPt-MWCNT flexible TCFs (b) before and (c) after postmodification MW plasma irradiation.

simple postmodification approach to bridge different MNP-CNTs to fabricate CNT-based thin films with high optical transparency and low electrical conductivity; however, lower thermal stability of the functional groups attached on the surfaces of MNPs would highly reduce the strength of the bridge junction, lowering their potential for TCF applications.

4.3. Microwave (MW) Plasma Irradiation. The constraints in the abovementioned postmodification treatments created limitations for large-scale production of MNP-CNT flexible TCFs. Thus, a simple but effective technique has yet to be realized. For this purpose, we developed a microwave (MW) plasma irradiation technique for the postmodification treatment of the prepared MNP-CNT flexible TCFs. MW plasma irradiation, which involves the generation of plasma cells by supplying energy to a neutral gas to form accelerating electrons or ions in the MW electromagnetic field, can

provide rapid heating and uniform temperature distribution [55]. This irradiation method is known to be efficient for the following purposes: (1) treating carbon surfaces with damage-free processing to enhance the textural characteristics of the nanotubes and to improve their strength [56, 57]; (2) coating substrates with inorganic nanomaterials [58]; (3) synthesizing metallic NPs [59, 60]; (4) converting metallic thin films coated on substrates to NP structures [61]. However, very few studies have reported the use of MW plasma treatment for the fabrication of junctions between the CNTs and MNPs. Through postmodification MW plasma treatment, we observed, for the first time, smaller MNPs attached on MWCNTs of MNP-MWCNT nanocomposites that melted and fused into larger agglomerates [39]. For example, the average diameter of the observed AgPt alloy NPs of AgPt-MWCNT-PET films was approximately 26 ± 8 nm after MW plasma treatment, which was much larger than that of the as-produced NPs (3.8 ± 0.65 nm), as shown in Figure 12. More

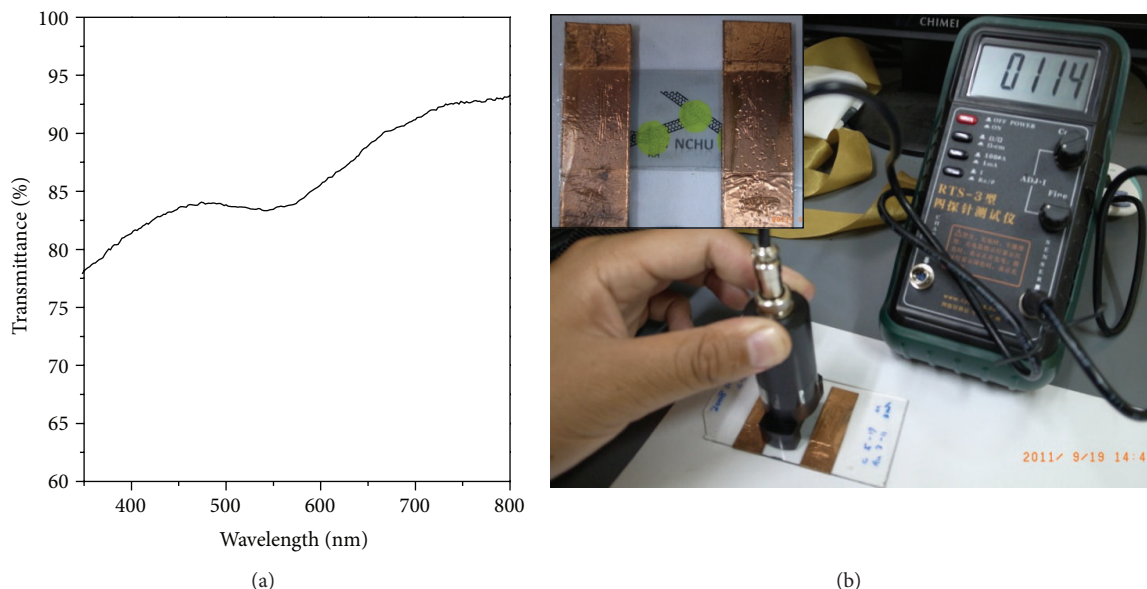


FIGURE 13: UV-Vis transmittance spectrum and sheet resistance analysis of prepared Au-MWCNT flexible TCFs.

importantly, the abovementioned coalescence can provide an additional advantage in that the MNPs strongly adhere to the walls of the MWCNTs to form the intra- or interjunctions between the MWCNTs and the MNPs, lowering the contact resistance between MWCNTs and resulting in improved mechanical integrity and excellent electrical conductivity.

5. Improved Performances of Our Synthesized MNP-CNT Flexible-TCFs

As shown by the above results, our group successfully fabricated flexible, transparent, and conducting composite thin films, constructed from MWCNTs, and supported single- or bimetallic NPs such as Au, Pt, and AgPt on a flexible PET substrate, through the combination of a polyol process for synthesizing nanocomposites of MWCNTs and MNPs with an ultrasonic atomization–spin coating method for preparing thin films. These nanocomposites were then exposed to microwave plasma irradiation, which could lower the contact resistance between the MNPs and CNTs and reinforce the network bridges. In the following section, we will briefly review some results on the optical, electrical, and mechanical performances of our prepared MNP-MWCNT flexible TCFs.

Au NPs, offering unique characteristics of high surface reactivity, biocompatibility, nontoxicity, and tunable optical properties, have been widely used in various applications [61–64]. In particular, the decoration of Au NPs on CNTs for applications in biosensors, transistors, and catalysis has been investigated extensively because of the synergistic effect of hybridization of CNTs with Au NPs [65–67]. We successfully obtained Au-MWCNT flexible TCFs with excellent transparency and electrical conductivity. Characterization of the films for optical transmission and electrical properties

showed that the optical transmittance was 83–88% at 550 nm and the electrical resistance was 110–160 ohm/sq in four-probe measurements (Figure 13). These values were much better than those of the film that was not exposed to MW plasma treatment (Table 2), indicating that the junctions fabricated between the Au NPs and MWCNTs by MW-plasma heat-induced coalescence were effective in reducing the number of defects and in increasing the number of charge-transfer pathways, which in turn enhanced the optical transmittance and electrical conductivity.

The AgPt bimetallic-NP system has received enormous interest for the following reasons [68]: (1) there is a reduction in the poisoning effect; (2) there is a significant improvement in the catalytic and optical response properties; (3) silver-based materials render these NPs competitive alternatives to Au, Pt, and Pd nanocolloids in low-cost applications because silver is much more cost-effective than other noble metals; (4) the use of AgPt bimetallics as potential lead-free solder materials has been studied in recent years. Herein, we report the successful formation of large-scale AgPt-MWCNT TCFs (Figure 14(a)), where the AgPt-MWCNT composites were spin-coated on PET films using the ultrasonic atomizer technique in the presence of SDS surfactants. In addition, in order to enhance the electrical flexibility and to improve the mechanical property of the films, the AgPt NPs were annealed under MW plasma irradiation. Characterization of the films showed an optical transmittance of 80% at 550 nm and a two-probe electrical resistance of 154.36 ohm/sq (Figures 14(a) and 14(b)). We also analyzed the strain-dependent electrical resistance characteristics by a two-point bending test to explore the feasibility of the as-prepared films (Figure 14(c)). The test confirmed that the sheet resistance of the fabricated films reached a value as low as 154 ohm/sq, which was consistent with the two-probe measured data. It is interesting

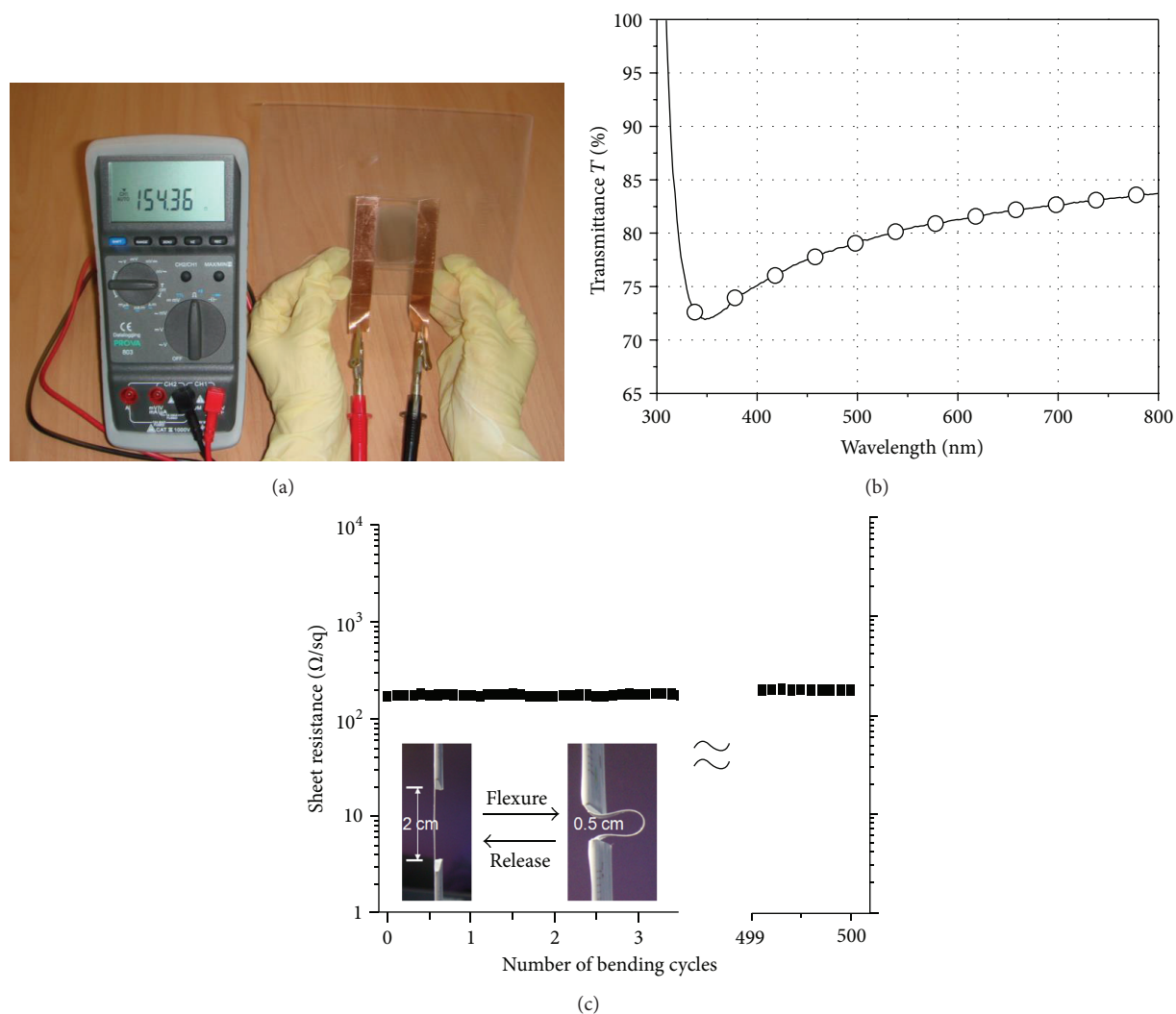


FIGURE 14: (a) Photograph and sheet resistance analysis, (b) UV-Vis transmittance spectrum, and (c) flexibility test of the representative AgPt-MWCNT flexible TCFs.

TABLE 2: Optical transmittance and electrical conductivity of prepared Au-MWCNT flexible TCFs with and without post-modification MW plasma irradiation treatment.

| | | Sample 1 | Sample 2 |
|------------------------------|-----------------------------|----------|----------|
| Before MW plasma irradiation | Sheet resistance (ohm/sq) | 246.7 | 283.7 |
| | Transmittance at 550 nm (%) | 75.1 | 71.4 |
| After MW plasma irradiation | Sheet resistance (ohm/sq) | 152.2 | 156.8 |
| | Transmittance at 550 nm (%) | 87.9 | 83.5 |

to note that the conductivity of the films did not decrease even after 500 bending cycles; the sheet resistance remained at approximately 154 ($\pm 1\%$) ohm/sq.

The resulting performances of flexible tests of CNT-based flexible TCFs made from MWCNT, Au-MWCNT nanocomposites, and AgPt-MWCNT nanocomposites with the postmodification treatment of MW plasma irradiation are summarized in Table 3. The electrical conductivity of the as-produced MNP-MWCNT thin films was higher than that of films without decorating MNPs, which is attributed to

the junction fabricated between the MWCNTs and MNPs to increase the number of effective charge-transfer pathways and reduce the contact resistance. In addition, the films could be bent without causing a decrease in the electrical conductivity of MW-plasma-treated Au-MWCNT and AgPt-MWCNT flexible TCFs. However, the MWCNTs, whose sheet resistance dramatically increased to 3400 ohm/sq from 200 ohm/sq owing to the destruction of charge-transfer pathways and the increase in contact resistance after the bending tests, did not exhibit this characteristic. This result

TABLE 3: Sheet resistance (ohm/sq) of the prepared flexible TCFs of MWCNT, Au-MWCNT, and AgPt-MWCNT before and after the flexibility test by two-point bending measurement.

| Bending cycles | Original | 100 | 250 | 500 |
|----------------|----------|-------|-------|-------|
| MWCNT | 200 | 3.4 K | 3.6 K | 3.7 K |
| Au-MWCNT | 157 | 157 | 155 | 158 |
| AgPt-MWCNT | 175 | 179 | 176 | 177 |

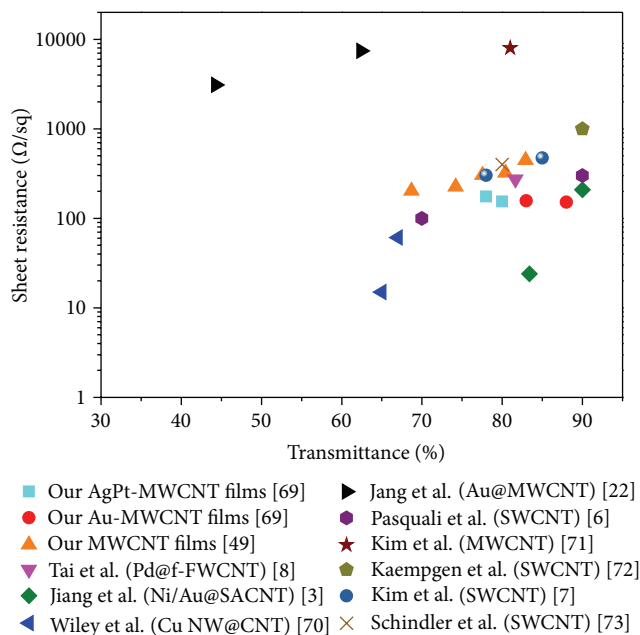


FIGURE 15: Comparison of the sheet resistance of our AgPt-MWCNT, Au-MWCNT, and MWCNT thin films after MW plasma treatment (two-probe resistance) with that of other CNT-based thin films with or without metallic NPs decoration reported in the literature, as a function of the transmittance at 550 nm.

indicates that the existence of MNPs can provide strong adhesion to the sidewalls of the MWCNTs through the intra- or interjunctions, thereby forming a robust MNP-MWCNT network of effective conducting pathways and enhanced mechanical ability.

6. Conclusion

Flexible, transparent, and conducting composite thin films, constructed from CNT-supported MNPs, have attracted a lot of attention owing to their potential in various applications. In this chapter, in addition to reviewing some of the synthesis processes for MNP-CNT flexible TCFs reported in the recent literature, we have also introduced our research results in this area. Through the combination of a polyol process for synthesizing composites of MWCNTs and MNPs with an ultrasonic atomization-spin coating method for preparing flexible thin films, we have successfully prepared Au NP-MWCNT, Pt NP-MWCNT, and AgPt NP-MWCNT flexible TCFs. More importantly, by subsequently exposing these nanocomposites to microwave plasma irradiation, improved optoelectronic

and mechanical properties of the films could be achieved owing to the formation of junction bridges between MWCNTs with MNPs, leading to lower contact resistance between the NPs and CNTs and reinforced frameworks. It is worth noting that our results are competitive with other MWCNT-based composite flexible transparent films (Figure 15) [3, 6–8, 40, 46, 69–73]. Synthesis of MNP-CNT flexible TCFs by our inexpensive, effective, convenient, and feasible method can offer a potential means for the development of various CNT-based substrates decorated with several different MNPs, which is favorable for industrial scalability and for use in next-generation flexible touch screens and optoelectronic devices.

Acknowledgment

The authors gratefully acknowledge the support through the National Science Council of Taiwan, Taiwan, under Project nos. NSC-101-2113-M-005-014-MY3 and NSC-101-2622-M-005-002-CC2.

References

- [1] G. Gruner, “Carbon nanotube films for transparent and plastic electronics,” *Journal of Materials Chemistry*, vol. 16, no. 35, pp. 3533–3539, 2006.
- [2] G. Jo, M. Choe, C.-Y. Cho et al., “Large-scale patterned multi-layer graphene films as transparent conducting electrodes for gan light-emitting diodes,” *Nanotechnology*, vol. 21, no. 17, Article ID 175201, 2010.
- [3] C. Feng, K. Liu, J. S. Wu et al., “Flexible, stretchable, transparent conducting films made from superaligned carbon nanotubes,” *Advanced Functional Materials*, vol. 20, no. 6, pp. 885–891, 2010.
- [4] S. I. Na, S. S. Kim, J. Jo, and D. Y. Kim, “Efficient and flexible ITO-free organic solar cells using highly conductive polymer anodes,” *Advanced Materials*, vol. 20, no. 21, pp. 4061–4017, 2008.
- [5] K. A. Sierros, N. J. Morris, S. N. Kukureka, and D. R. Cairns, “Dry and wet sliding wear of ITO-coated PET components used in flexible optoelectronic applications,” *Wear*, vol. 267, no. 1–4, pp. 625–631, 2009.
- [6] B. Dan, G. C. Irvin, and M. Pasquali, “Continuous and scalable fabrication of transparent conducting carbon nanotube films,” *ACS Nano*, vol. 3, no. 4, pp. 835–843, 2009.
- [7] S. Paul and D.-W. Kim, “Preparation and characterization of highly conductive transparent films with single-walled carbon nanotubes for flexible display applications,” *Carbon*, vol. 47, no. 10, pp. 2436–2441, 2009.
- [8] Y.-A. Li, N.-H. Tai, S.-K. Chen, and T.-Y. Tsai, “Enhancing the electrical conductivity of carbon-nanotube-based transparent

- conductive films using functionalized few-walled carbon nanotubes decorated with palladium nanoparticles as fillers,” *ACS Nano*, vol. 5, no. 8, pp. 6500–6506, 2011.
- [9] Y. Lin, K. A. Watson, M. J. Fallbach et al., “Rapid, solventless, bulk preparation of metal nanoparticle-decorated carbon nanotubes,” *ACS Nano*, vol. 3, no. 4, pp. 871–884, 2009.
- [10] S. Sahoo, S. Husale, S. Karna, S. K. Nayak, and P. M. Ajayan, “Controlled assembly of ag nanoparticles and carbon nanotube hybrid structures for biosensing,” *Journal of the American Chemical Society*, vol. 133, no. 11, pp. 4005–4009, 2011.
- [11] L. Dong, S. Youkey, J. Bush, J. Jiao, V. M. Dubin, and R. V. Chebiam, “Effects of local Joule heating on the reduction of contact resistance between carbon nanotubes and metal electrodes,” *Journal of Applied Physics*, vol. 101, no. 2, Article ID 024320, 2007.
- [12] B. Wu, Y. Kuang, X. Zhang, and J. Chen, “Noble metal nanoparticles/carbon nanotubes nanohybrids: synthesis and applications,” *Nano Today*, vol. 6, no. 1, pp. 75–90, 2011.
- [13] X. J. Zhou, A. J. Harmer, N. F. Heinig, and K. T. Leung, “Parametric study on electrochemical deposition of copper nanoparticles on an ultrathin polypyrrole film deposited on a gold film electrode,” *Langmuir*, vol. 20, no. 12, pp. 5109–5113, 2004.
- [14] W.-Y. Ko, W.-H. Chen, S.-D. Tzeng, S. Gwo, and K.-J. Lin, “Synthesis of pyramidal copper nanoparticles on gold substrate,” *Chemistry of Materials*, vol. 18, no. 26, pp. 6097–6099, 2006.
- [15] W.-Y. Ko, W.-H. Chen, C.-Y. Cheng, and K.-J. Lin, “Architectural growth of cu nanoparticles through electrodeposition,” *Nanoscale Research Letters*, vol. 4, no. 12, pp. 1481–1485, 2009.
- [16] C. R. Carpenter, P. H. Shipway, and Y. Zhu, “Electrodeposition of nickel-carbon nanotube nanocomposite coatings for enhanced wear resistance,” *Wear*, vol. 271, no. 9–10, pp. 2100–2105, 2011.
- [17] Z. He, J. Chen, D. Liu, H. Zhou, and Y. Kuang, “Electrodeposition of Pt-Ru nanoparticles on carbon nanotubes and their electrocatalytic properties for methanol electrooxidation,” *Diamond and Related Materials*, vol. 13, no. 10, pp. 1764–1770, 2004.
- [18] Z. He, J. Chen, D. Liu, H. Tang, W. Deng, and Y. Kuang, “Deposition and electrocatalytic properties of platinum nanoparticles on carbon nanotubes for methanol electrooxidation,” *Materials Chemistry and Physics*, vol. 85, no. 2–3, pp. 396–401, 2004.
- [19] T. M. Day, P. R. Unwin, and J. V. Macpherson, “Factors controlling the electrodeposition of metal nanoparticles on pristine single walled carbon nanotubes,” *Nano Letters*, vol. 7, no. 1, pp. 51–57, 2007.
- [20] S. C. Motshekga, S. K. Pillai, S. S. Ray, K. Jalama, and R. W. M. Krause, “Recent trends in the microwave-assisted synthesis of metal oxide nanoparticles supported on carbon nanotubes and their applications,” *Journal of Nanomaterials*, vol. 2012, Article ID 691503, 15 pages, 2012.
- [21] P. C. Sherrell, J. Chen, J. M. Razal et al., “Advanced microwave-assisted production of hybrid electrodes for energy applications,” *Energy and Environmental Science*, vol. 3, no. 12, pp. 1979–1984, 2010.
- [22] B. Zhang, X. Ni, W. Zhang et al., “Structural rearrangements of ru nanoparticles supported on carbon nanotubes under microwave irradiation,” *Chemical Communications*, vol. 47, no. 38, pp. 10716–10718, 2011.
- [23] R. Voggu, S. Pal, S. K. Pati, and C. N. R. Rao, “Semiconductor to metal transition in swnts caused by interaction with gold and platinum nanoparticles,” *Journal of Physics Condensed Matter*, vol. 20, no. 21, Article ID 215211, 2008.
- [24] T. Ramulifho, K. I. Ozoemena, R. M. Modibedi, C. J. Jafta, and M. K. Mathe, “Fast microwave-assisted solvothermal synthesis of metal nanoparticles (Pd, Ni, Sn) supported on sulfonated MWCNTs: Pd-based bimetallic catalysts for ethanol oxidation in alkaline medium,” *Electrochimica Acta*, vol. 59, pp. 310–320, 2012.
- [25] V. Selvaraj, M. Alagar, and K. S. Kumar, “Synthesis and characterization of metal nanoparticles-decorated PPY-CNT composite and their electrocatalytic oxidation of formic acid and formaldehyde for fuel cell applications,” *Applied Catalysis B*, vol. 75, no. 1–2, pp. 129–138, 2007.
- [26] J. Y. Kim, Y. Jo, S.-K. Kook, S. Lee, and H. C. Choi, “Synthesis of carbon nanotube supported Pd catalysts and evaluation of their catalytic properties for Csingle bondC bond forming reactions,” *Journal of Molecular Catalysis A*, vol. 323, no. 1–2, pp. 28–32, 2010.
- [27] J. F. Marêché, D. Bégin, G. Furdin et al., “Monolithic activated carbons from resin impregnated expanded graphite,” *Carbon*, vol. 39, no. 5, pp. 771–773, 2001.
- [28] D. B. Mawhinney, V. Naumenko, A. Kuznetsova, J. T. Yates Jr., J. Liu, and R. E. Smalley, “Infrared spectral evidence for the etching of carbon nanotubes: ozone oxidation at 298K,” *Journal of the American Chemical Society*, vol. 122, no. 10, pp. 2383–2384, 2000.
- [29] R. V. Hull, L. Li, Y. Xing, and C. C. Chusuei, “Pt nanoparticle binding on functionalized multiwalled carbon nanotubes,” *Chemistry of Materials*, vol. 18, no. 7, pp. 1780–1788, 2006.
- [30] X. Lu and T. Imae, “Size-controlled in situ synthesis of metal nanoparticles on dendrimer-modified carbon nanotubes,” *Journal of Physical Chemistry C*, vol. 111, no. 6, pp. 2416–2420, 2007.
- [31] W. Yang, Y. Wang, J. Li, and X. R. Yang, “Polymer wrapping technique: an effective route to prepare pt nanoflower/carbon nanotube hybrids and application in oxygen reduction,” *Energy & Environmental Science*, vol. 3, pp. 144–149, 2010.
- [32] Y. L. Hsin, K. C. Hwang, and C.-T. Yeh, “Poly(vinylpyrrolidone)-modified graphite carbon nanofibers as promising supports for ptru catalysts in direct methanol fuel cells,” *Journal of the American Chemical Society*, vol. 129, no. 32, pp. 9999–10010, 2007.
- [33] A. R. Tao, S. Habas, and P. Yang, “Shape control of colloidal metal nanocrystals,” *Small*, vol. 4, no. 3, pp. 310–325, 2008.
- [34] B. Lim, M. J. Jiang, J. Tao, P. H. C. Camargo, Y. M. Zhu, and Y. N. Xia, “Shape-controlled synthesis of pd nanocrystals in aqueous solutions,” *Advanced Functional Materials*, vol. 19, no. 2, pp. 189–200, 2009.
- [35] C.-Y. Lu, M.-C. Wei, S.-H. Chang, and M.-Y. Wey, “Study of the activity and backscattered electron image of Pt/CNTs prepared by the polyol process for flue gas purification,” *Applied Catalysis A*, vol. 354, no. 1–2, pp. 57–62, 2009.
- [36] O. Winjobi, Z. Zhang, C. Liang, and W. Li, “Carbon nanotube supported platinum-palladium nanoparticles for formic acid oxidation,” *Electrochimica Acta*, vol. 55, no. 13, pp. 4217–4221, 2010.
- [37] L. Li and Y. Xing, “Pt-Ru nanoparticles supported on carbon nanotubes as methanol fuel cell catalysts,” *Journal of Physical Chemistry C*, vol. 111, no. 6, pp. 2803–2808, 2007.
- [38] L. Qiu, V. G. Pol, Y. Wei, and A. Gedanken, “Sonochemical decoration of multi-walled carbon nanotubes with nanocrystalline tin,” *New Journal of Chemistry*, vol. 28, no. 8, pp. 1056–1059, 2004.

- [39] W.-Y. Ko, J.-W. Su, C.-H. Guo, and K.-J. Lin, "Extraordinary mechanical flexibility in composite thin films composed of bimetallic agpt nanoparticle-decorated multi-walled carbon nanotubes," *Carbon*, vol. 50, no. 6, pp. 2244–2251, 2012.
- [40] H. Park, J.-S. Kim, B. G. Choi et al., "Sonochemical hybridization of carbon nanotubes with gold nanoparticles for the production of flexible transparent conducting films," *Carbon*, vol. 48, no. 5, pp. 1325–1330, 2010.
- [41] S. B. Yang, B.-S. Kong, D.-H. Jung et al., "Recent advances in hybrids of carbon nanotube network films and nanomaterials for their potential applications as transparent conducting films," *Nanoscale*, vol. 3, no. 4, pp. 1361–1373, 2011.
- [42] S. B. Yang, B.-S. Kong, J. Geng, and H.-T. Jung, "Enhanced electrical conductivities of transparent double-walled carbon nanotube network films by post-treatment," *Journal of Physical Chemistry C*, vol. 113, no. 31, pp. 13658–13663, 2009.
- [43] B.-S. Kong, D.-H. Jung, S.-K. Oh, C.-S. Han, and H.-T. Jung, "Single-walled carbon nanotube gold nano hybrids: application in highly effective transparent and conductive films," *Journal of Physical Chemistry C*, vol. 111, no. 23, pp. 8377–8382, 2007.
- [44] K. Higashitani, C. E. McNamee, and M. Nakayama, "Formation of large-scale flexible transparent conductive films using evaporative migration characteristics of au nanoparticles," *Langmuir*, vol. 27, no. 6, pp. 2080–2083, 2011.
- [45] T. Tokuno, M. Nogi, J. Jiu, and K. Sukanuma, "Hybrid transparent electrodes of silver nanowires and carbon nanotubes: a low-temperature solution process," *Nanoscale Research Letters*, vol. 7, pp. 1–7, 2012.
- [46] W.-Y. Ko, J.-W. Su, C.-H. Guo, S.-J. Fu, C.-Y. Hsu, and K.-J. Lin, "Highly conductive, transparent flexible films based on open rings of multi-walled carbon nanotubes," *Thin Solid Films*, vol. 519, no. 22, pp. 7717–7722, 2011.
- [47] M. Terrones, H. Terrones, F. Banhart, J.-C. Charlier, and P. M. Ajayan, "Coalescence of single-walled carbon nanotubes," *Science*, vol. 288, no. 5469, pp. 1226–1229, 2000.
- [48] F. Banhart, "The formation of a connection between carbon nanotubes in an electron beam," *Nano Letters*, vol. 1, no. 6, pp. 329–332, 2001.
- [49] C. Jin, K. Suenaga, and S. Iijima, "Plumbing carbon nanotubes," *Nature Nanotechnology*, vol. 3, no. 1, pp. 17–21, 2008.
- [50] J. A. Rodríguez-Manzo, F. Banhart, M. Terrones et al., "Heterojunctions between metals and carbon nanotubes as ultimate nanocontacts," *Proceedings of the National Academy of Sciences of the United States of America*, vol. 106, no. 12, pp. 4591–4595, 2009.
- [51] J. A. Rodríguez-Manzo, M.-S. Wang, F. Banhart, Y. Bando, and D. Golberg, "Multibranch junctions of carbon nanotubes via cobalt particles," *Advanced Materials*, vol. 21, no. 44, pp. 4477–4482, 2009.
- [52] A. Velamakanni, C. W. Magnuson, K. J. Ganesh et al., "Site-specific deposition of au nanoparticles in CNT films by chemical bonding," *ACS Nano*, vol. 4, no. 1, pp. 540–546, 2010.
- [53] H. Ismaili, F. Lagugné-Labarthe, and M. S. Workentin, "Covalently assembled gold nanoparticle-carbon nanotube hybrids via a photoinitiated carbene addition reaction," *Chemistry of Materials*, vol. 23, no. 6, pp. 1519–1525, 2011.
- [54] S. Park, H. R. Kim, J. Kim et al., "Assembly of strands of multiwall carbon nanotubes and gold nanoparticles using alkanedithiols," *Carbon*, vol. 49, no. 2, pp. 487–494, 2011.
- [55] H. Conrads and M. Schmidt, "Plasma generation and plasma sources," *Plasma Sources Science and Technology*, vol. 9, no. 4, pp. 441–454, 2000.
- [56] C. Chen, A. Ogino, X. Wang, and M. Nagatsu, "Plasma treatment of multiwall carbon nanotubes for dispersion improvement in water," *Applied Physics Letters*, vol. 96, no. 13, Article ID 131504, 2010.
- [57] W. Lin, K.-S. Moon, S. Zhang et al., "Microwave makes carbon nanotubes less defective," *ACS Nano*, vol. 4, no. 3, pp. 1716–1722, 2010.
- [58] A. Irzh, I. Genish, L. Klein, L. A. Solovyov, and A. Gedanken, "Synthesis of zno and zn nanoparticles in microwave plasma and their deposition on glass slides," *Langmuir*, vol. 26, no. 8, pp. 5976–5984, 2010.
- [59] B. Hu, S.-B. Wang, K. Wang, M. Zhang, and S.-H. Yu, "Microwave-assisted rapid facile "green" synthesis of uniform silver nanoparticles: self-assembly into multilayered films and their optical properties," *Journal of Physical Chemistry C*, vol. 112, no. 30, pp. 11169–11174, 2008.
- [60] W. Liang and A. T. Harris, "Facile size and shape control of templated au nanoparticles under microwave irradiation," *Materials Letters*, vol. 65, no. 14, pp. 2307–2310, 2011.
- [61] C. Y. Hsu, J. W. Huang, S. Gwo, and K. J. Lin, "The facile fabrication of tunable plasmonic gold nanostructure arrays using microwave plasma," *Nanotechnology*, vol. 21, no. 3, Article ID 035302, 2010.
- [62] Y. Zhang, Y. Tang, Y. H. Hsieh et al., "Communication Towards a high-throughput label-free detection system combining localized-surface plasmon resonance and microfluidics," *Lab on a Chip*, vol. 12, pp. 3012–3015, 2012.
- [63] C. Y. Hsu, J. W. Huang, and K. J. Lin, "Communication high sensitivity and selectivity of human antibody attachment at the interstices between substrate-bound gold nanoparticles," *Chemical Communications*, vol. 47, pp. 872–874, 2011.
- [64] W.-H. Chen, W.-Y. Ko, S.-J. Fu, C.-H. Zeng, and K.-J. Lin, "Surface plasmon-induced photoluminescence in Au-CdSe hybrid architectonic solids," *Journal of the Chinese Chemical Society*, vol. 57, no. 4 B, pp. 790–794, 2010.
- [65] D. R. Kauffman and A. Star, "Chemically induced potential barriers at the carbon nanotube-metal nanoparticle interface," *Nano Letters*, vol. 7, no. 7, pp. 1863–1868, 2007.
- [66] Y. Shi, R. Yang, and P. K. Yuet, "Easy decoration of carbon nanotubes with well dispersed gold nanoparticles and the use of the material as an electrocatalyst," *Carbon*, vol. 47, no. 4, pp. 1146–1151, 2009.
- [67] V. Tzitzios, V. Georgakilas, E. Oikonomou, M. Karakassides, and D. Petridis, "Synthesis and characterization of carbon nanotube/metal nanoparticle composites well dispersed in organic media," *Carbon*, vol. 44, no. 5, pp. 848–853, 2006.
- [68] Z. Peng and H. Yang, "Ag-Pt alloy nanoparticles with the compositions in the miscibility gap," *Journal of Solid State Chemistry*, vol. 181, no. 7, pp. 1546–1551, 2008.
- [69] W.-Y. Ko, J.-W. Su, C.-H. Guo, and K.-J. Lin, "Extraordinary mechanical flexibility in composite thin films composed of bimetallic agpt nanoparticle-decorated multi-walled carbon nanotubes," *Carbon*, vol. 50, no. 6, pp. 2244–2251, 2012.
- [70] A. R. Rathmell, S. M. Bergin, Y.-L. Hua, Z.-Y. Li, and B. J. Wiley, "The growth mechanism of copper nanowires and their properties in flexible, transparent conducting films," *Advanced Materials*, vol. 22, no. 32, pp. 3558–3563, 2010.
- [71] M. Kaempgen, G. S. Duesberg, and S. Roth, "Transparent carbon nanotube coatings," *Applied Surface Science*, vol. 252, no. 2, pp. 425–429, 2005.

- [72] S. Manivannan, J. H. Ryu, H. E. Lim, M. Nakamoto, J. Jang, and K. C. Park, "Properties of surface treated transparent conducting single walled carbon nanotube films," *Journal of Materials Science: Materials in Electronics*, vol. 21, no. 1, pp. 72–77, 2010.
- [73] A. Schindler, J. Brill, N. Fruehauf, J. P. Novak, and Z. Yaniv, "Solution-deposited carbon nanotube layers for flexible display applications," *Physica E*, vol. 37, no. 1-2, pp. 119–123, 2007.

Research Article

Graphene Supported Pt/Ni Nanoparticles as Magnetically Separable Nanocatalysts

Ru Liu, Qingshan Zhao, Yang Li, Guoliang Zhang, Fengbao Zhang, and Xiaobin Fan

State Key Laboratory of Chemical Engineering, Key Laboratory for Green Chemical Technology, School of Chemical Engineering & Technology, Tianjin University, Tianjin 300072, China

Correspondence should be addressed to Xiaobin Fan; xiaobinfan@tju.edu.cn

Received 12 March 2013; Accepted 10 September 2013

Academic Editor: Teng Li

Copyright © 2013 Ru Liu et al. This is an open access article distributed under the Creative Commons Attribution License, which permits unrestricted use, distribution, and reproduction in any medium, provided the original work is properly cited.

Efficient recovery of nanocatalysts, especially the graphene supported noble metal catalysts, is a challenge. In this study, we report a simple one-step route to prepare the graphene supported Pt/Ni nanocatalysts with ideal superparamagnetic properties. We demonstrated that they had excellent catalytic activities in the catalytic reduction of aromatic nitro compounds and could be easily separated from the reaction mixtures by applying an external magnetic field.

1. Introduction

Graphene [1], a one-atom-thick planar sheet of hexagonally arrayed sp^2 carbon atoms, has attracted tremendous attention in recent years [2–5]. Especially, graphene has been emerging as a promising supporting in heterogeneous catalytic processes [6–10] due to its large surface areas [11], impressive mechanical strength [12, 13], chemical inertness, and strong interactions with metal clusters. In recent years, many monometallic and bimetallic catalytic nanoparticles, such as Pd [14], Au [15], Pt [16], Au@Pd [17], and Pt-on-Pd [18], have been successfully dispersed on graphene. The obtained hybrids show impressive catalytic performances in various reactions. However, most of the time, noble metals act as key components of these nanocatalysts, and the efficient recovery of these noble metals from reaction systems remains a challenge. In this respect, a promising solution to solve this problem is the magnetic separation by which the magnetically separable nanoparticles are employed to efficiently separate the catalyst from reaction mixture [19, 20]. In fact, a number of functionalized magnetically separable nanoparticles have been employed in organic reactions as C–C coupling [21], hydrogenation [22], oxidation [23], amination [24], and nitrile hydration [25].

Here, we report a one-step route to prepare the graphene supported Pt/Ni hybrids (Pt/Ni-G) (Scheme 1), which have

superparamagnetic properties and show superior catalytic activities in the model reaction of p-nitrophenol (4-NP) reduction.

2. Experimental

2.1. Synthesis of Pt/Ni-G Hybrids. Graphite oxide was prepared by the modified Hummers method [26] and exfoliated into graphene oxide (GO) at a concentration of 0.5 mg/mL by sonication in water [27]. Typically, 100 mL of graphene oxide (GO) was dispersed in 50 mL Tannin (TA) aqueous solution (5 mg/mL) under sonication for 30 min. Then, the excess TA was discarded by centrifugation and the as-prepared TA-functionalized GO was dissolved into 50 mL of water. The concentrations of H_2PtCl_6 and $NiSO_4$ were adjusted to 4.8×10^{-4} and 1.2×10^{-2} M in the TA-GO solution, respectively; thus, Pt:Ni became 1:25. Nitrogen was purged through the solution for 5 min, and then the solution was stirred in airtight conditions. After 30 min of stirring, 0.3 mL of $N_2H_4 \cdot H_2O$ (80%) and 2 mL of KOH solution (9.0 M) were injected into the solution. The solution turned black immediately and was kept stirred for 15 min. Finally, the product was washed 8–10 times with ethanol and deionized water for purification purposes.



SCHEME 1: Illustration of preparing Pt/Ni-G hybrids.

2.2. Catalytic Reduction of *p*-Nitrophenol by Pt/Ni-G Hybrids.

To investigate the catalytic activity of the as-prepared hybrids, the reduction of *p*-nitrophenol (4-NP) was tested in a quartz cuvette. In brief, 20 μL of 10^{-2} M aqueous 4-NP and 40 μL of ultrasonically dispersed Pt/Ni-G solution (0.1 mg/mL) were introduced into 2 mL deionized water, resulting in a constant metal loading of 4.0 μg . Then, 0.3 mL of 10^{-1} M aqueous NaBH_4 was rapidly added. The yellow color of the solution gradually vanished, indicating the formation of *p*-aminophenol (4-AP) [28]. The time-dependent UV-Vis absorption spectra were recorded in a scanning range of 200–600 nm at $25 \pm 1^\circ\text{C}$.

2.3. Characterization. The as-prepared Pt/Ni-graphene hybrids were characterized by high-resolution transmission electron microscopy (HRTEM) (Philips Tecnai G2 F20), scanning electron microscopy (SEM) (Hitachi S-4800), energy dispersive X-ray spectroscopy (EDX) (Philips Tecnai G2 F20 & Hitachi S-4800), and X-ray photoelectron spectroscopy (XPS) (PerkinElmer, PHI 1600 spectrometer). The X-ray diffraction (XRD) was conducted on a Bruker-Nonius D8 FOCUS diffractometer. The catalytic activity of Pt/Ni-G hybrids was measured by UV absorption spectra on a UV-2802H system with a temperature controller.

3. Results and Discussion

3.1. Synthesis of Pt/Ni-G Hybrids. The XRD diffraction pattern of the Pt/Ni-graphene hybrids was recorded to identify the product (Figure 1). The main diffraction peaks show the face-centered cubic (fcc) structure of both metallic nickel and nickel oxide [29]. Corresponding XPS pattern has authenticated this result. No peaks of Pt are observed because of the pretty low proportion of Pt: Ni, but the 2θ of Ni (111) peak shifts to a lower angle compared to that of nickel nanoparticles, indicating the alloy formation where the lattice expansion occurred due to the substitution of nickel atoms by larger platinum atoms [30]. Based on the Ni (111) peak, the crystallite size diameter (D_c) of supported nanoparticles is calculated to be about 14.7 nm by Debye-Scherrer equation.

Further evidence for the chemical state and composition of the hybrids was obtained by X-ray photoelectron spectra (XPS). Compared with GO (Figure 2(a)), the full range XPS spectra of the obtained hybrids (Figure 2(b)) show an obvious decrease of O : C atomic ratio. This result should be attributed to the partial removal of the oxide functional groups from GO during the reduction procedure (Figures 2(c) and 2(d)).

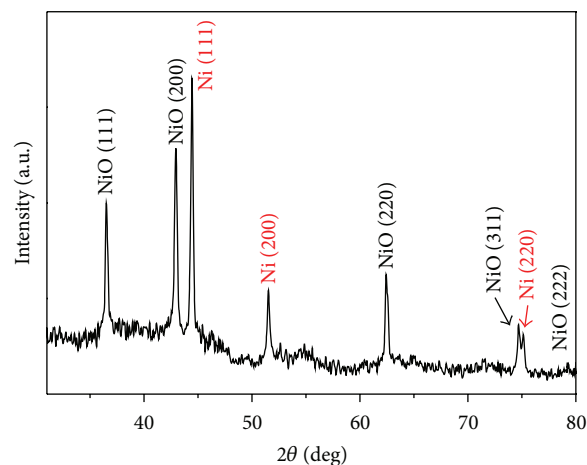


FIGURE 1: XRD pattern of the as-prepared Pt/Ni-G hybrids.

In addition, clear evidence for the existence of Pt and Ni in the hybrids is readily observed. The Pt 4f spectrum (Figure 2(e)) consists of two peaks for metallic platinum at 71.3 (Pt $4f_{7/2}$) and 74.2 eV (Pt $4f_{5/2}$), without the peaks for Pt^{2+} and Pt^{4+} at 72.8 and 74.6 eV, respectively [31]. This result indicates that Pt is present in the zero-valent metallic state in the alloy nanoparticles. In contrast, the Ni $2p_{3/2}$ spectrum (Figure 2(f)) shows a complex structure with intense satellite signals of high binding energy adjacent to the main peaks, which may be ascribed to a multielectron excitation (shake-up peaks) [32]. After these shake-up peaks are considered, the Ni $2p_{3/2}$ spectrum has been deconvoluted into two peaks; the first small one located at 852.6 eV corresponds to metallic nickel, and the main one located at 854.0 eV is assigned to NiO [33]. From the intensities of the deconvoluted XPS signal of Ni, it is obvious that the surface of the nanoparticles is predominately NiO.

The surface morphological study was carried out by using TEM. As shown in Figure 3(a), spherical nanoparticles were homogeneously dispersed on the surfaces of graphene. The sizes of nanoparticles are in the range of 12–19 nm, with a mean size of 15.4 nm. This value is in close agreement with the diameter of 14.7 nm obtained from XRD.

Interestingly, it is easy to find that the graphene supported nanoparticles show a dark core and a comparatively pale shell under the HRTEM image of Pt/Ni-G (Figure 3(b)), indicating the core-shell structure. The lattice spacing in the core of the graphene supported Pt/Ni nanoparticles (marked as “a,” Figure 3(b)) is 0.207 nm, whereas those of pure Pt (111) and Ni (111) are 0.23 and 0.203 nm, respectively. The supported Pt/Ni nanoparticles also show NiO lattice fringes on the particle surface (marked as “b”), with the d-spacing of 0.24 nm corresponding to the NiO (200) planes [34, 35]. These results suggest the alloy formation of Pt and Ni, and the particles would be covered by a NiO layer that was formed by the surface oxidation.

These results are further supported by line scanning analysis. As shown in Figure 3(c), Pt is primarily in the 8 nm core while Ni uniformly is distributed on the whole surface of the Pt/Ni nanoparticle.

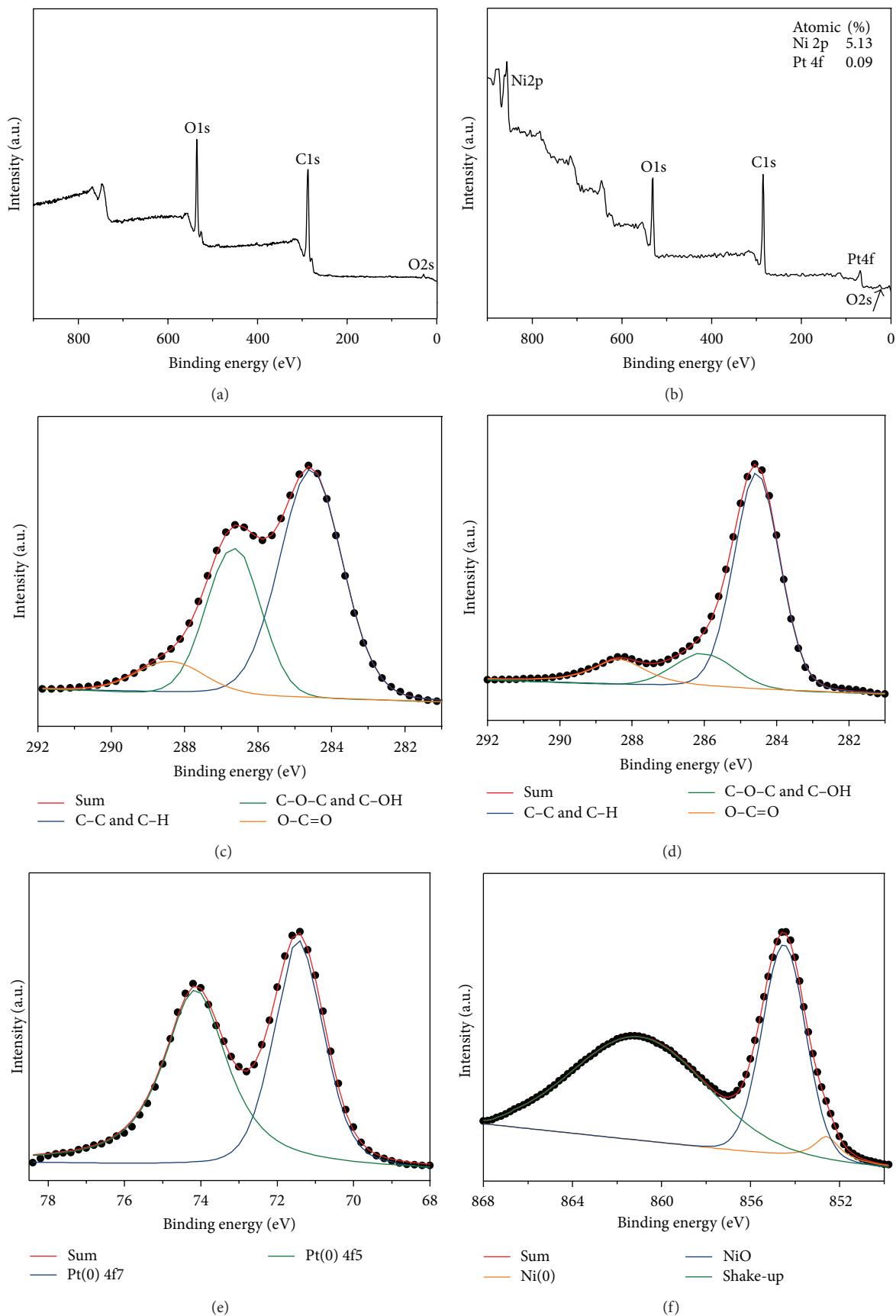


FIGURE 2: Survey XPS spectra of GO (a) and Pt/Ni-G (b). C1s XPS spectra of GO (c) and Pt/Ni-G (d). Pt 4f spectra (e) and Ni 2p3 spectra (f) of Pt/Ni-G.

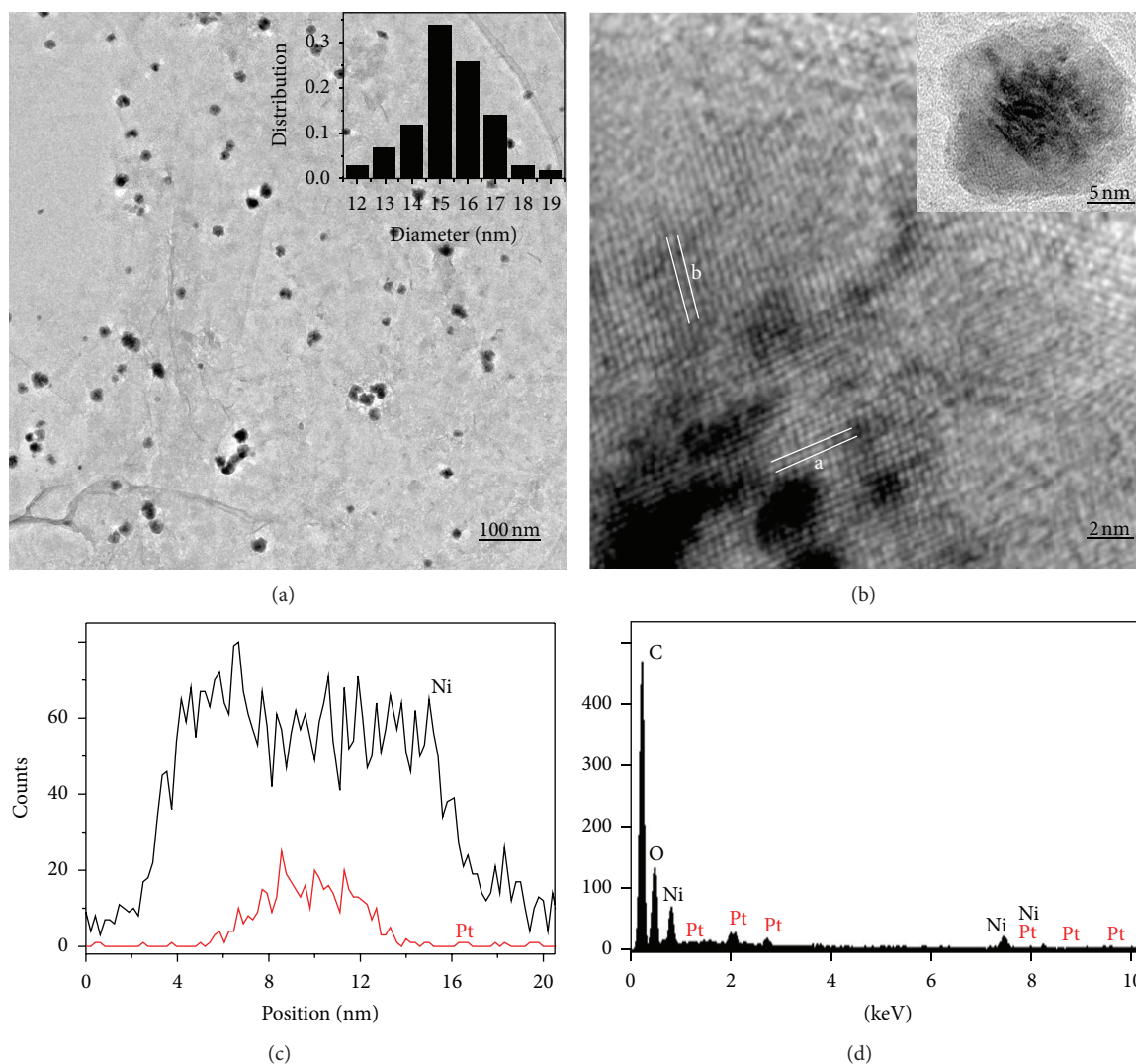


FIGURE 3: TEM image and size distribution (total no.: 101, mean diameter: 15.4 nm) (a) and HRTEM image (b) of Pt/Ni-G bimetallic nanoparticles homogeneously decorated on the surface of graphene. Line scanning analysis (c) and corresponding EDX results (d).

Interestingly, quantitative analysis by EDX (Figure 3(d)) suggests that the Pt:Ni atomic ratio is 1:26, a value close to the stoichiometric ratio (1:25) of the metal precursors. But the surface Pt:Ni atomic ratio measured by XPS is only 1:57 (Figure 2(b)). Given that XPS can only penetrate several nanometers of the surface, this result strongly supports the formation of a NiO layer out of the supported Pt/Ni alloy. Quantitative energy dispersive X-ray spectroscopy (EDS) mapping confirms that both Pt and Ni are homogeneously distributed on the whole surface of graphene, shown in Figure 4.

3.2. Magnetic Characterization. Figure 5(a) shows the magnetization versus field plots (M versus H hysteresis loops) of Pt/Ni-G hybrids by Quantum Design SQUID-VSM magnetometer under -10 to 10 KOe at room temperature. The saturation magnetization (M_s) for the sample is 11.6 emu/g. And the curve does not exhibit hysteresis, indicating that

Pt/Ni-G hybrids at room temperature show superparamagnetic behavior. Previous studies on magnetic nanoparticles have demonstrated that when the size of the magnetic particles decreases they change from multidomain to single domain [36]. Therefore, when particles become small enough (typically below 35 nm [37]), the magnetic moment in the domain fluctuates in direction, leading to superparamagnetism (SPM).

3.3. Catalytic Reaction. To probe the catalytic performances of the obtained hybrids, reduction of p-nitrophenol (4-NP) to its corresponding amino derivative was used as the model reaction. In brief, the catalytic reduction of 4-NP by excessive NaBH_4 was carried out at room temperature under solvent free condition by using as-synthesized Pt/Ni-G hybrids catalysts. The reaction process was monitored by the UV-Vis spectrophotometry and conducted in the absence of catalysts first. It was observed that the yellow color of the solution deepened after the addition of NaBH_4 , and a red shift of the peak from

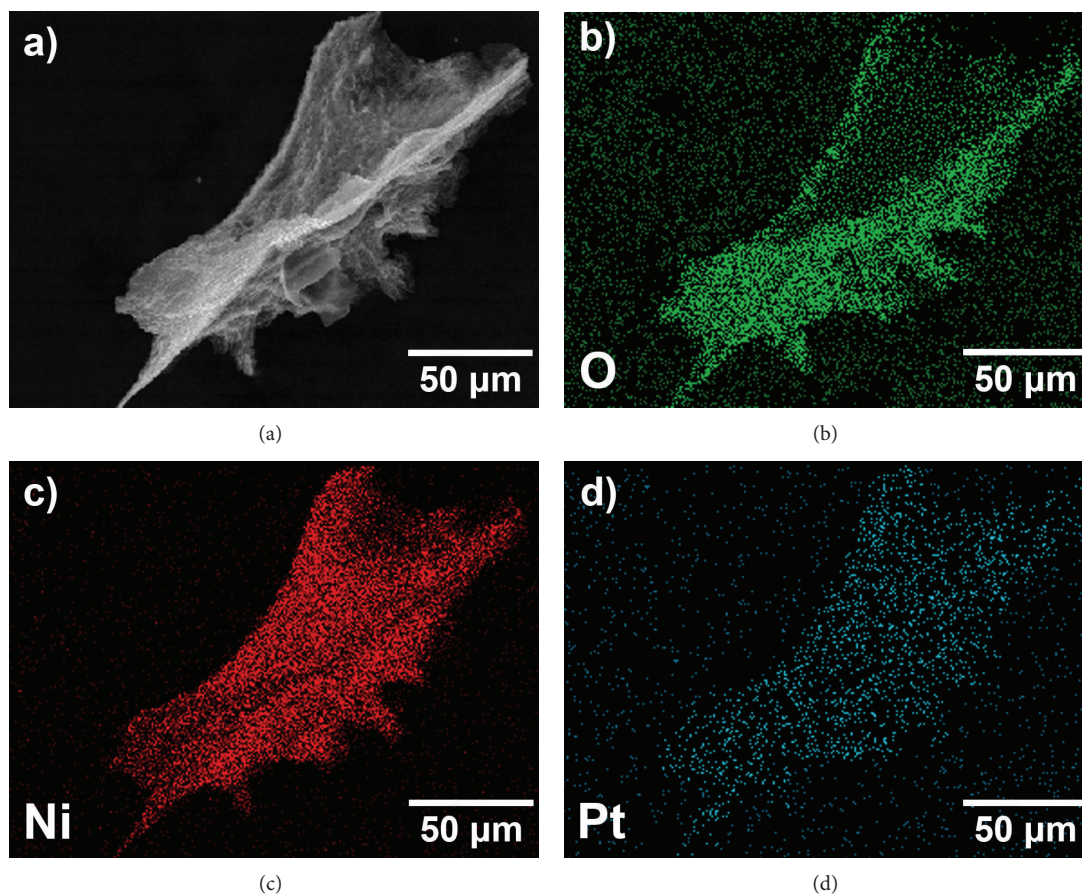


FIGURE 4: SEM image of Pt/Ni-G (a) and corresponding quantitative EDS element mapping of O (b), Ni (c), and Pt (d).

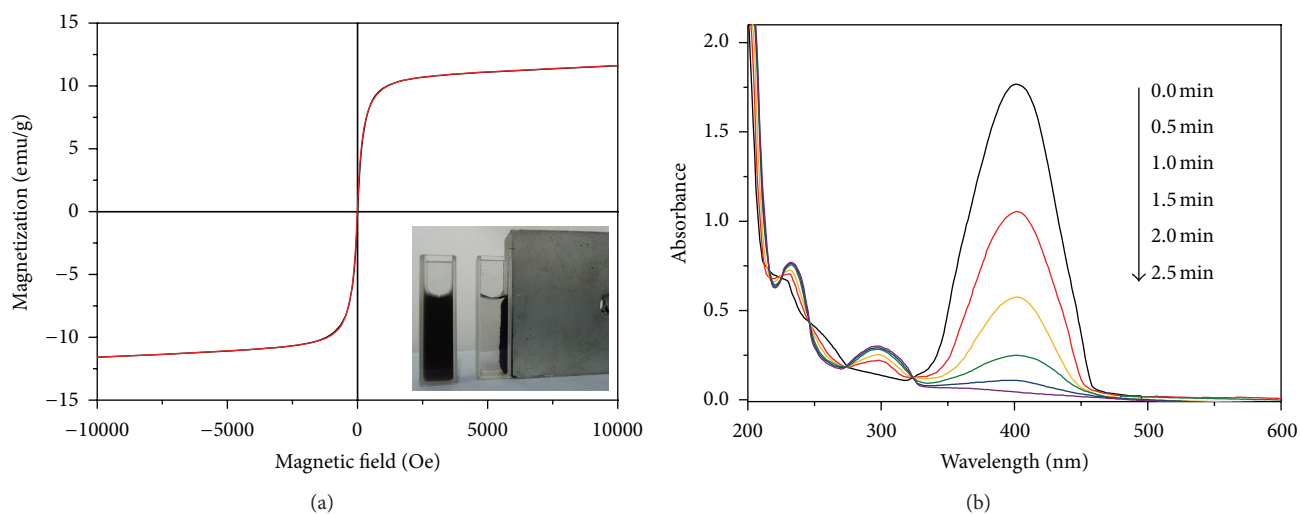


FIGURE 5: Hysteresis loop of Pt/Ni-G hybrids measured by SQUID magnetometer at 300 K (a). Successive UV-Vis spectra showing the reduction of 4-NP catalyzed by 4.0 μg Pt/Ni-G hybrids (b).

317 to 400 nm occurred. This phenomenon was caused by the formation of p-nitrophenolate ions in alkaline condition [38]. The intensity of the absorbance remained unchanged at 400 nm even after several days, indicating that no reduction of 4-NP occurred. However, in the presence of the Pt/Ni-G

hybrids, quick reduction of 4-NP to p-aminophenol (4-AP) by NaBH_4 was observed (Figure 5(b)). The absorption of 4-NP at 400 nm completely vanished within 2.5 minutes, accompanied by the fast appearance of the new peaks of 4-AP at 300 nm [39].

The excellent catalytic activity of the Pt/Ni-G hybrids can be attributed to the alloy nature of the supported Pt/Ni nanoparticles, which usually show superior catalytic performance than their monometallic counterparts [40]. In addition, by dispersing on the two-dimensional graphene sheets with large surface areas, the Pt/Ni nanoparticles can prevent aggregation that shields their active catalytic sites. Therefore, 4-NP molecules readily access the catalytic Pt/Ni nanoparticles from two sides of the graphene sheets with limited mass transfer hindrance. Importantly, the Pt/Ni-G hybrids can be easily recycled by using an external magnetic field after the reaction and reused without observable decrease in their catalytic activities.

4. Conclusions

In summary, we developed a simple one-step route to prepare the graphene supported Pt/Ni nanoparticles (Pt/Ni-G). The supported Pt/Ni nanoparticles had a mean diameter of 15 nm and showed superparamagnetic behavior. Catalytic investigation revealed the excellent catalytic activity of the obtained hybrids in the catalytic reduction of aromatic nitro compounds. Notably, the Pt/Ni-G hybrids could be easily separated from the reaction mixtures by applying an external magnetic field. Given their excellent catalytic performances, as well as their magnetically separable nature, these Pt/Ni-G hybrids are ideal recoverable nanocatalysts and may find potential applications in a variety of reactions.

Acknowledgments

This study was supported by the National Natural Science Funds for Excellent Young Scholars (no. 21222608), Research Fund of the National Natural Science Foundation of China (no. 21106099), Foundation for the Author of National Excellent Doctoral Dissertation of China (no. 201251), the Tianjin Natural Science Foundation (no. 11JCYBJC01700), and the Programme of Introducing Talents of Discipline to Universities (no. B06006).

References

- [1] K. S. Novoselov, A. K. Geim, S. V. Morozov et al., "Electric field in atomically thin carbon films," *Science*, vol. 306, no. 5696, pp. 666–669, 2004.
- [2] A. K. Geim and K. S. Novoselov, "The rise of graphene," *Nature Materials*, vol. 6, no. 3, pp. 183–191, 2007.
- [3] M. H. Rummeli, C. G. Rocha, F. Ortman et al., "Graphene: piecing it together," *Advanced Materials*, vol. 23, no. 39, pp. 4471–4490, 2011.
- [4] M. J. Allen, V. C. Tung, and R. B. Kaner, "Honeycomb carbon: a review of graphene," *Chemical Reviews*, vol. 110, no. 1, pp. 132–145, 2010.
- [5] S. Stankovich, D. A. Dikin, G. H. B. Dommett et al., "Graphene-based composite materials," *Nature*, vol. 442, no. 7100, pp. 282–286, 2006.
- [6] Y. Li, X. Fan, J. Qi et al., "Palladium nanoparticle-graphene hybrids as active catalysts for the Suzuki reaction," *Nano Research*, vol. 3, no. 6, pp. 429–437, 2010.
- [7] J. Wang, C. An, J. Liu et al., "Graphene oxide coupled AgBr nanosheets: an efficient dual-functional visible-light-responsive nanophotocatalyst with enhanced performance," *Journal of Materials Chemistry A*, vol. 1, no. 8, pp. 2827–2832, 2013.
- [8] X. Cui, C. Zhang, R. Hao, and Y. Hou, "Liquid-phase exfoliation, functionalization and applications of graphene," *Nanoscale*, vol. 3, no. 5, pp. 2118–2126, 2011.
- [9] T. Xue, S. Jiang, Y. Qu et al., "Graphene-supported hemin as a highly active biomimetic oxidation catalyst," *Angewandte Chemie—International Edition*, vol. 51, no. 16, pp. 3822–3825, 2012.
- [10] Q. Zhao, D. Chen, Y. Li, G. Zhang, F. Zhang, and X. Fan, "Rhodium complex immobilized on graphene oxide as an efficient and recyclable catalyst for hydrogenation of cyclohexene," *Nanoscale*, vol. 5, no. 3, pp. 882–885, 2013.
- [11] M. J. McAllister, J.-L. Li, D. H. Adamson et al., "Single sheet functionalized graphene by oxidation and thermal expansion of graphite," *Chemistry of Materials*, vol. 19, no. 18, pp. 4396–4404, 2007.
- [12] D. A. Dikin, S. Stankovich, E. J. Zimney et al., "Preparation and characterization of graphene oxide paper," *Nature*, vol. 448, no. 7152, pp. 457–460, 2007.
- [13] F. Scarpa, S. Adhikari, and A. Srikantha Phani, "Effective elastic mechanical properties of single layer graphene sheets," *Nanotechnology*, vol. 20, no. 6, Article ID 065709, 2009.
- [14] T. Jin, S. Guo, J. I. Zuo, and S. Sun, "Synthesis and assembly of Pd nanoparticles on graphene for enhanced electrooxidation of formic acid," *Nanoscale*, vol. 5, no. 1, pp. 160–163, 2013.
- [15] T. Zeng, X. Zhang, Y. Ma, H. Niu, and Y. Cai, "A novel Fe₃O₄-graphene-Au multifunctional nanocomposite: green synthesis and catalytic application," *Journal of Materials Chemistry*, vol. 22, no. 35, pp. 18658–18663, 2012.
- [16] P. Kundu, C. Nethravathi, P. A. Deshpande, M. Rajamathi, G. Madras, and N. Ravishankar, "Ultrafast microwave-assisted route to surfactant-free ultrafine Pt nanoparticles on graphene: synergistic co-reduction mechanism and high catalytic activity," *Chemistry of Materials*, vol. 23, no. 11, pp. 2772–2780, 2011.
- [17] H. Chen, Y. Li, F. Zhang, G. Zhang, and X. Fan, "Graphene supported Au-Pd bimetallic nanoparticles with core-shell structures and superior peroxidase-like activities," *Journal of Materials Chemistry*, vol. 21, no. 44, pp. 17658–17661, 2011.
- [18] S. Guo, D. Wen, Y. Zhai, S. Dong, and E. Wang, "Platinum nanoparticle ensemble-on-graphene hybrid nanosheet: one-pot, rapid synthesis, and used as new electrode material for electrochemical sensing," *ACS Nano*, vol. 4, no. 7, pp. 3959–3968, 2010.
- [19] D. Astruc, F. Lu, and J. R. Aranzas, "Nanoparticles as recyclable catalysts: the frontier between homogeneous and heterogeneous catalysis," *Angewandte Chemie—International Edition*, vol. 44, no. 48, pp. 7852–7872, 2005.
- [20] S. Shylesh, V. Schünemann, and W. R. Thiel, "Magnetically separable nanocatalysts: bridges between homogeneous and heterogeneous catalysis," *Angewandte Chemie—International Edition*, vol. 49, no. 20, pp. 3428–3459, 2010.
- [21] S. Ceylan, C. Friese, C. Lammel, K. Mazac, and A. Kirschning, "Induktives heizen in der organischen synthese durch verwendung funktionalisierter magnetischer nanopartikel in mikroreaktoren," *Angewandte Chemie*, vol. 120, no. 46, pp. 9083–9086, 2008.
- [22] Y. Chi, Q. Yuan, Y. Li et al., "Synthesis of Fe₃O₄@SiO₂-Ag magnetic nanocomposite based on small-sized and highly dispersed

- silver nanoparticles for catalytic reduction of 4-nitrophenol," *Journal of Colloid and Interface Science*, vol. 383, no. 1, pp. 96–102, 2012.
- [23] C. Kamonsatikul, T. Khamnaen, P. Phiriyawirut, S. Charoenchaidet, and E. Somsook, "Synergistic activities of magnetic iron-oxide nanoparticles and stabilizing ligands containing ferrocene moieties in selective oxidation of benzyl alcohol," *Catalysis Communications*, vol. 26, pp. 1–5, 2012.
- [24] Y.-H. Liu, J. Deng, J.-W. Gao, and Z.-H. Zhang, "Triflic acid-functionalized silica-coated magnetic nanoparticles as a magnetically separable catalyst for synthesis of gem-dihydroperoxides," *Advanced Synthesis and Catalysis*, vol. 354, no. 2-3, pp. 441–447, 2012.
- [25] V. Polshettiwar and R. S. Varma, "Nanoparticle-supported and magnetically recoverable ruthenium hydroxide catalyst: efficient hydration of nitriles to amides in aqueous medium," *Chemistry—A European Journal*, vol. 15, no. 7, pp. 1582–1586, 2009.
- [26] A. Lerf, H. He, M. Forster, and J. Klinowski, "Structure of graphite oxide revisited," *The Journal of Physical Chemistry B*, vol. 102, no. 23, pp. 4477–4482, 1998.
- [27] S. Park and R. S. Ruoff, "Chemical methods for the production of graphenes," *Nature Nanotechnology*, vol. 4, no. 4, pp. 217–224, 2009.
- [28] T. R. Mandlimath and B. Gopal, "Catalytic activity of first row transition metal oxides in the conversion of p-nitrophenol to p-aminophenol," *Journal of Molecular Catalysis A*, vol. 350, no. 1-2, pp. 9–15, 2011.
- [29] F. Davar, Z. Fereshteh, and M. Salavati-Niasari, "Nanoparticles Ni and NiO: synthesis, characterization and magnetic properties," *Journal of Alloys and Compounds*, vol. 476, no. 1-2, pp. 797–801, 2009.
- [30] S. K. Singh and Q. Xu, "Bimetallic Ni-Pt nanocatalysts for selective decomposition of hydrazine in aqueous solution to hydrogen at room temperature for chemical hydrogen storage," *Inorganic Chemistry*, vol. 49, no. 13, pp. 6148–6152, 2010.
- [31] H. Gao, F. Xiao, C. B. Ching, and H. Duan, "One-step electrochemical synthesis of PtNi nanoparticle-graphene nanocomposites for nonenzymatic amperometric glucose detection," *ACS Applied Materials and Interfaces*, vol. 3, no. 8, pp. 3049–3057, 2011.
- [32] K. T. Ng and D. M. Hercules, "Studies of nickel-tungsten-alumina catalysts by X-ray photoelectron spectroscopy," *The Journal of Physical Chemistry*, vol. 80, no. 19, pp. 2094–2102, 1976.
- [33] R. Schulz, A. van Neste, P. A. Zielinski et al., "A novel method to produce nanocrystalline metastable supported catalysts," *Catalysis Letters*, vol. 35, no. 1-2, pp. 89–106, 1995.
- [34] Y. Li, L. Tang, and J. Li, "Preparation and electrochemical performance for methanol oxidation of Pt/graphene nanocomposites," *Electrochemistry Communications*, vol. 11, no. 4, pp. 846–849, 2009.
- [35] I. S. Lee, N. Lee, J. Park et al., "Ni/NiO core/shell nanoparticles for selective binding and magnetic separation of histidine-tagged proteins," *Journal of the American Chemical Society*, vol. 128, no. 33, pp. 10658–10659, 2006.
- [36] N. Amin, S. Arajs, and E. Matijevic, "Magnetic properties of submicronic α -Fe₂O₃ particles of uniform size distribution at 300 K," *Physica Status Solidi (A)*, vol. 104, no. 1, pp. K65–K68, 1987.
- [37] T. Seto, H. Akinaga, F. Takano, K. Koga, T. Orii, and M. Hirasawa, "Magnetic properties of monodispersed Ni/NiO core-shell nanoparticles," *The Journal of Physical Chemistry B*, vol. 109, no. 28, pp. 13403–13405, 2005.
- [38] N. Pradhan, A. Pal, and T. Pal, "Silver nanoparticle catalyzed reduction of aromatic nitro compounds," *Colloids and Surfaces A*, vol. 196, no. 2-3, pp. 247–257, 2002.
- [39] J. Huang, S. Vongehr, S. Tang, H. Lu, and X. Meng, "Highly catalytic Pd-Ag bimetallic dendrites," *The Journal of Physical Chemistry C*, vol. 114, no. 35, pp. 15005–15010, 2010.
- [40] H.-L. Jiang and Q. Xu, "Recent progress in synergistic catalysis over heterometallic nanoparticles," *Journal of Materials Chemistry*, vol. 21, no. 36, pp. 13705–13725, 2011.

Research Article

Effect of Modified and Nonmodified Carbon Nanotubes on the Rheological Behavior of High Density Polyethylene Nanocomposite

Adewunmi A. Ahmad,¹ Abdulhadi A. Al-Juhani,¹ Selvin Thomas,²
S. K. De,¹ and Muataz A. Atieh¹

¹ Department of Chemical Engineering, King Fahd University of Petroleum and Minerals (KFUPM) P.O. Box 5050, Dhahran 31261, Saudi Arabia

² Chemical Engineering Technology Department & Yanbu Research Center, Yanbu Industrial College, P.O. Box 30436, Yanbu Industrial City 21477, Saudi Arabia

Correspondence should be addressed to Muataz A. Atieh; motazali@kfupm.edu.sa

Received 31 March 2013; Revised 2 September 2013; Accepted 8 September 2013

Academic Editor: Sulin Zhang

Copyright © 2013 Adewunmi A. Ahmad et al. This is an open access article distributed under the Creative Commons Attribution License, which permits unrestricted use, distribution, and reproduction in any medium, provided the original work is properly cited.

This paper reports the results of studies on the rheological behavior of nanocomposites of high density polyethylene (HDPE) with pristine multiwall carbon nanotubes (CNT) as well as phenol and 1-octadecanol (C18) functionalized CNT at 1, 2, 3, 4, 5, and 7 wt% loading. The viscosity reduction at 1 wt% CNT follows the order, pristine CNT < phenol functionalized CNT < C18 functionalized CNT. As the filler loading increases from 1 to 2, 3, and 4 wt%, neat HDPE and filled HDPE systems show similar moduli and viscosity, particularly in the low frequency region. As the filler loading increases further to 5 and 7 wt%, the viscosity and moduli become greater than the neat HDPE. The storage modulus, $\tan\delta$, and the Cole-Cole plots show that CNT network formation occurs at higher CNT loading. The critical CNT loading or the rheological percolation threshold, where network formation occurs is found to be strongly dependant on the functionalization of CNT. For pristine CNT, the rheological percolation threshold is around 4 wt%, but for functionalized CNT it is around 7 wt%. The surface morphologies of CNT and functionalized CNT at 1 wt% loading showed good dispersion while at 7 wt% loading, dispersion was also achieved, but there are few regions with agglomeration of CNT.

1. Introduction

High density polyethylene (HDPE) is a commodity thermoplastic polymer and is widely used in different applications due to its outstanding features such as regular chain structure, combination of low cost and low energy demand for processing, excellent biocompatibility, and good mechanical properties [1, 2]. Properties of HDPE can be further manipulated by the addition of organic or inorganic particles into the polymer matrix [3, 4]. The nanofiller reinforced HDPE composites have been studied for various fillers like nanoclay, metal oxide nano particles, and carbon nanotubes [5–7].

The dispersion of carbon nanotubes is a great challenge in the fabrication of polymer composites. Good dispersion

of CNT into any polymer matrix is very difficult to achieve. Techniques such as surfactant-assisted processing, solution-evaporation methods with high-energy sonication, and covalent functionalization of the nanotubes with a polymer matrix have been exploited, but good dispersion was not always achievable in all polymer matrices [8–10]. Enhancement of interfacial interaction on incorporation of surfactants as the processing aid was reported by Gong et al. in epoxy/CNT composites [11]. They observed an increase in glass transition temperature from 63°C to 88°C and 30% increase in elastic modulus at 1 wt% loading of surfactant modified CNT, even though good dispersion of CNT was still not achieved. Zou et al. found that HDPE/CNT composites fabricated at higher screw speed provide improved dispersion of CNT in HDPE

[12]. Ha et al. studied the effect of the molecular weight of HDPE and polycarbonate (PC) on the dispersion of CNT, and rheological properties of the composites [13]. The use of a high melt viscosity polymer as the matrix material restricted the mobility of CNT, and also hindered the dispersion of CNT due to the high entanglement density of the polymer matrix compared to the low molecular weight matrices.

Poor dispersion of nanoparticles in the polymer matrices leads to formation of aggregates and filler networks, particularly at higher filler loadings. Osman and Atallah studied the rheological behaviour of HDPE composites with surface treated and untreated noncolloidal calcium carbonate (CaCO_3) particles and observed particle agglomeration and cluster formation with increase in filler volume fraction [14]. While the presence of clusters increased the viscosity, surface coating caused a reduction in the extent of polymer chain entanglements and drop in viscosity. Tang et al. reported significant changes in rheological properties for the HDPE/organoclay composites compatibilized with maleic anhydride grafted PE [6]. Non-Newtonian viscosity behavior was observed at all organoclay loadings, and the low-frequency storage modulus showed a plateau and storage and loss moduli increased with increase in organoclay loading.

McNally et al. prepared PE/CNT composites with weight fractions ranging from 0.1 to 10 wt% using melt extrusion and studied the rheological and electrical properties [15]. The storage modulus (G') versus frequency curves approached a plateau between 8.5 and 10 wt% indicating the rheological percolation threshold with the formation of an interconnected nanotube structure, indicative of "pseudo-solid-like" behavior. The high percolation threshold was attributed by the authors to the coating of the PE over CNT and geometry of the die which reduced the entanglements. Valentino et al. studied the melt rheological investigations of melt mixed HDPE/CNT composites, and the percolation threshold was obtained in between 1 and 2.5 wt% of CNT loading [16].

A drop in the viscosity of nanoparticle-filled polymer melts prepared by blending organic nanoparticles, either synthesized by intramolecular cross-linking of single poly(styrene) (PS) chains or using branched, dendritic poly(ethylene) (PE), with linear atactic PS over a large concentration range was reported recently [17–19]. Merkel et al. attributed the decrease in the viscosity to the excluded free volume induced around the nanoparticles [20]. However, Kharchenko et al. reported a significant increase in the viscosity of CNT-filled polymer materials, even at very low loadings [21]. A similar increase in viscosity has been reported in the case of clay-polymer nanocomposites by Ren and Krishnamoorti [22]. Therefore, a conclusive outcome with respect to the behavior of viscosity is not yet achieved in nano filled polymer composites.

The role of surface modification and the effect of nanofiller loading on the rheological behavior of the polymer nanocomposites have not been resolved as yet, and there exists scope for research in this area and with this objective in mind, the present investigation was undertaken. The paper

reports the results of studies on the effects of functionalization of CNT and its loading on the rheological behavior of HDPE/CNT composites.

2. Materials and Methods

The CNT was purchased from Cheap Tube Inc., 112 Mercury Drive, Brattleboro, VT 05301, USA. The specifications of CNT are as follows: range of diameter 20–30 nm, length of the tube 10–30 μm , and purity >95 wt%. The density of CNT is 2.1 g/cm^3 . The HDPE pellets (HDPE HMA 014) were obtained from ExxonMobil Corporation, USA. The melt flow index and density of the HDPE pellets are 4.0 g/10 min (ASTM D4101-10) and 0.960 g/cm^3 , respectively. The CNT surface was functionalized with phenol and 1-octadecanol (both were purchased from Sigma Aldrich, USA) by techniques as reported earlier by Thomas et al. [23, 24].

HDPE was melt blended with 1, 2, 3, 4, 5, and 7 wt% of pristine and functionalized CNT using a Brabender mixer at 150°C for 10 min at a rotor speed of 120 rpm. The blended mixtures were then hot pressed at 150°C under 9 MPa using Carver hot-press.

ARES controlled strain rheometer (TA Instruments) was used for all rheological measurements. It was equipped with heavy transducer (range 0.02–20 N for normal force; 2×10^{-5} to $2 \times 10^{-1}\text{ Nm}$ for torque). The linear and nonlinear viscoelastic experiments were performed using 25 mm parallel plates. The plates were heated for at least 20 min to stabilize the temperature. For reproducibility of results, a presteady shear rate of 0.1 s^{-1} was applied for 20 s for all the tests in the parallel plates and time delay of 100 s before the actual tests. Dynamic oscillation frequency sweep of 0.015–100 rad/s in the linear viscoelastic range (strain 2%) with parallel plate under nitrogen atmosphere were done at 200°C . The samples were left to equilibrate for 5 min prior to each measurement. The steady shear viscosity measurements of the samples were done in parallel-plate geometry with a diameter of 25 mm at 200°C at strain rates ranging from 0.01 to 100 s^{-1} .

3. Results

Figure 1 shows the frequency dependence of the dynamic viscosity at different loadings of CNT and modified CNT in the HDPE composites. HDPE shows the typical rheological flow in the experimental frequencies. Incorporation of CNT at 1 wt% loading reduces the dynamic viscosity in the low frequency region. As for the 2 wt% loading, the dynamic viscosity of functionalized CNT slightly reduces but the pristine CNT viscosity increases. In the case of 3 wt% loading of the nanofillers, the viscosity of HDPE increases in the whole range of frequencies studied, but the effect is less pronounced in the case of functionalized CNT. In the case of 4 wt% loading, the viscosity of HDPE increases in the whole range of frequencies, but the increase is well noticed in the pristine CNT and phenol. As the filler loading increases to 5 and 7 wt%, the dominant role of the hydrodynamic factor (i.e., increase in relative effect of hydrodynamic forces with

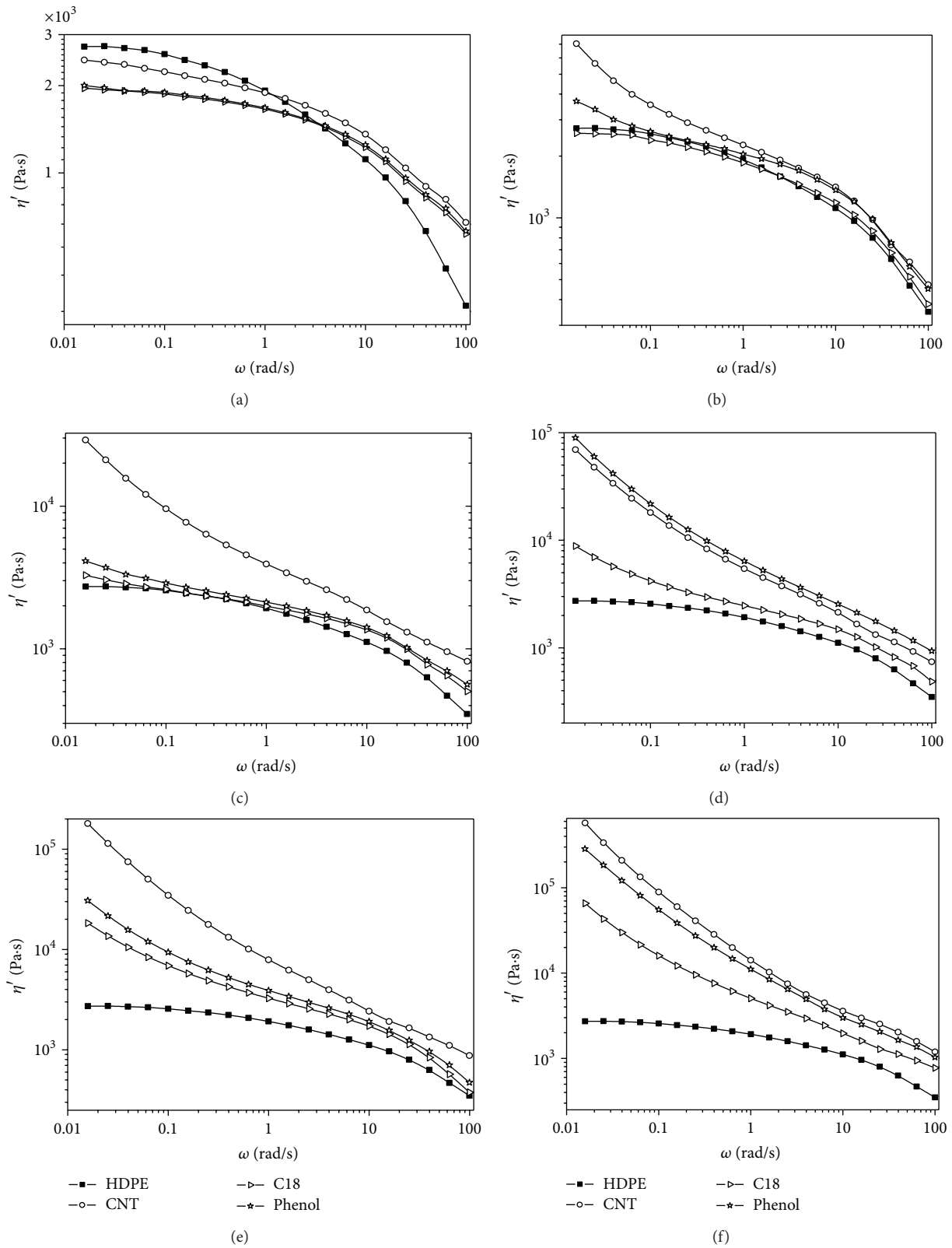


FIGURE 1: Variation of dynamic viscosity of HDPE composite with frequency. (a) 1, (b) 2, (c) 3, (d) 4, (e) 5, and (f) 7 wt% loading of nanofiller.

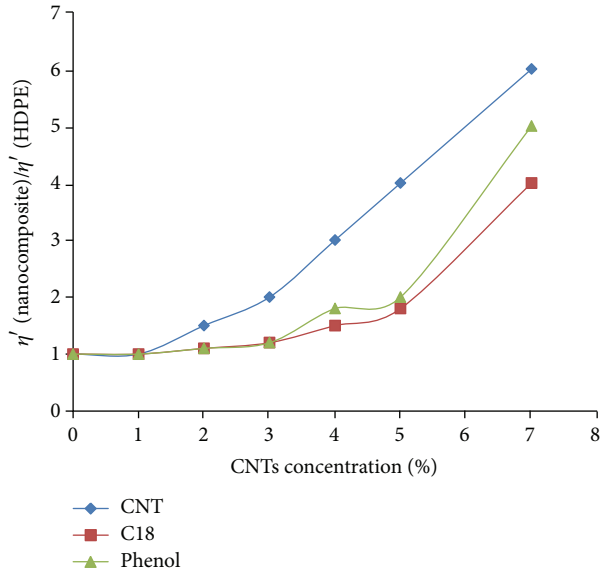


FIGURE 2: Dependence of the ratio of the $(\eta')_{\text{composite}}/(\eta')_{\text{HDPE}}$ at 1 rad/s on the nano filler loading.

respect to the Brownian contribution) becomes more apparent, and viscosity showed a sharp increase at all frequencies on incorporation of both CNT and modified CNT.

Figure 2 shows the variation of the viscosity ratio versus the concentration of the CNT at a frequency of 1 Hz. For the 1 wt% of modified CNT, the viscosity ratio drops to less than one indicating a drop in viscosity. The composites with functionalized CNT show lower viscosity ratio as compared to the unfunctionalized CNT at all concentrations.

The steady shear viscosity against strain rate is given in Figure 3. As in dynamic viscosity measurements, 1 wt% loading of pristine and functionalized CNT show reduction in viscosity compared to HDPE. At 2 wt% loading, the viscosity of C18 slightly reduced than neat HDPE, while the viscosity of phenol is almost the same as that of neat HDPE. However, the pristine CNT viscosity increased drastically. The increase in loading to 3 and 4 wt% reverses the trend, and the viscosity of the composites is higher than the polymer. When the loading becomes 5 and 7 wt%, the viscosity is much higher than HDPE. Moreover, the lower frequency region showed marked difference in viscosities for the different grades of CNT. At higher frequencies there is not much difference in viscosities for HDPE and the composites. Among the two functionalized grades of CNT, the C18 functionalization showed higher reduction in viscosity compared to the phenol functionalization.

The plots of storage modulus against frequency at different loadings of pristine CNT and functionalized CNT are given in Figure 4. It is interesting to note that in the case of nano filler loading of 1 wt%, neat HDPE shows the highest storage modulus, which decreases on addition of pristine CNT and functionalized CNT, and the effect is pronounced in the low and medium frequency region. At higher frequencies, however, both filled and unfilled HDPE have similar moduli. This effect is similar to that observed in the case of viscosity

changes. At 2 wt% loading, there is a gradual increase in the storage modulus at low frequency below 0.1 rad/s while the storage modulus is almost the same for the pristine CNT and functionalized CNT's at higher frequency region. As the nanofiller loading increases to 3 and 4 wt%, storage modulus of the filled system increases sharply, particularly in the low frequency region. In the case of 5 and 7 wt% loading of nano filler, the increase in storage modulus becomes pronounced and the filled HDPE registers higher storage modulus than the neat HDPE in all frequencies. It is observed that the functionalized CNT shows lower modulus than the pristine CNT at all loadings except at 4 wt% loading where functionalized phenol exhibited the highest storage modulus. Furthermore, a plateau is observed in the low frequency region at 3 wt% loading of pristine CNT and 4 wt% loading of pristine CNT and phenol and the same is observed at 5 and 7 wt% in the case of functionalized CNT.

Figure 5 shows the plots of $\tan \delta$ versus frequency. For the unfilled HDPE sample, $\tan \delta$ is greater than one and decreases as ω increases, which is typical for liquid-like materials. At 1 wt% loading of the nano filler this behavior does not change, regardless of the type of CNT. Likewise, at 2 wt% loading, $\tan \delta$ of pristine CNT and functionalized CNT is greater than one at low frequency region and then decreases in all cases as frequency reaches maximum. However, at 3 wt% of pristine CNT, $\tan \delta$ shows a value of less than one and it increases as ω increases in the low frequency range, until it reaches a maximum. In the case of functionalized CNT, at 3 wt%, $\tan \delta$ is greater than one and there is a tendency to increase with the increase in frequency in the low frequency region and reach a maximum. As for the 4 wt% loading, $\tan \delta$ of the pristine CNT and phenol is less than one at low frequency region and remains almost constant as ω reaches maximum. But at higher loading (i.e., at 5 and 7 wt%) of the nano filler, irrespective of whether it is pristine or functionalized, the compositions have $\tan \delta$ less than one and there is sharp increase in $\tan \delta$ with increase in frequency in the low frequency region till the maximum is reached.

Figure 6 presents the plots of G' versus G'' , which is a typical Cole-Cole plot. As can be clearly seen from Figure 6, the plots for both filled and unfilled compositions at 1 wt% of CNT follow the same path, with no changes in the slope. However, the slope in the plots decreases sharply, as the nanofiller concentration exceeds 1 wt%, and this is true for both pristine and functionalized CNT.

The interaction and compatibility of the CNTs in iPP matrices and the morphology of the cross section and profile section of the nanocomposites were investigated. For this purpose, SEM was conducted on fractured surfaces of the nanocomposites for 1.0 wt and 7 wt% of CNTs, CNTs-C18, and CNTs-Phenol and compared with SEM image of neat HDPE as shown in Figures 7(a)–7(g). Although, different fractured surfaces of the composites were scanned for SEM, there was however no clear disparity between the image of neat HDPE and images obtained for CNT/HDPE and CNT-C18/HDPE in Figures 7(a)–7(e). However, there is a clear difference between the fractured surface of HDPE and the CNT-Phenol/HDPE (Figures 7(f) and 7(g)).

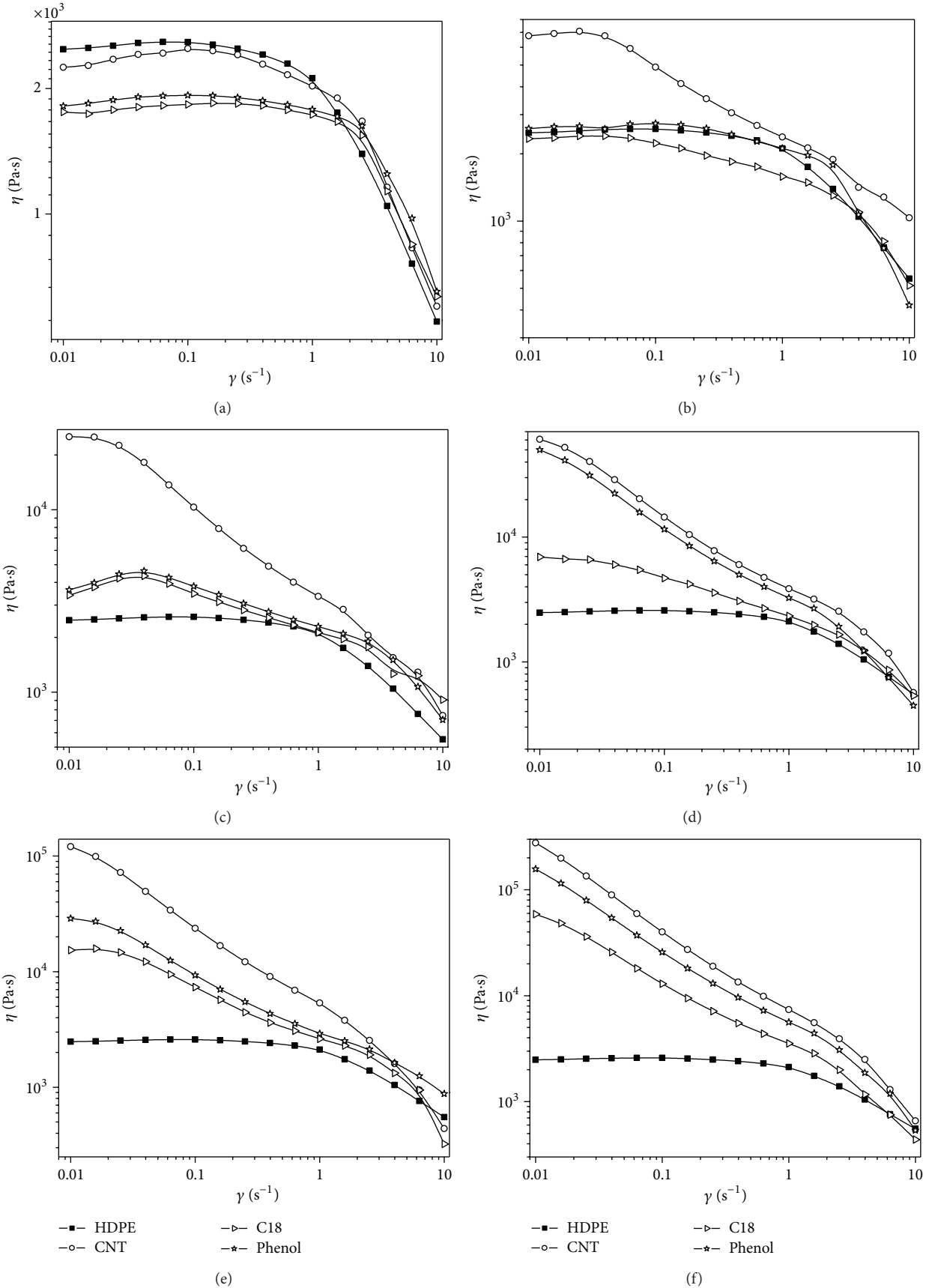


FIGURE 3: Variation of steady shear viscosity of HDPE composite with frequency. (a) 1, (b) 2, (c) 3, (d) 4, (e) 5, and (f) 7 wt% loading of nanofiller.

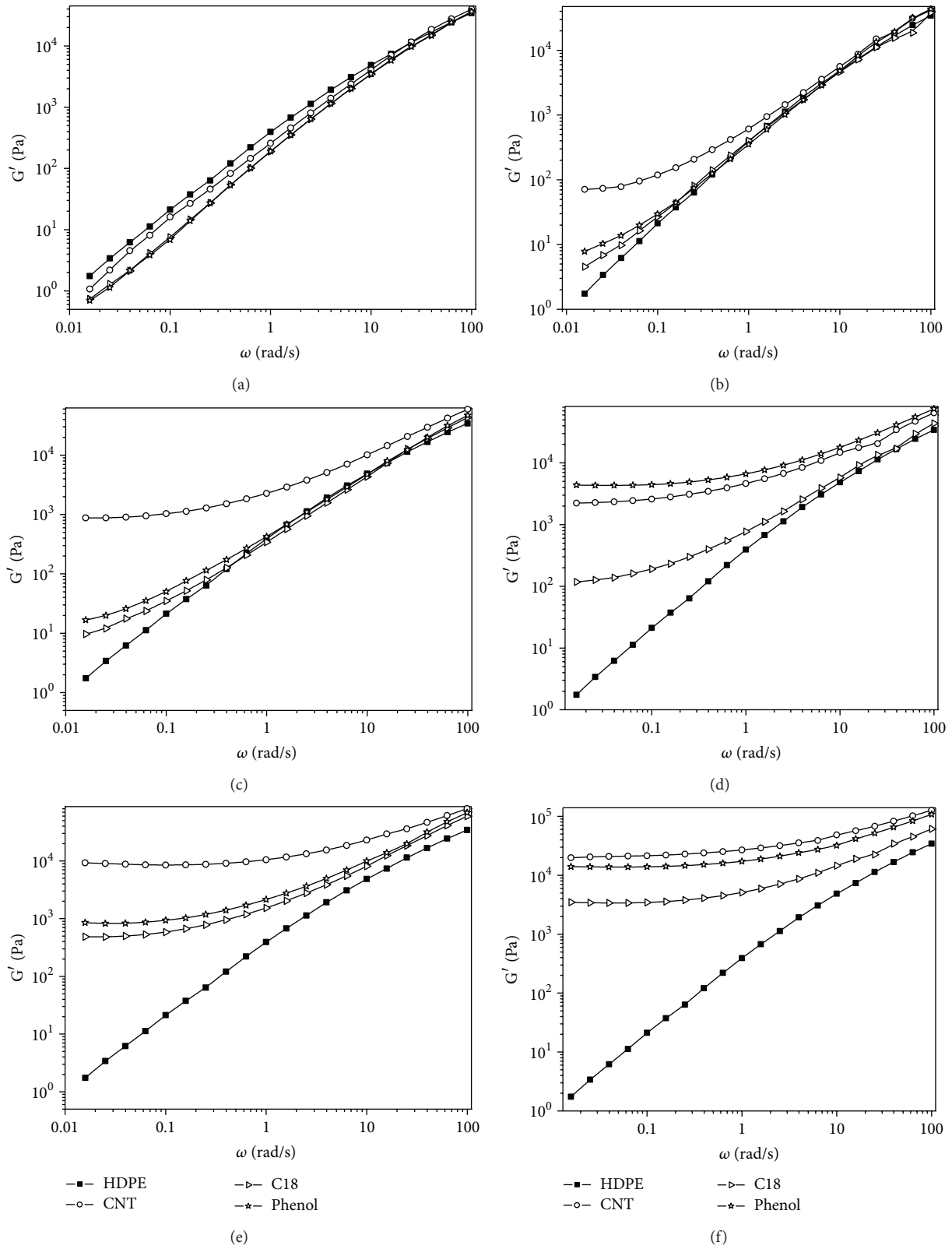


FIGURE 4: Variation of storage modulus of HDPE composites with frequency. (a) 1, (b) 2, (c) 3, (d) 4, (e) 5, and (f) 7 wt% loading of nanofiller.

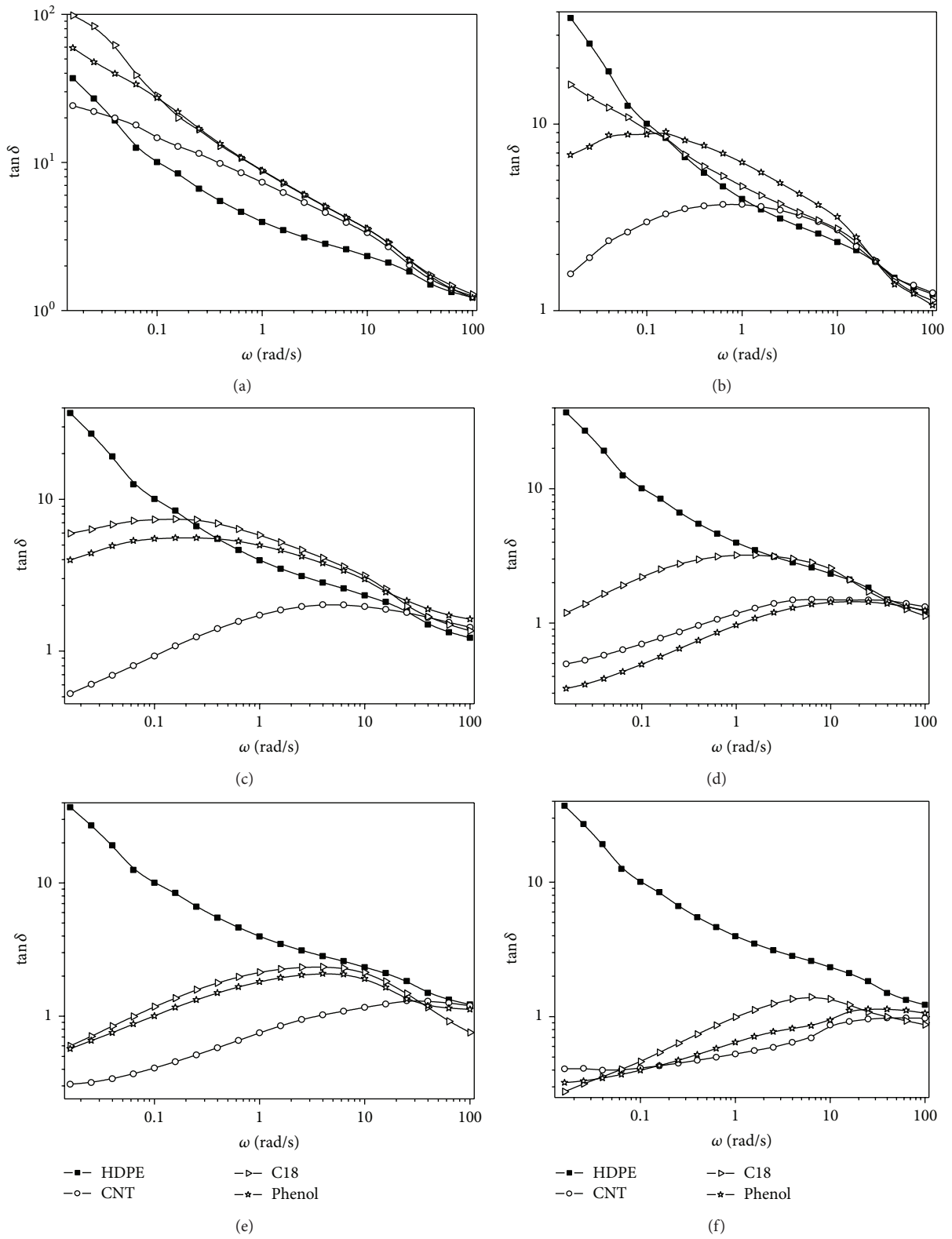


FIGURE 5: Variation of $\tan \delta$ of HDPE composites with frequency. (a) 1, (b) 2, (c) 3, (d) 4, (e) 5, and (f) 7 wt% loading of nanofiller.

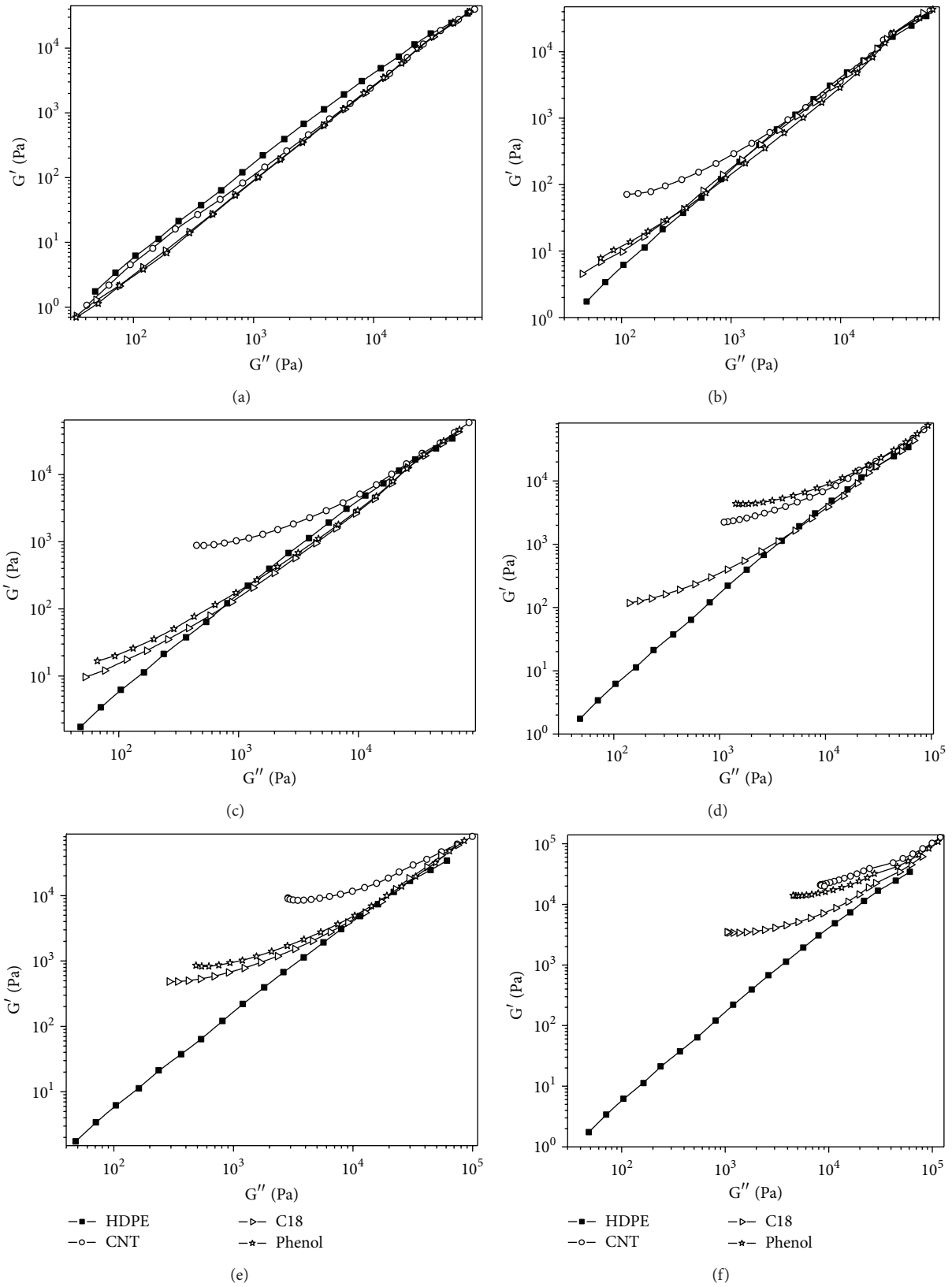


FIGURE 6: Modified Cole-Cole plots of HDPE composites. (a) 1, (b) 2, (c) 3, (d) 4, (e) 5, and (f) 7 wt% loading of nanofiller.

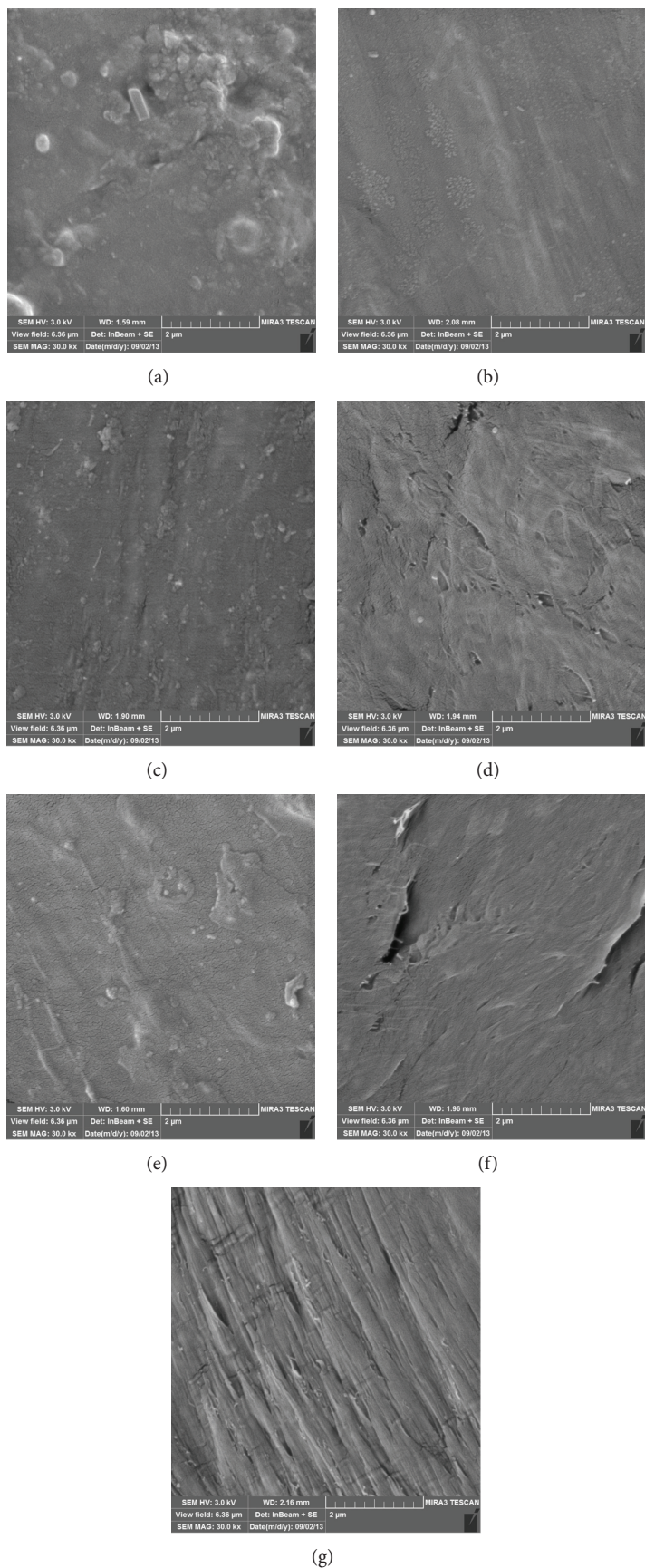


FIGURE 7: SEM images of the net HDPE, pristine CNT, and functionalized CNT. (a) net HDPE, (b) 1 wt% CNT, (c) 7 wt% CNT, (d) 1 wt% C18, (e) 7 wt% C18, (f) 1 wt% phenol, and (g) 7 wt% phenol.

4. Discussion

In reference to Figure 1, the decrease in viscosity at 1 wt% is believed to be due to the increase in disentanglement of the polymer chains induced by the nanofiller, acting as streamliners for the flow of polymer chains as reported earlier [25–27]. The reduction in viscosity is pronounced in the case of functionalized CNT, and it is believed that the de-aggregation of the nanoparticles contributes further to the disentanglement process. It is also interesting to observe that the range of the frequency where the viscosity is constant, the Newtonian plateau viscosity, increases due to the presence of pristine and functionalized CNT in the same order of that of the percent reduction of the viscosity. In the high frequency region, however, the changes in the viscosity follow different trend and both pristine and functionalized CNT show higher viscosity than the neat polymer, due to the hydrodynamic effect. It is believed that chemical modification of CNT surface assists in deaggregation of the nanoparticles and subsequent disentanglement of the polymer chains and a drop in viscosity, as compared to the pristine CNT. Moreover, the functionalization may lead to the decrease in the aspect ratio of CNT due to the de-aggregation of the tubules by the functionalizing agents [28, 29].

As the nano filler loading increases to 2 wt%, the proposed hydrodynamic factor plays a dominant role in controlling the viscosity in the whole range of frequency studied. The same trend is observed at 3 wt% loading. But in the case of functionalized CNT, the de-aggregation of the filler particles counterbalances the hydrodynamic factor. It is also evident that the functionalization of CNT causes greater decrease in viscosity than the pristine CNT and the viscosity follows the order, neat polymer < C18 modified CNT < phenol modified CNT < CNT. The effect becomes pronounced as the nano filler loading increases to 5 and 7 wt%. Figure 2 shows that the viscosity ratio increases with the increase in nanofiller concentration and the relative increase is less in the case of functionalized CNT, as compared to pristine CNT.

Although the reduction in viscosity by the addition of rigid fillers in a matrix is uncommon, there are reports on the contrary. Recently, similar observation was made by Thomas et al. in the case of isotactic-polypropylene (iPP)/CNT composites [30]. However, the drop in viscosity for the present system of HDPE/CNT is observed at 1 wt% loading, whereas in the case of iPP/CNT, the drop in viscosity was observed at a loading of 0.5 wt% and below and the same phenomenon was not observed at 1 wt% loading. The presently used HDPE grade has high molecular mass with a linear structure, which is likely to increase the entanglements of the polymer chains, and thus the loading of CNT needed for reduction in viscosity is likely to be greater in HDPE than that in iPP. This is also in agreement with a previous report by Adesina et al. on processability of nanoclay-filled linear and branched grades of polyethylene [31]. A few more similar observations were reported related to linear polystyrene (PS) composites filled with organic nanoparticles [17–19]. Also, Jain et al. reported decrease in viscosity for silica filled PP composites [32].

The results of steady shear viscosity measurements (Figure 3) are in conformity with the above observations on changes in dynamic viscosity on incorporation of nano filler, and it can be argued that Cox-Merz rule is followed in this type of composite system. The 1 wt% loading of the nano filler shows a reduction in the steady shear viscosity, and the effect is pronounced in the case of functionalized CNT. As the filler loading increases to 2 and 3 wt%, irrespective of the type of nano filler, the viscosity of the composite overshoots the viscosity of neat HDPE. But the chemically modified CNT shows lower viscosity than the pristine CNT in all loadings. Ma et al. have reported on the rheological modeling of pristine and chemically modified CNT aggregate suspensions, and the increase in viscosity at higher loadings was attributed to the formation of filler network [33, 34].

Figure 4 shows that at 1 wt% loading of the nano filler, there is no clear plateau in the plots of storage modulus versus frequency in the low frequency region. But as the pristine CNT concentration increases to 2 and 3 wt%, a plateau is observed, which is indicative of filler network formation. The plateau in G' values in the low frequency range has been cited by several researchers for polymer nanocomposites, including nanoclay-filled as well as carbon nanotubes filled composites, and they attributed this behavior to the formation of physical networks of the nanofillers inside the host matrix [15, 16, 35–38]. For nanoclay-filled polymers, for example, Solomon et al. examined the melt-state rheology of nanoclay/polypropylene system at various clay loadings [35]. Above clay loadings of 2.0 wt% the nanocomposite materials exhibited apparent low-frequency plateau in G' , and they concluded that the rheological percolation threshold for the formation of network was at 2.0 wt% loading.

However, no such plateau is not observed in the case of functionalized CNT at 3 wt% loading. As the CNT loading increases further beyond 3 wt% (i.e., 4, 5 and 7 wt%), even the functionalized CNT shows plateau in the low frequency region, indicating network formation, as observed in the case of pristine CNT. Therefore, it can be suggested that the rheological percolation threshold for the HDPE/CNT system is strongly dependant on the functionalization of CNT and for the pristine CNT it is around 3 wt% but for the functionalized CNT it is around 7 wt%.

In reference to Figure 5, in the low frequency range for the filler loadings of 5 and 7 wt% (Figures 5(e) and 5(f)), $\tan \delta$ is less than unity, and it increases with respect to frequency in the low frequency range till it reaches a maximum, which could be ascribed to the formation of CNT network. This effect is also slightly noticeable at 4 wt% but less pronounced in the case of 3 wt% loading of nano filler, particularly in the case of functionalized CNT (Figures 5(c) and 5(d)). However, at 1 wt% loading of the nano filler this behaviour is not observed for both pristine and functionalized CNT (Figure 5(a)). The observation on increase in $\tan \delta$ with increase in ω in the low frequency range has been observed earlier in the case of several polymer nanocomposites and has been explained on the basis of formation of physical network of the nanofillers in the host polymer matrix at and higher

than the rheological percolation threshold [15, 38]. Accordingly, we are of the opinion that the rheological percolation threshold of pristine CNT-HDPE system is around 3 and 4 wt%, whereas the same for the functionalized CNT-HDPE systems is around 7 wt%. The decrease in slope in the plots of G' versus G'' (Figure 6) can be attributed to the formation of physical network in the host matrix as has been suggested by Pötschke et al. and Prashanta et al. [39, 40].

5. Conclusion

The dynamic viscosity, steady shear viscosity and storage modulus of HDPE decrease at low loading (i.e., 1 wt%) of both pristine CNT and functionalized CNT, and the decrease follows the order, pristine CNT < phenol functionalized CNT < C18 functionalized CNT. As the nanofiller loading is increased to 2 and 3 wt%, the rheological behavior changes and the viscosity and storage modulus increase and overshoot the values for neat HDPE. The effect becomes pronounced as the nanofiller loading is increased to 4, 5, and 7 wt%. The rheological results are indicative of formation of filler networks in the polymer matrix and the rheological percolation threshold for the network to form is strongly dependant on the functionalization of CNT. For example, for the unfunctionalized CNT the percolation threshold is around 4 wt%, but for functionalized CNT, it is around 7 wt%. The surface morphologies of CNT and functionalized CNT at 1 wt% loading showed good dispersion while at 7 wt% loading, dispersion was also achieved, but there are few regions with agglomeration of CNT.

References

- [1] K. Chrissafis, K. M. Paraskevopoulos, I. Tsiaoussis, and D. Bikiaris, "Comparative study of the effect of different nanoparticles on the mechanical properties, permeability, and thermal degradation mechanism of HDPE," *Journal of Applied Polymer Science*, vol. 114, no. 3, pp. 1606–1618, 2009.
- [2] G. Sui, W. H. Zhong, X. Ren, X. Q. Wang, and X. P. Yang, "Structure, mechanical properties and friction behavior of UHMWPE/HDPE/carbon nanofibers," *Materials Chemistry and Physics*, vol. 115, no. 1, pp. 404–412, 2009.
- [3] Q. Dong, Q. Zheng, M. Du, and M. Zhang, "Temperature-dependence of dynamic rheological properties for high-density polyethylene filled with graphite," *Journal of Materials Science*, vol. 40, no. 13, pp. 3539–3541, 2005.
- [4] W. Zheng, X. Lu, and S.-C. Wong, "Electrical and mechanical properties of expanded graphite-reinforced high-density polyethylene," *Journal of Applied Polymer Science*, vol. 91, no. 5, pp. 2781–2788, 2004.
- [5] M. A. Osman and A. Atallah, "Effect of the particle size on the viscoelastic properties of filled polyethylene," *Polymer*, vol. 47, no. 7, pp. 2357–2368, 2006.
- [6] Y. Tang, C. Yang, P. Gao, L. Ye, C. Zhao, and W. Lin, "Rheological study on high-density polyethylene/organoclaycomposites," *Polymer Engineering and Science*, vol. 51, no. 1, pp. 133–142, 2011.
- [7] J. F. Vega, J. Martínez-Salazar, M. Trujillo et al., "Rheology, processing, tensile properties, and crystallization of polyethylene/carbon nanotube nanocomposites," *Macromolecules*, vol. 42, no. 13, pp. 4719–4727, 2009.
- [8] J. Sandler, M. S. P. Shaffer, T. Prasse, W. Bauhofer, K. Schulte, and A. H. Windle, "Development of a dispersion process for carbon nanotubes in an epoxy matrix and the resulting electrical properties," *Polymer*, vol. 40, no. 21, pp. 5967–5971, 1999.
- [9] M. S. P. Shaffer and A. H. Windle, "Fabrication and characterization of carbon nanotube/poly (vinyl alcohol) composites," *Advanced Materials*, vol. 11, no. 11, pp. 937–941, 1999.
- [10] M. Bratcher, B. Gersten, H. Ji, and J. Mays, "Study in the dispersion of carbon nanotubes," *MRS Proceedings*, vol. 706, 2001.
- [11] X. Gong, J. Liu, S. Baskaran, R. D. Voise, and J. S. Young, "Surfactant-assisted processing of carbon nanotube/polymer composites," *Chemistry of Materials*, vol. 12, no. 4, pp. 1049–1052, 2000.
- [12] Y. Zou, Y. Feng, L. Wang, and X. Liu, "Processing and properties of MWNT/HDPE composites," *Carbon*, vol. 42, no. 2, pp. 271–277, 2004.
- [13] H. Ha, S. C. Kim, and K. Ha, "Morphology and properties of polyamide/multi-walled carbon nanotube composites," *Macromolecular Research*, vol. 18, no. 7, pp. 660–667, 2010.
- [14] M. A. Osman and A. Atallah, "Interparticle and particle-matrix interactions in polyethylene reinforcement and viscoelasticity," *Polymer*, vol. 46, no. 22, pp. 9476–9488, 2005.
- [15] T. McNally, P. Pötschke, P. Halley et al., "Polyethylene multi-walled carbon nanotube composites," *Polymer*, vol. 46, no. 19, pp. 8222–8232, 2005.
- [16] O. Valentino, M. Sarno, N. G. Rainone et al., "Influence of the polymer structure and nanotube concentration on the conductivity and rheological properties of polyethylene/CNT composites," *Physica E*, vol. 40, no. 7, pp. 2440–2445, 2008.
- [17] M. E. Mackay, T. T. Dao, A. Tuteja et al., "Nanoscale effects leading to non-einstein-like decrease in viscosity," *Nature Materials*, vol. 2, no. 11, pp. 762–766, 2003.
- [18] A. Tuteja, M. E. Mackay, C. J. Hawker, and B. Van Horn, "Effect of ideal, organic nanoparticles on the flow properties of linear polymers: non-einstein-like behavior," *Macromolecules*, vol. 38, no. 19, pp. 8000–8011, 2005.
- [19] M. E. Mackay, A. Tuteja, P. M. Duxbury et al., "General strategies for nanoparticle dispersion," *Science*, vol. 311, no. 5768, pp. 1740–1743, 2006.
- [20] T. C. Merkel, B. D. Freeman, R. J. Spontak et al., "Ultrapermselective, reverse-selective nanocomposite membranes," *Science*, vol. 296, no. 5567, pp. 519–522, 2002.
- [21] S. B. Kharchenko, J. F. Douglas, J. Obrzut, E. A. Grulke, and K. B. Migler, "Flow-induced properties of nanotube-filled polymer materials," *Nature Materials*, vol. 3, no. 8, pp. 564–568, 2004.
- [22] J. Ren and R. Krishnamoorti, "Nonlinear viscoelastic properties of layered-silicate-based intercalated nanocomposites," *Macromolecules*, vol. 36, no. 12, pp. 4443–4451, 2003.
- [23] S. P. Thomas, A. A. Abdullateef, M. A. Al-Harathi et al., "Electrical properties of natural rubber nanocomposites: effect of 1-octadecanol functionalization of carbon nanotubes," *Journal of Materials Science*, vol. 47, no. 7, pp. 3344–3349, 2012.
- [24] S. P. Thomas, A. A. Abdullateef, M. A. Al-Harathi et al., "Effect of phenol functionalization of carbon nanotubes on properties of natural rubber nanocomposites," *Journal of Applied Polymer Science*, vol. 124, no. 3, pp. 2370–2376, 2012.
- [25] J. S. Oh, K. H. Ahn, and J. S. Hong, "Dispersion of entangled carbon nanotube by melt extrusion," *Korea Australia Rheology Journal*, vol. 22, no. 2, pp. 89–94, 2010.

- [26] J. Li, P. C. Ma, W. S. Chow, C. K. To, B. Z. Tang, and J.-K. Kim, "Correlations between percolation threshold, dispersion state, and aspect ratio of carbon nanotubes," *Advanced Functional Materials*, vol. 17, no. 16, pp. 3207–3215, 2007.
- [27] P.-C. Ma and J.-K. Kim, *Carbon Nanotubes for Polymer Reinforcement*, CRC Press, Boca Raton, Fla, USA, 2011.
- [28] G. K. Batchelor and J. T. Green, "hydrodynamic interaction of two small freely-moving spheres in a linear flow field," *Journal of Fluid Mechanics*, vol. 56, no. 2, pp. 375–400, 1972.
- [29] G. K. Batchelor and J. T. Green, "The determination of the bulk stress in a suspension of spherical particles to order c^2 ," *Journal of Fluid Mechanics*, vol. 56, no. 3, pp. 401–427, 1972.
- [30] S. P. Thomas, S. A. Girei, A. A. Al-Juhani, K. Mezghani, S. K. De, and M. A. Atieh, "Effect of phenol functionalized carbon nanotube on mechanical, dynamic mechanical, and thermal properties of isotactic polypropylene nanocomposites," *Polymer Engineering and Science*, vol. 52, no. 3, pp. 525–531, 2012.
- [31] A. A. Adesina, A. A. Al-Juhani, N. Tabet, A. Ul-Hamid, and I. A. Hussein, "Rheology and enhancement of extrusion of linear and branched polyethylenes using low amount of organoclay," *Journal of Applied Polymer Science*, vol. 126, no. 2, pp. 713–723, 2012.
- [32] S. Jain, J. G. P. Goossens, G. W. M. Peters, M. Van Duin, and P. J. Lemstra, "Strong decrease in viscosity of nanoparticle-filled polymer melts through selective adsorption," *Soft Matter*, vol. 4, no. 9, pp. 1848–1854, 2008.
- [33] W. K. A. Ma, F. Chinesta, A. Ammar, and M. R. MacKley, "Rheological modeling of carbon nanotube aggregate suspensions," *Journal of Rheology*, vol. 52, no. 6, pp. 1311–1330, 2008.
- [34] A. W. K. Ma, F. Chinesta, and M. R. MacKley, "The rheology and modeling of chemically treated carbon nanotubes suspensions," *Journal of Rheology*, vol. 53, no. 3, pp. 547–577, 2009.
- [35] M. J. Solomon, A. S. Almusallam, K. F. Seefeldt, A. Somwangth-anaroj, and P. Varadan, "Rheology of polypropylene/clay hybrid materials," *Macromolecules*, vol. 34, no. 6, pp. 1864–1872, 2001.
- [36] M.-K. Seo and S.-J. Park, "Electrical resistivity and rheological behaviors of carbon nanotubes-filled polypropylene composites," *Chemical Physics Letters*, vol. 395, no. 1–3, pp. 44–48, 2004.
- [37] S. H. Lee, M. W. Kim, S. H. Kim, and J. R. Youn, "Rheological and electrical properties of polypropylene/MWCNT composites prepared with MWCNT masterbatch chips," *European Polymer Journal*, vol. 44, no. 6, pp. 1620–1630, 2008.
- [38] Q. Zhang, D. R. Lippits, and S. Rastogi, "Dispersion and rheological aspects of SWNTs in ultrahigh molecular weight polyethylene," *Macromolecules*, vol. 39, no. 2, pp. 658–666, 2006.
- [39] P. Pötschke, T. D. Fornes, and D. R. Paul, "Rheological behavior of multiwalled carbon nanotube/polycarbonate composites," *Polymer*, vol. 43, no. 11, pp. 3247–3255, 2002.
- [40] K. Prashantha, J. Soulestin, M. F. Lacrampe, M. Claes, G. Dupin, and P. Krawczak, "Multi-walled carbon nanotube filled polypropylene nanocomposites based on masterbatch route: improvement of dispersion and mechanical properties through PP-g-MA addition," *Express Polymer Letters*, vol. 2, no. 10, pp. 735–745, 2008.

Research Article

Enhanced Strain-Dependent Electrical Resistance of Polyurethane Composites with Embedded Oxidized Multiwalled Carbon Nanotube Networks

R. Benlikaya,^{1,2} P. Slobodian,^{1,3} and P. Riha⁴

¹ Centre of Polymer Systems, University Institute, Tomas Bata University, Nad Ovcirnou 3685, 760 01 Zlin, Czech Republic

² Balikesir University, Faculty of Necatibey Education, Department of Secondary Science and Mathematics Education, 10100 Balikesir, Turkey

³ Tomas Bata University, Faculty of Technology, Polymer Centre, TGM 275, 760 01 Zlin, Czech Republic

⁴ Institute of Hydrodynamics, Academy of Sciences, Pod Patankou 30/5, 166 12 Prague 6, Czech Republic

Correspondence should be addressed to P. Slobodian; slobodian@ft.utb.cz

Received 15 March 2013; Accepted 18 August 2013

Academic Editor: Sulin Zhang

Copyright © 2013 R. Benlikaya et al. This is an open access article distributed under the Creative Commons Attribution License, which permits unrestricted use, distribution, and reproduction in any medium, provided the original work is properly cited.

The effect of different chemical oxidation of multiwalled carbon nanotubes with H_2O_2 , HNO_3 , and $KMnO_4$ on the change of electrical resistance of polyurethane composites with embedded oxidized nanotube networks subjected to elongation and bending has been studied. The testing has shown about twenty-fold increase in the electrical resistance for the composite prepared from $KMnO_4$ oxidized nanotubes in comparison to the composites prepared from the pristine and other oxidized nanotubes. The evaluated sensitivity of $KMnO_4$ treated composite in terms of the gauge factor increases with strain to nearly 175 at the strain 11%. This is a substantial increase, which ranks the composite prepared from $KMnO_4$ oxidized nanotubes among materials as strain gauges with the highest electromechanical sensitivity. The observed differences in electromechanical properties of the composites are discussed on basis of their structure which is examined by the measurements of Fourier transform infrared spectroscopy, X-ray photoelectron spectroscopy, and scanning electron microscope. The possible practical use of the composites is demonstrated by monitoring of elbow joint flexion during two different physical exercises.

1. Introduction

In recent years there has been an increase in the studies on the composites composed of thermoplastic polyurethane (TPU) with carbon nanomaterials such as multiwalled carbon nanotubes (MWCNTs) [1], carbon nanofibers [2], and single- or multi-walled carbon nanotube networks (SWCNT-N, MWCNT-N), or buckypaper [3–5]. Thermoplastic polyurethane elastomers exhibit useful properties as abrasion resistance. However, since these polymers are not chemically cross-linked, they exhibit lower recoverability following elongation than cross-linked elastomers [6].

The carbon nanotube networks (CNT-Ns) can proportionally transfer their unique properties into composites and

bring about substantial improvements in their properties such as the strength, the electrical and thermal conductivity, the electromagnetic interference shielding compared to the polymer composites with CNT particulate filler [7]. Using CNT-Ns as a strain sensor has also potential advantage since the networks have high sensitivity to local distributions of stress and strain as well as the ability to sense stresses and strains in different directions in the host materials [8]. In this respect the strain sensitivities of epoxy [8], poly (methyl-methacrylate) [9], and thermoplastic polyurethane composites [5] with MWCNT-Ns or SWCNT-Ns have already been studied. Moreover, there are also some studies on the effect of the functionalization of CNT-Ns with plasma [10, 11] as well as the carboxylic acid and amine groups [5] on

the electrical properties [5, 11], thermal properties [5], and mechanical properties [10, 11] of polyurethane [5], polyimide [10] and polycarbonate [11] composites with CNT-Ns. Lima and coworkers stated that the range of property design possibilities of the elastomeric polyurethane composite is possible by tailoring the functional group content and the carbon nanotube load [5]. Nevertheless, according to our knowledge, no study related to examination of the effect of functionalized MWCNT-Ns with various oxidants on the strain sensitivity of TPU/MWCNT-N composites has been published yet. There are some studies showing various properties of CNT-polymer bulk composites to be affected by various oxidation conditions of nanotubes [12]. Rein and coworkers investigated the coupling between the electrical and mechanical properties of the CNT-N films made of SWCNTs and MWCNTs when embedded in several types of epoxies and observed different electromechanical responses [8]. However, this coupling is not affected only by the nanotube type but also by the interaction of the polymer matrix and CNT-N films [13].

In this study, the thermoplastic polyester-based polyurethane composite with various MWCNT-Ns, oxidized by three agents as H_2O_2 , HNO_3 , and KMnO_4 , is investigated in terms of their electrical resistance change during elongation and bending. The observed differences in electromechanical properties of TPU composites are discussed on basis of their structure which is examined by the Fourier transform infrared spectroscopy (FTIR), the X-ray photoelectron spectroscopy (XPS), and the scanning electron microscope (SEM).

2. Experimental

2.1. Materials. Purified MWCNTs produced by the chemical vapor deposition of acetylene were supplied by Sun Nanotech Co. Ltd., China, and characterized in our previous studies [4, 7, 14]. The thermoplastic polyurethane elastomer Desmopan DP 2590A was supplied by Bayer Material Science.

KMnO₄ oxidation: the oxidized MWCNTs were prepared in a glass reactor with a reflux condenser filled with 250 mL of 0.5 M H_2SO_4 , into which 5 g of KMnO_4 as oxidizing agent and 2 g of MWCNTs were added. The dispersion was sonicated at 85°C for 15 hours using thermostatic ultrasonic bath (Bandelin Electronic DT 103H). The dispersion was filtered, and then MWCNTs were washed with concentrated HCl to remove MnO_2 and then washed with water until pH = 7.

HNO₃ oxidation: 2 g of MWCNTs was added to 250 mL of HNO_3 (concentrated) and heated at 140°C for 2 hours. After that the dispersion was cooled and filtered. The sediment was washed by deionized water and dried at 40°C for 24 hours.

H₂O₂ oxidation: 1.5 g of MWCNTs was added to 30 mL of H_2O_2 and simultaneously stirred at 50 rpm (Heidolph, type MR HEI-standard) and heated for 72 hours at 65°C. Each day 5 mL of fresh hydrogen peroxide was added to original dispersion to refresh the activity of H_2O_2 . In the end the dispersion was filtered and rinsed by water. The resulting product was dried at 40°C for 24 hours.

For making an entangled MWCNT network, a porous polyurethane membrane and a vacuum filtration method were used. The homogenized dispersion of MWCNTs was vacuum filtered through the membrane. The formed networked layer had thickness about 35 μm . The partial infiltration of MWCNTs into the filter pores creates an effective interlocking of MWCNT network layer with TPU filter which even strengthens when the porous filter is transformed into the polymeric film in the course of compression molding at 175°C. The detailed preparation of TPU membrane, MWCNT networks, and the composite was described in our previous paper [4].

The network of pristine MWCNTs is denoted below as MWCNT-N, and the ones of oxidized MWCNTs are denoted as MWCNT-N (KMnO_4), MWCNT-N (HNO_3), MWCNT-N (H_2O_2). The composites of the size 10 × 30 mm were melt welded onto the surface of TPU tensile test specimen (dog-bone shaped) for extension and bending tests [4]. The shape and dimension are chosen according to standard EN ISO 3167. The resulting structure of prepared samples sensitive to deformation consists of three-layers structure. There is TPU specimen, TPU/MWCNT composite layer created from melted TPU filtering membrane with interfiltrated nanotubes, and pure MWCNT network originated on filter during filtration.

2.2. Characterization of MWCNT-N and TPU/MWCNT-N Composite. TEM of CNT material was performed using microscope JEOL JEM 2010 at the accelerating voltage of 160 kV. The sample for TEM was fabricated on 300 mesh copper grid with a carbon film (SPI, USA) from MWCNT dispersion in acetone prepared by ultrasonication, which was deposited on the grid and dried.

The structure of MWCNT-Ns on the composites was analyzed by scanning electron microscope (SEM) Vega LMU, produced by Tescan Ltd. The samples were deposited on carbon targets and covered with a thin Au/Pd layer. For the observations the regime of secondary electron was chosen.

XPS signals measured from MWCNT-Ns were recorded using a Thermo Scientific K-Alpha XPS system (Thermo Fisher Scientific, UK) equipped with a microfocused, monochromatic Al $K\alpha$ X-ray source (1486.6 eV). An X-ray beam of 400 μm size was used at 6 mA × 12 kV. The spectra were acquired in the constant analyzer energy mode with pass energy of 200 eV for the survey. Narrow regions were collected using the snapshot acquisition mode (150 eV pass energy) enabling rapid collection of data (5 s per region). The narrow region data was postprocessed using Jansson's algorithm to remove the analyser point spread function which resulted in improved resolution of the spectra for peak deconvolution [15].

The resistance change of the composites was monitored by a two-point technique under different tensile loading. The time-dependent resistance change was measured by means of the Vernier LabQuest Interface System connected to the Differential Voltage Probe and the Wheatstone bridge with sampling frequency 200 Hz.

Fourier transform infrared (FTIR) analyses of the MWCNT-Ns and the composite samples were performed

TABLE 1: Summary of FTIR measurements for the pristine and oxidized MWCNT-Ns.

| Possible assignments | Wavenumber (cm^{-1}) | | | |
|---|---------------------------------|------------------------------------|----------------------------|-----------------------------|
| | MWCNT-N | MWCNT-N (H_2O_2) | MWCNT-N (HNO_3) | MWCNT-N (KMnO_4) |
| OH stretch | 3435 | 3459 | 3428 | 3427 |
| C–H stretch (CH_2 , CH_3) | 2908, 2840 | 2977, 2888 | 2980, 2880 | 2978, 2888 |
| C=O stretch (carboxyl or ketone) | 1705 | 1718 | 1726 | 1710 |
| Intermediate oxidized products—quinone groups | 1652 | 1637 | 1661, 1635 | 1641 |
| C=C stretch | 1559 | 1565 | 1580 | 1569 |
| CH_2/CH_3 bending | 1460 | 1443 | 1437 | 1440 |
| Skeletal C–C tangential motions + C–O stretch | 1222 | 1219, 1167 | 1184 | 1190 |
| C–O stretch | 1082 | 1083, 1052 | 1084, 1049 | 1087, 1046 |

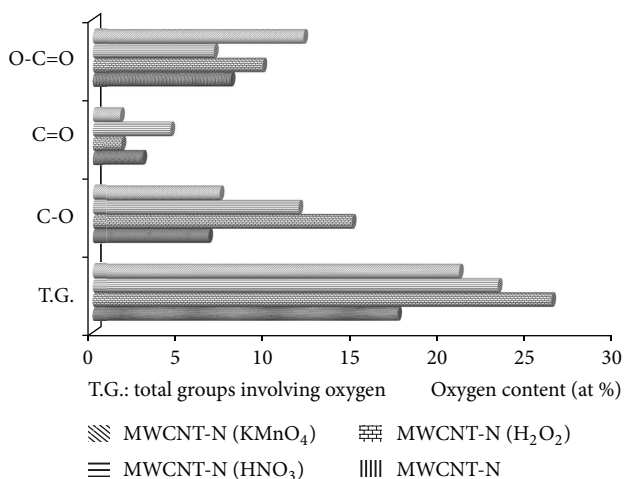


FIGURE 1: Oxygen content (at %) on MWCNT-Ns oxidized by different reagents.

on FT-IR spektrometr Nicolet 6700. Transmission accessory was used for the MWCNT-Ns samples in powder form prepared by KBr. FTIR-attenuated total reflectance (ATR) spectra of the interface of TPU/MWCNT composite layer where upper network made of pure CNT was washed out were obtained using Ge plate for ATR and repeated three times. The MWCNT-Ns were used for FTIR-ATR spectra of TPU/MWCNT composites as a background.

3. Results

3.1. FTIR Measurements. Table 1 summarizes the frequencies of some functional groups in FTIR spectra of MWCNT-Ns. The OH stretch is shifted to lower wavelength for only MWCNT-N (H_2O_2) which could show the increase in the amount of hydrogen bonded hydroxyl groups. On the other hand, C–H stretching of MWCNTs is shifted to lower wavelength for all oxidation treatments.

A weak C=O peak at 1705 cm^{-1} was observed in pristine MWCNT-N, which shows that there is carbonyl or carboxylic

group in its surface. The reason why pristine MWCNT-N has carbonyl and OH groups could be partial oxidation of the surfaces of MWCNTs during purification by the manufacturer [16]. The higher shift in the carbonyl stretching mode is seen for MWCNT-N (HNO_3) than for other oxidized MWCNT-Ns. The reason may be a kind of C=O group or other groups that interacts with the C=O group. Zhang and coworkers found that even if the acid mixture and dilute nitric acid produce carboxylic group on the surface of SWCNTs, the strength vibration peaks are not at the same location due to possible different hydrogen bonding interactions [17]. The results summarized in Table 1 also show that there are probably no anhydride/lactone groups on the surfaces of MWCNTs since these groups are usually observed at around 1750 cm^{-1} or more high wavenumber [18–20].

The peak assigned to quinone group at 1652 cm^{-1} in pristine MWCNT-N is usually shifted to higher wavelength in oxidized MWCNT-Ns. Coupling effects (i.e., both of intermolecular and inner molecular hydrogen bonding with hydroxyl groups) also might be responsible for the downshift in the C=O stretching mode, besides the production of surface-bound quinone groups with extended conjugation [21].

The up-shift in the C=C stretching mode of MWCNT-Ns was observed for all oxidized MWCNT-Ns. The highest shift was observed for MWCNT-N (HNO_3) compared to other MWCNT-N. This treatment may suggest a change in the structure of the MWCNT-N [17].

The C–H (CH_2/CH_3) bending at 1460 cm^{-1} and the peak at 1222 cm^{-1} for MWCNT-N are shifted to higher wavelength for all oxidized MWCNT-Ns. The peak at around 1170 cm^{-1} assigned to C–OH group was also observed on MWCNT after H_2O_2 oxidation in another study [22]. A new band around 1050 cm^{-1} in FTIR spectra of oxidized MWCNT-Ns was also observed, which could be assigned to alcoholic C–O stretching vibration [22]. Overall, the observed changes in FTIR spectra of oxidized MWCNT-Ns confirm the efficiency of the oxidizing process and formation of the new oxygen-containing functional groups on the surface of carbon nanotubes.

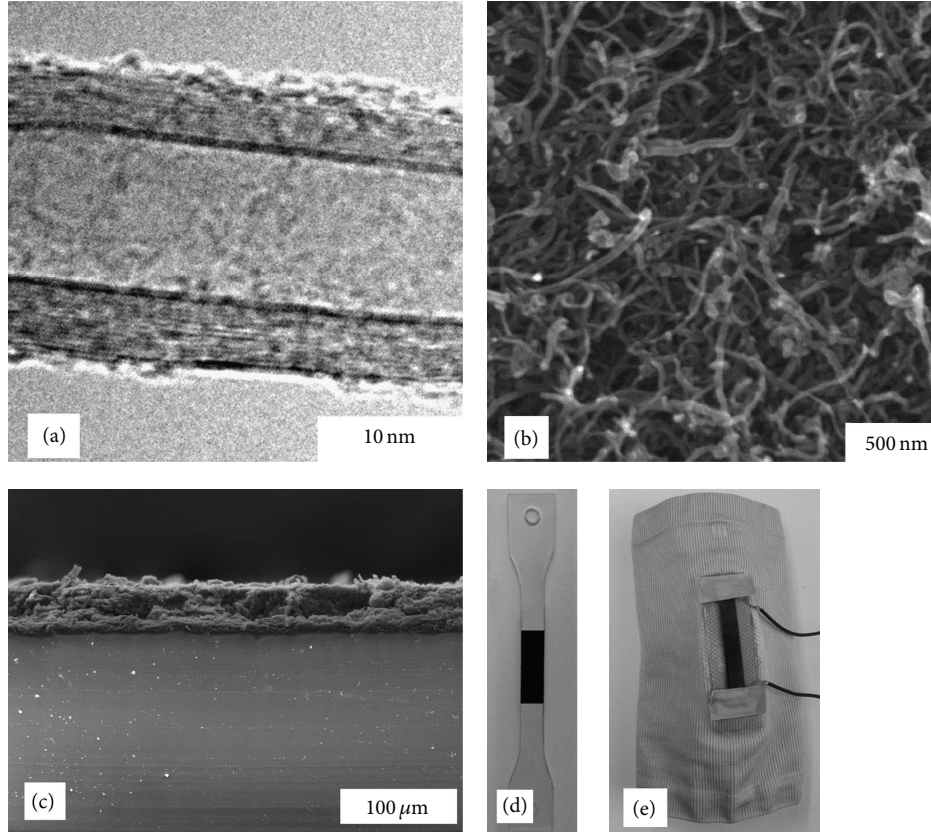


FIGURE 2: (a) TEM micrograph of nanotube structure; (b) SEM micrograph of the surface of entangled MWCNT network; (c) the composite cross-section after the compression molding; (d) photograph of TPU dog-bone shaped specimen; (e) and (a) position of measuring strip of TPU/MWCNT network composite on the elastic elbow bandage.

3.2. XPS Data. The X-ray photoelectron spectroscopy was performed on the MWCNT-N specimens to get information on the functional groups attached onto the nanotube surface. The surface composition (in atomic %) was determined by considering the integrated peak areas of C1 and the respective sensitivity factors. The fractional concentration of a particular element A was computed using

$$\% A = \frac{(I_A/s_A)}{\sum (I_n/s_n)} \times 100\%, \quad (1)$$

where I_A denotes the signal intensity of element A , I_n integrated peak areas, and s_A and s_n the Scofield sensitivity factors corrected for the analyzer transmission.

The main binding energy peak (284.5 eV) in XPS spectra of MWCNT-Ns was assigned to the C1s-sp², while the other ones were assigned to C–O (286.2 eV), C=O (287.1 eV), O–C=O (288.6–289 eV), and C1s- π - π^* (291.1–291.5 eV). XPS data in Figure 1 show that all MWCNT-Ns have C–OH, C=O, and O–C=O groups on their surface and that MWCNT-N (KMnO₄), MWCNT-N (HNO₃), and MWCNT-N (H₂O₂) have maximum percentage of O–C=O, C=O, and C–OH, respectively. FTIR data of these MWCNT-Ns also confirm the presence of these functional groups on the surface. It was also stated in an other study that MWCNTs treated with (NH₄)₂S₂O₈, H₂O₂, and O₃ have higher concentrations of

carbonyl and hydroxyl functional groups, while more aggressive oxidants (e.g., HNO₃, KMnO₄) form higher fractional concentrations of carboxyl groups [23]. The acidic potassium permanganate (KMnO₄) is a strong oxidizing agent and produces more surface acidic groups than nitric acid [24].

The study of Fang and coworkers shows that XPS analysis is a useful and simple method for evaluating the content variation of amorphous carbon in SWNT samples by analyzing the sp³/sp² carbon ratio [25]. According to our XPS results of MWCNT-Ns the carbon ratios are 2.50, 2.71, 3.50, and 1.69 for MWCNT-N, MWCNT-N (H₂O₂), MWCNT-N (HNO₃), and MWCNT-N (KMnO₄), respectively. The reason why the total oxygen amount for MWCNT-N (KMnO₄) is less than that in case of other oxidants could be due to removing away more amount of the oxygen species originated from amorphous carbon structures during the acidified KMnO₄ oxidation process.

3.3. From Tubes to Strain Sensing Element. Figures 2(a)–2(e) summarize pathway of CNT application for strain sensing element. Part (a) represents TEM analyses of one individual MWCNT tube which typically consists of about 15–35 rolled layers of graphene. The SEM micrograph of the upper surfaces of MWCNT-N network created from entangled tubes is presented in part (b). Comparing results for each principal

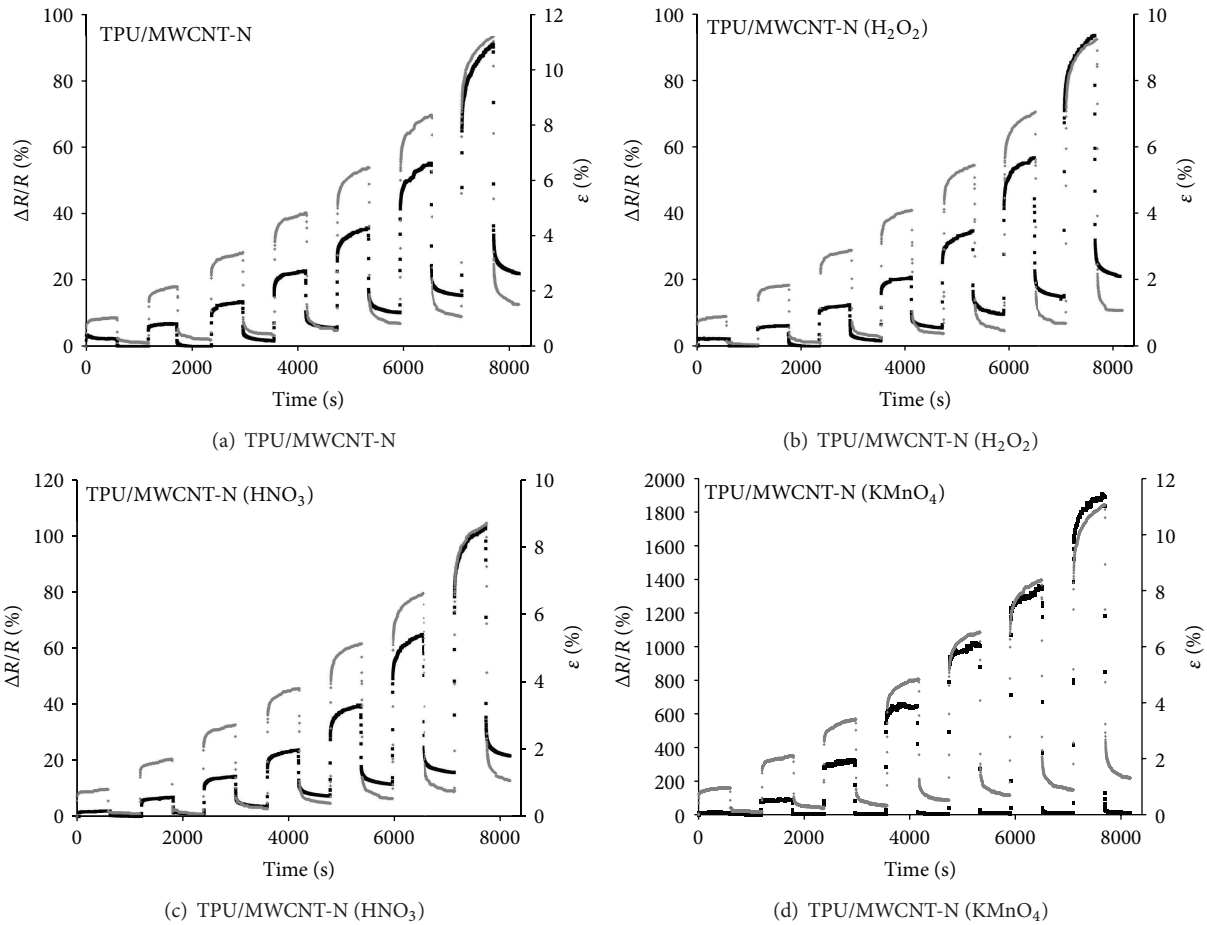


FIGURE 3: Response of the relative resistance change and strain of the TPU composites versus the step increase of tensile strength (a) TPU/MWCNT-N, (b) TPU/MWCNT-N (H_2O_2), (c) TPU/MWCNT-N (HNO_3), and (d) TPU/MWCNT-N ($KMnO_4$).

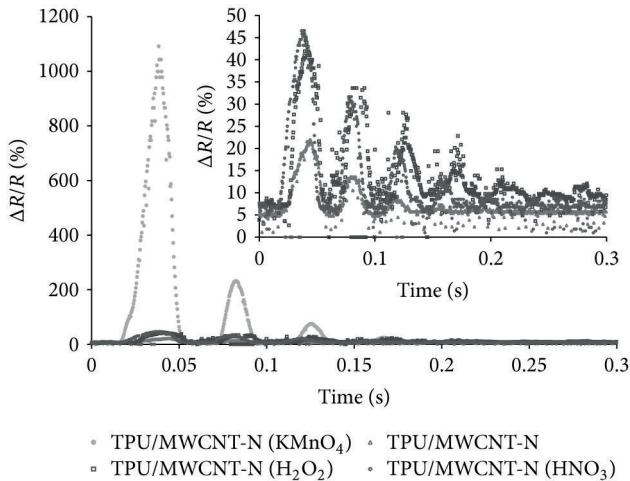


FIGURE 4: Time-dependent response of the strips of the TPU composites anchored tightly on one side to the initial deflection of free ending.

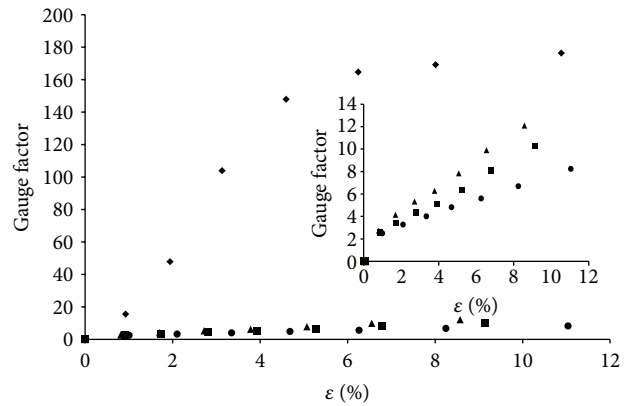


FIGURE 5: Gauge factors of the TPU composites.

material it was found that the structures of networks slightly differ from each to other. $MWCNT-N (KMnO_4)$ seems to

have smoother surface than others with more densely packed nanotubes and smaller diameters of pores. On the other hand, the most porous structure belongs to $MWCNT-N (HNO_3)$. The composite cross-section after the compression molding is

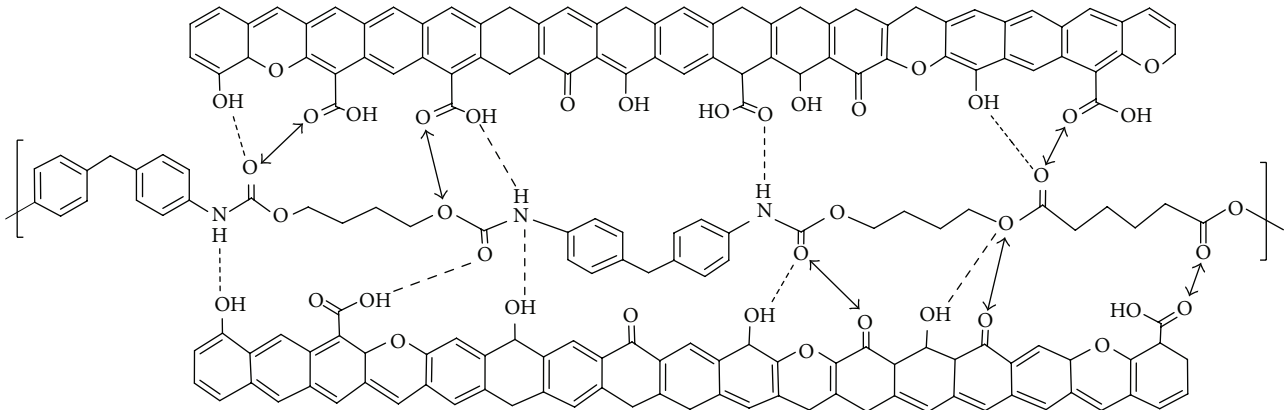


FIGURE 6: The possible interactions between TPU and MWCNT-Ns. The distances among the functional groups are drawn randomly. They give no information about the strength of hydrogen bonding. Two headed arrows and dashed lines show repulsion forces and intermolecular hydrogen bonding, respectively.

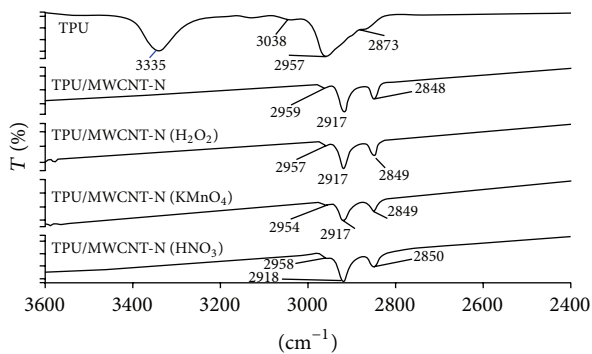


FIGURE 7: FTIR spectra of TPU and the composites between 2400 and 3600 cm^{-1} .

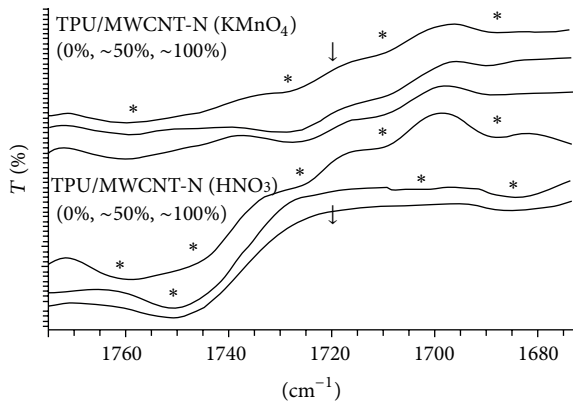


FIGURE 8: Comparison of FTIR spectra of TPU/MWCNT-N (KMnO_4) and TPU/MWCNT-N (HNO_3) for various elongations.

shown in Figure 2(c) (upper black layer represents both pure MWCNT network and TPU/MWCNT composite interlayer while lower part is body of TPU specimen). Moreover, the melted polymer apparently encloses MWCNTs from MWCNT network surface in the course of molding at 175°C, making firm connection between the polymer and layer of

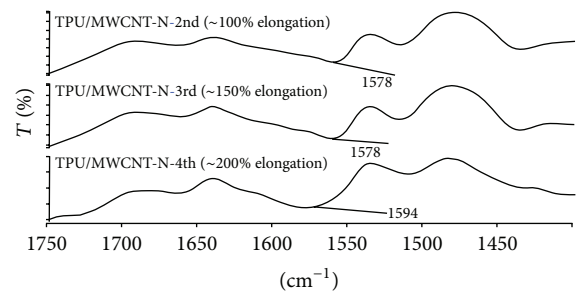


FIGURE 9: FTIR spectra of TPU/MWCNT-N for various elongation.

entangled nanotubes. MWCNT network and TPU filtering membrane can be easily melt welded onto the surface of TPU tensile test specimen (dog-bone shaped) for extension and resistance tests, Figure 2(d). As an example of practical use of TPU/MWCNT composite as a strain sensing element, a strip of TPU/MWCNT-N composite was fixed on the elastic bandage to monitor human elbow flexion.

3.4. Tensile Deformation and Gauge Factor of MWCNT-N/PU Composites. The relative electrical resistance change, defined as $\Delta R/R_0 = (R - R_0)/R_0$, where R_0 is the electrical resistance of the measured sample before the first elongation and R is the resistance while elongating, versus the percentage of mechanical strain is presented in Figure 3. The composite specimens are deformed by the tensile stress with increasing value in each cycle 0.43, 0.73, 1.07, 1.37, 1.71, 2.09, and 2.47 MPa. The increasing stress obviously enhances composite plastic deformation. Consequently, the residual strain increases in the off-load state with increasing number of cycles. The similar residual increase of the resistance is also observed except the resistance of TPU/MWCNT-N (KMnO_4) composite which is reversible. Thus the nanotube oxidation by KMnO_4 has a stabilizing effect on the cyclic resistance change. The testing has shown also the sixteen-fold increase in the resistance for the composite prepared from

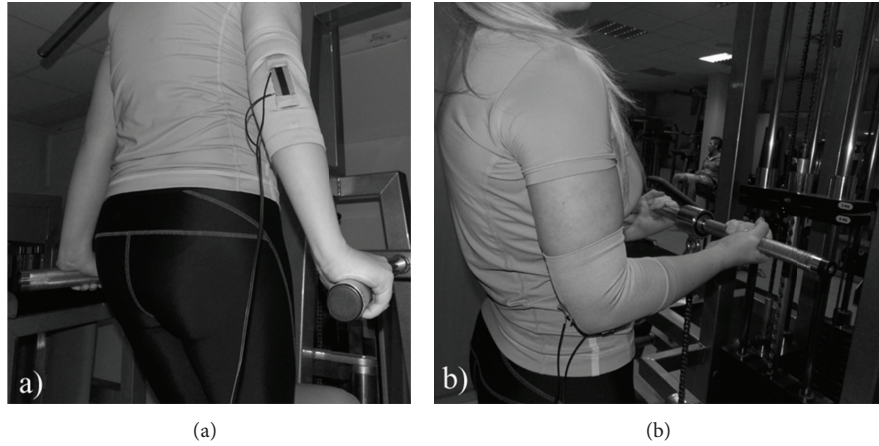


FIGURE 10: Measurement of elbow joint flexion during (a) the bodyweight dips and (b) the cable-based arm curls.

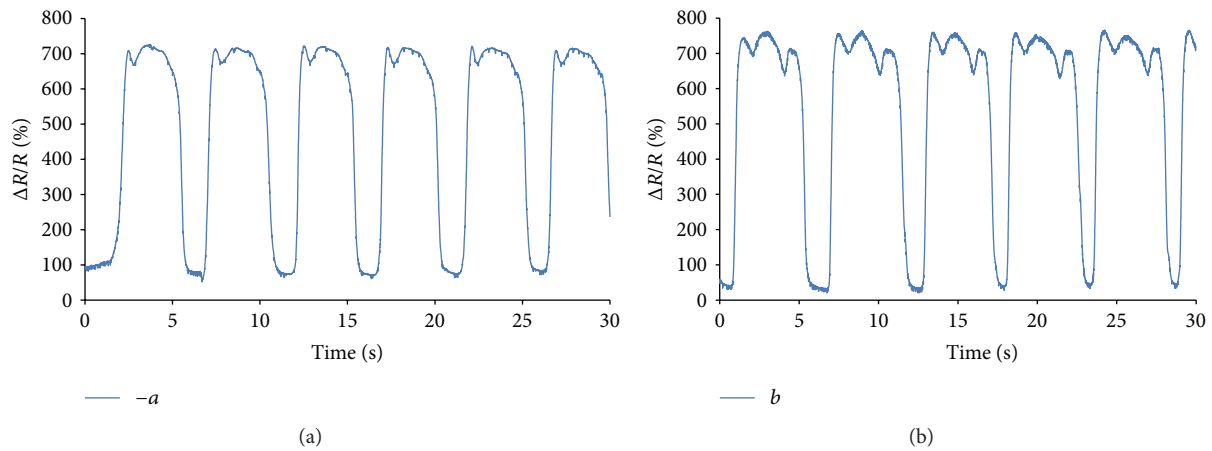


FIGURE 11: Time-dependent resistance change of TPU/MWCNT-N (KMnO_4) composite strain sensor during (a) the bodyweight dips and (b) the cable-based arm curls.

KMnO_4 oxidized nanotubes in comparison to the composites prepared from the pristine and other oxidized nanotubes.

Figure 4 shows fast resistance change of the strips of composites anchored tightly on one side to bending deformation induced by the tip deflection of free ending. The oxidation treatment evidently causes the increase in the resistance change which is highest for TPU/MWCNT-N (KMnO_4) composite.

The sensitivity of electrically conductive materials is usually evaluated by a gauge factor GF which is defined as the relative resistance change divided by the applied strain ϵ , $GF = (\Delta R/R_0)/\epsilon$ [26]. The gauge factors of the composites given in Figure 5 were calculated by using maximum values of resistance change and strain for each cycle in Figure 3. The gauge factor of CNT thin film was found to be 65 under room temperature for very low strain up to 0.05% [27]. Wang and coworkers found the Gauge factors of iodine-doped and iodine-undoped carbon nanotubes as 125 and 65, respectively [28].

The calculated gauge factors of our composites increase with the strain up of the maximum measured gauge factor which is for TPU/MWCNT-N, TPU/MWCNT-N (H_2O_2),

TPU/MWCNT-N (HNO_3), and TPU/MWCNT-N (KMnO_4) about 8, 10, 12, and 175 for the strains 11, 9.1, 8.6 and 10.9%, respectively.

3.5. FTIR Spectra of the Composite Interfaces. As shown above, the type of MWCNTs significantly affects the resulting sensitivity of composites to strain. Rein and coworkers suggested in their study [8] that the source of the large difference in sensitivity between carbon nanotube network types in epoxy resins is the interaction between the polymer and MWCNTs [13]. The difference in the maximum strain values of the investigated composites could arise from the interactions in MWCNT-Ns and/or between TPU and MWCNT-Ns. At first FTIR spectra for the interface of the composites were measured using the MWCNT-Ns as a background.

In the polyester-based polyurethane, the NH groups as proton donor and the oxygens in carbonyl groups of urethane and ester groups as proton acceptors behave in formation of hydrogen bonding. When MWCNT-Ns have hydroxyl, carboxyl, ketone, and ether groups on their surface, these groups can also play a part in forming hydrogen bonding

TABLE 2: Some peaks in FTIR spectra of TPU and TPU/MWCNT-Ns composites.

| Possible assignments | Wavenumber (cm ⁻¹) | | | | |
|--|--------------------------------|-------------|--|---------------------------------|----------------------------------|
| | TPU | TPU/MWCNT-N | TPU/MWCNT-N (H ₂ O ₂) | TPU/MWCNT-N (HNO ₃) | TPU/MWCNT-N (KMnO ₄) |
| C=O stretch | — | 1759, 1744 | 1748 | 1759, 1743 | 1759 |
| Free C=O stretch | 1728 | 1726 | 1715 | 1723 | 1725 |
| C=O stretch for hydrogen bonded urethane group | 1706 | 1710, 1690 | 1700, 1683 | 1708, 1689 | 1707, 1688 |
| C=O stretch for hydrogen bonded ester group | 1662 | 1665 | 1652 | 1664 | 1662 |
| NH bending + C=C stretch | 1597 | 1574 | 1573 | 1574 | 1577 |
| C-N stretch + N-H bending | 1531 | 1535 | 1538 | 1539 | 1539 |

between the polymer and MWCNT-Ns. Possible interactions between TPU and MWCNT-Ns are shown in Figure 6 by considering FTIR and XPS data of MWCNT-Ns.

Some changes observed in FTIR spectra of TPU/MWCNT composites compared with that of pure TPU are given in Figure 7 and Table 2. The broad -NH absorption between 3230 and 3430 cm⁻¹ has been removed in TPU/MWCNT-N composites which could show that all NH groups are hydrogen bonded with some groups on the MWNTs. The CH bands (CH₂/CH₃) seen at 2957 and 2873 cm⁻¹ in TPU are divided in the composites into three parts such as around 2960, 2917, and 2850 cm⁻¹ due to the interaction with MWCNT-Ns.

The observed changes in three different carbonyl peaks of TPU can be seen in Table 2. When the ones at 1728 and 1706 cm⁻¹ split into two or three parts in the composites due to some interactions shown in Figure 6, some of three carbonyl peaks remained unchanged or shifted to higher/lower wavelengths for different composites. The more shifting to higher wavelength for all carbonyl peaks was observed for TPU/MWCNT-N (H₂O₂) due to probable hydrogen bonding between the C=O groups on TPU and -OH groups on the MWCNT-N.

3.6. FTIR Spectra of the Composite Interfaces Subjected to Strain. FTIR spectra related to the composite interfaces reveal some differences among the amounts of functional groups on the MWCNT-Ns. Hence FTIR spectra of TPU and the interfaces of TPU composites subjected to 7 various strains were examined. The values of strain could not be calculated properly due to the pressure of the ATR tip on the samples. Important differences among them are given in Figures 8 and 9.

Some peaks in the C=O stretch region of TPU/MWCNT-N (HNO₃) which could interact with the -OH/-COOH groups on the MWCNT-N disappeared or shifted to lower wavenumber in the 2nd and 3rd elongations as follows from Figure 8, owing to new interactions of carbonyl groups on TPU with the functional groups on MWCNT-N (HNO₃). On the other hand, the peaks in the C=O stretch region of TPU/MWCNT-N (KMnO₄) remained unchanged. Figure 9 shows that hydrogen bond between NH group in TPU

and C=O/-OH/-COOH group in the pristine MWCNT-N, schematically illustrated in Figure 6, was damaged in the 4th elongation. Such a situation was not observed for other TPU composites. The reason seems to be that there are less oxygenated groups on the pristine MWCNT-N in comparison with oxidized nanotube networks (Figure 1). The disappeared/changed interactions at interfaces of the composites with strain may influence the stress transfer between TPU and MWCNT networks. Hence, the observation may also give information about why TPU/MWCNT-N (HNO₃) and TPU/MWCNT-N have lower resistance change with strain than TPU/MWCNT-N (KMnO₄) when the interactions between MWCNTs may be affected due to the difference in the amount of functional groups on their surfaces.

3.7. Practical Use of TPU/MWCNT-N (KMnO₄) Composite.

The possible practical use of TPU/MWCNT-N (KMnO₄) composite is demonstrated by monitoring of elbow joint flexion during two different physical exercises, namely, body-weight dips and cable-based arm curls (Figure 10). The strip of the composite was adhered to an elastic bandage (83% of polyamide and 17% of elastolan) by means of dimethyl formamide/methyl isobutyl ketone (1:3) solution. The electrical contacts were fixed to the strip by a silver-colloid electroconductive paint Dotite D-550 (SPI Supplies), and the resistance was measured lengthwise by the two-point technique using multimeter Sefram 7338.

Figures 11(a) and 11(b) show waveforms of the test performed by the volunteer with the bandage. The data are reversible and sensitive so that the composite can be used, for example, for the similar measurements in orthopedics and rehabilitation.

4. Conclusions

Multi-walled carbon nanotubes were used in their pure and oxidized forms to prepare entangled networks as a part of TPU/MWCNT-N composites. The response of composites to deformation was measured by their electrical resistance change in the course of extension/relaxation cycles and bending. The results show that the composite with KMnO₄ oxidized nanotube network has an enhanced electrical resistance

with loading in comparison with the network prepared from the pristine and other oxidized nanotubes. The evaluated sensitivity of TPU/MWCNT-N (KMnO_4) composite in terms of the gauge factor increases with strain from values around 5 at the start of deformation to 175 at the strain 11%. This is a substantial increase, which ranks the composite among the materials with the highest electromechanical sensitivity.

The distinct resistance and sensitivity increase with elongation and bending may come probably from the different porous structure of MWCNT (KMnO_4) network, the interaction between TPU and MWCNT-N (KMnO_4) and the increased number of carboxyl groups detached on MWCNT-N (KMnO_4) surface. The short oxidized nanotubes, forming densely packed network with small pores, probably lose mechanical contacts with other ones more easily in the course of composite elongation than the longer pristine nanotubes. The unchanged interactions between TPU and MWCNT-N (KMnO_4) at the composite interface during the elongation, discussed in details in Section 3.6, may ensure stress transfer from the elastic TPU to the network and its extensive rearrangement and loss of nanotube contacts. Similarly, the increased presence of carboxyl groups on the surface of MWCNT-N (KMnO_4) in comparison with other investigated networks (Figure 1) enhances interaction of nanotubes via two interaction points (carbonyl and hydroxyl groups). Thus during elongation more chemical links between nanotubes fade which results also in loss of conductive points, and consequently, the resistance rise.

Conflict of Interests

Petr Slobodian declares that there is no conflict of interests.

Acknowledgments

The work was supported by the internal Grant of TBU in Zlin No. IGA/FT/2013/018 funded from the resources of Specific University Research and Operational Program of Research and Development for Innovations cofunded by the European Regional Development Fund (ERDF), the national budget of Czech Republic within the framework of the Centre of Polymer Systems project (reg. no. CZ.1.05/2.1.00/03.0111). This paper was also written with the support of the Operational Programme “Education for Competitiveness” co-funded by the European Social Fund (ESF) and the national budget of the Czech Republic, within the “Advanced Theoretical and Experimental Studies of Polymer Systems” project (reg. no. CZ.1.07/2.3.00/20.0104). The Fund of Institute of Hydrodynamics, no. of project AV0Z20600510, is also acknowledged for support.

References

- [1] A. K. Barick and D. K. Tripathy, “Preparation, characterization and properties of acid functionalized multi-walled carbon nanotube reinforced thermoplastic polyurethane nanocomposites,” *Materials Science and Engineering B*, vol. 176, no. 18, pp. 1435–1447, 2011.
- [2] A. K. Barick and D. K. Tripathy, “Effect of nanofiber on material properties of vapor-grown carbon nanofiber reinforced thermoplastic polyurethane (TPU/CNF) nanocomposites prepared by melt compounding,” *Composites Part A*, vol. 41, no. 10, pp. 1471–1482, 2010.
- [3] Q. Fan, Z. Qin, T. Villmow et al., “Vapor sensing properties of thermoplastic polyurethane multifilament covered with carbon nanotube networks,” *Sensors and Actuators B*, vol. 156, no. 1, pp. 63–70, 2011.
- [4] P. Slobodian, P. Riha, and P. Saha, “A highly-deformable composite composed of an entangled network of electrically-conductive carbon-nanotubes embedded in elastic polyurethane,” *Carbon*, vol. 50, no. 10, pp. 3446–3453, 2012.
- [5] A. M. F. Lima, V. G. de Castro, R. S. Borges, and G. G. Silva, “Electrical conductivity and thermal properties of functionalized carbon nanotubes/polyurethane composites,” *Polímeros*, vol. 22, pp. 117–124, 2012.
- [6] D. M. Crawford, R. G. Bass, and T. W. Haas, “Strain effects on thermal transitions and mechanical properties of thermoplastic polyurethane elastomers,” *Thermochemica Acta*, vol. 323, no. 1–2, pp. 53–63, 1998.
- [7] R. Olejnik, P. Slobodian, P. Riha, and P. Saha, “An electrically-conductive and organic solvent vapors detecting composite composed of an entangled network of carbon nanotubes embedded in polystyrene,” *Journal of Nanomaterials*, vol. 2012, Article ID 365062, 7 pages, 2012.
- [8] M. D. Rein, O. Breuer, and H. D. Wagner, “Sensors and sensitivity: carbon nanotube buckypaper films as strain sensing devices,” *Composites Science and Technology*, vol. 71, no. 3, pp. 373–381, 2011.
- [9] I. Kang, M. J. Schulz, J. H. Kim, V. Shanov, and D. Shi, “A carbon nanotube strain sensor for structural health monitoring,” *Smart Materials and Structures*, vol. 15, no. 3, pp. 737–748, 2006.
- [10] Q. Jiang, Y. Li, J. Xie, J. Sun, D. Hui, and Y. Qiu, “Plasma functionalization of bucky paper and its composite with phenylethynyl-terminated polyimide,” *Composites Part B*, vol. 45, pp. 1275–1281, 2013.
- [11] P. Pötschke, N. P. Zschoerper, B. P. Moller, and U. Vohrer, “Plasma functionalization of multiwalled carbon nanotube bucky papers and the effect on properties of melt-mixed composites with polycarbonate,” *Macromolecular Rapid Communications*, vol. 30, no. 21, pp. 1828–1833, 2009.
- [12] Z. Špitalský, C. A. Krontiras, S. N. Georga, and C. Galotis, “Effect of oxidation treatment of multiwalled carbon nanotubes on the mechanical and electrical properties of their epoxy composites,” *Composites Part A*, vol. 40, no. 6–7, pp. 778–783, 2009.
- [13] M. D. Rein, H. Bar, O. Breuer, R. Yoseph, and H. D. Wagner, “Electromechanical properties of carbon nanotube buckypapers,” in *Proceedings of the 17th International Conference on Composite Materials (ICCM-17 '09)*, Edinburgh, UK, July 2009.
- [14] P. Slobodian, P. Riha, A. Lengalova, P. Svoboda, and P. Saha, “Multi-wall carbon nanotube networks as potential resistive gas sensors for organic vapor detection,” *Carbon*, vol. 49, no. 7, pp. 2499–2507, 2011.
- [15] P. A. Jansson, Ed., *Deconvolution of Spectra and Images*, Academic Press, San Diego, Calif, USA, 1997.
- [16] F. A. Abuilawi, T. Laoui, M. Al-Harhi, and M. A. Atieh, “Modification and functionalization of multiwalled carbon nanotube (MWCNT) via fisher esterification,” *Arabian Journal for Science and Engineering*, vol. 35, no. 1, pp. 37–48, 2010.

- [17] J. Zhang, H. Zou, Q. Qing et al., "Effect of chemical oxidation on the structure of single-walled carbon nanotubes," *Journal of Physical Chemistry B*, vol. 107, no. 16, pp. 3712–3718, 2003.
- [18] P. E. Fanning and M. A. Vannice, "A DRIFTS study of the formation of surface groups on carbon by oxidation," *Carbon*, vol. 31, no. 5, pp. 721–730, 1993.
- [19] T. G. Ros, A. J. Van Dillen, J. W. Geus, and D. C. Koningsberger, "Surface oxidation of carbon nanofibres," *Chemistry*, vol. 8, pp. 1151–1162, 2002.
- [20] C. Moreno-Castilla, M. V. López-Ramón, and F. Carrasco-Marín, "Changes in surface chemistry of activated carbons by wet oxidation," *Carbon*, vol. 38, no. 14, pp. 1995–2001, 2000.
- [21] U. J. Kim, C. A. Furtado, X. Liu, G. Chen, and P. C. Eklund, "Raman and IR spectroscopy of chemically processed single-walled carbon nanotubes," *Journal of the American Chemical Society*, vol. 127, no. 44, pp. 15437–15445, 2005.
- [22] Y. Liang, H. Zhang, B. Yi, Z. Zhang, and Z. Tan, "Preparation and characterization of multi-walled carbon nanotubes supported PtRu catalysts for proton exchange membrane fuel cells," *Carbon*, vol. 43, no. 15, pp. 3144–3152, 2005.
- [23] K. A. Wepasnick, B. A. Smith, K. E. Schrote, H. K. Wilson, S. R. Diegelmann, and D. H. Fairbrother, "Surface and structural characterization of multi-walled carbon nanotubes following different oxidative treatments," *Carbon*, vol. 49, no. 1, pp. 24–36, 2011.
- [24] J. Chen, Q. Chen, and Q. Ma, "Influence of surface functionalization via chemical oxidation on the properties of carbon nanotubes," *Journal of Colloid and Interface Science*, vol. 370, no. 1, pp. 32–38, 2012.
- [25] H.-T. Fang, C.-G. Liu, C. Liu, F. Li, M. Liu, and H.-M. Cheng, "Purification of single-wall carbon nanotubes by electrochemical oxidation," *Chemistry of Materials*, vol. 16, no. 26, pp. 5744–5750, 2004.
- [26] P. Slobodian, R. Olejnik, P. Riha, and P. Saha, "Effect of functionalized nanotubes with HNO_3 on electrical sensory properties of carbon nanotubes/polyurethane composite under elongation," in *Mathematical Methods and Techniques in Engineering and Environmental Science*, M. Demiralp, Z. Bojkovic, and A. Repanovici, Eds., pp. 312–316, WSEAS Press, 2011.
- [27] T. W. Tombler, C. Zhou, L. Alexseyev et al., "Reversible electromechanical characteristics of carbon nanotubes under local-probe manipulation," *Nature*, vol. 405, no. 6788, pp. 769–772, 2000.
- [28] W.-L. Wang, K.-J. Liao, Y. Li, and Y.-T. Wang, "Piezoresistive effect of doped carbon nanotube/cellulose films," *Chinese Physics Letters*, vol. 20, no. 9, pp. 1544–1547, 2003.

Research Article

Methanol Adsorption on Graphene

Elsebeth Schröder

Microtechnology and Nanoscience (MC2), Chalmers University of Technology, 412 96 Göteborg, Sweden

Correspondence should be addressed to Elsebeth Schröder; schroder@chalmers.se

Received 14 March 2013; Accepted 11 August 2013

Academic Editor: Sulin Zhang

Copyright © 2013 Elsebeth Schröder. This is an open access article distributed under the Creative Commons Attribution License, which permits unrestricted use, distribution, and reproduction in any medium, provided the original work is properly cited.

The adsorption energies and orientation of methanol on graphene are determined from first-principles density functional calculations. We employ the well-tested vdW-DF method that seamlessly includes dispersion interactions with all of the more close-ranged interactions that result in bonds like the covalent and hydrogen bonds. The adsorption of a single methanol molecule and small methanol clusters on graphene is studied at various coverages. Adsorption in clusters or at high coverages (less than a monolayer) is found to be preferable, with the methanol C-O axis approximately parallel to the plane of graphene. The adsorption energies calculated with vdW-DF are compared with previous DFT-D and MP2-based calculations for single methanol adsorption on flakes of graphene (polycyclic aromatic hydrocarbons). For the high coverage adsorption energies, we also find reasonably good agreement with previous desorption measurements.

1. Introduction

Methanol (CH_3OH) is the simplest of the alcohols, and it is used, for example, as a solvent, an alternative fuel, and as a source for producing other chemicals. Methanol is the second most abundant organic molecule in the atmosphere after methane (CH_4), and along with other insoluble aerosol particles methanol is believed to play a role in the formation of ice in the atmosphere, as discussed and modeled, for example, in [1, 2]. Methanol is also found in the interstellar medium, as methanol ice dust grains.

In experiments where molecules are adsorbed on graphite, methanol is often used as a solvent for the larger molecules at target, and thus the adsorption properties of methanol affect the adsorption of the other molecule. Gaining access to detailed adsorption data for methanol on graphite, such as positions and energetics like those provided here, is thus valuable both directly and as input data for larger simulations of molecules on graphite embedded in the (methanol) solvent. For studies of atmospheric (water) ice formation and interstellar (methanol) ice formation the graphite surface is found to be a suitable model for the particles on which the ice forms [3, 4], further motivating our study of methanol adsorption on graphite.

In this paper, we calculate by first-principles density functional theory (DFT) the adsorption energy of methanol

on graphite at various degrees of coverage (less than one molecular monolayer) and we determine the distance from and the optimal angle of the methanol molecule C-O axis with the plane of graphite. For the DFT calculations we use the method vdW-DF [5, 6].

Previously, the adsorption energies of methanol from graphene or flakes of graphene were calculated [7] by the semiempirical theory method DFT-D [8]. In the study [7] the adsorption of methanol on to very small flakes of graphene—benzene and coronene—was also calculated by the higher-accuracy correlation method second-order Møller-Plesset perturbation theory (MP2). Desorption energies from highly oriented pyrolytic graphite (HOPG) or from various sizes of single-walled carbon nanotubes (SWCNTs) have also previously been measured in a number of desorption experiments [3, 9, 10].

The purpose of this study is to provide first-principles theory results of methanol interactions with graphite for larger-scale simulations and for interpretations of experiments. For this we determine basic information about adsorbed methanol on graphene, such as the optimal orientation the interaction (adsorption) energy at various coverages and distances from graphene. These data are then available as input to and/or for fine-tuning of molecular dynamics simulations of the methanol adsorption process.

In the following, we first introduce the methanol-graphene system, the vdW-DF method, and the setup of our calculations. Next, we describe our results both at low and high coverage of methanol on graphene and then discuss the relation to the theory results of [7] and some of the available experimental results.

2. Materials and Methods

On some surfaces methanol chemisorbs. When this is the case, traditional semilocal DFT methods, based on the generalized gradient expansion (GGA), may suffice for describing the adsorption. For instance, this is the case on the oxide surfaces α -Al₂O₃ (0001) and α -Cr₂O₃ (0001) on which we previously studied methanol adsorption [11, 12]. However, on graphene a number of small molecules physisorb, or at least owe a significant part of their adsorption energy to the dispersion interaction. Then GGA methods are inadequate.

We here use the vdW-DF method [5, 6]. It includes the van der Waals (vdW) interactions (also termed the London dispersion interactions), that are especially important on intermediate to long ranges, along with all the traits of GGA for short-range interactions. Thus, vdW-DF delivers a description of the system that takes care of both the vdW interaction between the fragments (and within the fragments) and the short-ranged interaction within the molecules, like the covalent bonding, hydrogen bonding, possible ionic interactions, and so forth, all from first principles.

Over the past few years, our group has carried out a series of physisorption studies of relatively small molecules on graphene: n-alkanes (of length 1 to 10 C atoms) [13], phenol [14], small polycyclic aromatic hydrocarbons (PAHs) [15, 16], trihalomethanes [17], adenine [18], and with somewhat different computational details, all of the five nucleobases of DNA and RNA [19]. General considerations of use of the vdW-DF method for such systems, as well as further method discussions, can be found in [13–18] mentioned above.

We here use the DFT program GPAW [20, 21] with a fast-Fourier-transform implementation of vdW-DF [5, 6, 22]. Pre- and postprocessing is carried out in the python environment ASE [23].

We use periodic orthorhombic unit cells as detailed in Table 1, with 8–60 graphene C-atoms per unit cell. The unit cell side lengths in the plane of graphene range from 4.29 to 12.87 Å with one, three, or five methanol molecules per unit cell, as illustrated for one molecule in Figure 1 and for three and five molecules in Figure 2.

The wave functions are sampled on a regular grid with points 0.12 Å apart (the charge density is sampled at points half that distance apart) to obtain sufficient accuracy for high-quality results from the vdW-DF calculations [13, 25]. The reciprocal space k -point sampling is $2 \times 2 \times 1$ for the largest and $6 \times 8 \times 1$ for the smallest unit cell, except for the calculation of isolated methanol where only the Γ -point is used.

In all calculations, the atomic positions are allowed to relax. We use the molecular-dynamics optimization method “fast inertial relaxation engine” (FIRE) [26] and require that

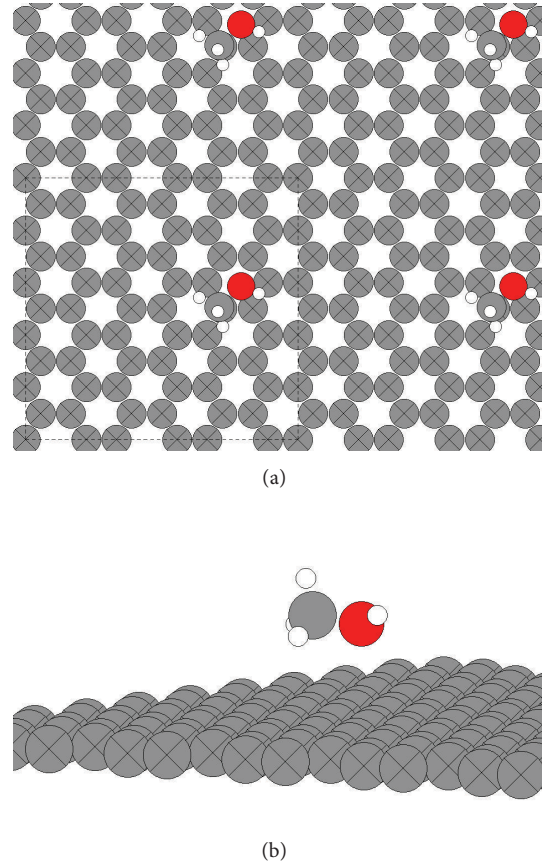


FIGURE 1: Schematic view of a single methanol molecule adsorbed on graphene in the $3\sqrt{3}a_g \times 5a_g \times 19$ Å periodically repeated unit cell. The configuration with the C-O axis approximately parallel with graphene is shown. Gray circles with a cross are graphene C atoms. Other gray/red/small white circles are the methanol C, O, and H atoms. In the top panel the unit cell is outlined by thin broken lines.

the remaining force on each atom has a size of less than 0.01 eV/Å.

We determine the adsorption energy per adsorbate, E_a , as the difference in total energies of the full system $E_{\text{tot, MeOH cluster on graphene}}^{\text{vdW-DF}}$ and each fragment isolated,

$$E_a = \frac{\left[E_{\text{tot, MeOH cluster on graphene}}^{\text{vdW-DF}} - E_{\text{tot, graphene}}^{\text{vdW-DF}} - N E_{\text{tot, MeOH}}^{\text{vdW-DF}} \right]}{N}, \quad (1)$$

where N is the number of molecules in the cluster (here 1, 3, or 5). The first two terms in (1) are found using the unit cell size of the full system (Table 1), whereas the last term is calculated in a $3\sqrt{3}a_g \times 5a_g \times 19$ Å unit cell with only Γ -point sampling.

The data points of the potential energy curve in Figure 3 are obtained with a slightly longer unit cell than the other calculations: because we need to calculate the methanol-graphene interaction at up to relatively large separations (11 Å) the unit cell height is increased to 23 Å, all other settings remaining the same.

TABLE 1: Theory data for adsorption of methanol on graphene. Included is the adsorption energy E_a , the distance of the methanol O atom from graphene, d_o , the adsorption configuration (C–O axis approximately parallel with the plane of graphene or C–O axis approximately perpendicular to the plane of graphene with the O atom pointing up or down), molecular coverage, and the orthogonal unit cell used in the calculations, given in units of $a_g = \sqrt{3} a_0$ with $a_0 = 1.43 \text{ \AA}$. All unit cells are 19 \AA in the direction perpendicular to the plane of graphene. The coverages in our calculations are estimated from the approximate molecular area of methanol on graphene 17.6 \AA^2 determined from X-ray diffraction studies in [24].

| | Structure | Unit cell | Coverage | | E_a | | d_o |
|--|-----------|----------------------|----------|----------|-------|-----------|-------|
| | | | [ML] | [kJ/mol] | [meV] | [Å] | |
| Theory, vdW-DF (our calculations) | | | | | | | |
| Single molecule | Parallel | $3\sqrt{3} \times 5$ | 0.11 | 20.6 | 214 | 3.33 | |
| | Parallel | $3\sqrt{3} \times 4$ | 0.14 | 20.7 | 215 | 3.33 | |
| | Parallel | $3\sqrt{3} \times 3$ | 0.18 | 21.1 | 219 | 3.33 | |
| | O down | $3\sqrt{3} \times 3$ | 0.18 | 14.6 | 151 | 3.20 | |
| | O up | $3\sqrt{3} \times 3$ | 0.18 | 15.5 | 160 | 4.87 | |
| | Parallel | $1\sqrt{3} \times 2$ | 0.83 | 30.5 | 316 | 3.55 | |
| Three cluster | Parallel | $3\sqrt{3} \times 3$ | 0.55 | 30.4 | 315 | 3.31–3.54 | |
| Five cluster | Parallel | $3\sqrt{3} \times 3$ | 0.92 | 34.9 | 361 | 3.35–4.50 | |
| Theory, DFT-D and MP2-based (Pankewitz and Klopper) ^a | | | | | | | |
| Single molecule, DFT-D with BP86 | Parallel | Benzene | | 14.8 | | 3.35 | |
| Single molecule, DFT-D with BP86 | Parallel | Coronene | | 18.7 | | 3.32 | |
| Single molecule, DFT-D with BP86 | Parallel | 112-C PAH | | 20.0 | | 3.32 | |
| Single molecule, DFT-D with BP86 ^b | O up | Coronene | | ~11 | | ~4.8 | |
| Single molecule, SCS-MP2 with PB86 | Parallel | Benzene | | 13.8 | | ~3.4 | |
| Single molecule, SCS-MP2 with PB86 | Parallel | Coronene | | 18.3 | | ~3.3 | |

^aOrbital-based calculations with a TZVP basis, [7].

^bEnergy estimated from Figure 8 of [7].

3. Results and Discussion

In Table 1, we list the adsorption energies E_a for the various methanol-graphene systems that we consider. Also shown for each calculation is the coverage of methanol on graphene in units of molecular monolayers (ML), derived from the estimated area per molecule 17.6 \AA^2 at 1 ML obtained by Morishige et al. [24] from X-ray diffraction studies of a methanol film on graphene.

In the $3\sqrt{3}a_g \times 3a_g$ unit cell, we test starting the calculations with methanol oriented such that the C–O axis is either parallel or perpendicular to graphene (with the O atom pointing away from or towards graphene). As evident from Table 1, the almost-parallel orientation, after relaxation of the atomic positions, is energetically more favorable than the two perpendicular orientations (“O up” and “O down”). While the parallel orientation gives rise to a 219 meV (21.1 kJ/mol) binding, the perpendicular orientations only bind with 160 and 151 meV (15.5 and 14.6 kJ/mol). For the remaining calculations, we therefore start methanol oriented parallel to graphene (We did check starting with the “O down” orientation in the small $1\sqrt{3}a_g \times 2a_g$ unit cell, but after full relaxation of the atomic positions methanol ended up with an orientation parallel to graphene).

Ignoring the E_a of the two perpendicular orientations (“O up” and “O down”) we see that E_a grows with increasing coverage, from 214 meV at 0.11 ML to 361 meV at 0.92 ML, the exception being the single molecule in the $1\sqrt{3}a_g \times 2a_g$ unit cell. We also find that the methanol-graphene distance,

here measured as the distance to O in methanol, d_o , slightly increases with coverage, although the trend is not clear for the cluster calculations.

As seen by the growth in E_a with coverage, the methanol molecules interact attractively, across unit cell boundaries (due to periodic boundary conditions) and for the cluster calculations also within the unit cell. The nearest-neighbor adsorbate-adsorbate distance in our single-molecule calculations varies from 12.4 \AA in the largest unit cell to 4.3 \AA in the smallest unit cell. In the cluster calculations, the O-to-O nearest-neighbor separation is 3.0 \AA in the three-adsorbate cluster (one such interaction per unit cell) and 2.9 \AA in the five-adsorbate cluster (two such nearest neighbors per unit cell).

It should be noted that the cluster calculations are started with methanol distributed at “reasonable” intermolecular separations, of 3–5 Å O–O separation for the closest molecules, not specifically in any expected cluster-configuration, and the relative orientations are not optimized for the orientations at for, example, a full ML [24].

It is possible to partition the adsorption energy into the contributions from the substrate-adsorbate interaction and the adsorbate-adsorbate interaction. The adsorbate-adsorbate interaction energy is found from the total energy of the system with the graphene substrate removed, all other atom positions unchanged, and subtracting the total energy of an isolated molecule (times three or five for the clusters).

For the $3\sqrt{3}a_g \times 4a_g$ unit cell this attractive interaction across cell boundaries amounts to a mere 2 meV per

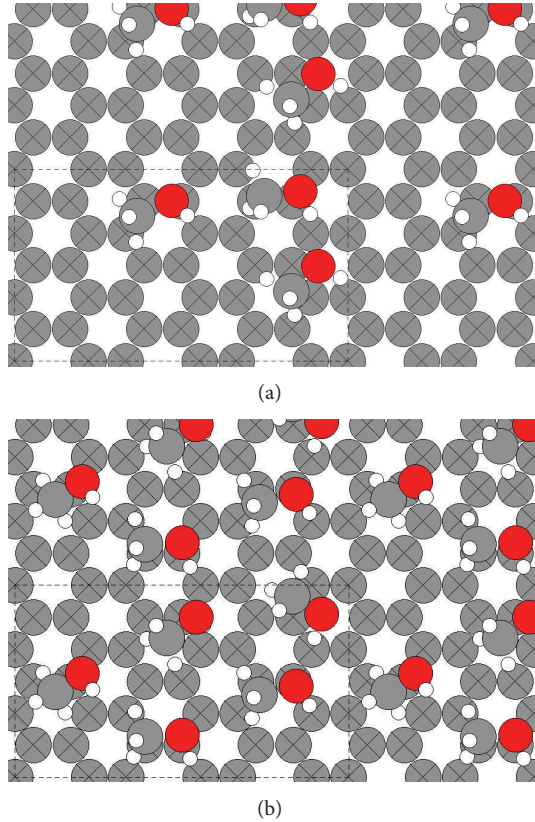


FIGURE 2: Three- and five-molecule clusters in the $3\sqrt{3}a_g \times 3a_g \times 19 \text{ \AA}$ unit cell.

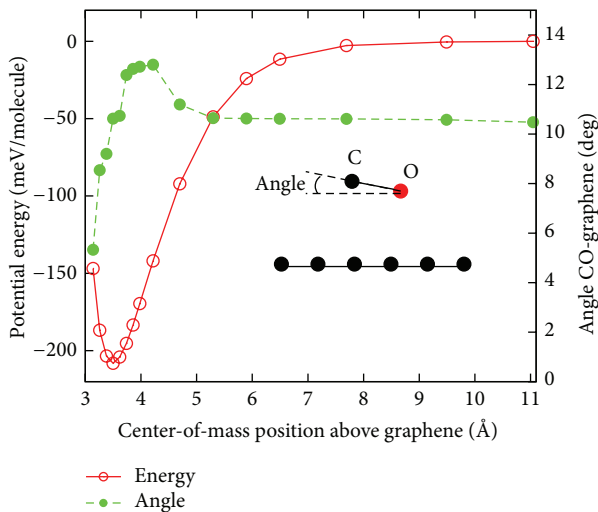


FIGURE 3: Potential energy of a single molecules of methanol on graphene at various distances from graphene (open circles, left graph axis). In each calculated point of the curve the atoms of the methanol molecule are allowed to relax according to the forces on the atoms, with the constraint that the center-of-mass position is fixed. The angle that the C-O axis makes with the graphene plane is shown in the curve with solid circles (right graph axis). The insert defines the angle.

molecule (0.2 kJ/mol), it increases to 7 meV (0.7 kJ/mol) for the $3\sqrt{3}a_g \times 3a_g$ unit cell, and to 125 meV (12.1 kJ/mol) for the much more dense phase in the $1\sqrt{3}a_g \times 2a_g$ unit cell. For the three-cluster system the sum of adsorbate-adsorbate interactions per unit cell is 366 meV, thus, in average 122 meV per molecule (11.8 kJ/mol). However, as noted above and seen also in the top panel of Figure 2, one pair of molecules per unit cell is closer together than the other pair interactions, and this pair interaction is, thus, expected to dominate the sum of interaction energies. This explains why the three-cluster system yields an adsorbate-adsorbate energy at only 0.55 ML that is almost the same as the evenly distributed molecules in the $1\sqrt{3}a_g \times 2a_g$ unit cell at 0.83 ML.

In the five-cluster calculations, the adsorbates are in reality almost uniformly distributed within the unit cell and can hardly be considered a “cluster”. The coverage is close to a full ML and all molecules are relatively close to each other, although two O-O separations stand out as being smaller. We find the sum of adsorbate-adsorbate interactions per unit cell 909 meV, which yields an average 182 meV per adsorbate (17.5 kJ/mol), which is the largest adsorbate-adsorbate interaction energy of this study.

Thus, the methanol-methanol interactions are important as they contribute to a large fraction of the adsorption energy, but the methanol-graphene interaction is stronger. As discussed for example, in [3] this facilitates the formation of a full methanol monolayer prior to forming multilayers because the energy gain for the methanol molecule is larger when binding to graphene than to other methanol molecules.

In Figure 3, the potential-energy curve of various graphene-methanol separations is shown. In this figure, each data point (circle) is found by keeping the center of mass of methanol relative to the plane of graphene at the distance d_{cm} , shown on the bottom axis of the figure. The atoms of the molecule are allowed to move in all directions, as long as d_{cm} remains unchanged. Thus, the orientation of the C-O axis changes with distance from graphene, as shown by the filled circles of Figure 3. When methanol is squeezed close to graphene ($d_{\text{cm}} \approx 3.2 \text{ \AA}$) the angle is smallest (the orientation is closest to being parallel), as a way for methanol to “avoid” a too close contact to graphene of any of its atoms. At the adsorption distance, the angle is approximately 10.6° . As the fragments are further separated, the angle grows a bit until the distance $d_{\text{cm}} \approx 5 \text{ \AA}$, where the vdW interaction is too weak to change the angle from the initial angle 10.6° (each calculation is started with methanol in the adsorption configuration, translated towards or away from graphene).

Pankowitz and Klopper [7] carried out nonperiodic DFT-D calculations of methanol adsorbed on SWCNTs and PAH-models of graphene of size from benzene up to a PAH with 112 C atoms. Although the DFT-D calculations are semiempirical and, thus, can be less accurate (depending on the choice of empirical parameters for each type of calculation) the adsorption energies on PAH (Table 1) agree reasonably with the present results, when the smaller substrate size in the DFT-D calculations (due to lack of periodicity) is taken into account [18, 27]. For adsorption on to benzene and the PAH coronene (24 C) they also carried out spin-component-scaled

MP2 (SCS-MP2). Their SCS-MP2 result for methanol on coronene is in good agreement with the present results. From the DFT-D calculations, we can estimate that approximately 1.3 kJ/mol of the methanol-substrate interaction is missing on coronene compared to graphene or a rather large (112-C) PAH molecule. Their SCS-MP2 coronene result of 18.3 kJ/mol should, therefore, probably be corrected to ~ 19.6 kJ/mol for a single methanol molecule adsorption on graphene. For our largest unit cell, we find 20.6 kJ/mol and less than a 0.1 kJ/mol correction for the periodicity. Thus, our calculated energy for single methanol molecule adsorption deviates less than 1 kJ/mol (or 5%) from the estimate of the size-modified SCS-MP2 results. The distance of methanol O from graphene, d_{O} , turns out identical in the two calculations.

Interestingly, in the DFT-D calculations Pankewitz and Klopper find a second, much weaker, local minimum with the methanol O atom pointing away from coronene, much like our “O-up” configuration. For this configuration, the energies and substrate-to-O distances are very similar, with 15.1 kJ/mol at 4.83 Å in the vdW-DF calculations and approximately 11 kJ/mol at 4.8 Å in the DFT-D calculations. In the binding energy curve of Figure 3, we do see a change in methanol angle with graphene as the distance is varied, but at the 4.5–5 Å center-of-mass distance from graphene the interactions are probably too weak for the computational relaxation procedure to rotate the initially almost-parallel molecule to obtain the O-up structure.

Although we did no effort in fitting a full monolayer of methanol on to graphene, it is still of interest to compare our high-coverage results with other calculations of closely packed methanol molecules. S. L. Boyd and R. J. Boyd [28] used DFT with B3LYP at various basis set levels to calculate the binding energies and structures of (free-floating) methanol clusters of up to 14 molecules. They expect the intermolecular interaction to be dominated by the hydrogen bonds, for which B3LYP behaves reasonably. They find that the binding energy in the optimal clusters to be 27 kJ/mol, which is larger than our largest molecule-molecule energy 17.5 kJ/mol (for the 5-molecule cluster), but then, in our calculations, there is still room for more molecules, and the molecules are constrained by the adsorption to graphene to form interactions only in two dimensions. Our smallest O-O distance of 2.9 Å (in the five-molecule cluster) compares well with the optimal O-O distance 2.77 Å in the trimer calculations of [28].

A number of experiments of methanol desorption from HOPG or SWCNTs have previously been carried out [3, 9, 10]. Although the desorption energies vary between the experiments, the energies for 1 ML coverage or less all fall in the range 28–51 kJ/mol (48 ± 3 kJ/mol at 1 ML [10], 33–48 kJ/mol at <1 ML [3], 28 kJ/mol at <1 ML [9]), with a tendency to increase with increasing coverage. The desorption energy range is in reasonable agreement with our results, that are in the range 20–35 kJ/mol (absent the less favorable methanol orientations), with increasing adsorption energy for increasing coverage (Table 1). None of the mentioned experiments measure the distance of methanol from the substrate nor the orientation of methanol. Further comparison to experiments

that are presently in progress will appear in a forthcoming publication [29].

4. Conclusions

By use of the first-principles vdW-DF method, we calculate adsorption energies and determine adsorption geometries of methanol on graphene. Our results are in reasonable agreement with other available calculations and experiments. This suggests that the data obtained here may be used as input parameters or tests of results from calculations and models that (unlike DFT) rely on external information, either from experiment or from (preferentially) first-principles calculations. This could, for example, be models that are on larger length scales or with time dependency, such as molecular dynamics calculations.

Acknowledgments

The author thanks Nikola Markovic, Chalmers, and Jan B. C. Pettersson, Göteborg University, for introduction to this problem and for discussions. The work was partially funded by the Swedish Research Council (VR) and the Chalmers Areas of Advances Nano and Materials. The computations were performed on resources provided by the Swedish National Infrastructure for Computing (SNIC) at C3SE.

References

- [1] X. Kong, P. U. Andersson, E. S. Thomson, and J. B. C. Pettersson, “Ice formation via deposition mode nucleation on bare and alcohol-covered graphite surfaces,” *Journal of Physical Chemistry C*, vol. 116, no. 16, pp. 8964–8974, 2012.
- [2] E. S. Thomson, X. Kong, P. U. Andersson, N. Markovic, and J. B. C. Pettersson, “Collision dynamics and solvation of water molecules in a liquid methanol film,” *The Journal of Physical Chemistry Letters*, vol. 2, no. 17, pp. 2174–2178, 2011.
- [3] A. S. Bolina, A. J. Wolff, and W. A. Brown, “Reflection absorption infrared spectroscopy and temperature programmed desorption investigations of the interaction of methanol with a graphite surface,” *Journal of Chemical Physics*, vol. 122, no. 4, Article ID 044713, 12 pages, 2005.
- [4] A. J. Wolff, C. Carlstedt, and W. A. Brown, “Studies of binary layered $\text{CH}_3\text{OH}/\text{H}_2\text{O}$ ices adsorbed on a graphite surface,” *The Journal of Physical Chemistry C*, vol. 111, no. 16, pp. 5990–5999, 2007.
- [5] M. Dion, H. Rydberg, E. Schröder, D. C. Langreth, and B. I. Lundqvist, “Van der waals density functional for general geometries,” *Physical Review Letters*, vol. 92, no. 24, Article ID 246401, 4 pages, 2004, Erratum in *Physical Review Letters*, vol. 95, Article ID 109902, 1 page, 2005.
- [6] T. Thonhauser, V. R. Cooper, S. Li, A. Puzder, P. Hyldgaard, and D. C. Langreth, “Van der Waals density functional: self-consistent potential and the nature of the van der Waals bond,” *Physical Review B*, vol. 76, no. 12, Article ID 125112, 2007.
- [7] T. Pankewitz and W. Klopper, “Ab initio modeling of methanol interaction with single-walled carbon nanotubes,” *Journal of Physical Chemistry C*, vol. 111, no. 51, pp. 18917–18926, 2007.
- [8] S. Grimme, “Accurate description of van der Waals complexes by density functional theory including empirical corrections,”

- Journal of Computational Chemistry*, vol. 25, no. 12, pp. 1463–1473, 2004.
- [9] H. Ulbricht, R. Zacharia, N. Cindir, and T. Hertel, “Thermal desorption of gases and solvents from graphite and carbon nanotube surfaces,” *Carbon*, vol. 44, no. 14, pp. 2931–2942, 2006.
- [10] U. Burghaus, D. Bye, K. Cosert et al., “Methanol adsorption in carbon nanotubes,” *Chemical Physics Letters*, vol. 442, no. 4–6, pp. 344–347, 2007.
- [11] Ø. Borck and E. Schröder, “First-principles study of the adsorption of methanol at the α -Al₂O₃(0001) surface,” *Journal of Physics: Condensed Matter*, vol. 18, no. 1, article 1, 2006.
- [12] Ø. Borck and E. Schröder, “Adsorption of methanol and methoxy on the α -Cr₂O₃(0001) surface,” *Journal of Physics: Condensed Matter*, vol. 18, no. 48, article 10751, 2006.
- [13] E. Londero, E. K. Karlson, M. Landahl, D. Ostrovskii, J. D. Rydberg, and E. Schröder, “Desorption of n-alkanes from graphene: a van der Waals density functional study,” *Journal of Physics: Condensed Matter*, vol. 24, no. 42, Article ID 424212, 2012.
- [14] S. D. Chakarova-Käck, Ø. Borck, E. Schröder, and B. I. Lundqvist, “Adsorption of phenol on graphite(0001) and α -Al₂O₃(0001): nature of van der Waals bonds from first-principles calculations,” *Physical Review B*, vol. 74, no. 15, Article ID 155402, 7 pages, 2006.
- [15] S. D. Chakarova-Käck, E. Schröder, B. I. Lundqvist, and D. C. Langreth, “Application of van der Waals density functional to an extended system: adsorption of benzene and naphthalene on graphite,” *Physical Review Letters*, vol. 96, no. 14, Article ID 146107, 4 pages, 2006.
- [16] S. D. Chakarova-Käck, A. Vojvodic, J. Kleis, P. Hyldgaard, and E. Schröder, “Binding of polycyclic aromatic hydrocarbons and graphene dimers in density functional theory,” *New Journal of Physics*, vol. 12, Article ID 013017, 2010.
- [17] J. Åkesson, O. Sundborg, O. Wahlström, and E. Schröder, “A van der Waals density functional study of chloroform and other trihalomethanes on graphene,” *Journal of Chemical Physics*, vol. 137, no. 17, Article ID 174702, 9 pages, 2012.
- [18] K. Berland, S. D. Chakarova-Käck, V. R. Cooper, D. C. Langreth, and E. Schröder, “A van der Waals density functional study of adenine on graphene: single-molecular adsorption and overlayer binding,” *Journal of Physics: Condensed Matter*, vol. 23, no. 13, Article ID 135001, 2011.
- [19] D. Le, A. Kara, E. Schröder, P. Hyldgaard, and T. S. Rahman, “Physisorption of nucleobases on graphene: a comparative van der Waals study,” *Journal of Physics: Condensed Matter*, vol. 24, no. 42, Article ID 424210, 2012.
- [20] Open-source, “grid-based PAW-method DFT code GPAW,” <https://wiki.fysik.dtu.dk/gpaw/>.
- [21] J. J. Mortensen, L. B. Hansen, and K. W. Jacobsen, “Real-space grid implementation of the projector augmented wave method,” *Physical Review B*, vol. 71, no. 3, Article ID 035109, 11 pages, 2005.
- [22] G. Román-Pérez and J. M. Soler, “Efficient implementation of a van der Waals density functional: application to double-wall carbon nanotubes,” *Physical Review Letters*, vol. 103, no. 9, Article ID 096102, 4 pages, 2009.
- [23] “Python-based atomic simulation environment,” <https://wiki.fysik.dtu.dk/ase/>.
- [24] K. Morishige, K. Kawamura, and A. Kose, “X-ray diffraction study of the structure of a monolayer methanol film adsorbed on graphite,” *The Journal of Chemical Physics*, vol. 93, no. 7, pp. 5267–5270, 1990.
- [25] E. Ziambaras, J. Kleis, E. Schröder, and P. Hyldgaard, “Potassium intercalation in graphite: a van der Waals density-functional study,” *Physical Review B*, vol. 76, Article ID 155425, 15 pages, 2007.
- [26] E. Bitzek, P. Koskinen, F. Gahler, M. Moseler, and P. Gumbsch, “Structural relaxation made simple,” *Physical Review Letters*, vol. 97, no. 17, Article ID 170201, 4 pages, 2006.
- [27] A. Quandt and I. Boustani, “Boron nanotubes,” *ChemPhys-Chem*, vol. 6, no. 10, pp. 2001–2008, 2005.
- [28] S. L. Boyd and R. J. Boyd, “A density functional study of methanol clusters,” *Journal of Chemical Theory and Computation*, vol. 3, no. 1, pp. 54–61, 2007.
- [29] J. B. C. Pettersson et al., unpublished.

Research Article

Energy Dissipation and the High-Strain Rate Dynamic Response of Vertically Aligned Carbon Nanotube Ensembles Grown on Silicon Wafer Substrate

P. Raju Mantena,¹ Tezeswi Tadepalli,¹ Brahmananda Pramanik,¹ Veera M. Boddu,² Matthew W. Brenner,² L. David Stephenson,² and Ashok Kumar²

¹ Composite Structures and Nano-Engineering Research, Department of Mechanical Engineering, University of Mississippi, University, MS 38677, USA

² U.S. Army Engineer Research and Development Center—Construction Engineering Research Laboratory (ERDC-CERL), Champaign, IL 61821, USA

Correspondence should be addressed to P. Raju Mantena; meprm@olemiss.edu

Received 14 March 2013; Revised 3 August 2013; Accepted 12 August 2013

Academic Editor: Teng Li

Copyright © 2013 P. Raju Mantena et al. This is an open access article distributed under the Creative Commons Attribution License, which permits unrestricted use, distribution, and reproduction in any medium, provided the original work is properly cited.

The dynamic mechanical behavior and high-strain rate response characteristics of a functionally graded material (FGM) system consisting of vertically aligned carbon nanotube ensembles grown on silicon wafer substrate (VACNT-Si) are presented. Flexural rigidity (storage modulus) and loss factor (damping) were measured with a dynamic mechanical analyzer in an oscillatory three-point bending mode. It was found that the functionally graded VACNT-Si exhibited significantly higher damping without sacrificing flexural rigidity. A Split-Hopkinson pressure bar (SHPB) was used for determining the system response under high-strain rate compressive loading. Combination of a soft and flexible VACNT forest layer over the hard silicon substrate presented novel challenges for SHPB testing. It was observed that VACNT-Si specimens showed a large increase in the specific energy absorption over a pure Si wafer.

1. Introduction

Functionally graded materials (FGMs) are a new generation of engineered materials wherein the microstructural details are spatially varied through nonuniform distribution of the reinforcement phase(s). These FGMs are being investigated for applications in blast, ballistic protection of building structures and other armor applications. A fundamental knowledge and understanding of the dynamic behavior of vertically aligned carbon nanotubes (VACNTs) with functionally graded stiffness modulus is needed to understand the energy transfer mechanisms and their dependence on the microstructures of carbon nanotube (CNT) ensembles. This information is expected to lead to novel, strong, lightweight, and robust composites for enhanced protection.

An in-depth study of the dynamic behavior of FGMs is accomplished by using reinforcements with different

properties, sizes, and shapes, as well as by interchanging the roles of the reinforcement and matrix phases in a continuous manner. The result is a microstructure that produces continuously or discretely changing thermal and mechanical properties at the macroscopic or continuum scale. Thus FGMs are designed for optimal performance when functional requirements vary with location. This concept of engineering the material's microstructure allows designers to fully integrate the material and structural considerations into the final design of structural components.

The concepts of FGMs have also been extended to functionally graded ceramic-metal hybrids (ceramets), cementitious materials, and piezoelectric materials as well. Functionally graded materials are ideal candidates for applications involving severe thermal gradients, ranging from thermal structures in advanced aircraft and aerospace engines to computer circuit boards. High flexural rigidity with high

vibration damping is a desirable property for aerospace and automotive applications to ensure a large load-bearing capacity and increased fatigue life.

Nanometer-scale structures such as carbon nanotubes (CNTs) and nanowires with exceptional thermal, electronic, and mechanical properties are undergoing intense experimental and theoretical investigations for a large range of possible applications. With the ready availability of free-standing VACNTs, integrating high flexural rigidity and damping into structures is feasible. Increasing the energy dissipation characteristics by introducing stiffness gradients through topological defects and entanglements of the CNTs will also be beneficial in designing shock and impact resistant light-weight protection systems. In this paper, the dynamic mechanical behavior and high-strain rate dynamic response characteristics of a functionally graded material system consisting of vertically aligned carbon nanotubes grown on a silicon wafer substrate (VACNT-Si) are presented.

2. Materials and Methods

2.1. VACNT-Si Specimen Preparation. A well-established chemical vapor deposition approach is used for the synthesis of the VACNTs on silicon wafers [1–4]. The carbon source, anhydrous m-xylene (purity $\geq 99\%$), and the catalyst, ferrocene (purity: 98%) were obtained from Sigma Aldrich, St. Louis, MO, USA. Ultra-high-purity nitrogen gas and ultra-high-purity 99.999% hydrogen were supplied by S.J. Smith Welding Supply, Urbana, IL, USA. Silicon wafers, 100 mm (3.94 inches) diameter type P boron doped, were purchased from Wafer World Inc., Palm Beach County, FL, USA. The silicon wafers were surface cleaned and etched with nitric acid (Fisher Scientific, Gardena, CA, USA) and hydrofluoric acid (Mallinckrodt Chemicals, Phillipsburg, NJ, USA). Reagent grade deionized water (Thermo Scientific, Middleton, VA, USA) was used for dilutions and rinsing and during silicon wafer dicing. Silicon wafers 6 mm (0.24 inches) \times 55 mm (2.17 inches) are prepared by first coating the wafer in photoresist to protect it from the dicing process. Then using a diamond saw, the wafers are diced into required sample sizes. To remove the photoresist, the samples are sonicated in acetone for 2 minutes and then transferred into a new acetone bath where they are sonicated for an additional 2 minutes.

The samples are cleaned by sonicating them in nitric acid for 2 minutes and then in deionized water for 2 minutes. Surface etching is done by agitating the samples in 51% hydrofluoric acid for 60 s. Immediately the sample is extracted and rinsed in deionized water for 2 minutes, and then rinsed in another bath of deionized water for 2 minutes. The samples are dried using forced air. The preparation of the catalytic solution involves dissolving ferrocene in the m-xylene solvent. The mixture is agitated and then finally sonicated to fully dissolve the ferrocene powder. The concentration of ferrocene is 5% by weight.

The cleaned and etched Si substrate is then placed in a quartz tube (2" diameter, 38" long). The tube is tilted at a 2° angle to facilitate CNT growth on the Si surface and prevent clogging at the injection point. A bundle of glass wool is also inserted in the inlet portion of the tube to

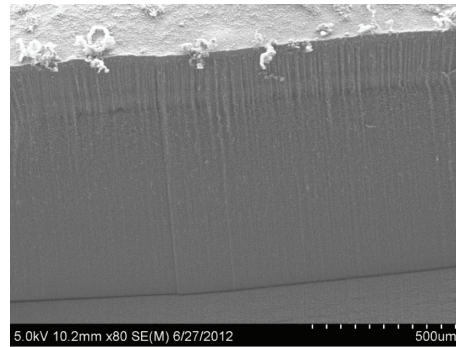


FIGURE 1: Scanning electron micrograph of vertically aligned carbon nanotubes (VACNTs) grown on a silicon wafer using the chemical vapor deposition approach.

create a more uniform flow profile. The tube is flushed with a 2500 mL/min flow of nitrogen to remove oxygen. Under the flow of nitrogen, the tube is heated in a programmable tubular furnace (GSL-1500x, MTI, Richmond, VA, USA) from room temperature to 300°C in 30 min and then brought from 300 to the process temperature 820°C. During this time, a heating tape is wrapped around the inlet portion of the quartz tube to preheat the gases and vaporize the carbon source and ferrocene solution and allowed to reach about 350°C.

Once the processing temperature is reached, the temperature is fixed within 1°C and the furnace is held for a minimum of 15 minutes at the process temperature before CNT growth is initiated to ensure that the sample has been properly heated. The hydrogen gas is then turned on and tuned to a flow rate of 200 mL/min and allowed to stabilize for approximately 5 minutes. The solution of m-xylene and ferrocene is then injected at a constant flow rate of ~ 16 mL/hr which continues for 60 min. After this period of processing, the flow of solution is terminated, the furnace heating power is shut off, the hydrogen gas is shut off, and the inlet heating power is turned off. Nitrogen is still flowed through the tube to aid in cooling and preventing oxygen and other contaminants from entering the tube. Once the tube has reached room temperature, the nitrogen flow is shut off and the CNT coated Si sample is removed for measurement. A typical scanning electron micrograph (SEM) of the synthesized VACNTs is shown in Figure 1.

2.2. Dynamic Mechanical Analysis. The dynamic mechanical properties [5, 6] of pure Si wafer and VACNT-Si were analyzed with a TA Instruments Model Q800 DMA. The pure silicon wafer rectangular beam specimen was 6 mm (0.24 inches) in width, 0.4 mm (0.016 inches) in thickness and 55 mm (2.17 inches) in length. VACNT forest was grown on one side of the pure silicon wafer beam to a height of about 0.5 mm (0.02 inches) (Figures 2(a) and 2(b) inset). A three-point oscillatory bending mode was utilized for evaluating the dynamic modulus and loss factor (damping) of both the pure Si wafer and the VACNT-Si specimens.

The specimens were simply supported at the ends on two roller pins (Figure 2(a)) with a span of 50 mm (1.97 inches) and loaded from top with a fixed roller pin positioned at

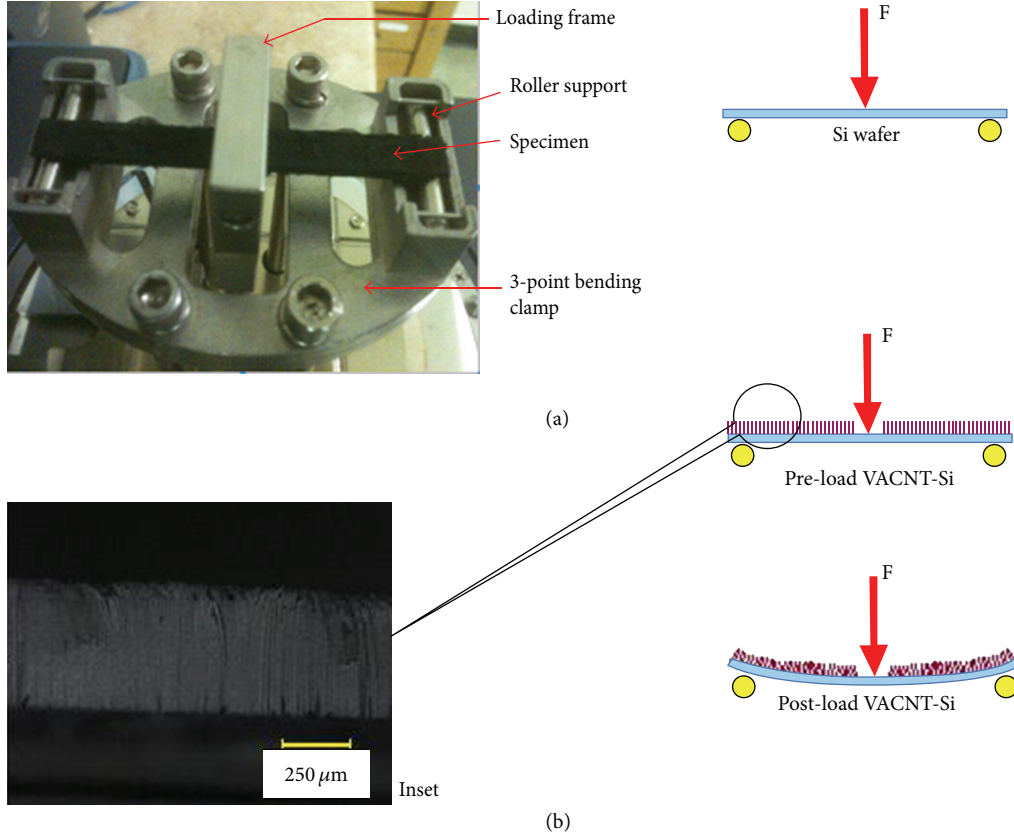


FIGURE 2: Experimental setup for DMA testing; (a) sample in three-point bending at a prespecified $10\ \mu\text{m}$ amplitude and 1 Hz oscillation frequency, and (b) energy dissipation caused by the entanglement of VACNTs on silicon wafer substrate during cyclic flexural deformation (inset: digital microscope image of VACNTs on silicon wafer substrate).

midspan of the beam. VACNT forest was carefully scraped off the specimen-roller contact areas, to avoid localized flexure of VACNTs under the line of centric loading and also over the two end lines of support (Figure 2(b)). All specimens were subjected to a temperature ramp from ambient (30°C) to 120°C , at a constant heating rate of $2^\circ\text{C}\cdot\text{min}^{-1}$ during the DMA testing. Raw data obtained from DMA experiments include the required amount of force (F) and corresponding sample response-delay in phase angle (δ) for a prespecified $10\ \mu\text{m}$ amplitude at 1 Hz oscillation frequency. The dynamic mechanical parameters, such as storage modulus (E'), loss modulus (E''), and $\tan \delta$ (damping loss factor, ratio of E'' to E'), are estimated in data analysis.

The DMA stiffness model for a rectangular cross-section specimen under three-point bending load condition is given by [7]

$$\begin{aligned}
 E &= K \cdot G, \\
 K &= \frac{F}{d}, \\
 G &= \left(\frac{L^3}{6I} \right) \left[1 + \frac{6}{10} (1 + \nu) \left(\frac{t}{L} \right)^2 \right], \\
 E' &= E \cos \delta,
 \end{aligned} \tag{1}$$

where E = elastic modulus, K = estimated stiffness, G = geometry factor, F = measured force, d = prespecified amplitude, L = length (half span), $I = bt^3/12$ (area moment of inertia of beam cross-section), b = beam width, t = thickness, and ν = specimen Poisson's ratio.

Whereas the required force (F) and phase angle (δ) are true indicators of the test sample's flexural rigidity and damping the estimated storage modulus, however, is influenced by the data input for specimen thickness and Poisson's ratio. The pure silicon wafer, being anisotropic, has two different Poisson ratios, and there are no data available for the VACNTs. As such, a reported [8] in-plane Poisson's ratio of $\nu_{xy} = 0.064$ for silicon has been used for both pure Si wafer and the VACNT-Si DMA test specimens. Regarding sample thickness, since the VACNT forest was scraped off the area where cyclic loading was applied, the effectual pure Si wafer thickness of $0.4\ \text{mm}$ (0.016 inches) was also used as input data for the VACNT-Si specimen thickness. The ensuing "apparent" storage modulus from such approximations is provided later in the results section along with the required force (F) and phase angle (δ), which are more accurate indicators of the test sample's flexural rigidity and damping.

2.3. High-Strain Rate Testing. The high-strain rate testing of pure Si wafer and VACNT-Si was conducted using

a split-Hopkinson pressure bar (SHPB, also known as Kolsky Bar). It is capable of testing materials at high compressive strain rates typically ranging from 10^2 to 10^4 per second depending on the bar length and requirements of stress equilibrium and constant strain rate. The simplifying assumptions in the theory of SHPB are [9]

- (a) bars are elastic,
- (b) one-dimensional planar wave in the bars,
- (c) uniaxial stress state in the specimen, and
- (d) uniform state of stress in specimen, that is, negligible wave propagation effects.

The dynamic stress-strain, strain rate, and energy absorption can be obtained from the incident, reflected, and transmitted strain pulses. Based on force equilibrium considerations, the specimen strain (ε_s) is computed from the reflected (ε_r) and transmitted (ε_t) pulses in

$$\varepsilon_s = \frac{C_0}{L} \int_0^t (\varepsilon_t - \varepsilon_r - \varepsilon_r - \varepsilon_t) dt, \quad (2a)$$

$$\dot{\varepsilon}_s = \frac{-2C_0}{L} \int_0^t \varepsilon_r dt, \quad (2b)$$

where C_0 is the wave velocity in the Hopkinson bars and L is the specimen length.

For a specimen of cross-sectional area A_s , the stress and the strain rate in the specimen are given by the following, respectively:

$$\sigma_s = E \frac{A}{A_s} \varepsilon_t = K_1 \varepsilon_t, \quad (3)$$

$$\dot{\varepsilon}_s = \frac{-2C_0}{L} \varepsilon_r = K_2 \varepsilon_r, \quad (4)$$

where, E and A are Young's modulus and cross-sectional area of the Hopkinson bars, K_1 and K_2 are the stress and the strain rate multiplying factors for a given specimen and test setup. On superposition with the stress-versus-time data, the transient stress-strain response is obtained.

The energy absorbing capacity of the specimen is defined as the energy required for deforming a given specimen to a specific strain [10]. The absorption energy per unit volume up to ultimate failure strain ε_u can be evaluated by integrating the area under the stress-strain curve for each specimen as shown in the following

$$W = \int_0^{\varepsilon_u} \sigma_s d\varepsilon_s. \quad (5)$$

The diameter of our SHPB is 0.75 inches (19.05 mm), so the maximum size of a square sample that can fit is 0.5 inches (12.7 mm) on each side. In the current study layered specimens that are a combination of soft and flexible (VACNTs) and very hard (silicon) materials are investigated. The soft VACNT forest layer considered by itself requires the use of low impedance bars made of materials such as

aluminum or polycarbonate. However, due to the hard silicon wafer substrate, there is an increased possibility for the softer aluminum or polycarbonate bars to get scoured/dented, which necessitates the usage of harder maraging steel bars. There are no standards available in the literature for SHPB specimen design of this nature, and the challenge is to determine the optimal specimen dimensions by trial experiments.

Also the specimens need to be dimensioned such that the thickness-to-side ratio (aspect ratio) is optimized for a good response signal during SHPB testing. The aspect ratio of the specimen controls the strain rate as well. The range for aspect ratios is different for soft materials and hard materials [9, 11]. For soft materials, the range of thickness/diameter aspect ratio (for circular specimens) is between 0.25 and 0.5. In the case of metals it is between 0.5 and 1.0, and for ceramics it is between 1.0 and 2.0. There are other considerations as well that depend on the specimen dimensions such as stress equilibrium (thickness dependent), friction and radial inertia (diameter dependent).

The VACNT-Si specimens were placed with the Si substrate on the incident bar side and the VACNT coating facing the transmission bar side. Glycerin was applied as couplant between the Si substrate and the incident bar face. The transmission bar was carefully placed in contact with the VACNT forest layer surface without precompressing the forest layer. The tests were conducted at constant force (as determined by a reservoir pressure of 10 psi applied to the striker bar). Since this is a new material system, trials with various specimen sizes were evaluated. Specific results for square samples of approximate size 6 mm (0.24 inches) \times 6 mm (0.24 inches) \times 0.4 mm (0.016 inches) for the pure Si wafer and 6 mm (0.24 inches) \times 6 mm (0.24 inches) \times 0.93 mm (0.037 inches) for VACNT-Si are reported here. Three specimens each of pure Si wafer and VACNT-Si processed at 820°C were tested in compression and the results analyzed.

3. Results and Discussion

Three specimens each of pure Si wafer and VACNT-Si were tested in the DMA under three-point oscillatory flexural load over a temperature range from ambient (30°C) to 120°C. The flexural rigidity and damping of these specimens were investigated in terms of the required force (F , line force at midspan to achieve 10 μ m amplitude, Figures 3(a) and 3(b)), "apparent" storage modulus (E' , Figures 3(c) and 3(d)), and the damping loss factor ($\tan\delta$, ratio of dissipated energy to stored energy, Figures 3(e) and 3(f)). As can be observed, these values remain constant over the 120°C test temperature range, without a demonstrated peak of loss factor along with drop in storage modulus, which is more typical for viscoelastic materials around their glass transition temperature [5, 6].

Both the required force and "apparent" storage modulus show a negligible drop for the VACNT-Si specimens, but still within experimental scatter. This could perhaps be attributed to some degradation and/or chemical erosion of specimen surface during the growth of VACNTs at an elevated 820°C. On the other hand, damping loss factor ($\tan\delta$)

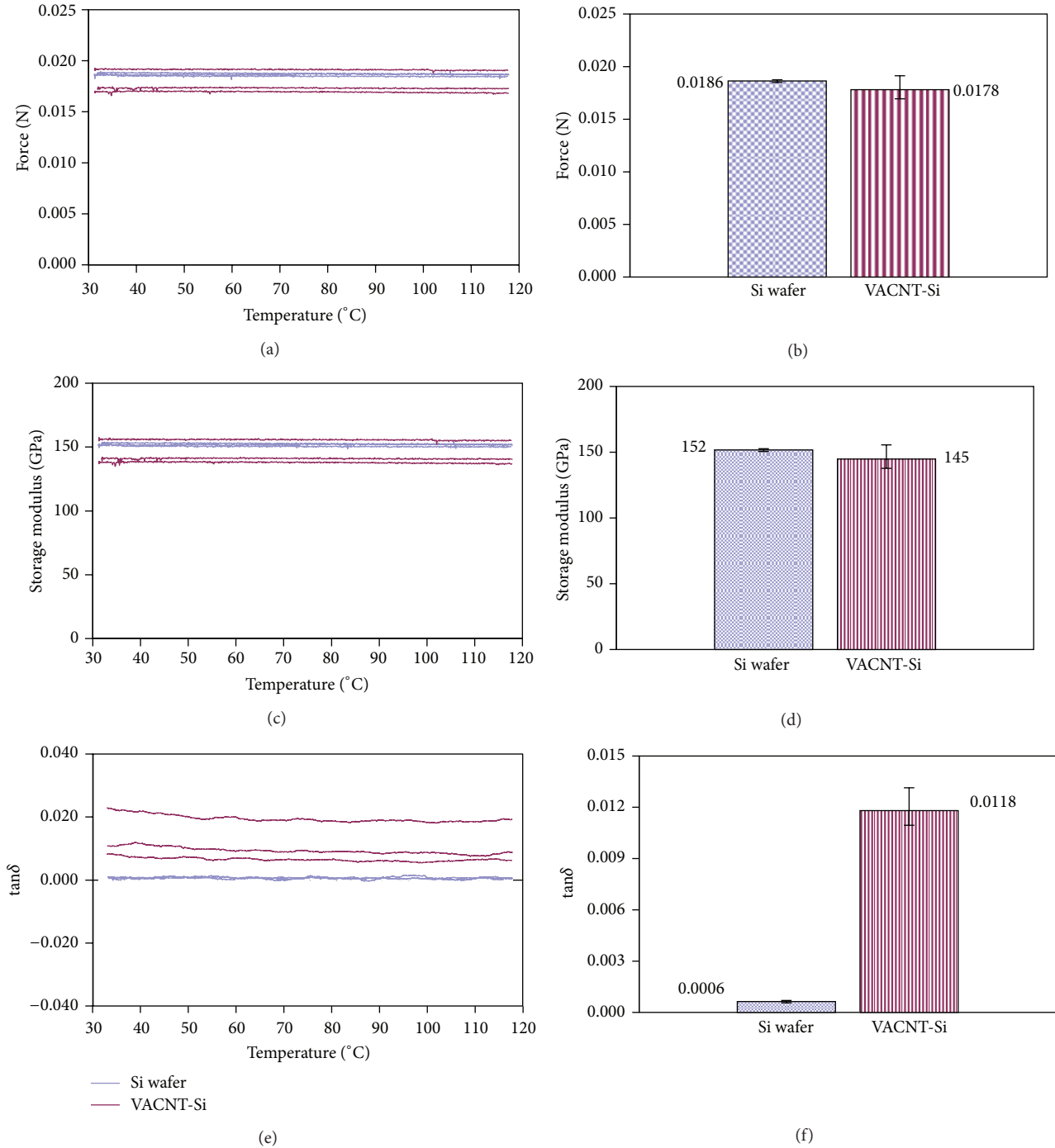


FIGURE 3: DMA results for three specimens each of pure Si wafer and VACNT-Si (processed at 820°C) analyzed over a temperature range from ambient (30°C) to 120°C; ((a) and (b)) the required line force F at midspan to achieve 10 μm amplitude; ((c) and (d)) the “apparent” storage modulus, E' ; and ((e) and (f)) associated damping loss factor, $\tan\delta$.

shows a remarkable increase of about 1800% for the samples with VACNTs grown on pure Si wafer (Figures 3(e) and 3(f)). Interfacial friction between individual VACNTs (with very large surface area to diameter), caused by their entanglements under cyclic deformation (Figure 2(b)), is believed to be the primary energy dissipation mechanism for such high improvement in loss factor.

As mentioned previously, the combination of the soft VACNT forest layer with the hard silicon wafer presented novel challenges for SHPB testing. The VACNT forest layer is typical of an open-cell foam structure consisting of well-arranged one-dimensional units [12]. Various energy absorption mechanisms such as localized higher mode buckling of VACNTs under static compressive loading and

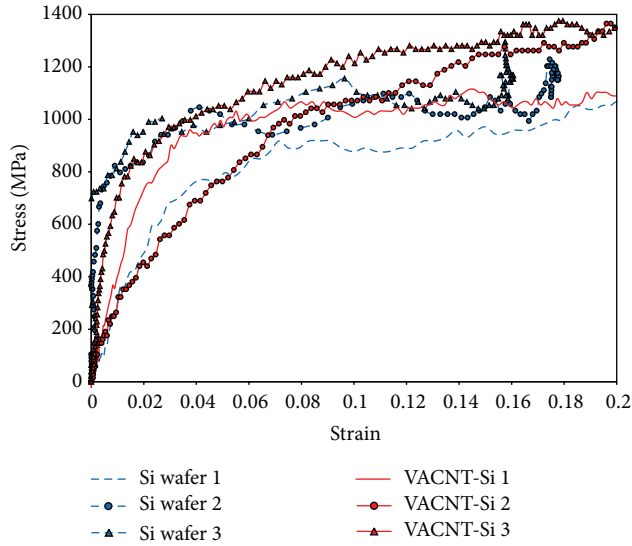


FIGURE 4: High strain rate response of pure Si wafer and VACNT-Si (processed at 820°C) over the strain rate range of 4600/s to 7500/s (shown only up to 0.2 strain).

nanoindeentation along with surface entanglement and van der Waals interactions with neighboring nanotubes have been reported in the literature [13, 14]. To the authors' knowledge, this type of layered material combination with such a contrast in properties has not been tested using SHPB for analyzing the high-strain rate dynamic response.

It was observed that the pure Si wafer specimens achieve a lower stress for a given strain, as compared to VACNT-Si specimens for average strain rates ranging from 4600/s to 7500/s (Figure 4). Since the nanoreinforced functionally graded material systems are being developed for light-weight structural applications, the specific energy absorption given by the ratio of energy absorbing capacity (5) to the mass density is reported in Figures 5 and 6.

An average increase of around 250% in specific energy absorption (Joules/Kg) was observed for VACNT-Si layered specimens in comparison with pure Si wafer specimens for the strain rates mentioned above (Figure 5). It was also observed that the VACNT-Si specimens achieved an average increase of around 450% in the rate of specific energy absorption (Joules/Kg/sec), when compared with pure Si wafer (Figure 6).

4. Conclusion

The dynamic mechanical behavior and high-strain rate dynamic response characteristics of a functionally graded material system consisting of vertically aligned carbon nanotube ensembles grown on a silicon wafer substrate (VACNT-Si) have been investigated. The functionally graded VACNT-Si exhibited significantly higher damping without sacrificing the flexural rigidity. Interfacial friction between individual VACNTs caused by their entanglements under cyclic deformation is believed to be the primary energy dissipation mechanism for such a large improvement in loss factor.

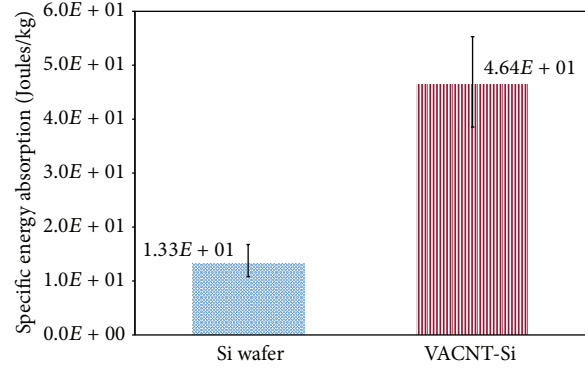


FIGURE 5: Specific energy absorption of pure Si wafer and VACNT-Si (processed at 820°C).

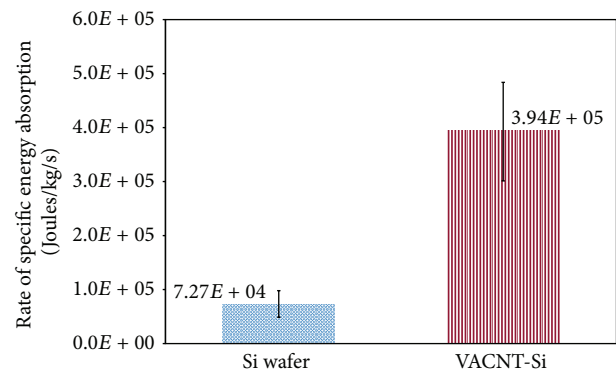


FIGURE 6: Rate of specific energy absorption for pure Si wafer and VACNT-Si (processed at 820°C).

In the case of high-strain rate compressive loading, a large increase in specific energy absorption as well as the rate of specific energy absorption was observed for VACNT-Si layered specimens as compared with pure Si wafer.

Acknowledgment

This research was funded by Grant no. W9132T-12-P0057 from the US Army Engineer Research and Development Center—Construction Engineering Research Laboratory (ERDC-CERL), Champaign, IL, USA. The authors would like to thank Mr. Damian Stoddard and Mr. Kiyun Kim, mechanical engineering graduate students at the University of Mississippi, for their help with the DMA and Hopkinson bar experiments.

References

- [1] C. M. Seah, S. P. Chai, and A. R. Mohamed, "Synthesis of aligned carbon nanotubes," *Carbon*, vol. 49, no. 14, pp. 4613–4635, 2011.
- [2] Y. J. Jung, B. Q. Wei, R. Vajtai et al., "Mechanism of selective growth of carbon nanotubes on SiO₂/Si patterns," *Nano Letters*, vol. 3, no. 4, pp. 561–564, 2003.
- [3] C. Daraio, V. F. Nesterenko, and S. Jin, "Highly nonlinear contact interaction and dynamic energy dissipation by forest of

- carbon nanotubes,” *Applied Physics Letters*, vol. 85, no. 23, pp. 5724–5726, 2004.
- [4] S. Handuja, S. P. Singh, P. Srivastava, and V. D. Vankar, “Growth of long aligned carbon nanotubes on amorphous hydrogenated silicon nitride by thermal chemical vapor deposition,” *Materials Letters*, vol. 63, no. 15, pp. 1249–1251, 2009.
- [5] Y. Zeng, L. Ci, B. J. Carey, R. Vajtai, and P. M. Ajayan, “Design and reinforcement: vertically aligned carbon nanotube-based sandwich composites,” *ACS Nano*, vol. 4, no. 11, pp. 6798–6804, 2010.
- [6] B. Pramanik and P. R. Mantena, “Viscoelastic response of graphite platelet and CTBN reinforced vinyl ester nanocomposites,” *Materials Sciences and Applications*, vol. 2, no. 11, pp. 1667–1674, 2011.
- [7] *Dynamic Mechanical Analyzer, Q Series, Calculation Based on Clamp Type*, Revision F, TA Instruments, New Castle, Del, USA, 2004.
- [8] M. A. Hopcroft, W. D. Nix, and T. W. Kenny, “What is the Young’s modulus of silicon?” *Journal of Microelectromechanical Systems*, vol. 19, no. 2, Article ID 5430873, pp. 229–238, 2010.
- [9] B. A. Gama, S. L. Lopatnikov, and J. W. Gillespie Jr., “Hopkinson bar experimental technique: a critical review,” *Applied Mechanics Reviews*, vol. 57, no. 4, pp. 223–250, 2004.
- [10] F. Yi, Z. Zhu, F. Zu, S. Hu, and P. Yi, “Strain rate effects on the compressive property and the energy-absorbing capacity of aluminum alloy foams,” *Materials Characterization*, vol. 47, no. 5, pp. 417–422, 2001.
- [11] B. Song and W. Chen, “Split Hopkinson pressure bar techniques for characterizing soft materials,” *Latin American Journal of Solids and Structures*, vol. 2, no. 2, pp. 113–152, 2005.
- [12] A. Cao, P. L. Dickrell, W. G. Sawyer, M. N. Ghasemi-Nejhad, and P. M. Ajayan, “Super-compressible foamlike carbon nanotube films,” *Science*, vol. 310, no. 5752, pp. 1307–1310, 2005.
- [13] T. Tong, Y. Zhao, L. Delzeit, M. A. Kashani, M. Meyyappan, and A. Majumdar, “Height independent compressive modulus of vertically aligned carbon nanotube arrays,” *Nano Letters*, vol. 8, no. 2, pp. 511–515, 2008.
- [14] S. B. Hutchens, A. Needleman, and J. R. Greer, “Analysis of uniaxial compression of vertically aligned carbon nanotubes,” *Journal of the Mechanics and Physics of Solids*, vol. 59, no. 10, pp. 2227–2237, 2011.

Research Article

Thin, Flexible Supercapacitors Made from Carbon Nanofiber Electrodes Decorated at Room Temperature with Manganese Oxide Nanosheets

S. K. Nataraj,¹ Q. Song,¹ S. A. Al-Muhtaseb,² S. E. Dutton,¹ Q. Zhang,³ and E. Sivaniah¹

¹ Biological and Soft System Sector, Cavendish Laboratory, University of Cambridge, Cambridge CB3 0HE, UK

² Department of Chemical Engineering, Qatar University, P.O. Box 2713, Doha, Qatar

³ Department of Materials, Cranfield University, Cranfield, Bedfordshire MK43 0AL, UK

Correspondence should be addressed to S. K. Nataraj; skn30@cam.ac.uk

Received 31 March 2013; Accepted 11 July 2013

Academic Editor: Sulin Zhang

Copyright © 2013 S. K. Nataraj et al. This is an open access article distributed under the Creative Commons Attribution License, which permits unrestricted use, distribution, and reproduction in any medium, provided the original work is properly cited.

We report the fabrication and electrochemical performance of a flexible thin film supercapacitor with a novel nanostructured composite electrode. The electrode was prepared by *in situ* coprecipitation of two-dimensional (2D) MnO₂ nanosheets at room temperature in the presence of carbon nanofibers (CNFs). The highest specific capacitance of 142 F/g was achieved for CNFs-MnO₂ electrodes in sandwiched assembly with PVA-H₄SiW₁₂O₄₀·*n*H₂O polyelectrolyte separator.

1. Introduction

Developments in producing efficient microelectronic devices depend on the associated micropower sources like supercapacitors or batteries [1–3]. In order to achieve high power performance and long term stability of thin supercapacitors, research efforts have been devoted to the application of nanostructured electrodes and suitable coupling with polyelectrolyte components [4]. As supercapacitors are becoming increasingly miniaturised, the use of nanomaterials and their preparation routes pose new challenges. It is generally acknowledged that size and shape are critical factors in inducing novel and unexpected properties to nanomaterials. The properties observed depend highly on anisotropy effects and region dependent surface reactivity [5–7]. Meanwhile, the demand for ultrathin flexible energy storage tools is increasing, especially in miniaturized electronic devices.

Pseudocapacitive electrode materials composed of metal oxides like RuO₂, SnO₂, and MnO₂ are of particular interest due to the intrinsic reversibility of surface redox reactions which contribute to large capacitance [8–10]. Recently, hydrous manganese oxides (MnO₂·*x*H₂O) have attracted attention due to their low cost and environmentally favourable aspects (such as low toxicity). Nanostructured

MnO₂ with larger surface area provides shorter lengths for the conduction of electrons and diffusion of cations.

In 2D nanostructural frameworks of MnO₂, MnO₆ octahedral share edges forming layers of MnO₂ held together by Van der Waals interactions. In the presence of high surface area substrate carbon this has been demonstrated to enhance charge transfer. In addition the layered MnO₂ nanosheets are amenable to release bending stresses [11, 12] and compatible with the metallic (e.g., copper) coated fabrics that act as current collectors. This is attributed to the layered structure with robust bonding within the MnO₂ sheets. In view of these advantages, MnO₂ nanosheets are being considered for use in thin, planar supercapacitors. Recently, MnO₂ deposition on large surface area reduced graphene oxide (RGO) and carbon nanotubes (CNTs), and activated or mesoporous carbons have been reported as supercapacitor electrodes [13–15]. Different polymorphs of manganese oxide such as α -, β -, γ -, and δ -type offering distinctive properties can be prepared in simple chemical synthesis routes [16–18].

In the study, we propose a new set of electrode materials prepared in a “green” low temperature process using cheap sustainable materials and the assembly of a supercapacitor via a simple one-step route. Two-dimensional (2D) birnessite-type MnO₂ nanosheets were coated on carbon nanofibers

(CNFs) by *in situ* coprecipitation at room temperature forming a nanocomposite material. The composite electrode was fabricated into a prototype supercapacitor device with thin flexible properties. We then measured the electrochemical performance of this nanostructured electrode with coupling of various polymer-based electrolytes.

2. Experimental Section

2.1. Materials. CNFs were prepared from polyacrylonitrile (PAN) (as described below). Polyvinyl alcohol (PVA; Alfa Aesar), KMnO_4 (Fischer Scientific), $\text{MnCl}_2 \cdot 4\text{H}_2\text{O}$ (ACROS Organics), silicotungstic acid ($\text{H}_4[\text{W}_{12}\text{SiO}_{40}]$) designated as STA, polyethyleneimine (PEI; Fluka), and KOH and NaOH (Aldrich) were of reagent grade and used as received. Cu coated nonwoven polyester fabric (as current collector) was obtained from RS Components (UK).

2.2. Preparation of CNFs from Polyacrylonitrile Polymer. Polyacrylonitrile polymer was dissolved in dimethylformamide (DMF) with homogeneous concentration of 10 wt% by stirring for 10 h at 60°C. The polymer nanofibers were then oxidised at 280°C in air and then carbonized at 1000°C in N_2 atmosphere.

2.3. Electrode: CNFs- MnO_2 . CNFs were dispersed (by stirring for 10 min) in a glass vessel containing 0.04 M KMnO_4 and 1.2 M NaOH. Then, 0.1 M MnCl_2 was added dropwise with vigorous stirring (~1000 rpm). The resulting precipitates were aged overnight with stirring at room temperature. The resulting carbon-Mn precursor suspension was filtered and washed several times and dried at 80°C in air for 3 h giving dark-brown composite.

2.4. Polyelectrolyte-Separator Films. Polyelectrolytes, which also act as electrode separators, were prepared by combination of PVA-KOH gel, PVA-PEI film, and PVA-STA film. Typical gel-like electrolyte films were prepared by dissolved PVA powder with water, and the electrolytic salt counterpart (i.e., KOH, PEI, or STA) following solutions was cast on clean glass plate forming free-standing polyelectrolyte films. As control experiments, conventional single cells were prepared using nickel-foam current collector and CNFs mat cut in squares (1 × 1 cm) separated by polypropylene filter.

2.5. Electrochemical Performance. Cyclic voltammetry measurements were performed using a Metrohm Autolab PGSTAT302/FRA2 system. Electrochemical behaviour of the composite electrode materials was performed in different thin film configurations, including that of a conventional single cell module in 6 M KOH electrolyte solutions. Cyclic voltammetry of the single cell was performed in different potential ranges in an aqueous KOH electrolyte (with concentration of 6 M). The capacitance was calculated using the relation $C = I[dV/dt]^{-1}$ at the zero potential point for voltage range of -1.0 to 1.0 V, where I is the current (averaged from charge and discharge values) and dV/dt is the scan rate.

3. Results and Discussion

Figure 1(a) shows the schematic diagram of the coating of MnO_2 nanosheets on the surface of CNFs by *in situ* coprecipitation of KMnO_4 and MnCl_2 and molar ratio of $[\text{Mn}^{2+}]/[\text{MnO}_4^-] = 2$, with the precipitant of NaOH at room temperature. The coprecipitation produced uniform sized nanosheets of birnessite- MnO_2 as verified by SEM and XRD (Figure 1). The formation of MnO_2 on carbon was confirmed by XRD analysis as shown in Figure 1(b). The three main Bragg peaks, at 2θ values of 12.40° (001), 26.97° (002), and 37° (003), match well with the pattern of birnessite $\text{Mn}_7\text{O}_{13} \cdot \text{H}_2\text{O}$ (JCPDS 42-1317) [19, 20]. Birnessite (a hydrated manganese oxide) often deviates from stoichiometry due to the substitution of some hydrated alkaline cations like Na^+ , K^+ , and Ca^{2+} , in the interlayer that compensates the layers negative charges [21]. EDS analysis on the prepared films indicates the intercalation of a small amount ($x < 0.35$) of alkali metals in $\text{A}_x\text{M}_7\text{O}_{13} \cdot \text{H}_2\text{O}$. Hereafter this generated phase of oxide is referred to by its generic stoichiometry, MnO_2 .

The size and distribution of nanosheets were found to depend on the concentration of NaOH. In some cases, the nanosheet morphology was not observed on the surface of carbon. These variations of microstructure originated from the rate of crystal growth related to the concentration of $[\text{OH}^-]$ [22]. As observed in SEM images shown in Figures 1(c)–1(f), the thickness of MnO_2 nanosheets coated on the surface of CNF appears to be uniform and is estimated to be ~8 nm, with lateral size at 50–100 nm. High magnification images show MnO_2 nanosheet coating on each individual fiber and coverage of the entire surface of the CNF. An SEM analysis of several areas of the decorated electrode showed an absence of nanosheet aggregation which is a common problem with coprecipitation chemistry. The size and shape of nanosheets were uniform over the entire surface of carbon substrate and different batches proved excellent reproducibility. However, the MnO_2 morphology can be easily changed by using different precursors or altering the processing conditions. We find that a nanoworm morphology can be obtained from manganese acetate upon oxidation as shown in Figure 2(a). As prepared composite fibers were assembled to form a thin flexible supercapacitor (Figure 2(b)) in combination with polyelectrolyte the complete cell is ~2 mm thick.

The capacitive performances of CNF- MnO_2 were evaluated by the potentiostatic charge/discharge method. Even though CV scans were performed with potential window of 1V for aqueous electrolytes and 1.5V for polyelectrolytes, representative voltage ranges are restricted to 1.0 and -1.0 V in Figure 2. Firstly, typical CV curves were measured for CNF- MnO_2 electrodes in 6 M KOH solution at different scan rates as presented in Figure 3(a). The shape of CV curves shifts progressively from rectangular to oval shapes with increasing scan rates. This phenomenon is probably caused by the internal resistance of the electrode in a conventional set-up inhibiting the charge collection from aqueous electrolyte (which hinders diffusion of K^+ in to the electrode). Further, the gravimetric capacitance of the CNFs in 6 M KOH was calculated to be 62, 56, 47, 31, 22, and 18 F/g

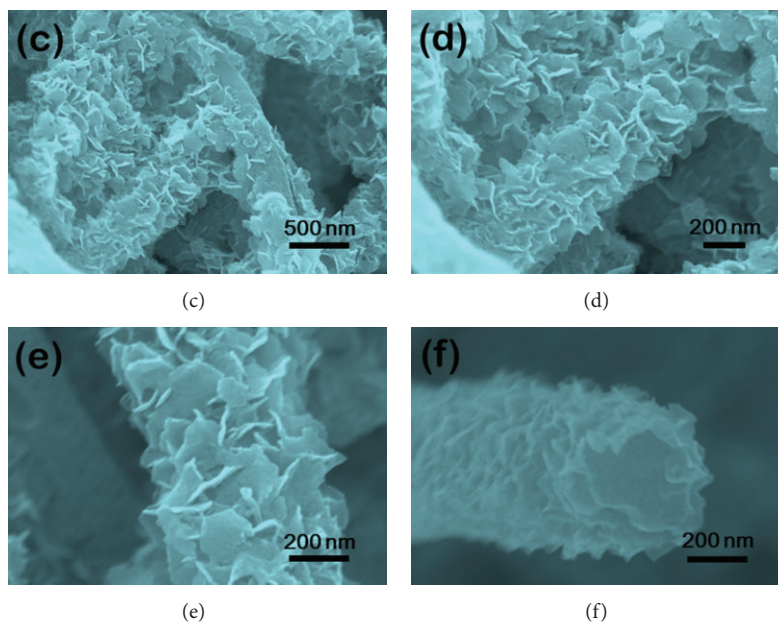
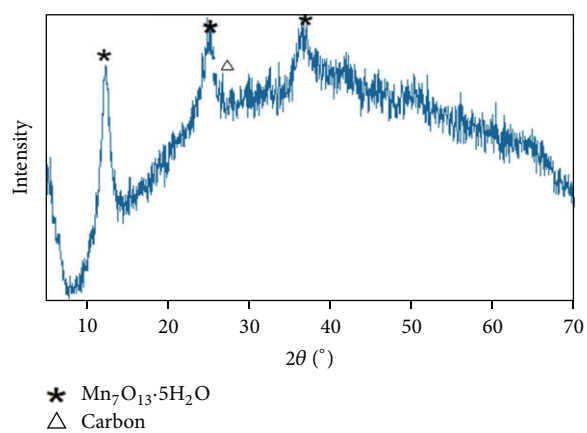
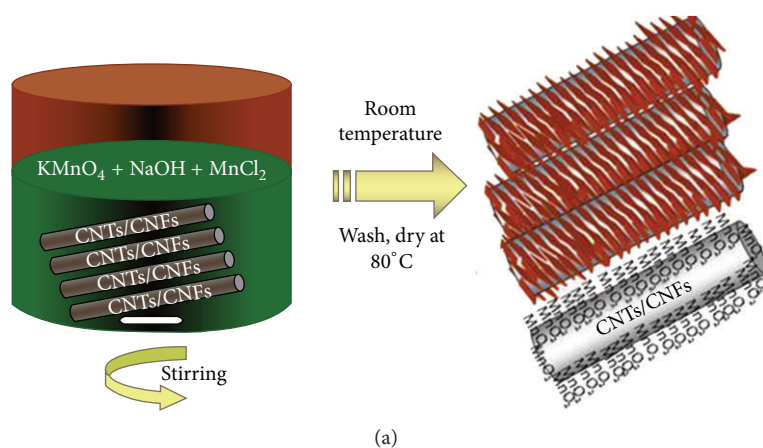


FIGURE 1: (a) Schematic of coating 2D MnO_2 nanosheets onto CNFs surfaces at room temperature. (b) XRD patterns of as prepared CNFs- MnO_2 crystal structures. (c)–(f) SEM images of CNF- MnO_2 mats with different magnifications.

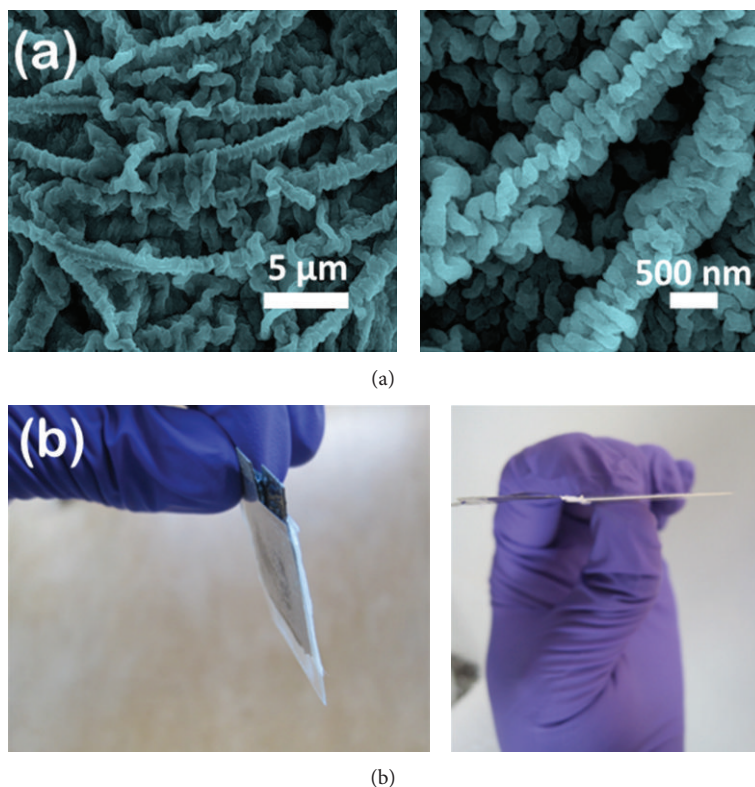


FIGURE 2: (a) Different morphology of MnO₂ with change in preparation conditions on CNFs. (b) Photos of as-assembled supercapacitor in (~2 mm thick) semiplane and its cross-sectional view.

for scan rate of 1, 5, 10, 20, 50, and 100 mV/s, respectively. For the KOH electrolyte in gel form (as shown in Figure 3(b)) in a sandwiched assembly, a larger induced current carrying capacity is due to the presence of a polyelectrolyte-electrode/electrode-current collector interface. The shape of the CV curves also deviated from rectangular, with the linearity in CV curves shifting to oxidation at 0.57 V and the corresponding reduction peak at around 0.31 V. These variations indicated the shift of capacitance behaviour from double layer to pseudocapacitive behaviour because of the occurrence of redox reactions of the MnO₂.

In order to utilise the redox reactions of MnO₂ to enhance the capacitance, it is necessary to enhance the interaction between MnO₂ and the polyelectrolyte and enable the cations in the polyelectrolyte to diffuse through the electrode freely. To further investigate the effect of excessive protonation in polyelectrolyte, highly proton conductive STA (capable of forming large water channels in STA's hydrate sphere hydrate sphere) in combination with PVA was used and tested for its electrochemical response as shown in Figure 3(c). STA forms stable Keggin type anions upon reduction of the tungsten (W)^{VI} centres within [SiW₁₂O₄₀]⁴⁻ anions and, when embedded into a PVA film, acts as a proton carrier. Strong redox peaks suggest that the proton forms a hydrogen bond with the water molecules from hydrated manganese oxide and enters as H₃O⁺ into 2D tunnels in the metal oxide and hopping continues from one active layer to the other through tunnelling mechanisms [23].

From CV charge-discharge cycles, the porous assembly of CNF-MnO₂ nanosheets with PVA-KOH gel showed large specific capacitances of ~100 F/g for slower scan rates, where the redox process is mainly governed by diffusion of ions. The diffusion of ions from the electrolyte, which can access almost all available pores of the composite electrode, leads to a complete insertion reaction in the reduction step and the reverse happens during the deinsertion process. The capacitance decreased to ~60 F/g at higher scan rate. This loss of capacitance could be mainly due to the slow diffusion of K⁺ ions from electrolytic layer into the pores of MnO₂ nanosheets. For the scan rate of 50 mV/s, the shape of CV curve shifted towards ideal double layer capacitive behaviour with gradual fading of redox peaks. This is because, when the scan rate is higher, the effective utilization of the redox reaction is limited only to the outer surface of MnO₂ electrode [24]. Further, as shown in Figure 3(d), a gravimetric capacitance of 142 F/g was achieved for CNF-MnO₂ electrode interfaced with PVA-H₄SiW₁₂O₄₀·*n*H₂O with slow scan rates. This twofold difference, in specific capacitance with respect to PVA-PEI blend polyelectrolyte (72 F/g) at the same scan rate, could be attributed to the difference of diffusion kinetics of polyion and electrons in the electrode. It is likely that the addition of STA to the PVA solution leads to the formation of stable complexes with hydrogen bonds keeping the charge-discharge mechanism intact. At a high scan rate (100 mV/s), CV curves shift to a rectangular shape indicating a dominance of capacitive behaviour over

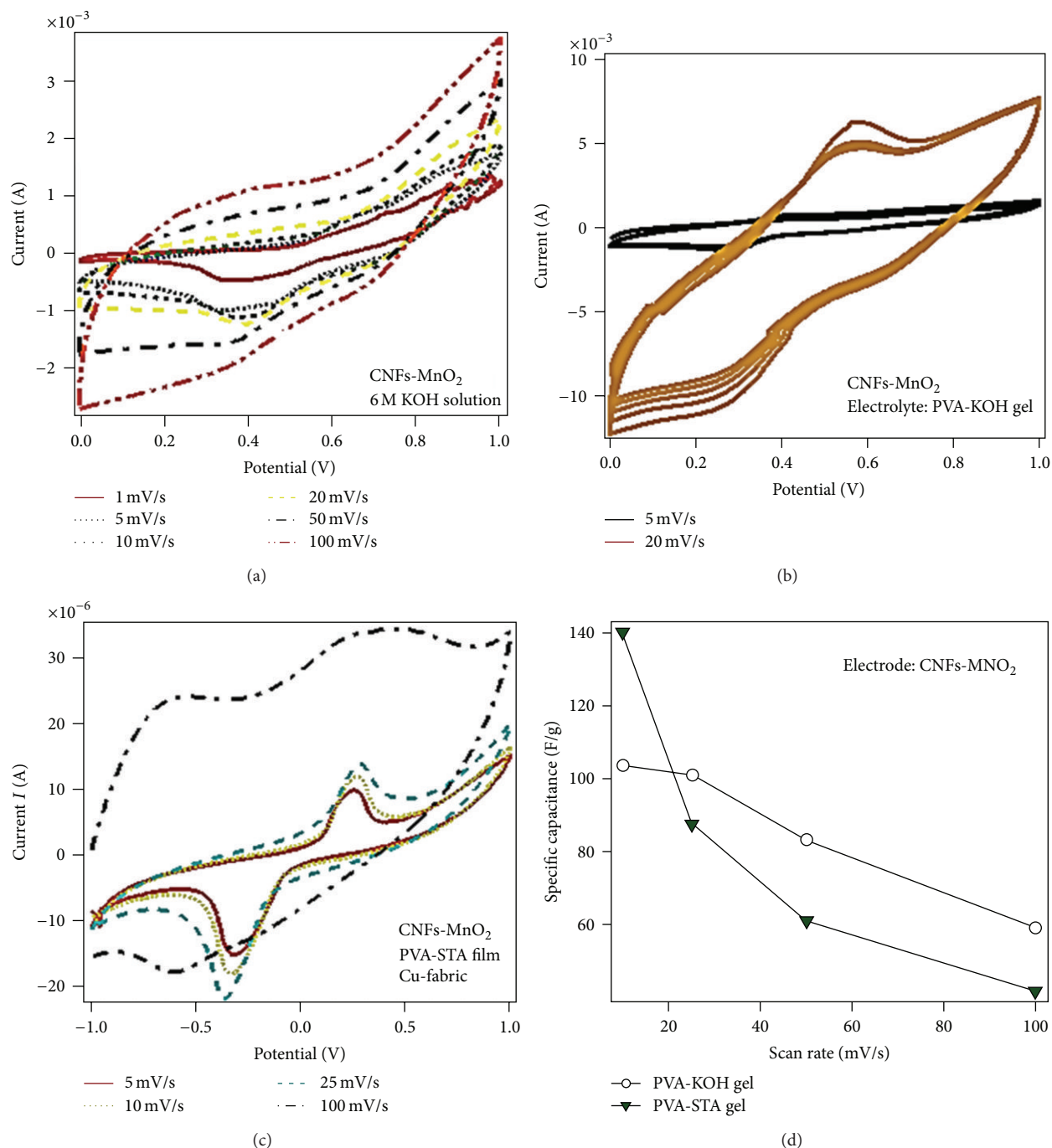


FIGURE 3: Cyclic voltammograms of composite (a) CNF- MnO₂ electrodes in 6 M KOH solution electrolyte, (b) in polyelectrolyte PVA-KOH gel, (c) CV performance of CNFs-MnO₂ electrode interfaced with PVA-H₄SiW₁₂O₄₀·nH₂O composite polyelectrolyte thin film, and (d) comparison of their specific capacitance plot against scan rates.

redox processes. This faster transfer of high induced charge is a result of current response to voltage reversal at the vertex potentials. Results of different polyelectrolyte systems showed significant reversible redox responses influencing the capacitive behaviour in the thin supercapacitor assembly. In short summary, CV measurements clearly show that the basic structure and geometry of the Keggin anions STA entrapped in PVA significantly enhance the capacitance value.

4. Conclusions

We successfully fabricated ~2 mm thick, flexible, and stable working supercapacitors using all-solid components. Two-dimensional nanosheets of MnO₂ were directly produced on carbon substrate in a simple one-step synthesis procedure at room temperature. The use of carbon, manganese dioxide, KOH, and heteropolyacid hybrids with PVA and PEI for

electrodes-electrolytes is biocompatible and/or biodegradable, nonhazardous, and environmentally benign. Furthermore, these flexible working devices are simple to prepare, and their fabrication and assembly are compatible with low-cost, roll-to-roll production.

Acknowledgment

This paper was made possible by the support of an NPRP grant from the QNRF. The statements made herein are solely the responsibility of the authors.

References

- [1] T. Liu, S. Xu, L. Wang et al., "Miniature supercapacitors composed of nickel/cobalt hydroxide on nickel-coated silicon microchannel plates," *Journal of Materials Chemistry*, vol. 21, no. 47, pp. 19093–19100, 2011.
- [2] Z. Lei, J. Zhang, and X. S. Zhao, "Ultrathin MnO₂ nanofibers grown on graphitic carbon spheres as high-performance asymmetric supercapacitor electrodes," *Journal of Materials Chemistry*, vol. 22, no. 1, pp. 153–160, 2012.
- [3] Y.-S. Ding, X.-F. Shen, S. Gomez, H. Luo, M. Aindow, and S. L. Suib, "Hydrothermal growth of manganese dioxide into three-dimensional hierarchical nanoarchitectures," *Advanced Functional Materials*, vol. 16, no. 4, pp. 549–555, 2006.
- [4] J. Bae, M. K. Song, Y. J. Park, J. M. Kim, M. Liu, and Z. L. Wang, "Fiber supercapacitors made of nanowire-fiber hybrid structures for wearable/flexible energy storage," *Angewandte Chemie International Edition*, vol. 50, no. 7, pp. 1683–1687, 2011.
- [5] L. Hu, H. Wu, and Y. Cui, "Printed energy storage devices by integration of electrodes and separators into single sheets of paper," *Applied Physics Letters*, vol. 96, no. 18, Article ID 183502, 3 pages, 2010.
- [6] A. Yu, I. Roes, A. Davies, and Z. Chen, "Ultrathin, transparent, and flexible graphene films for supercapacitor application," *Applied Physics Letters*, vol. 96, no. 25, Article ID 253105, 3 pages, 2010.
- [7] J. J. Yoo, K. Balakrishnan, J. Huang et al., "Ultrathin planar graphene supercapacitors," *Nano Letters*, vol. 11, no. 4, pp. 1423–1427, 2011.
- [8] M. Peckerar, Z. Dilli, M. Dornajafi et al., "A novel high energy density flexible galvanic cell," *Energy and Environmental Science*, vol. 4, no. 5, pp. 1807–1812, 2011.
- [9] X. Meng, Y. Zhong, Y. Sun, M. N. Banis, R. Li, and X. Sun, "Nitrogen-doped carbon nanotubes coated by atomic layer deposited SnO₂ with controlled morphology and phase," *Carbon*, vol. 49, no. 4, pp. 1133–1144, 2011.
- [10] L. Hu, W. Chen, X. Xie et al., "Symmetrical MnO₂-carbon nanotube-textile nanostructures for wearable pseudocapacitors with high mass loading," *ACS Nano*, vol. 5, no. 11, pp. 8904–8913, 2011.
- [11] M. Osada and T. Sasaki, "Two-dimensional dielectric nanosheets: novel nanoelectronics from nanocrystal building blocks," *Advanced Materials*, vol. 24, no. 2, pp. 210–228, 2012.
- [12] Y.-C. Chen, Y.-K. Hsu, Y.-G. Lin et al., "Highly flexible supercapacitors with manganese oxide nanosheet/carbon cloth electrode," *Electrochimica Acta*, vol. 56, no. 20, pp. 7124–7130, 2011.
- [13] J. Zhang, J. Jiang, and X. S. Zhao, "Synthesis and capacitive properties of manganese oxide nanosheets dispersed on functionalized graphene sheets," *Journal of Physical Chemistry C*, vol. 115, no. 14, pp. 6448–6454, 2011.
- [14] P. Hiralal, H. Wang, H. E. Unalan et al., "Enhanced supercapacitors from hierarchical carbon nanotube and nanohorn architectures," *Journal of Materials Chemistry*, vol. 21, no. 44, pp. 17810–17815, 2011.
- [15] P. Kossyrev, "Carbon black supercapacitors employing thin electrodes," *Journal of Power Sources*, vol. 201, pp. 347–352, 2012.
- [16] H. Xia, Y. S. Meng, X. Li, G. Yuan, and C. Cui, "Porous manganese oxide generated from lithiation/delithiation with improved electrochemical oxidation for supercapacitors," *Journal of Materials Chemistry*, vol. 21, no. 39, pp. 15521–15526, 2011.
- [17] O. Ghodbane, J.-L. Pascal, and F. Favier, "Microstructural effects on charge-storage properties in MnO₂-based electrochemical supercapacitors," *ACS Applied Materials and Interfaces*, vol. 1, no. 5, pp. 1130–1139, 2009.
- [18] W. Wei, X. Cui, W. Chen, and D. G. Ivey, "Manganese oxide-based materials as electrochemical supercapacitor electrodes," *Chemical Society Reviews*, vol. 40, no. 3, pp. 1697–1721, 2011.
- [19] X. Hu, Y. Masuda, T. Ohji, and K. Kato, "Dissolution-recrystallization induced hierarchical structure in ZnO: bunched rose-like and core-shell-like particles," *Crystal Growth and Design*, vol. 10, no. 2, pp. 626–631, 2010.
- [20] J. E. Post, "Manganese oxide minerals: crystal structures and economic and environmental significance," *Proceedings of the National Academy of Sciences of the United States of America*, vol. 96, no. 7, pp. 3447–3454, 1999.
- [21] A.-C. Gaillot, B. Lanson, and V. A. Drits, "Structure of birnessite obtained from decomposition of permanganate under soft hydrothermal conditions. 1. Chemical and structural evolution as a function of temperature," *Chemistry of Materials*, vol. 17, no. 11, pp. 2959–2975, 2005.
- [22] C. M. Julien, M. Massot, and C. Poinson, "Lattice vibrations of manganese oxides: part I—periodic structures," *Spectrochimica Acta A*, vol. 60, no. 3, pp. 689–700, 2004.
- [23] K.-D. Kreuer, "Proton conductivity: materials and applications," *Chemistry of Materials*, vol. 8, no. 3, pp. 610–641, 1996.
- [24] M. Toupin, T. Brousse, and D. Bélanger, "Charge storage mechanism of MnO₂ electrode used in aqueous electrochemical capacitor," *Chemistry of Materials*, vol. 16, no. 16, pp. 3184–3190, 2004.

Research Article

Carbon Micronymphaea: Graphene on Vertically Aligned Carbon Nanotubes

Jong Won Choi, Seul Ki Youn, and Hyung Gyu Park

Institute of Energy Technology, ETH Zürich, Sonneggstraße 3, 8092 Zürich, Switzerland

Correspondence should be addressed to Hyung Gyu Park; parkh@ethz.ch

Received 5 March 2013; Accepted 24 July 2013

Academic Editor: Nadya Mason

Copyright © 2013 Jong Won Choi et al. This is an open access article distributed under the Creative Commons Attribution License, which permits unrestricted use, distribution, and reproduction in any medium, provided the original work is properly cited.

This paper describes the morphology of carbon nanomaterials such as carbon nanotube (CNT), graphene, and their hybrid structure under various operating conditions during a one-step synthesis *via* plasma-enhanced chemical vapor deposition (PECVD). We focus on the synthetic aspects of carbon hybrid material composed of heteroepitaxially grown graphene on top of a vertical array of carbon nanotubes, called carbon micronymphaea. We characterize the structural features of this unique nanocomposite by uses of electron microscopy and micro-Raman spectroscopy. We observe carbon nanofibers, poorly aligned and well-aligned vertical arrays of CNT sequentially as the growth temperature increases, while we always discover the carbon hybrids, called carbon micronymphaea, at specific cooling rate of 15°C/s, which is optimal for the carbon precipitation from the Ni nanoparticles in this study. We expect one-pot synthesized graphene-on-nanotube hybrid structure poses great potential for applications that demand ultrahigh surface-to-volume ratios with intact graphitic nature and directional electronic and thermal transports.

1. Introduction

Unique properties of carbon nanotubes (CNTs) and graphene have allowed these nanocarbon allotropes to draw great attention in electronic devices, efficient heat and electron transfer media, and nanometric mechanical structures. Both CNT and graphene have long electron mean free paths [1, 2], large carrier mobilities [3, 4] at room temperature, excellent mechanical strengths [5, 6], and thermal conductivities [7, 8] much higher than any other heat conductors. A hybrid system made of CNT and graphene can be a three-dimensional conductive carbon network and thus advantageous for the reduction of the charge transfer resistance through CNTs, the transparency enhancement of CNT electrode, and the remarkable capacity delivery along the basal plane of graphene with a hold of each material's merit. For instance, the early numerical study on the carbon composite between a graphite and CNTs by Paulson et al. [9] has shown that the discrete Fermi surfaces allow electrons to move in a specific direction and make the contact resistance changed sensitively with respect to the lattice angle, thereby improving the conductance along the graphite by CNTs. By understanding the synergistic effect on electrical conductivity among CNTs graphite,

graphene, and their hybrids, researchers began to design an electronic device prototype including junction structures between graphene and tangentially dispersed CNTs, and experimentally verified the superiority of the graphene/CNT composite by demonstrating the improved electrochemical cell performance such as solar cell, supercapacitor, and battery by reporting lower sheet resistance, higher specific surface area, higher transmittance, higher reversibility, and a nearly rectangular cyclic voltammetric motion at an exceedingly high scan rate [10–15]. Despite these efforts, the comprehensive understandings of the optimal synthesis conditions and potential applications of the graphene-vertically aligned CNT hybrid are still not well defined because the aforementioned studies used the solution processing or mechanical approaches to make the hybrid composite. Recently, only few studies have been reported on the nanocomposite synthesis from graphene and vertically aligned CNTs and the growth mechanisms based on chemical vapor deposition (CVD). Those researchers have used Co film [16] and Ni film [17] as catalysts for synthesizing both CNTs and graphene layer on top under the thermal CVD method, depending on the initial catalyst thickness and annealing condition. The authors reported that they synthesized the multi- or

few-layered graphene by feeding a carbon precursor from the beginning during increasing the temperature up to 600°C without initial annealing process, and then they subsequently grew the carbon nanotubes after cleaving the catalyst film into nanoparticles above the temperature of 400°C. It is in general accepted that carbon nanostructure is classified into three regimes, based on the prepared catalyst thickness: single- or double-walled carbon nanotubes on the thin catalyst less than 1 nm [18–20], precipitated graphene on two orders of magnitude thicker catalysts [21–23], and Carbon nanofibers (CNFs) or multiwalled carbon nanotubes (MWCNTs) on the intermediately sized catalyst [24–26], meaning that the initial catalyst thickness is one of the key factors to decide the shape of carbon allotropes. Here, two questions arise. Are we able to synthesize the three dimensional graphene/vertically aligned CNT composite based on the intermediately thick catalyst? In addition, do the dissolved carbon atoms inside the catalyst particles precipitate to form the graphene layer? To explore the questions, we accordingly made our strategy to use: (1) the intermediately sized 7 nm thick Ni film as an initial catalyst, (2) plasma-enhanced CVD to provide more amount of the active carbon species into the catalyst particles, and (3) control of the growth temperature and the cooling rate of the chamber as a one-pot synthesis method. We expect the carbon micromorphology has enormous potentials such as three-dimensional electrodes, three-dimensional heat dissipation device, and alternatives of metal brush for the sliding electrical contacts.

2. Materials and Methods

The unordinary microcarbon Nymphaea structure was synthesized from a bilayer catalyst composed of 7 nm Ni and 20 nm Al layers on a Si substrate *via* a one-step, plasma-enhanced chemical vapor deposition process in a commercial system (Aixtron). Electron beam evaporation (Univex 450, Leybold) was used to prepare the bilayer catalyst on a Si substrate.

Prior to the growth, the CVD chamber was cleaned using O₂ plasma at 500°C for 5 minutes. Then, the catalyst substrates were loaded onto the substrate heater, and the chamber was evacuated below 2×10^{-3} mbar initially. The reactor temperature was kept above 200°C during loading/unloading to minimize moisture condensation out of surroundings. Under 200 sccm of NH₃ and 80 W of DC plasma at 500 V, the reactor was raised to the growth temperature (550°C, 650°C, and 750°C) at a ramp rate of 5°C/s and maintained there for 5 min for catalyst reduction. The fast ramping is known to defer catalyst sintering unfavorable for catalytic activity and nucleation density [27]. During the 15 min long growth step, 50 sccm of C₂H₂ (high purity > 99.6%) was added to the NH₃ flow under 120 W of DC discharge power at 500 V. Upon completion of growth, the reactor was cooled down at a desired linear rate under N₂ (10,000 sccm) flow and auxiliary heating to fit the cooling rate. The chamber pressure was maintained constant at 12 mbar throughout both annealing and growth processes and 37 mbar during the cooling process, respectively. Since one of the important

control parameters of our study is the sample cooling rate, we maintained a linear cooling curve by combined use of the fastest convective N₂ cooling and auxiliary PID-controlled heating. In this way, precise linear cooling rate was obtained between 5°C/s and 25°C/s up to the chamber temperature of 200°C. After the CVD chamber cools down to 200°C, morphologically various carbon nanostructures were synthesized. Subsequently, the resultant carbon nanostructures were characterized by scanning electron microscopy (SEM, Zeiss Ultra 55), transmission electron microscopy (TEM, Philips CM 12 at 100 keV), and micro-Raman spectroscopy (WiTec CRM 200 (532 nm excitation)) with a 100x objective lens.

3. Results and Discussion

Figure 1 illustrates various morphologies of carbon nanofibers, CNTs, and graphene-nanotube composite, including the growth condition. Since the relatively thick metal layer (7 nm Ni) at low temperatures is hard to cleave into a granular film necessary for growing a dense array of CNT [28, 29], we obtained only a mixture of poorly aligned, large diameter multiwall CNTs and some carbon nanofibers at 550°C (Figures 1(a)–1(c)). The vertical alignment at 650°C (Figures 1(d)–1(f)) and the dense array of MWCNT at 750°C (Figures 1(g)–1(i)) appear when we increased the annealing and growth temperatures. Interestingly, hybrid structure composed of one- and two-dimensional carbon allotropes was observed when we employed a moderate cooling rate of 15°C/s regardless of growth temperature (Figure 1(e) and insets on Figures 1(b) and 1(h)), while graphene layers were discovered neither at slower nor at faster cooling rate than 15°C/s. From most of the previous studies on the Ni-catalyzed graphene synthesis *via* precipitation mechanism, it is clearly revealed that a proper cooling process control is critical since the solubility of carbon in Ni is temperature dependent, and carbon atoms thereby precipitate to form a graphene layer on the surface upon cooling rate [21, 22, 30, 31]. Yu et al., in particular, have investigated the cooling rate effect on the formation of the graphene on flat Ni substrate and reported that: (1) cooling rate faster than 20°C/s results in a carbon quench effect, thus losing the mobility before they can diffuse onto Ni surface, (2) with slower cooling rate than 0.1°C/s, there is enough time for the carbon to diffuse into the bulk, leading to lack of carbon segregation at the surface, and (3) under a medium cooling manipulation, a finite amount of carbon can definitely precipitate to form the graphene at the Ni catalyst surface [21]. Furthermore, Chen et al. amazingly found that single- to multi-layer graphene bridges across the gaps among Ni particles, thus forming a continuous graphene pocket out of agglomerated Ni particles [32]. Considering those facts, it is reasonable to speculate that our continuous graphene layer is precipitated upon a medium cooling rate process out of neighboring Ni nanoparticles, placed on top of CNT array. In addition, further investigation by energy dispersive X-ray spectra (EDX) analysis was carried out to check both the nanoparticles on top of CNTs and remaining species on bottom substrate. Very few Ni particles were observed above Al film on bottom substrate while neither

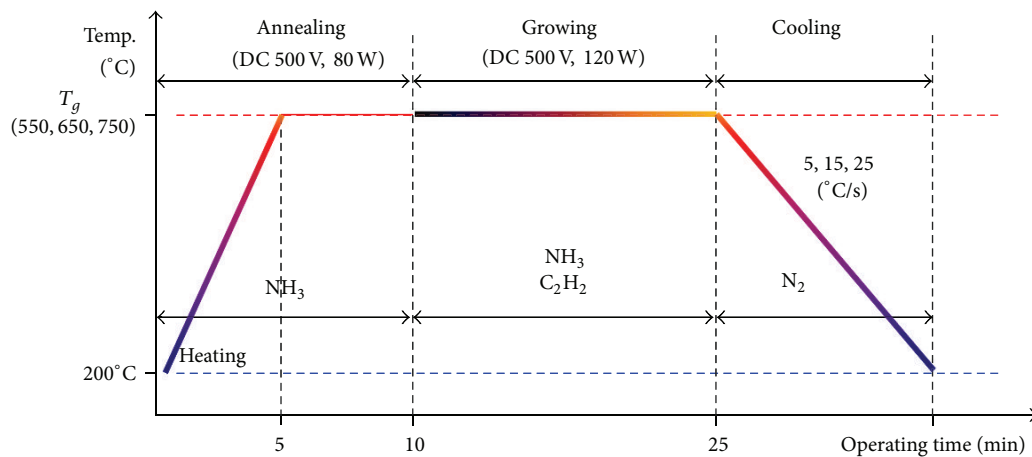
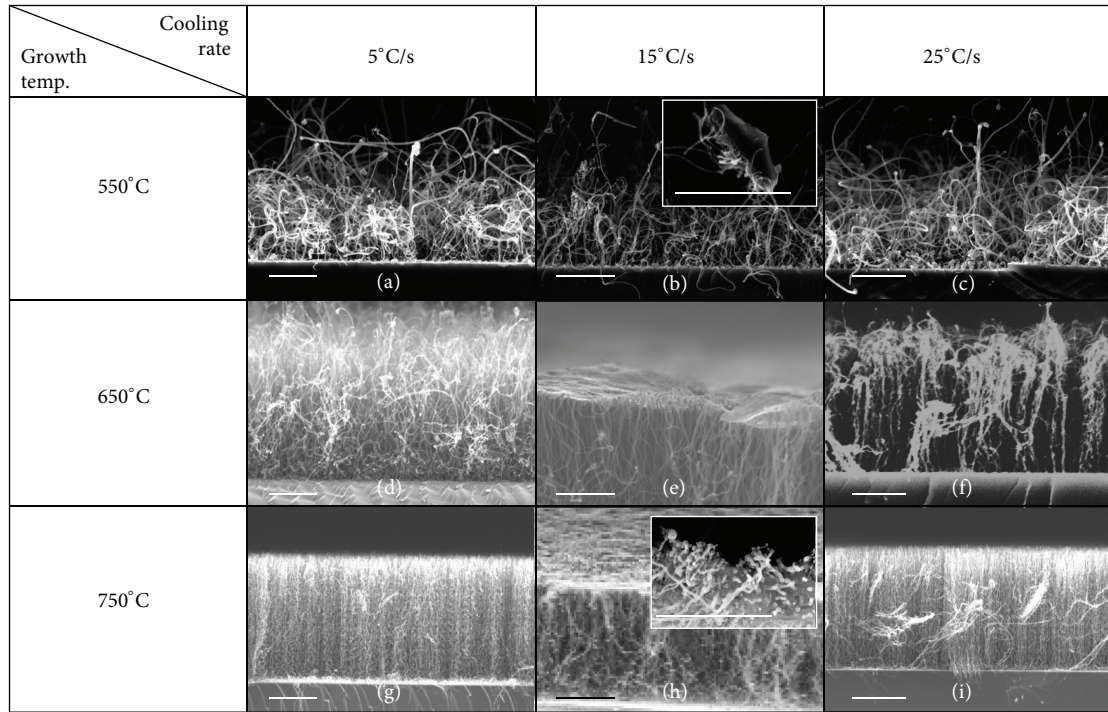


FIGURE 1: Various morphologies of carbon nanostructures with respect to growth temperatures and cooling rates, scale bar: 4 μm .

Al nor Al_2O_3 peak was found on CNT tips, from which we assert MWCNTs are grown with Ni particles by following the tip-growth mechanism and merely Ni nanoparticles on CNT tips play a role in graphene formation (not shown). To the best of our knowledge, such a fabrication method to form the carbon hybrids has not been reported yet. We thereby paid attention to the characteristics and growth mechanism of such an unusual hybrid carbon nanostructure as seen in Figure 1(e). Figures 2(a)-2(b) indicate our carbon micromorphology structure comprises a graphene roof on top of vertically aligned MWCNTs, of which the average outer diameter and height measured approximately by 20–25 nm and 4.7 μm , respectively (Figures 2(c)-2(d)). In addition, the precipitated graphene layers have cowrapped all the Ni domains together with ends of CNTs seen in the magnified

image of Figure 2(b), which agreed to Chen et al.'s report showing a similar morphology of graphene pocket based on the ball-like Ni nanoparticles under the cooling rate of 16.6°C/s [32]. In order to investigate the junction geometry in detail, the hybrid composite was further analyzed by TEM, which provides important information that not only a MWCNT but also graphene is located under the individual Ni nanoparticle (Figure 2(e) inset), and furthermore graphene layers are bridging across the vicinity to form the continuous layer (left-handed side of dot line) heteroepitaxially as shown in Figure 2(e). This reveals that the graphene could form independently once we grow the dense array of CNTs, thus offering the possibility of the continuous coverage in large scale under an optimized condition.

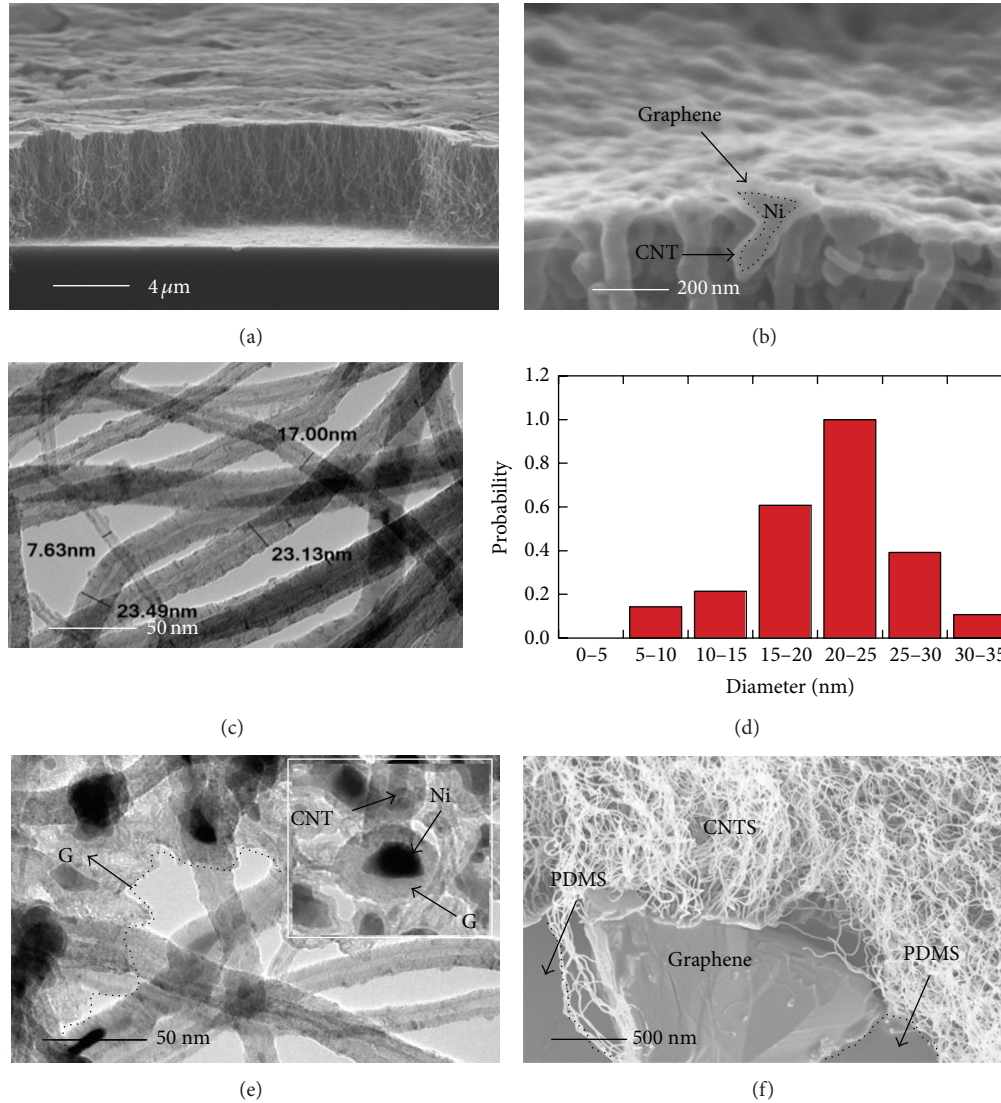


FIGURE 2: Morphologies of carbon micromorphs synthesized on 7 nm Ni catalyst on 20-nm Al film; (a) 15° inclined view, (b) magnified junction between graphene and MWCNTs, (c) TEM image of MWCNT, (d) outer diameter distribution of MWCNTs array, (e) graphene bridging the neighboring Ni islands, and (f) reversely transferred sample onto PDMS substrate.

On the other hand, for the preparation to check the Raman spectrum of the bare graphene sheet separately out of hybrid composite, we stripped out the hybrid sample from the substrate by stamping with the sticky PDMS film; therefore we could obtain the reverse structure comprised of a graphene layer on PDMS and free standing open MWCNTs upon the graphene as illustrated in Figure 2(f). Care was taken to focus several spots of exposed bare graphene layer for the investigation of the Raman spectra. Finally, we compared four Raman spectra of the carbon micromorphs, bare graphene, bare MWCNTs separated from hybrid composite onto SiO₂ substrate by a sharp knife, and MWCNTs array grown at the same temperature but faster cooling rate. The black line in Figure 3 indicates the height of G' peak (~2681 cm⁻¹) is higher than G peak (~1596 cm⁻¹) with G' to G Raman peak ratio between 1.43 and 1.53, corresponding

more or less to 4–7 layers according to literatures [28, 29, 33], from which we confirmed the upper layer on CNT array is not a remaining thin Ni layer but the multilayered graphene. In addition, the large D peak is caused from the highly disordered structure when the graphene edges are heteroepitaxially connected [34]. Both green and blue lines show a typical MWCNTs array. The position of G peak (~1590 cm⁻¹) is located at lower wave number than that of bare graphene (~1596 cm⁻¹) since CNT has much higher wall number (mainly 22) compared with the graphene layers (4–7) [21, 35]. In addition, we report the distinguishable change of G peak (1594.1 cm⁻¹) and G' peak (~2676 cm⁻¹) when MWCNTs array and graphene layers are connected to each other in a carbon micromorph structure, which are located at the middle wave number between the bare graphene and CNT (Figure 3, red line). Furthermore, we believe that larger

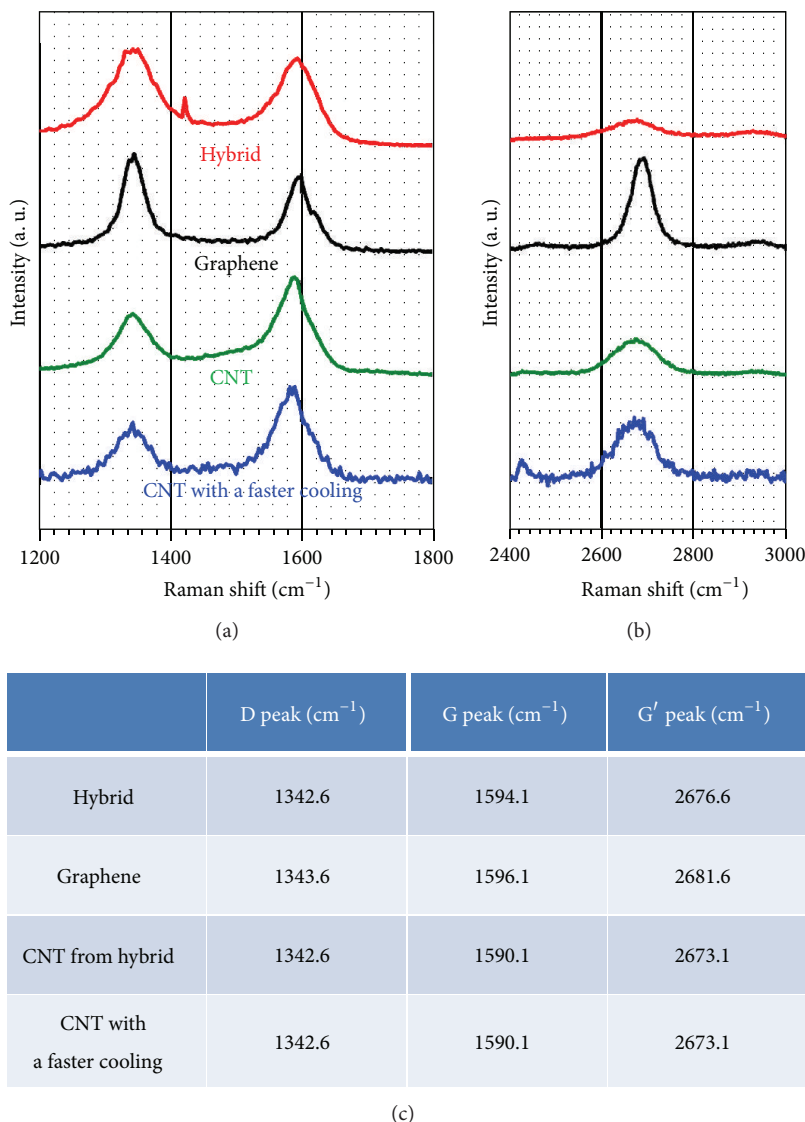


FIGURE 3: Raman spectra at 532 nm among carbon micronymphaea (red), bare graphene (black) out of hybrids, bare MWCNTs out of hybrids (green), and MWCNTs synthesized at the same growth temperature as hybrids, but under faster cooling rate (blue).

defects of the hybrid are attributed to the discontinuous junction between ends of CNTs and graphene sheet. The junction structure and the Raman spectra need further investigation.

As briefly mentioned in the introduction, there are few previous studies on the synthesis of a carbon hybrid structure with the vertically aligned CNTs based on Co or Ni films using thermal CVD process. These studies proposed that graphene should be first segregated on the surface of continuous thin-film catalyst during increasing the temperature in the presence of a carbon precursor. After the temperature reaches 500–600°C, the catalyst film under the graphene is broken into particles, and subsequently MWCNTs are synthesized with lifting up the catalyst particles. However, our results suggest a definitely different growth mechanism of the hybrid composite as depicted in Figure 4. First, 7 nm Ni film is cloven into nanoparticles during the annealing

process in the plasma-induced NH_3 surroundings at high temperature. Second, MWCNT array grows *via* the tip-growth mechanism, lifting up the Ni from Al film at early stage. At this moment, an excessive carbon source is dissolved inside the Ni catalyst. Third, depending upon cooling at an optimal rate, carbon atoms can be precipitated to form graphitic layers along the Ni islands in lateral directions and subsequently bridge across the gaps between the particles to merge one another heteroepitaxially with the time, which was proved by control experiments in Figure 1. We could not obtain the carbon micronymphaea structure at a cooling rate far from the optimal one. In addition to the cooling rate, we believe that an initial catalyst thickness and annealing time could also affect the graphene quality such as number of layer and the continuity as well as the morphology of vertically aligned CNTs.

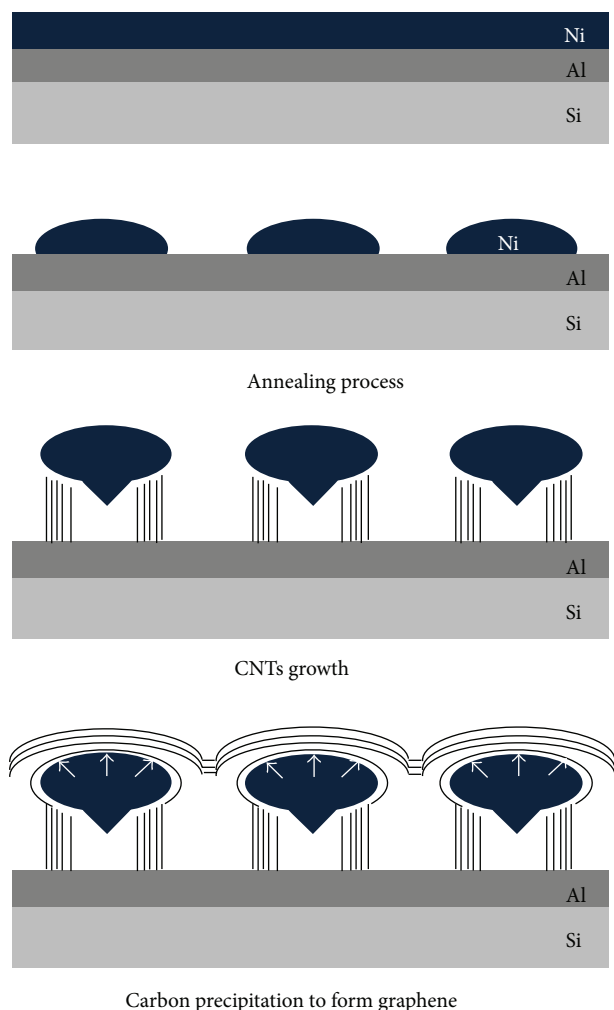


FIGURE 4: Proposed growth mechanism of carbon micromorphology.

4. Conclusions

In this study we demonstrated various morphologies of one-pot PECVD synthesized carbon nanostructures at different growth temperatures and cooling rates using a set of 7 nm Ni layer and C_2H_2 precursor. We focused on the characterization and the growth mechanism of a unique carbon hybrid structure, named a carbon micromorphology; a few layers of graphene are grown on Ni particles instead of flat substrate and vertically combined with MWCNTs below them. Out of the results, we report when we synthesize CNTs array with the catalyst that is also available to the synthesis of graphene, we can realize either CNTs or CNT/graphene hybrid with respect to the cooling rate, even under the same growth condition. Finally, a carbon micromorphology is recommended to replace the three-dimensional carbon electrode structure not only to increase the overall specific surface area but also to apply the equipotential to individual CNTs *via* cowrapped graphene layer.

Acknowledgments

This work was partially funded by Swiss National Science Foundation (Contracts Nos. 200021-137964 and 200021-146856) and Strategic Korean-Swiss Cooperative Program in Science and Technology (FY 2010). The authors gratefully acknowledge the support from the Microfabrication Center (FIRST), the Electron Microscopy Center (EMEZ), and Professor C. Hierold of ETH Zurich. Dr. E. B. Meier's help in transmission electron microscopy is greatly recognized. Hyung Gyu Park and Seul Ki Youn acknowledge their travel support from COST action MP0901 NanoTP.

References

- [1] M. S. Purewal, B. H. Hong, A. Ravi, B. Chandra, J. Hone, and P. Kim, "Scaling of resistance and electron mean free path of single-walled carbon nanotubes," *Physical Review Letters*, vol. 98, no. 18, Article ID 186808, 2007.
- [2] W.-K. Tse, E. H. Hwang, and S. Das Sarma, "Ballistic hot electron transport in graphene," *Applied Physics Letters*, vol. 93, no. 2, Article ID 023128, 2008.
- [3] S. D. Li, Z. Yu, C. Rutherglen, and P. J. Burke, "Electrical properties of 0.4 cm long single-walled carbon nanotubes," *Nano Letters*, vol. 4, no. 10, pp. 2003–2007, 2004.
- [4] F. Giannazzo, S. Sonde, R. L. Nigro, E. Rimini, and V. Raineri, "Mapping the density of scattering centers limiting the electron mean free path in graphene," *Nano Letters*, vol. 11, no. 11, pp. 4612–4618, 2011.
- [5] R. F. Zhang, Q. Wen, W. Z. Qian, D. S. Su, Q. Zhang, and F. Wei, "Superstrong ultralong carbon nanotubes for mechanical energy storage," *Advanced Materials*, vol. 23, no. 30, pp. 3387–3391, 2011.
- [6] C. Lee, X. D. Wei, J. W. Kysar, and J. Hone, "Measurement of the elastic properties and intrinsic strength of monolayer graphene," *Science*, vol. 321, no. 5887, pp. 385–388, 2008.
- [7] E. Pop, D. Mann, Q. Wang, K. Goodson, and H. Dai, "Thermal conductance of an individual single-wall carbon nanotube above room temperature," *Nano Letters*, vol. 6, no. 1, pp. 96–100, 2006.
- [8] A. A. Balandin, S. Ghosh, W. Bao et al., "Superior thermal conductivity of single-layer graphene," *Nano Letters*, vol. 8, no. 3, pp. 902–907, 2008.
- [9] S. Paulson, A. Helser, M. Buongiorno Nardelli et al., "Tunable resistance of a carbon nanotube-graphite interface," *Science*, vol. 290, no. 5497, pp. 1742–1744, 2000.
- [10] H. Q. Zhu, Y. M. Zhang, L. Yue et al., "Graphite-carbon nanotube composite electrodes for all vanadium redox flow battery," *Journal of Power Sources*, vol. 184, no. 2, pp. 637–640, 2008.
- [11] Y. Tang and J. H. Gou, "Synergistic effect on electrical conductivity of few-layer graphene/multi-walled carbon nanotube paper," *Materials Letters*, vol. 64, no. 22, pp. 2513–2516, 2010.
- [12] U. Khan, I. O'Connor, Y. K. Gun'Ko, and J. N. Coleman, "The preparation of hybrid films of carbon nanotubes and nano-graphite/graphene with excellent mechanical and electrical properties," *Carbon*, vol. 48, no. 10, pp. 2825–2830, 2010.
- [13] D. S. Yu and L. M. Dai, "Self-assembled graphene/carbon nanotube hybrid films for supercapacitors," *Journal of Physical Chemistry Letters*, vol. 1, no. 2, pp. 467–470, 2010.

- [14] B. A. Zhang, Q. B. Zheng, Z. D. Huang, S. W. Oh, and J. K. Kim, "SnO₂-graphene-carbon nanotube mixture for anode material with improved rate capacities," *Carbon*, vol. 49, no. 13, pp. 4524–4534, 2011.
- [15] C. Y. Li, Z. Li, H. W. Zhu et al., "Graphene nano-"patches" on a carbon nanotube network for highly transparent/conductive thin film applications," *Journal of Physical Chemistry C*, vol. 114, no. 33, pp. 14008–14012, 2010.
- [16] D. Kondo, S. Sato, and Y. Awano, "Self-organization of novel carbon composite structure: graphene multi-layers combined perpendicularly with aligned carbon nanotubes," *Applied Physics Express*, vol. 1, no. 7, Article ID 0740033, 2008.
- [17] V. Jousseume, J. Cuzzocrea, N. Bernier, and V. T. Renard, "Few graphene layers/carbon nanotube composites grown at complementary-metal-oxide-semiconductor compatible temperature," *Applied Physics Letters*, vol. 98, no. 12, Article ID 123103, 2011.
- [18] R. Martel, T. Schmidt, H. R. Shea, T. Hertel, and P. Avouris, "Single- and multi-wall carbon nanotube field-effect transistors," *Applied Physics Letters*, vol. 73, no. 17, pp. 2447–2449, 1998.
- [19] C. H. Yu, L. Shi, Z. Yao, D. Li, and A. Majumdar, "Thermal conductance and thermopower of an individual single-wall carbon nanotube," *Nano Letters*, vol. 5, no. 9, pp. 1842–1846, 2005.
- [20] D. Takagi, Y. Homma, H. Hibino, S. Suzuki, and Y. Kobayashi, "Single-walled carbon nanotube growth from highly activated metal nanoparticles," *Nano Letters*, vol. 6, no. 12, pp. 2642–2645, 2006.
- [21] Q. K. Yu, J. Lian, S. Siriponglert, H. Li, Y. P. Chen, and S.-S. Pei, "Graphene segregated on Ni surfaces and transferred to insulators," *Applied Physics Letters*, vol. 93, no. 11, Article ID 113103, 2008.
- [22] K. S. Kim, Y. Zhao, H. Jang et al., "Large-scale pattern growth of graphene films for stretchable transparent electrodes," *Nature*, vol. 457, no. 7230, pp. 706–710, 2009.
- [23] A. Reina, X. T. Jia, H. John et al., "Layer area, few-layer graphene films on arbitrary substrates by chemical vapor deposition," *Nano Letters*, vol. 9, pp. 3087–3087, 2009.
- [24] M. Cantoro, S. Hofmann, S. Pisana et al., "Effects of pre-treatment and plasma enhancement on chemical vapor deposition of carbon nanotubes from ultra-thin catalyst films," *Diamond and Related Materials*, vol. 15, no. 4-8, pp. 1029–1035, 2006.
- [25] R. R. Mitchell, B. M. Gallant, C. V. Thompson, and Y. Shao-Horn, "All-carbon-nanofiber electrodes for high-energy rechargeable Li-O₂ batteries," *Energy and Environmental Science*, vol. 4, no. 8, pp. 2952–2958, 2011.
- [26] M. Bikshapathi, A. Sharma, A. Sharma, and N. Verma, "Preparation of carbon molecular sieves from carbon micro and nanofibers for sequestration of CO₂," *Chemical Engineering Research and Design*, vol. 89, no. 9, pp. 1737–1746, 2011.
- [27] C. T. Wirth, S. Hofmann, and J. Robertson, "State of the catalyst during carbon nanotube growth," *Diamond and Related Materials*, vol. 18, no. 5-8, pp. 940–945, 2009.
- [28] D. Graf, F. Molitor, K. Ensslin et al., "Spatially resolved raman spectroscopy of single- and few-layer graphene," *Nano Letters*, vol. 7, no. 2, pp. 238–242, 2007.
- [29] A. Das, B. Chakraborty, and A. K. Sood, "Raman spectroscopy of graphene on different substrates and influence of defects," *Bulletin of Materials Science*, vol. 31, no. 3, pp. 579–584, 2008.
- [30] A. N. Obraztsov, E. A. Obraztsova, A. V. Tyurnina, and A. A. Zolotukhin, "Chemical vapor deposition of thin graphite films of nanometer thickness," *Carbon*, vol. 45, no. 10, pp. 2017–2021, 2007.
- [31] H. J. Park, J. Meyer, S. Roth, and V. Skákalová, "Growth and properties of few-layer graphene prepared by chemical vapor deposition," *Carbon*, vol. 48, no. 4, pp. 1088–1094, 2010.
- [32] Z. P. Chen, W. C. Ren, B. L. Liu et al., "Bulk growth of mono-to few-layer graphene on nickel particles by chemical vapor deposition from methane," *Carbon*, vol. 48, no. 12, pp. 3543–3550, 2010.
- [33] A. C. Ferrari, J. C. Meyer, V. Scardaci et al., "Raman spectrum of graphene and graphene layers," *Physical Review Letters*, vol. 97, no. 18, Article ID 187401, 2006.
- [34] A. C. Ferrari, "Raman spectroscopy of graphene and graphite: disorder, electron-phonon coupling, doping and nonadiabatic effects," *Solid State Communications*, vol. 143, no. 1-2, pp. 47–57, 2007.
- [35] J. M. Caridad, F. Rossella, V. Bellani, M. Maicas, M. Patrini, and E. Diez, "Effects of particle contamination and substrate interaction on the Raman response of unintentionally doped graphene," *Journal of Applied Physics*, vol. 108, no. 8, Article ID 084321, 2010.

Research Article

Effect of Catalyst Morphology on the Quality of CVD Grown Graphene

Ya-Ping Hsieh,¹ Yi-Wen Wang,¹ Chu-Chi Ting,¹ Hsiang-Chen Wang,¹
Kuang-Yao Chen,² and Chang-Chung Yang²

¹ Graduate Institute of Opto-Mechatronics, National Chung Cheng University, 168 University Road, Min-Hsiung, Chiayi 62102, Taiwan

² Green Energy and Environment Research Laboratories, Industrial Technology Research Institute, Hsinchu, Taiwan

Correspondence should be addressed to Ya-Ping Hsieh; yphsieh@ccu.edu.tw

Received 15 March 2013; Revised 9 July 2013; Accepted 17 July 2013

Academic Editor: Nadya Mason

Copyright © 2013 Ya-Ping Hsieh et al. This is an open access article distributed under the Creative Commons Attribution License, which permits unrestricted use, distribution, and reproduction in any medium, provided the original work is properly cited.

The strong interest in graphene has motivated large effort in the scalable production of high-quality material. The potential of chemical vapor deposition on Cu foil to produce such graphene is impeded by lacking understanding of the relation between catalyst properties and graphene performance. We here present a systematic analysis of the catalyst morphology and its effect on electrical properties of graphene. We find that nanometer sized particles increase the density of bilayer regions but have no significant effect on carrier transport. Long wavelength roughness (waviness), on the other hand, generates defective graphitic regions that deteriorate carrier mobility. These findings shed light on the graphene formation process on Cu substrates and open a route to improve graphene quality for electronics applications.

1. Introduction

Graphene, a single atomic layer of carbon atoms, has generated enormous attention due to its physical properties. Proof-of-concept experiments demonstrated novel electronic and optoelectronic devices in transistors [1], solar cells [2, 3], photodetectors [4], and so forth. The desire for large-scale application of this material has motivated the development of a number of methods to synthesize large-area graphene sheets. Amongst these approaches, the chemical vapor deposition (CVD) synthesis of graphene on Cu substrate [5, 6] has shown great promise for producing high-quality single-layer graphene. Despite significant efforts, the properties of CVD graphene have yet to reach the requirements of electronics applications for mobility and uniformity. Recent reports emphasize the importance of the surface morphology of the catalytic Cu substrate in determining the homogeneity and electronic transport properties of the grown graphene film [7–9]. It was found that imperfections in the Cu substrate interfere with graphene growth. Furthermore, commonly

used Cu foil is usually covered with a layer of chromium oxide for anticorrosion protection [10] that can affect the properties of grown graphene. Consequently, the formation of smooth Cu surfaces free of contaminants becomes a necessary step for the synthesis of high-quality graphene.

Despite this importance of the catalyst pretreatment, little work has been done to correlate the condition of the Cu catalyst with the properties of the obtained graphene. We here present the first systematic study of the effect of catalyst morphology on the electrical and optical properties of graphene. We find that a higher density of surface particles supports the formation of bilayer graphene regions but has little effect on the electrical properties of the graphene film. Low frequency roughness (waviness), on the other hand, deteriorates the quality of graphene significantly as studied by Raman spectroscopy and electrical measurements.

These observations provide deeper understanding of the graphene growth and have large significance for the optimization of graphene quality for future applications.

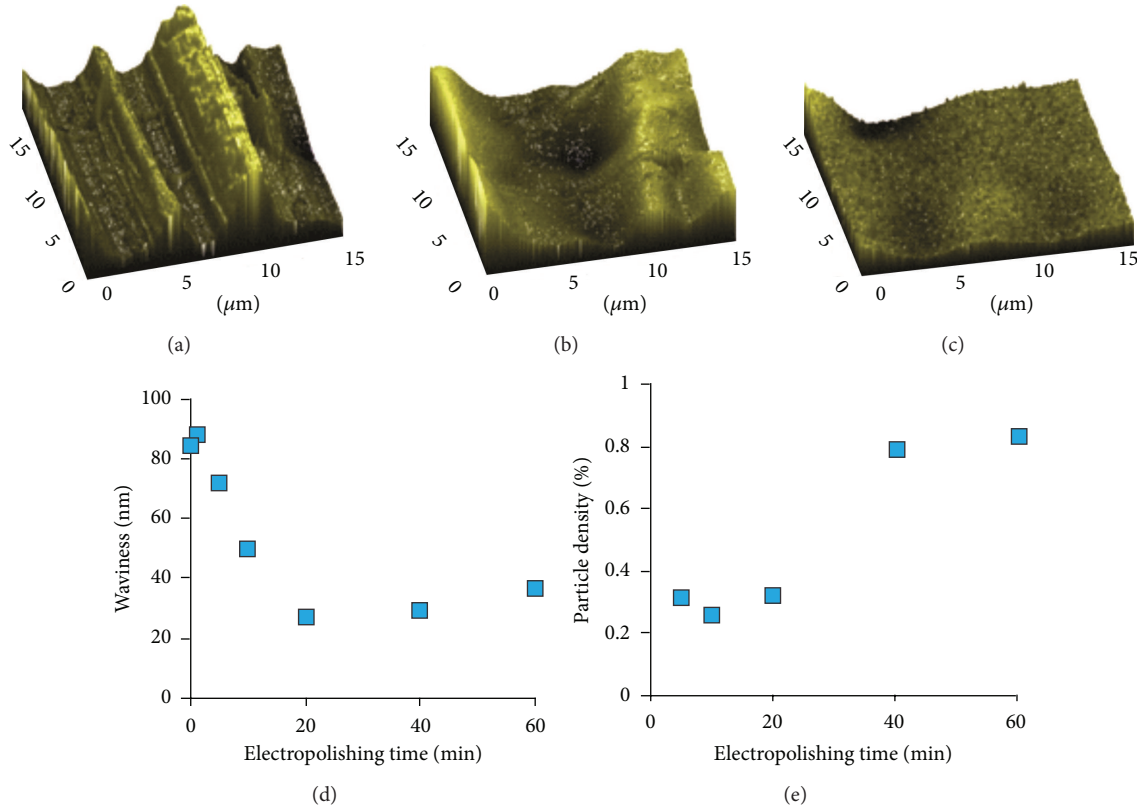


FIGURE 1: Change of Cu morphology upon electropolishing: (a)–(c) AFM images for 5 min (a), 10 min (b), 40 min (c) electropolishing, (d) waviness versus electropolishing time, and (e) particle density versus electropolishing time.

2. Experimental

Electrochemical polishing was employed to control the morphology of the Cu foil. First, copper foil (99.8%, Alfa-Aesar, no. 13382) was pre-cleaned by sonication in acetic acid for 5 min to remove the oxide layer. The dried Cu foil was then affixed on a glass slide to simplify handling. The Cu foil was placed into a breaker containing a solution of 300 mL of H_3PO_4 (85%) and 100 mL of polyethylene glycol (PEG, molecular weight 400, from Sigma-Aldrich Co.) as electrolytic solution. This Cu foil was then used as working electrode, and another Cu plate was used as counter electrode, and a DC power supply was used to apply a voltage of 1.5 V. After the electropolishing treatment, the sample was washed with copious amounts of deionized water and then rinsed with isopropyl alcohol, followed by blow-drying with N_2 .

In our acid etching pretreatment, nitric acid (TFB, TRANSENE Company, Inc.) and 37% HCl (J.T. Baker Company) were used as obtained.

The pretreated Cu foils were then used to carry out graphene growth. For this, the reactor chamber was pumped down to 10 mTorr using a vacuum pump. Hydrogen gas was introduced into the chamber during heating to 1000°C . The foils were annealed for 70 min to initiate Cu grain growth and to remove organic residue and surface oxide. Graphene growth was then performed at 1000°C for 100 min under a gas mixture of H_2 (100 sccm) and CH_4 (40 sccm). The sample was

then rapidly cooled under 10 sccm hydrogen flow. Graphene samples were transferred by a PMMA assisted process in which Cu was etched away by 5% FeCl_3 , and graphene was transferred onto SiO_2/Si wafers. Finally, the PMMA was dissolved by immersion in acetone.

Carrier mobility was obtained by Hall effect measurements of macroscopic (10×10 mm) films thus transferred employing a Van der Pauw geometry. Upon optimization of the transfer protocol, sample-to-sample variations were less than 10%.

Gwyddion software was used to extract the waviness and particle density from AFM images. The waviness parameter was defined as the RMS roughness of a sample after high-pass filtering removed features with wavevectors larger than $k = 5 \mu\text{m}^{-1}$.

A watershed algorithm was applied to identify particles and calculate their area densities.

3. Results and Discussion

In a first set of experiments we analyzed the effect of electropolishing duration on the morphology of the Cu foil. Atomic force microscope images reveal the change in roughness as time progresses (Figures 1(a)–1(c)). The images reveal, however, that the roughness does not simply decrease as assumed in previous electropolishing papers. Instead, two

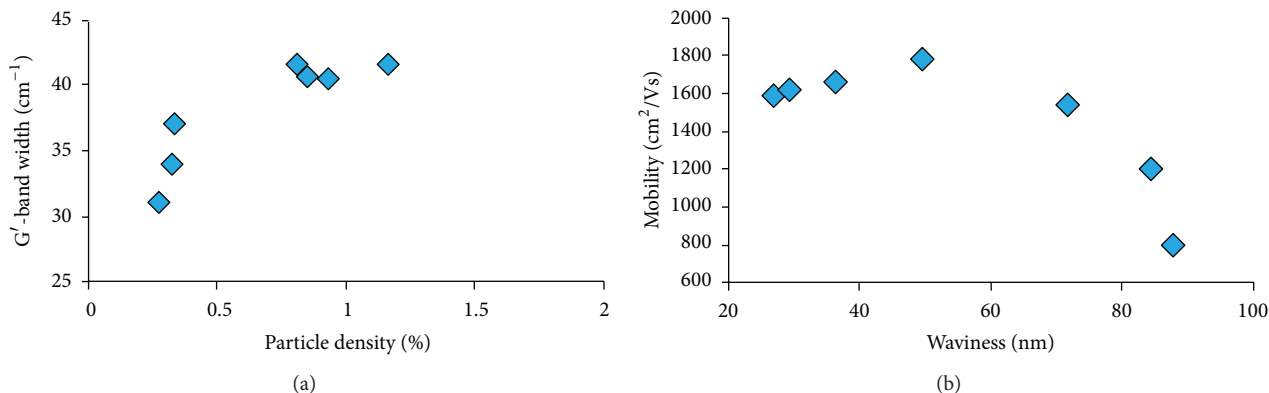


FIGURE 2: Graphene quality for different Cu morphology: (a) G' peak width versus particle density; (b) carrier Hall mobility versus waviness.

components of the roughness have to be distinguished: while the long range roughness (or waviness) decreases as a function of electropolishing time (Figure 1(d)), small particles start occurring (Figure 1(e)). This is thought to be caused by two different mechanisms taking place during electropolishing. The concentration of electric field around micrometer high protrusions causes preferential electrochemical etching of these features and consequently a decrease of the waviness [7]. Nanometer sized particles, however, exhibit too small field enhancement and are not affected by the same mechanism [11]. Consequently, protrusions will smooth out until they reach a critical size but will remain unchanged afterwards. Therefore, increasing electropolishing time represents a tradeoff between decreasing waviness and increasing particle density as shown when comparing Figures 1(d) and 1(e).

Based on the finding that waviness and particle density are both changed during electropolishing, we investigate the effect of each of the two parameters on the quality of graphene synthesized from thus pretreated Cu foils.

Raman spectroscopy reveals an increase of the G' peak width as a function of particle density (Figure 2(a)). This behaviour is attributed to an increasing fraction of bilayer regions in the sample. The G' Raman feature originates from a double resonance process of two optical phonons at the K-point which is very sensitive to changes in the graphene band structure. A larger number of allowed electronic transitions in bilayer graphene broaden the G' band which agrees with our observation. The absence of a sharp transition between single-layer and bilayer graphene between individual Raman spectra indicates that even in samples with high particle densities, both bilayer and single-layer graphene can be found within a laser spot of 5 μm diameter.

This observation agrees with previous reports that particles initiate growth of bilayer graphene due to local supersaturation by methane and subsequent nucleation of a second graphene layer [10]. These graphene layers, however, are small compared to the single-layer regions, and no effect of their presence on electrical transport was found.

This finding is significant, since several reports highlight the correlation of increased particle density with the formation of smaller graphene grains [9, 12]. The lacking strong

trend of graphene defectiveness or carrier mobility with particle density, however, does not support that conclusion. Instead, the observation confirms results by Tsen et al. [13] tailoring electrical transport across grain boundaries in polycrystalline graphene that intergrain carrier transport is not the limiting factor for the film mobility for well connected grains.

Surprisingly, however, we observe a strong correlation of the substrate waviness with the carrier mobility of the grown graphene (Figure 2(b)). It can be seen that beyond a critical value of ~ 70 nm, the carrier mobility decreases rapidly with waviness. This behaviour can be explained when examining the graphene growth process during CVD. Hydrocarbons are adsorbed on the Cu substrate and diffuse on the surface until they attach to the edge of an existing graphene grain or a step edge [14]. In the case of samples with larger waviness, more step edges occur. These features act as obstacles for high-quality graphene growth and instead form disordered graphitic regions. The presence of disordered graphene regions can have two effects. First, carrier transport through these regions proceeds less efficiently, and the overall mobility of the graphene film deteriorates. Even if the disordered material is not integrated in the graphene film but only positioned in contact with pristine graphene, it can produce additional carrier scattering through charged impurities, phonon coupling, or electrostatic interactions.

In order to confirm the detrimental effects of the waviness on the carrier transport, we chose a second approach to control the substrate waviness independently of the particle density. To achieve this waviness control, we etched copper foil in hydrochloric acid and commercial nickel etchant (TFB) for varying durations between 1 minute and 20 minutes. A clear increase in waviness can be seen for extended etching times (Figure 3(a)). No such trend on etching time was found for the particle density since isotropic erosion occurs in the acid etching process.

In agreement with the previous results shown in Figure 2(b), there is a strong effect of waviness on the carrier mobility (Figure 3(b)). Consequently, the sheet resistance, which is commonly used as a figure of merit, increases with waviness (Figure 3(c)). These observations support our previous hypothesis that an increasing roughness of the Cu

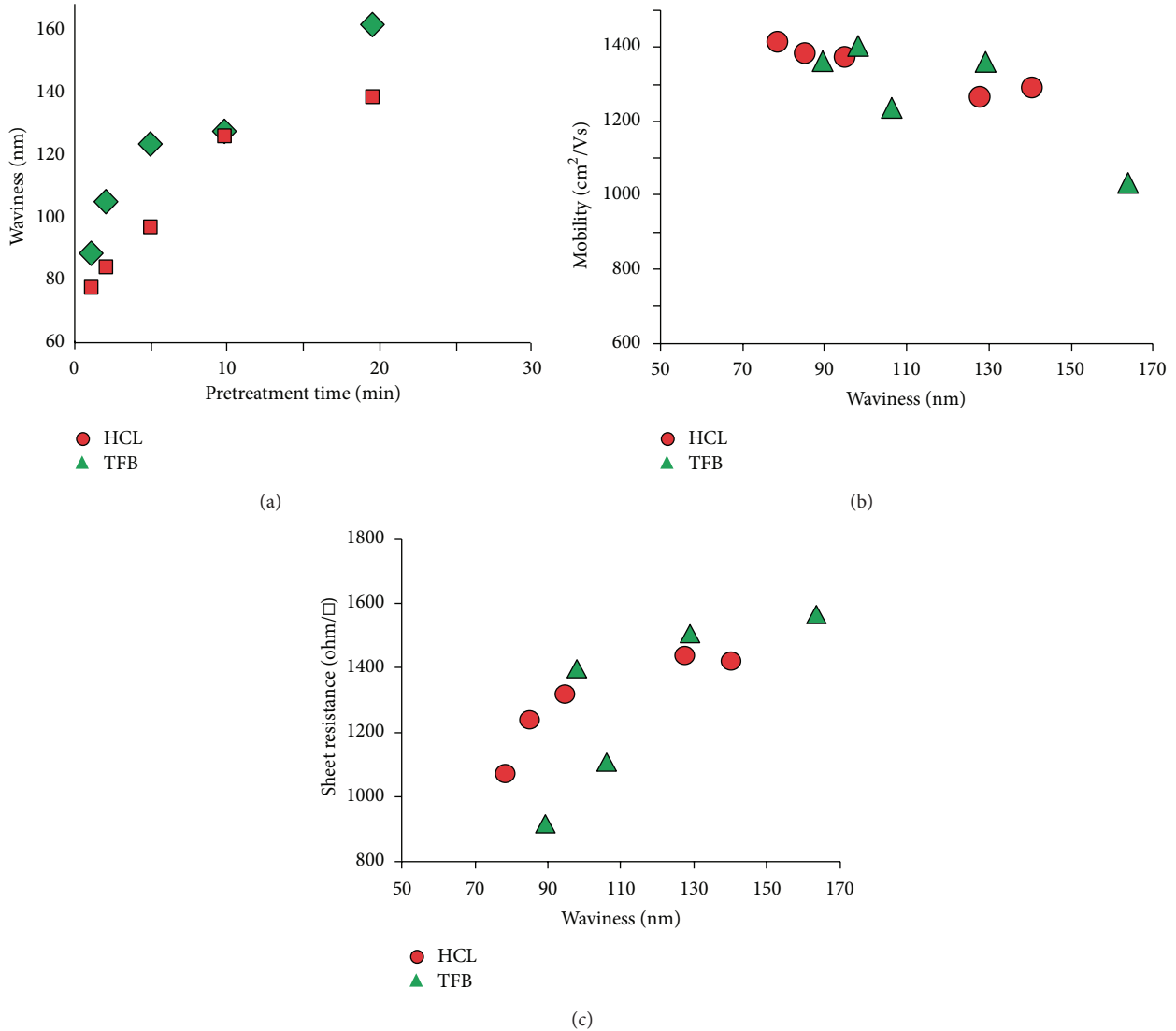


FIGURE 3: Effect of acid pretreatment conditions for 10 different graphene samples: (a) waviness versus etching time, (b) carrier Hall mobility versus waviness, and (c) film sheet resistance versus waviness.

substrate results in larger amounts of defective graphene which impedes carrier transport.

Raman spectroscopy was employed to further confirm this point. We find that longer etching increases the density of dark regions in the graphene film as seen when comparing Figures 4(a) and 4(b). The growth conditions for these two samples were the same while Cu foil was treated with 1 min acid (TFB) and 20 mins, respectively. Micro-Raman spectra of these dark regions reveal a higher D-band and G-band intensity at asimilar G' -band intensity. We conclude that the dark regions contain two types of carbon. The G' -band and part of the G-band originate from graphene, that is, growing from undamaged Cu regions and bridging the rough Cu areas. The D-band and the remainder of the G-band, however, come from defective graphene grown in the rough Cu areas. Consequently, the difference between Raman spectra obtained in the dark region and the pristine graphene

exhibits a pronounced D-band and a defect induced D' -band [15] akin to highly defective graphene (see inset Figure 4(c)).

4. Conclusion

In conclusion, we have analyzed the effect of catalyst surface morphology on the quality of graphene grown by CVD. We find that electropolishing can efficiently decrease the long wavelength roughness, or waviness, but at the expense of nanoparticle formation. These nanoparticles affect the probability of bilayer formation but have negligible effect on the electrical performance of the grown graphene. Increasing waviness, on the other hand, deteriorates the graphene quality and performance significantly as confirmed by etching experiments. Raman spectroscopy suggests that defective graphitic regions are forming in the high roughness areas

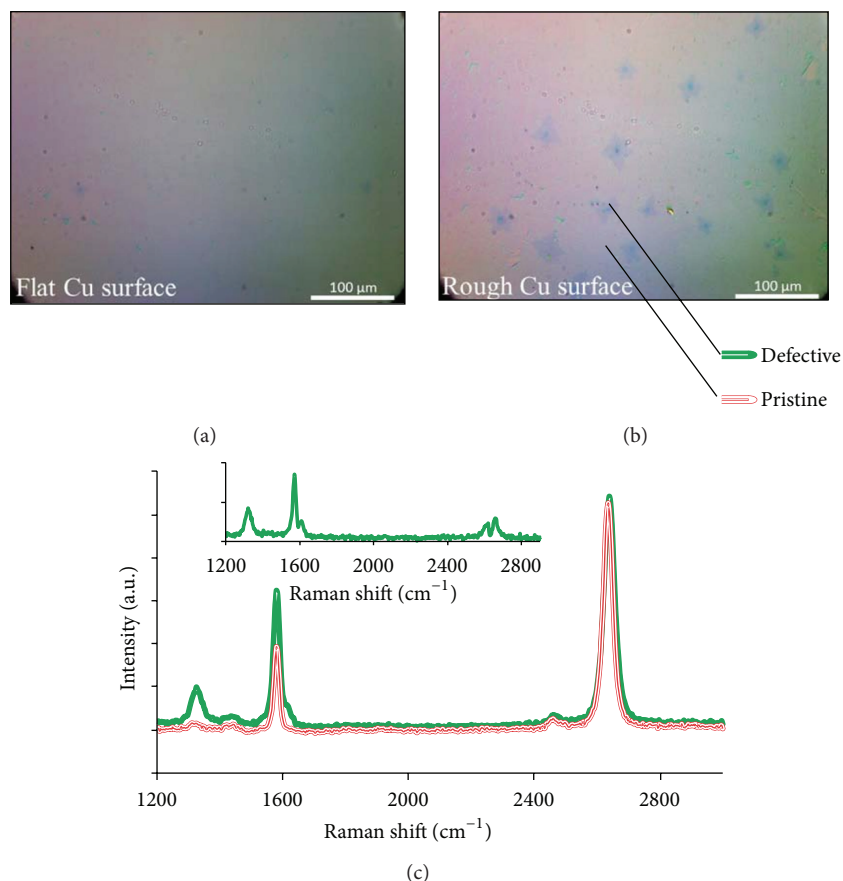


FIGURE 4: Graphene morphology upon acid etching. (a) and (b) Optical microscope images of graphene grown on (a) Cu foil with 1 min acid (TFB) treated and (b) 20 mins acid (TFB) treated Cu foil. (c) Raman spectra of dark and bright regions as indicated (inset: difference of spectra).

with detrimental effect on carrier mobility and sheet resistance.

These findings provide better insight into challenges for graphene formation but also suggest the limited importance of surface contaminants in the graphene formation process.

Acknowledgments

The authors acknowledge the financial support by the National Science Council, Taiwan, and the (Department of Industrial Technology) Ministry of Economic Affairs, Taiwan.

References

- [1] F. Xia, T. Mueller, R. G. Mojarad et al., "Photocurrent imaging and efficient photon detection in a graphene transistor," *Nano Letters*, vol. 9, no. 3, pp. 1039–1044, 2009.
- [2] X. Wang, L. Zhi, and K. Mullen, "Transparent, conductive graphene electrodes for dye-sensitized solar cells," *Nano Letters*, vol. 8, no. 1, pp. 323–327, 2008.
- [3] X. Li, H. Zhu, K. Wang et al., "Graphene-on-silicon schottky junction solar cells," *Advanced Materials*, vol. 22, no. 25, pp. 2743–2748, 2010.
- [4] S. L. Avila, K. M. Poulsen, R. Yakimova et al., "Non-Volatile photochemical gating of an epitaxial graphene/polymer heterostructure," *Advanced Materials*, vol. 23, no. 7, pp. 878–882, 2011.
- [5] A. Reina, X. Jia, J. Ho et al., "Large area, few-layer graphene films on arbitrary substrates by chemical vapor deposition," *Nano Letters*, vol. 9, no. 1, pp. 30–35, 2009.
- [6] L. Zhao, K. T. Rim, H. Zhou et al., "Influence of copper crystal surface on the CVD growth of large area monolayer graphene," *Solid State Communications*, vol. 151, no. 7, pp. 509–513, 2011.
- [7] Z. Luo, Y. Lu, D. W. Singer et al., "Effect of substrate roughness and feedstock concentration on growth of wafer-scale graphene at atmospheric pressure," *Chemistry of Materials*, vol. 23, no. 6, pp. 1441–1447, 2011.
- [8] Z. Yan, J. Lin, Z. Peng et al., "Toward the synthesis of wafer-scale single-crystal graphene on copper foils," *American Chemical Society Nano*, vol. 6, no. 10, pp. 9110–9117, 2012.
- [9] H. Kim, C. Mattevi, M. R. Calvo et al., "Activation energy paths for graphene nucleation and growth on Cu," *American Chemical Society Nano*, vol. 6, no. 4, pp. 3614–3623, 2012.
- [10] B. Zhang, W. H. Lee, R. Piner et al., "Low-temperature chemical vapor deposition growth of graphene from toluene on electropolished copper foils," *American Chemical Society Nano*, vol. 6, no. 3, pp. 2471–2476, 2012.

- [11] G. L. Wynick and C. J. Boehlert, "Use of electropolishing for enhanced metallic specimen preparation for electron backscatter diffraction analysis," *Materials Characterization*, vol. 55, no. 3, pp. 190–202, 2005.
- [12] M. Hofmann, Y. C. Shin, Y. P. Hsieh, M. S. Dresselhaus, and J. Kong, "A facile tool for the characterization of two-dimensional materials grown by chemical vapor deposition," *Nano Research*, vol. 5, no. 7, pp. 504–511, 2012.
- [13] A. W. Tsen, L. Brown, M. P. Levendorf et al., "Tailoring electrical transport across grain boundaries in polycrystalline graphene," *Science*, vol. 336, no. 6085, pp. 1143–1146, 2012.
- [14] E. Loginova, N. C. Bartelt, P. J. Feibelmarr, and K. F. McCarty, "Factors influencing graphene growth on metal surfaces," *New Journal of Physics*, vol. 11, Article ID 063046, 2009.
- [15] M. A. Pimenta, G. Dresselhaus, M. S. Dresselhaus, L. G. CanÇado, A. Jorio, and R. Saito, "Studying disorder in graphite-based systems by Raman spectroscopy," *Physical Chemistry Chemical Physics*, vol. 9, pp. 1276–1290, 2007.

Research Article

Effects of Increasing Electrodes on CNTs Yield Synthesized by Using Arc-Discharge Technique

Samy Yousef,¹ A. Khattab,² T. A. Osman,² and M. Zaki¹

¹ Department of Production Engineering and Printing Technology, Akhbar Elyom Academy, Giza 12566, Egypt

² Department of Mechanical Design and Production Engineering, Cairo University, Giza 12566, Egypt

Correspondence should be addressed to Samy Yousef; ahcann@hotmail.com

Received 14 January 2013; Revised 25 April 2013; Accepted 7 May 2013

Academic Editor: Nadya Mason

Copyright © 2013 Samy Yousef et al. This is an open access article distributed under the Creative Commons Attribution License, which permits unrestricted use, distribution, and reproduction in any medium, provided the original work is properly cited.

A new design of fully automatic system was built up to produce multiwalled carbon nanotube (MWCNT) using arc discharge technique in deionized water and extra pure graphite multiple electrodes (99.9% pure). The goal of the experimental research is to determine the yield of CNT in two different cases: (a) single plasma electrodes and (b) multiplasma electrodes, particularly 10 electrodes. The experiments were performed at constant parameters (75 A, 238 V). The obtained CNT was examined by scanning electron microscope (SEM), transmission electron microscope (HRTEM), X-ray diffraction (XRD), and thermogravimetric analysis (TGA). The results showed that the produced CNT is of type MWCNT, with a diameter of 5 nm, when using multiplasma electrodes and 13 nm when using single plasma electrodes. The yield of MWCNT was found to be 320% higher in case of comparing multielectrodes to that of single plasma electrodes. Under the experimental test conditions, a yield of 0.6 g/hr soot containing 40% by mass nanotube was obtained in case of single plasma electrodes and above 60% in case of multiplasma electrodes.

1. Introduction

Carbon nanotubes (CNTs) were observed in 1991 by Iijima who employed a method used to fabricate C60 fullerenes [1]. The properties and characteristics of CNTs are still being researched heavily and scientists have barely begun to tap the potential of these structures. CNTs have many unique and remarkable properties (chemical, physical, electrical, mechanical, and biomedical), which make them desirable for many applications, such as electronics, biology, medicine, energy, materials engineering, and aero science [2, 3]. Therefore, CNT yield production is very important because it controls the price of the product. Rajashree et al. (2009) and Chai et al. (2004) reviewed in detail CNT technology and its applications [4–6]. The common different methods for synthesis CNT are arc discharge [7–17], laser vaporization [18], and chemical vapor deposition (CVD) [19–21]. Among several methods for preparing CNT, the arc discharge is the most practical method for scientific purposes because it yields highly graphitized tubes due to the high process

temperature [22]. Multiwalled carbon nanotube (MWCNT) produced by electric arc discharge method is highly crystalline and exhibits fewer defects than MWNT produced by other methods [23, 24]. In the arc discharge method, a voltage is applied across two graphite rods as electrodes. Carbon from the anode vaporizes and condenses on the cathode as nanotube, amongst other forms of carbon [25]. To increase the yield and the purity of CNT by arc discharge, many research works have been devoted to study the rate of yielding through the investigation of various effective parameters such as submerged media, current intensity, applied voltage, electrode size, and electrode movement speed [26–32]. After production of the nanoparticles, a purification method by sonication and centrifugal separation will be conducted. In the present research, a number of electrodes are used in a fully automatic system in order to produce MWCNT, using arc discharge technique in deionized water. The results are compared in terms of the yield and purification of the CNT, in addition to the thermal resistance with that of conventional single electrode.

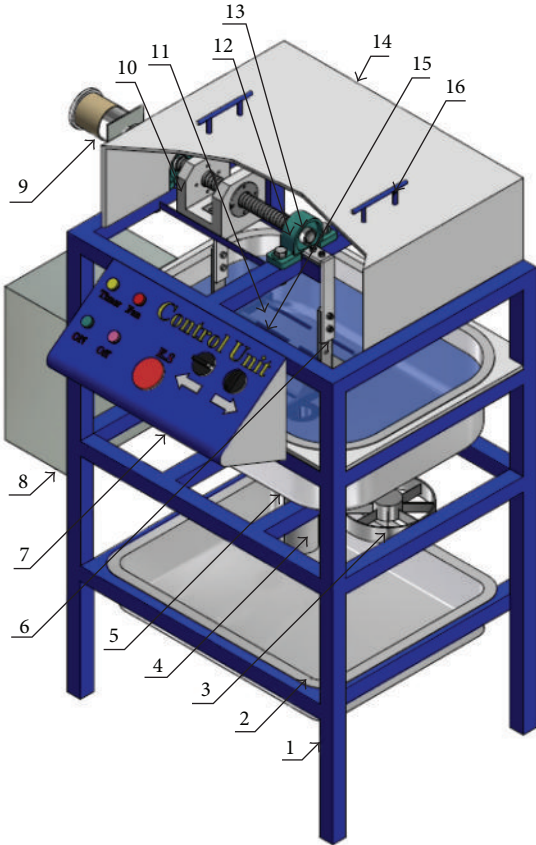
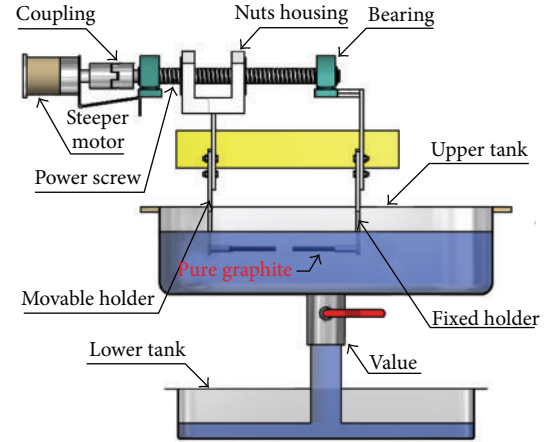


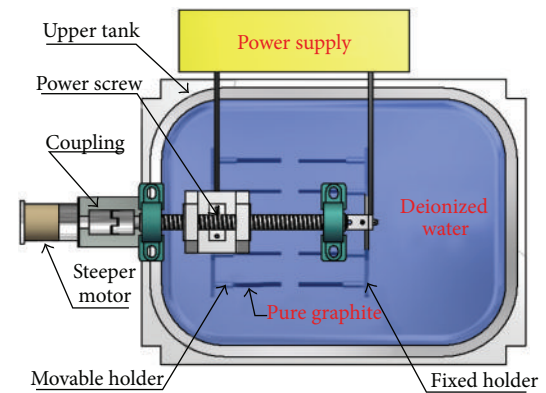
FIGURE 1: View of the fully automatic machine for producing CNTs. (1) Base frame, (2) lower tank, (3) fans for cooling, (4) valve, (5) upper tank, (6) carbon holder, (7) control unit, (8) electrical unit, (9) stepper motor, (10) nuts housing, (11) deionized water, (12) power screw, (13) bearing, (14) cover, (15) pure graphite, (16) cover hand.

2. Experimental

MWCNT was synthesized by a fully automatic designed apparatus using arc discharge technique in deionized water without catalyst at two different cases a single electrode and ten electrodes. The advantages of this apparatus compared to the existing arc discharge method are that it represents a cheap method equipped with fully automatic system. The gap between the electrodes can be set automatically by using a timer which results in an increase yield of carbon nanotubes. Figure 1 illustrates a view of the designed and manufactured machine. Five electrodes are clamped with left movable holder as cathodes which are moved by used power screw connected with stepper motor through an oldham coupling. Other five electrodes are clamped with the right fixed holder as anodes, as shown in Figure 2. A timer giving a signal to the stepper motor after every 70 seconds to compensate the electrodes consumption, the interval (70 seconds), has been identified experimentally. The height of the two holders can be adjusted by two bolts; Yousef et al. (2012) reviewed with details the designed system and its experimental procedure [33].



(a) Front view



(b) Top view

FIGURE 2: Clamping the two electrodes in holders and phases of the bright plasma formation; (a) clamping the two electrodes, (b) gap set, (c) initial plasma, and (d) formed fully bright plasma.

TABLE 1: Experimental conditions for single plasma electrodes case.

| Parameters | Single plasma electrodes |
|--------------------|---|
| Number of cathodes | One graphite electrodes with \varnothing 6 mm |
| Number of anodes | One graphite electrodes with \varnothing 6 mm |
| Applied voltage | 238 V |
| Electric current | 75 A (AC arc-discharge) |
| Environment | Cooling air, deionized water, and room temp. |

2.1. Synthesizing MWCNT Using Single Plasma Electrodes. Two electrodes are used in this experiment. The two pure graphite electrodes are clamped to the fixed and movable holders presenting one electrode as a cathode and another as anode, as shown in Figure 3(a). The experiment has been performed under AC arc discharge, 75 A and 238 V. The arc discharge and the resulted plasma are shown in Figures 3(b)–3(d), respectively. Table 1 summarizes the processing parameters used in this research work.

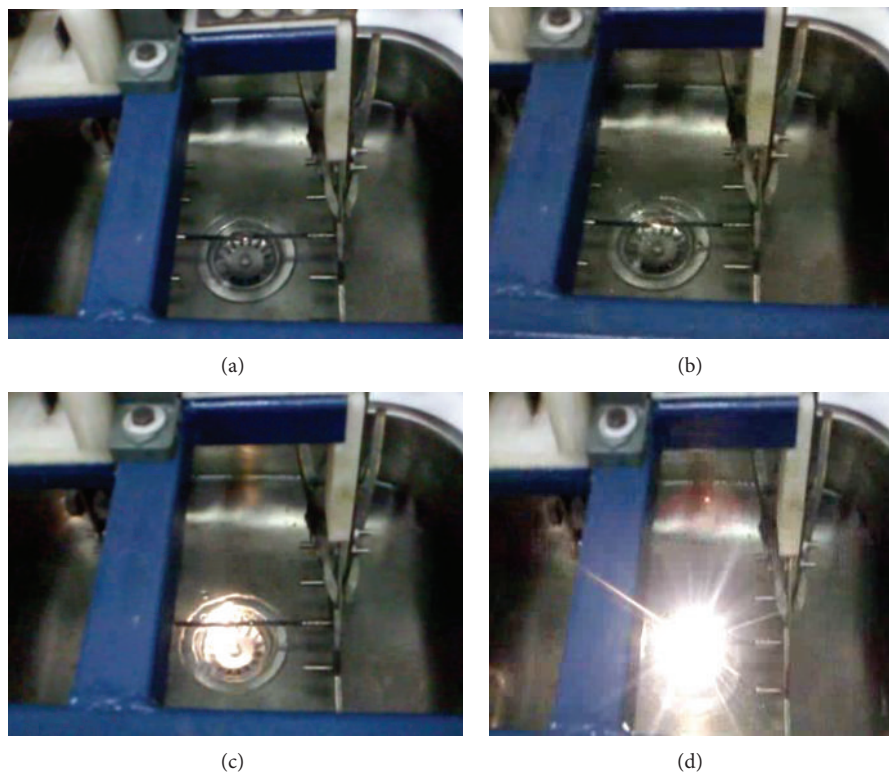


FIGURE 3: Clamping the two electrodes in holders and phases of the bright plasma formation.

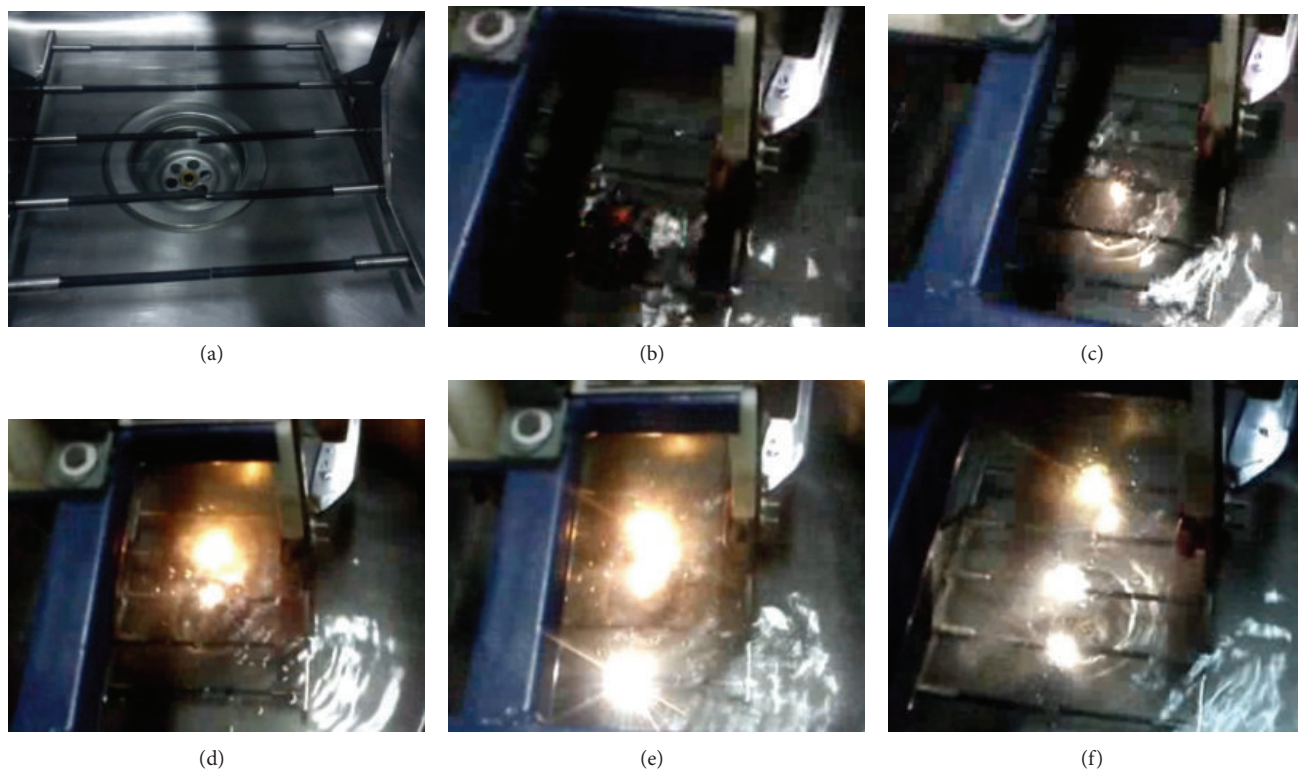


FIGURE 4: Continued.



FIGURE 4: Clamping the electrodes in fixed and movable holders and the bright plasma region between the multi plasma electrodes; (a) clamping the electrodes, (b) gap set, (c) initial plasmas, (d) Bright plasmas, (e) two bright plasma, (f) three bright plasma, (g) four bright plasma and (h) formed a fully bright plasma.



FIGURE 5: (a) Formed nanoparticles; (b) evaporation of the distilled water.

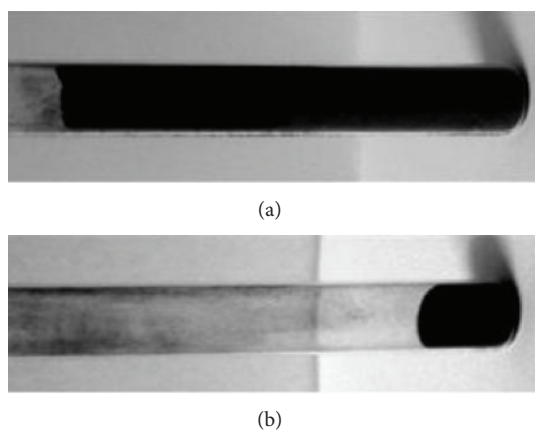


FIGURE 6: Fully dry soot at (a) multiplasma electrodes and (b) single plasma electrodes.

2.2. Synthesizing MWCNT Using Multiplasma Electrodes. Ten electrodes are used in this experiment. Clamping the ten pure graphite electrodes, five electrodes as cathodes, and five as anodes in the fixed and movable holders, respectively, as shown in Figure 4(a), the experiment is performed under

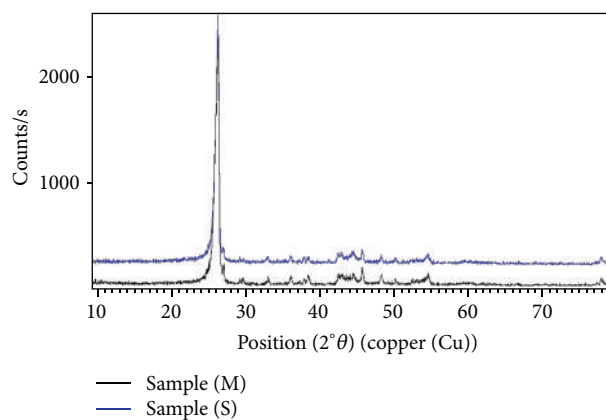
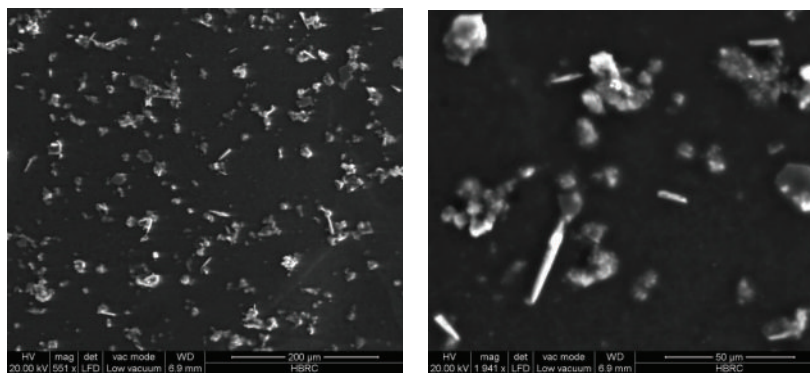
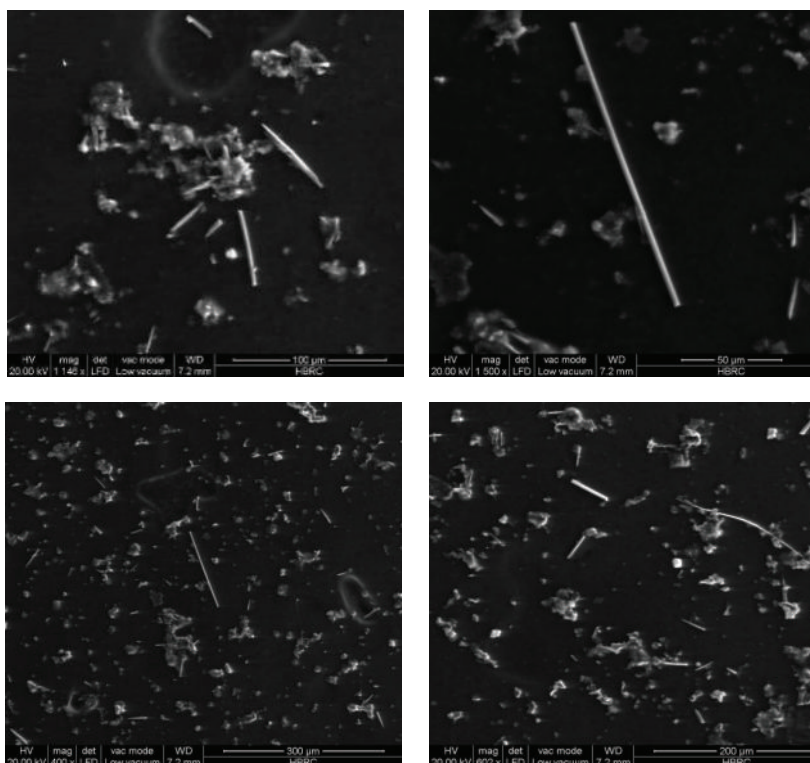


FIGURE 7: XRD pattern of MWNT at single and multi plasma electrodes.

the conditions of AC arc discharge, 75 A and 238 V, for all electrodes. The arc discharge in this case and the resulted plasma are shown in Figures 4(b)–4(h), respectively. Table 2 summarizes the processing parameters used in this case. In order to reach the strong bright plasma in the multiplasma arc discharge technique, the electrodes must be submerged to



(a) SEM micrograph of MWNT at single plasma electrode case



(b) SEM micrograph of MWNT at multiplasma electrodes case

FIGURE 8: SEM images of a synthesized CNT for the studied cases.

a depth of 30 mm in deionized water. The fixed gap between the faced electrodes is 1 mm. After clamping the multi electrodes in the two holders, the gap between the electrodes ends is set to a distance of 1 mm from the control unit. Due to the holders assembly manufacturing and electrode dimensions and sizes in terms of tolerances and allowances and probability of small misalignment of electrodes centre, the gaps between all electrodes are not equal. Therefore, the bright plasma generated will not complete until the gaps between all electrodes reach exactly 1 mm. Timer was used to give a signal to the stepper motor every interval of 70 seconds to compensate the electrodes wear.

3. Sample Preparation

The generated nano particles can be divided into two types: carbon nano particles that float on the water surface and sediment products, as shown in Figure 5(a). Due to the use of a large quantity of deionized water (about 13 liters) in each experiment, it was found that it is difficult to separate CNT from the deionized water by direct centrifugal. Therefore, it is decided to evaporate the water initially by heating until obtaining about 0.25 liters as shown in Figure 5(b), then to separate CNT by the centrifugal effect. A centrifugal separation device designated L-530 is found sufficient to concentrate the MWCNT. The purification is achieved by successive

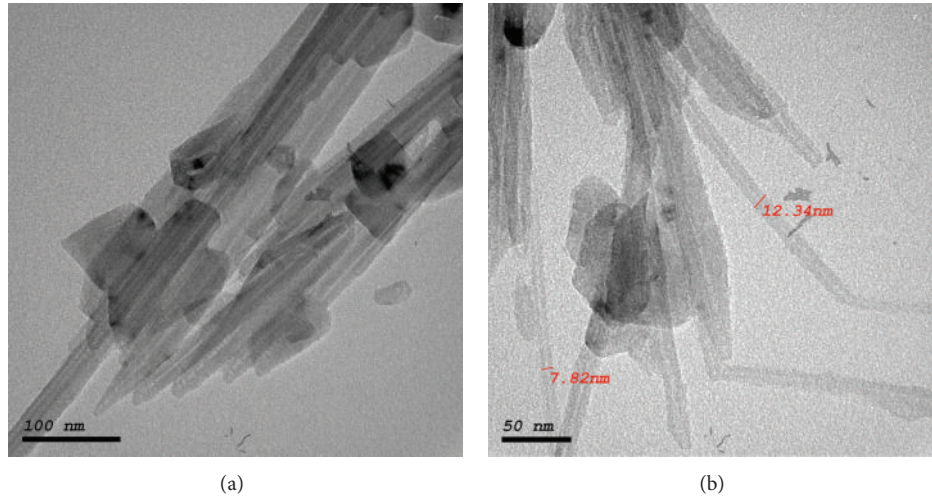


FIGURE 9: HRTEM image of single plasma electrodes case.

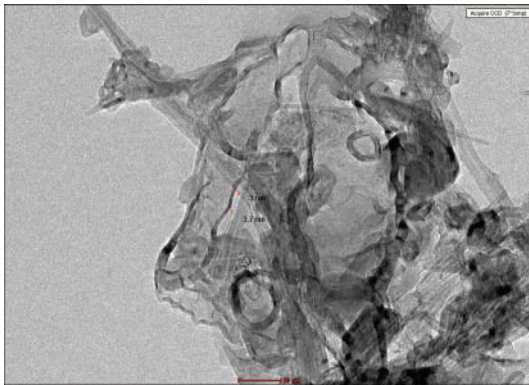


FIGURE 10: HRTEM image of multiplasma electrodes case before oxidation.

separation and decantation by using the centrifugal effect. CNT crude with distilled water was put in the glass tubes in the apparatus with running speed of 4000 rpm for 8 minutes. Due to the high specific gravity, the particles precipitated in the bottom of the glass tubes. After getting rid of the water, the precipitated particles were grouped in one glass tube. The tube was then placed in a furnace at a suitable temperature for fully soot drying as to shown in Figure 6. To find the yield of CNT, soot was heated in a close furnace up to 600°C for 2 hours [34–36] then weighed, the soot was weighed before and after oxidation and the percentage weight loss was calculated.

4. Results and Discussion

The morphology of MWCNT synthesized by a new design and the degree of purification were observed by SEM BPI-T as well as HRTEM: JEM-2100 and X-ray diffraction (XRD) and Shimadzu TGA-50H for the two different cases; single and multiplasma electrodes were evaluated.

TABLE 2: Experimental conditions for multiplasma electrodes case.

| Parameters | Multiplasma electrodes |
|--------------------|--|
| Number of cathodes | 5 Graphite Electrodes with Ø 6 mm |
| Number of anodes | 5 Graphite Electrodes with Ø 6 mm |
| Applied voltage | 238 V |
| Electric current | 75 A (AC arc discharge) for all electrodes |
| Environment | Cooling air, deionized water, and room temp. |

4.1. X-Ray Diffraction. X-ray diffraction (XRD) is known to be the best method for characterization of CNT structures. Figure 7 shows the XRD pattern of the purified CNT for the two studied cases. At the single plasma electrodes case the strong and sharp reflection peak was found at 26.388° and for the case of multi electrode at 26.398°. The presence of these peaks in the XRD pattern of CNT indicates the concentric cylindrical nature of graphene sheets nested together and the nanotubes are multi-walled in nature [37].

4.2. Scanning Electron Microscope. Figure 8 illustrates the SEM images of a synthesized CNT at single and multi plasma electrodes. It is clear from the figure that aligned needles tubes resembling spaghetti shape were produced. It is worth noting that the percentages of aligned needle at multi electrodes are much larger than single plasma electrodes. For the purity of MWCNTs, by quantifying the percentage of unwanted materials per unit area within the sample SEM images, it is possible to estimate a degree of purity (e.g., 90% tubular material, 5% spherical particles, and 5% irregular objects) [38], the results have indicated that about 55% (single plasma case) and 70% (multi plasma case) were obtained as shown in Figures 8(a)-8(b), respectively.

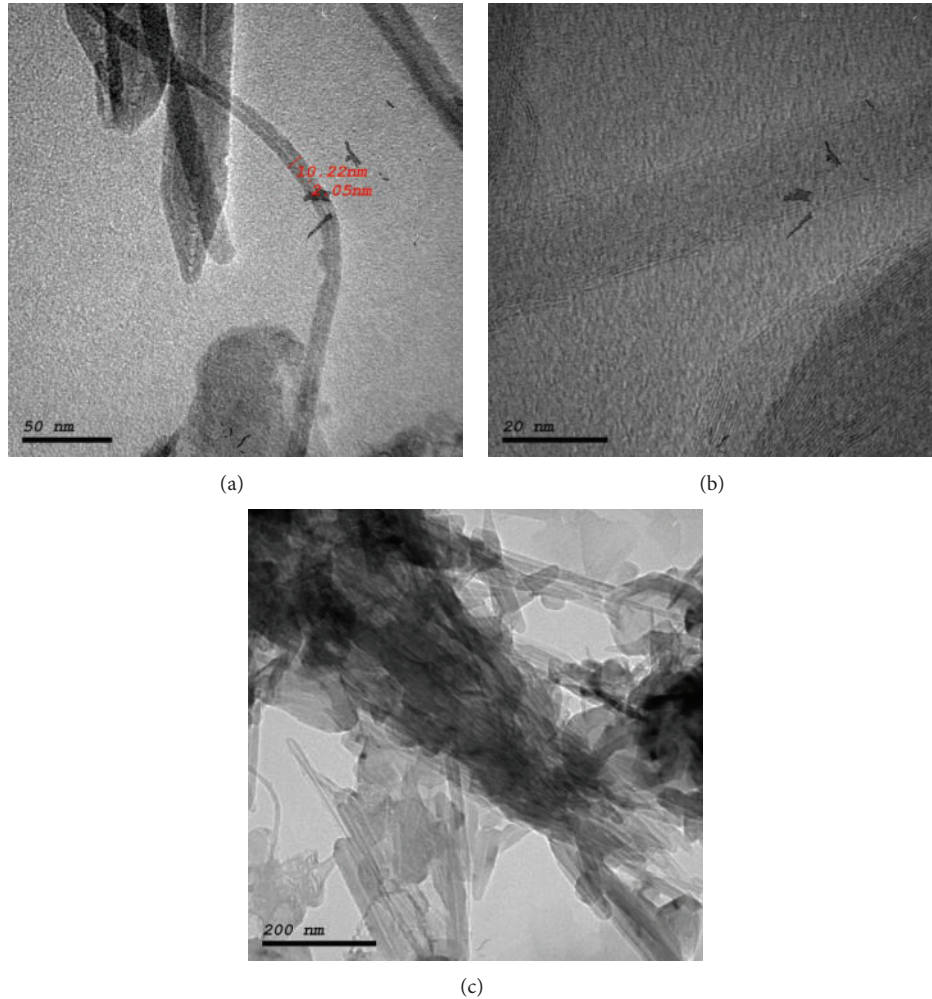


FIGURE 11: HRTEM image at multi plasma electrodes case after oxidation.

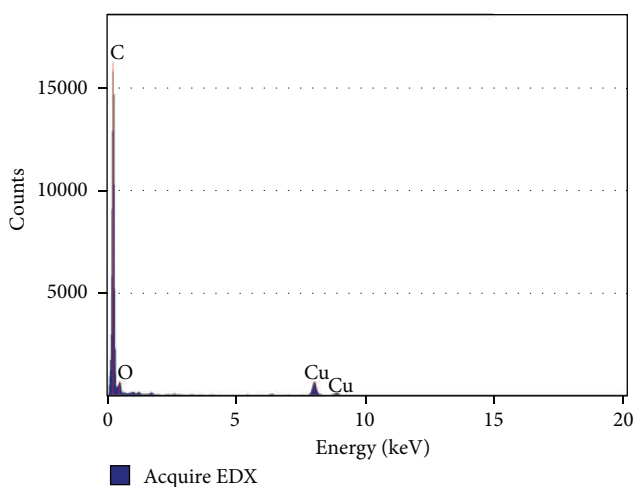


FIGURE 12: EDX analysis shows the high purity carbon.

4.3. High-Resolution Transmission Electron Microscope. HRTEM, JEM-2100, operating at 200 kV was used to characterize the MWNT synthesized for the two studied cases.

At single plasma electrodes case, the TEM images have demonstrated that the resulted was typically of 7–20 nm in diameter, as shown in Figure 9. On the other hand, for the multi plasma electrode CNTs were typically of 3–10 nm in diameter with configuration of nanotubes ends (capped) as shown in Figures 10 and 11. The inset shows the elemental analysis (EDX) which reveal that the total raw samples synthesized for the investigated cases were of highly purity and of good crystallinity. This refers to that there were no other elements found in the analysis, except some minute copper element which resulted from the copper gird in TEM device, as shown in Figure 12.

4.4. Thermogravimetric Analysis. The thermal stability of the synthesized CNT on all samples was analyzed by the thermo gravimetric analysis (TGA). Figure 13 shows the result of the TGA for the studied cases. There is no difference in the diminishing temperature for CNT which were synthesized at single plasma electrodes and multi-plasma electrodes. The graphitic particles started to oxidize at high temperature of about 600°C. On the other hand, the weight loss in the single

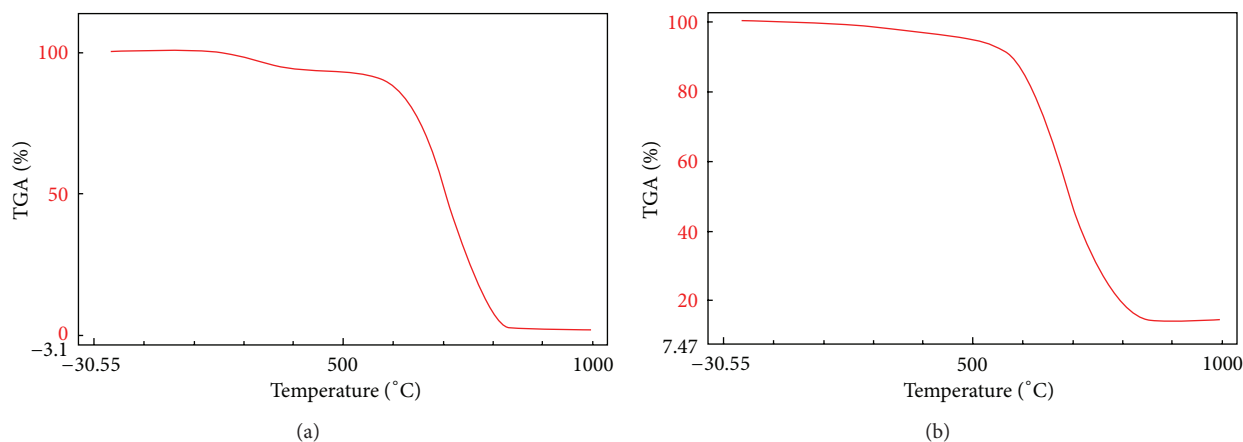


FIGURE 13: Result of the TGA for (a) single plasma electrodes and (b) multi plasma electrodes.

plasma electrodes is found to be 17% higher in the case of multi plasma electrodes. Thus, the thermal resistance for the multi electrodes was better than that of the single plasma electrodes.

5. Conclusion

The fabrication of MWCNT was achieved by a new designed “fully automatic system” for producing it by using AC arc discharge technique in deionized water for two different cases, the first is single plasma and the second is multi plasma electrodes. The experimental conditions of tests were: 75 A and 238 V which produce CNT of 5 nm in diameter. The total yield in this research was observed to be dependent on the number of the electrodes used in the experiment. The yield of MWCNT in the case of multi electrodes is found to be 320% higher than that of single plasma electrodes before oxidation. After oxidation, the ratio was found to be nearly the same. Furthermore, it was found that the purity of MWCNT for single plasma electrodes was 40% yielding with 0.6 g/hr. On the other hand, the purity of MWCNT for multi plasma electrodes was found to be more than 70% yielding with 2 g/hr.

References

- [1] S. Iijima, “Helical microtubules of graphitic carbon,” *Nature*, vol. 354, pp. 56–58, 1991.
- [2] H. Shimoda, L. Fleming, K. Horton, and O. Zhou, “Formation of macroscopically ordered carbon nanotube membranes by self-assembly,” *Physica B*, vol. 323, no. 1–4, pp. 135–136, 2002.
- [3] P. G. Collins and P. Avouris, “Chapter 3 the electronic properties of carbon nanotubes,” *Contemporary Concepts of Condensed Matter Science*, vol. 3, pp. 49–81, 2008.
- [4] H. Rejashree, Y. Manohr, G. Harshal, V. Mohit, and K. Vilasro, “Carbon nanotubes and its applications,” *Pharmaceutical and Clinical Research*, vol. 2, pp. 0974–2441, 2009.
- [5] S. Chai, S. Zein, and A. Mohamed, *A Review on Carbon Nanotubes Production Via Catalytic Methane Decomposition*, NAPCOI, 2004.
- [6] J. Prasek, J. Drbohlavova, J. Chomoucka et al., “Methods for carbon nanotubes synthesis—review,” *Journal of Materials Chemistry*, vol. 21, no. 40, pp. 15872–15884, 2011.
- [7] C. Journet, W. K. Maser, P. Bernier et al., “Large-scale production of single-walled carbon nanotubes by the electric-arc technique,” *Nature*, vol. 388, no. 6644, pp. 756–758, 1997.
- [8] T. Sugai, H. Omote, S. Bandow, N. Tanaka, and H. Shinohara, “Production of fullerenes and single-wall carbon nanotubes by high-temperature pulsed arc discharge,” *Journal of Chemical Physics*, vol. 112, no. 13, pp. 6000–6005, 2000.
- [9] Y. Liu, S. Xiaolong, Z. Tingkai, Z. Jiewu, M. Hirscher, and F. Philipp, “Amorphous carbon nanotubes produced by a temperature controlled DC arc discharge,” *Carbon*, vol. 42, no. 8–9, pp. 1852–1855, 2004.
- [10] T. Zhao, Y. Liu, and J. Zhu, “Temperature and catalyst effects on the production of amorphous carbon nanotubes by a modified arc discharge,” *Carbon*, vol. 43, no. 14, pp. 2907–2912, 2005.
- [11] M. Cadek, R. Murphy, B. McCarthy et al., “Optimisation of the arc-discharge production of multi-walled carbon nanotubes,” *Carbon*, vol. 40, no. 6, pp. 923–928, 2002.
- [12] Y. Liu, S. Xiaolong, Z. Tingkai, Z. Jiewu, M. Hirscher, and F. Philipp, “Amorphous carbon nanotubes produced by a temperature controlled DC arc discharge,” *Carbon*, vol. 42, no. 8–9, pp. 1852–1855, 2004.
- [13] H. Qiu, Z. Shi, L. Guan et al., “High-efficient synthesis of double-walled carbon nanotubes by arc discharge method using chloride as a promoter,” *Carbon*, vol. 44, no. 3, pp. 516–521, 2006.
- [14] R. B. Mathur, S. Seth, C. Lal et al., “Co-synthesis, purification and characterization of single- and multi-walled carbon nanotubes using the electric arc method,” *Carbon*, vol. 45, no. 1, pp. 132–140, 2007.
- [15] S.-D. Wang, M.-H. Chang, J.-J. Cheng, H.-K. Chang, and K. M.-D. Lan, “Unusual morphologies of carbon nanoparticles obtained by arc discharge in deionized water,” *Carbon*, vol. 43, no. 6, pp. 1322–1325, 2005.
- [16] A. Qader, A. S. Keiteb, and M. A. Jaleel, “Synthesis of carbon nanomaterials in deionized water with and without catalyst using arc discharge technique,” *Engineering Technician*, vol. 29, no. 2, 2011.
- [17] A. Aqel, K. M. M. A. El-Nour, R. A. A. Ammar, and A. Al-Warthan, “Carbon nanotubes, science and technology part (I) structure, synthesis and characterisation,” *Arabian Journal of Chemistry*, vol. 5, no. 1, pp. 1–23, 2012.

- [18] A. Thess, R. Lee, P. Nikolaev et al., "Crystalline ropes of metallic carbon nanotubes," *Science*, vol. 273, no. 5274, pp. 483–487, 1996.
- [19] M. J. Y. Yacaman, M. M. Yoshida, and L. Rendon, "Catalytic growth of carbon microtubules with fullerene structure," *Applied Physics Letters*, vol. 62, no. 2, pp. 202–204, 1993.
- [20] G. Che, B. B. Lakshmi, C. R. Martin, E. R. Fisher, and R. S. Ruoff, "Chemical vapor deposition based synthesis of carbon nanotubes and nanofibers using a template method," *Chemistry of Materials*, vol. 10, no. 1, pp. 260–267, 1998.
- [21] H. W. Zhu, C. L. Xu, D. H. Wu, B. Q. Wei, R. Vajtai, and P. M. Ajayan, "Direct synthesis of long single-walled carbon nanotube strands," *Science*, vol. 296, no. 5569, pp. 884–886, 2002.
- [22] M. Keidar and A. M. Waas, "On the conditions of carbon nanotube growth in the arc discharge," *Nanotechnology*, vol. 15, no. 11, pp. 1571–1575, 2004.
- [23] N. Grobert, "Carbon nanotubes—becoming clean," *Materials Today*, vol. 10, no. 1-2, pp. 28–35, 2007.
- [24] M. Ishigami, J. Cumings, A. Zettl, and S. Chen, "A simple method for the continuous production of carbon nanotubes," *Chemical Physics Letters*, vol. 319, no. 5-6, pp. 457–459, 2000.
- [25] Y. S. Park, K. S. Kim, H. J. Jeong, W. S. Kim, J. M. Moon, K. H. An et al., "Low pressure synthesis of single-walled carbon nanotubes by arc discharge," *Synthetic Metals*, vol. 126, no. 2-3, pp. 245–251, 2002.
- [26] M. Teymourzadeh and H. Kangarlou, "Synthesis of multi-walled carbon nanotubes in an arc discharge using hydrocarbons precursor as carbon sources," *Sciences*, vol. 18, no. 7, pp. 879–883, 2012.
- [27] Z. Shi, Y. Lian, X. Zhou et al., "Mass-production of single-wall carbon nanotubes by arc discharge method," *Carbon*, vol. 37, no. 9, pp. 1449–1453, 1999.
- [28] M. Jahanshahi, M. Shariaty-Niassar, A. A. Rostami, H. Molavi, and F. Toubi, "Arc-discharge carbon nanotube fabrication in solution: electrochemistry and voltametric tests," *Australian Journal of Basic and Applied Sciences*, vol. 4, no. 12, pp. 5915–5922, 2010.
- [29] H. W. Zhu, X. S. Li, B. Jiang et al., "Formation of carbon nanotubes in water by the electric-arc technique," *Chemical Physics Letters*, vol. 366, no. 5-6, pp. 664–669, 2002.
- [30] M. V. Antisari, R. Marazzi, and R. Krsmanovic, "Synthesis of multiwall carbon nanotubes by electric arc discharge in liquid environments," *Carbon*, vol. 41, no. 12, pp. 2393–2401, 2003.
- [31] S. J. Lee, H. K. Baik, J. E. Yoo, and J. H. Han, "Large scale synthesis of carbon nanotubes by plasma rotating arc discharge technique," *Diamond and Related Materials*, vol. 11, no. 3–6, pp. 914–917, 2002.
- [32] L. P. Biro, Z. E. Horvath, L. Szalmas, K. Kertesz, F. Weber, G. Juhasz et al., "Continuous carbon nanotube production in underwater AC electric arc," *Chemical Physics Letters*, vol. 372, no. 3-4, pp. 399–402, 2003.
- [33] S. Yousef, A. khattab, T. A. Osman, and M. Zaki, *Fully Automatic System For Producing Carbon Nanotubes (CNTs) By Using Arc-Discharge Technique Multi Electrodes*, ICIES, 2012.
- [34] P. M. Ajayan, T. W. Ebbesen, T. Ichihashi, S. Iijima, K. Tanigaki, and H. Hiura, "Opening carbon nanotubes with oxygen and implications for filling," *Nature*, vol. 362, no. 6420, pp. 522–525, 1993.
- [35] M. C. Paladugu, K. Maneesh, P. K. Nair, and P. Haridoss, "Synthesis of carbon nanotubes by arc discharge in open air," *Journal of Nanoscience and Nanotechnology*, vol. 5, no. 5, pp. 747–752, 2005.
- [36] R. Joshi, J. Engstler, P. K. Nair, P. Haridoss, and J. J. Schneider, "High yield formation of carbon nanotubes using a rotating cathode in open air," *Diamond and Related Materials*, vol. 17, no. 6, pp. 913–919, 2008.
- [37] M. S. S. Saravanan, S. P. K. Babu, K. Sivaprasad, and M. Jagannatham, "Technoeconomics of carbon nanotubes produced by open air arc discharge method," *Journal of Engineering Science and Technology*, vol. 2, no. 5, pp. 100–108, 2010.
- [38] J. H. Lehman, M. Terrones, E. Mansfield, K. E. Hurst, and V. Meunier, "Evaluating the characteristics of multiwall carbon nanotubes," *Carbon*, vol. 49, no. 8, pp. 2581–2602, 2011.

Research Article

On the Phononic Bandgap of Carbon Nanotubes

Kohei Yamamoto,¹ Hiroyuki Ishii,¹ Nobuhiko Kobayashi,¹ and Kenji Hirose²

¹ Institute of Applied Physics and Tsukuba Research Center for Interdisciplinary Materials Science,
University of Tsukuba, 1-1-1 Tennoudai, Tsukuba, Ibaraki 305-8573, Japan

² Green Innovation Research Laboratory, NEC Corporation, 34 Miyukigaoka, Tsukuba, Ibaraki 305-8501, Japan

Correspondence should be addressed to Nobuhiko Kobayashi; nkoba@bk.tsukuba.ac.jp

Received 14 April 2013; Accepted 4 June 2013

Academic Editor: Nadya Mason

Copyright © 2013 Kohei Yamamoto et al. This is an open access article distributed under the Creative Commons Attribution License, which permits unrestricted use, distribution, and reproduction in any medium, provided the original work is properly cited.

On the phononic bandgap of carbon nanotubes (CNTs), we show in what chirality CNTs have phononic bandgaps and its dependence on the diameters of CNTs. We find that, though the rule where CNTs have phononic bandgaps is the same as in the electronic structure case, the diameter dependence is different. The phononic bandgaps of the zigzag-CNTs reveal “three” kinds of diameter dependence due to the anisotropy of graphene phonon band around the K point in k -space. We also show the crossover from one- to two-dimensional characteristics in phononic bandgaps.

Recently phononic bandgaps attract much attention. Following an analogy of the photonic crystals, in the last decade, artificial crystals with specific structures have been studied systematically to construct the phononic bandgaps since periodic structures might exhibit bandgaps in the band structures for the wave propagation [1]. Since phonon waves cannot propagate in the phononic bandgaps, the materials with effective phononic bandgaps become candidates for the applications of phonon frequency filter (Figure 1(a)), phonon beam splitter, phonon waveguide [2], and sound or vibration protection devices and thermopower waves [3]. Also phononic bandgaps play important roles in view of the reduction of thermal phonon transport, which leads to the effective heat managements [4]. Thus the control and management of phononic bandgaps are very important for various applications and have been widely studied [5].

In this respect, Sigmund and Jensen [6] studied systematic design of phononic bandgaps with topology optimization and Gazonas et al. [7] studied the optimization of phononic bandgap structures using the genetic algorithm. They dealt with sonic or ultrasonic crystals which have midgap frequencies $\omega_g = 10^2$ – 10^6 Hz. Gorishnyy et al. [8] fabricated hypersonic phononic crystals with lithography technique, and Cheng et al. [9] constructed and tuned hypersonic bandgaps in colloidal crystals which have $\omega_g = 10^9$ – 10^{12} Hz.

These phonon bandgap engineering deal with the artificially made phononic crystals. To obtain phononic bandgaps on the higher frequency requires higher skills and techniques for the fabrication, and thus materials which can be easily synthesized and to exhibit selectable hypersonic phononic bandgaps are desired. In this paper, we show that carbon nanotubes (CNTs) [10], which are easily synthesizable, have highest phononic bandgaps with $\omega_g \sim 10^{13}$ Hz. Furthermore the magnitude of phononic bandgaps of CNTs changes from 0 THz to 2 THz according to the diameters.

So far, the electronic structures of CNTs have been studied and shown to exhibit fascinating properties such as extremely high electric conductivity. The band structures of CNTs show appearance and disappearance of bandgaps at the Fermi level depending on the diameter and chirality. Correspondingly, transport properties of CNTs change from metallic to semiconducting ones according to the magnitude of bandgaps [11, 12]. The emergence of bandgaps in the electronic structures can be explained in view of the electronic states of two-dimensional (2D) graphene. While bandgaps in the electronic states of CNTs are well known, those of the phononic band structures are not clearly understood. Here, we focus on the phononic bandgap problem of CNTs.

The phononic band structures of CNTs and graphene are calculated with use of the Brenner interatomic potential [13].

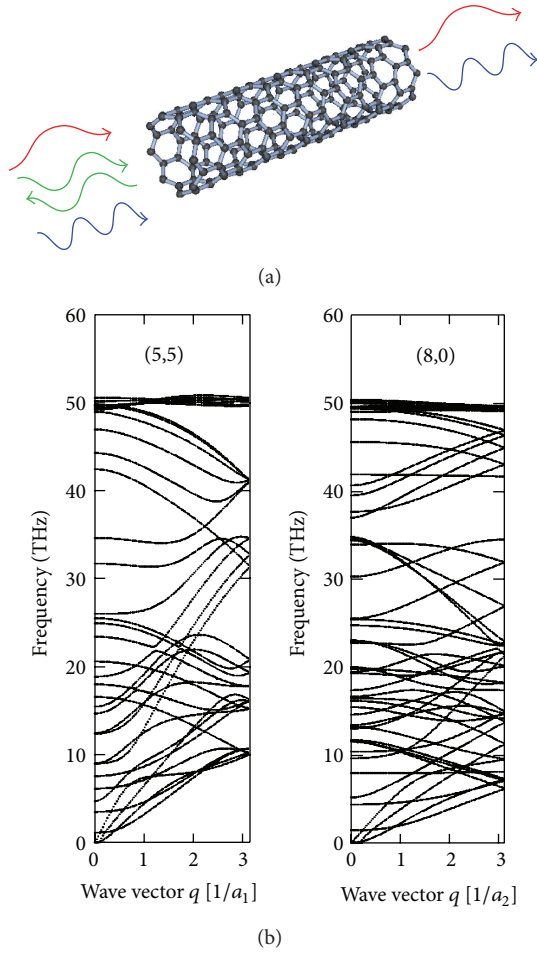


FIGURE 1: (a) Schematic view of (8,0) CNT for an application of elastic wave filter in the particular frequency around 36 THz. (b) Phonon band structures of CNTs with chirality (5,5) (left) and (8,0) (right). We see that (5,5) CNT exhibits no phononic bandgap up to 50 THz, while (8,0) CNT has a phononic bandgap around 36 THz, corresponding to 150 meV. Here a_1 and a_2 are unit cell lengths for (5,5) CNT and (8,0) CNT, respectively.

The coordinates of carbon atoms of CNTs are constructed by the rolling of graphene sheet, for which the interatomic distances are optimized by the total energy minimization in the Brenner potential. The force constants are constructed in the optimization process by finite difference of the interatomic forces, which are calculated from differentiation of the total energy. The phonon dispersion relations of the system are obtained by the diagonalization of the dynamical matrix, which is constructed from the force constants [14].

Figure 1(b) show the phonon bands of (5,5) and (8,0) CNTs. We see that there are no phononic bandgaps in the phonon band structure of (5,5) CNT, while (8,0) CNT has a phononic bandgap around the frequency of 36 THz. This shows that phononic bandgap appears in this quasi-one-dimensional nanometer-scale carbon material. Then we would like to ask what is the condition that CNTs have phononic bandgaps in the phonon bands and the relation

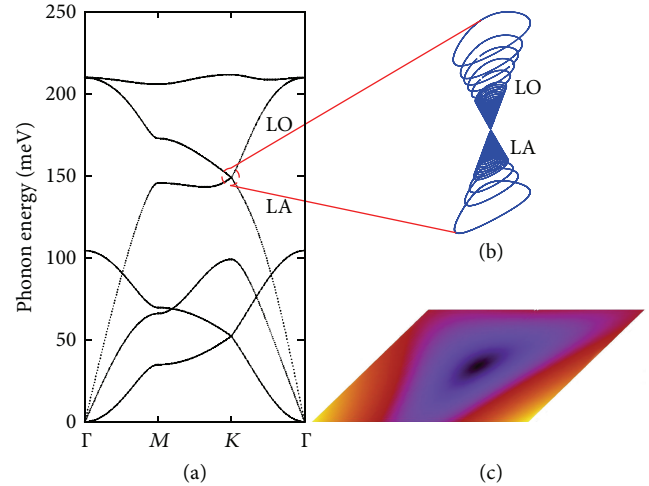


FIGURE 2: (a) Phonon band of graphene: the LA-mode tangents to the LO-mode at the K point. There are only LA and LO modes around 150 meV corresponding to the center of phononic bandgap of CNTs. (b) Blue lines are contours near the K point with equal phonon energy in the phonon band of graphene. Dirac's cone is isotropic close to the K point and becomes distorted away from the K point. (c) Surface plot of energy difference between LA and LO modes. Center black region indicates no energy difference at the K point. As the color becomes warmer, the energy difference becomes larger.

of magnitudes of phononic bandgaps with the diameters of CNTs.

Figure 2(a) shows the phonon band of graphene. We see that there are only two modes around 150 meV, and these two modes are crossed at the K point in k -space. These two correspond to the longitudinal acoustic (LA) mode and the longitudinal optical (LO) mode, and no other phonon bands are present. We note that this situation is very close to the electronic band structure of graphene around the Fermi level, where two kinds of linear-dispersion bands, bonding and anti-bonding π bands, are crossed at the K point. This shows that the K point is a special point also in the phonon band as in the electronic band. This evidence leads us to the conclusion that, as in the electronic bands of CNTs, whether the phonon bands have finite phononic bandgaps or not is determined by the conditions that the phonon bands of graphene crosses the K point or not by the rolling up to construct the CNTs. In the electronic band structures, the zone-folding method [15] reveals that bandgaps of CNTs are made from the band of graphene at wave vectors selected by the periodic boundary condition along the circumference direction on CNTs.

The same method is applied to the case of phononic bandgaps. CNTs with the index $n-m$ equal to the multiple of 3 have no phononic bandgaps. Thus the armchair CNTs with (n,n) chirality have no phononic bandgap, because the wave vector of phonon bands of the armchair CNTs always cross the K point of phonon bands of graphene. This is observed in Figure 1 (left), which shows the phonon band of (5,5) armchair CNT. On the other hand, the phonon bands of

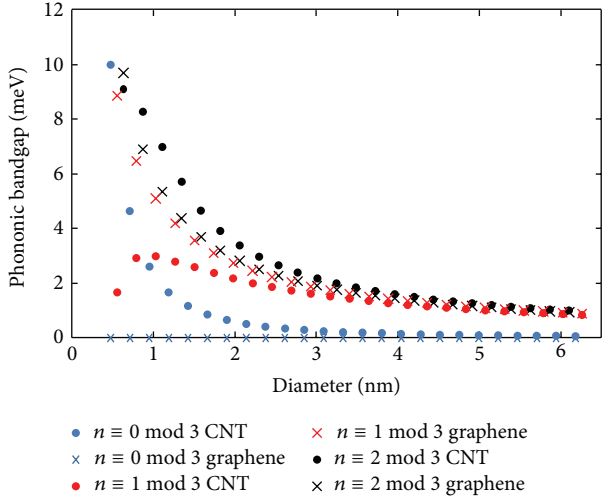


FIGURE 3: Diameter dependence of phononic bandgaps of zigzag-CNTs with chirality $(n, 0)$ from $n = 6$ to 77. Dots show phononic bandgaps from the phonon bands, and crosspoints show those by the zone-folding method. Blue colors are phononic bandgaps where n is the multiple of 3, red colors are those where n is the sum of multiples of 3 and 1, and black colors are those where n is the sum of multiple of 3 and 2.

the zigzag CNTs with $(n, 0)$ chirality in Figure 1 (right) have finite phononic bandgap.

Figure 3 shows the magnitudes of phononic bandgaps of the zigzag CNTs for various diameters and chirality $(n, 0)$ with n from 6 to 77. Dots show the phononic bandgaps obtained from the direct calculations of phonon bands, while the cross points show those by the zone-folding method, extraction from the graphene phonon band according to the wave vector selection rule on the periodic boundary conditions. We see that there are “three” kinds of diameter dependences of phononic bandgaps. Note that only two kinds of diameter dependences are present for the bandgaps of electronic states.

This difference is caused by the anisotropy of phononic bands of graphene around the K point. When n is the sum of multiples of 3 and 1, the allowed wave vector near the K point in the zone-folding method approaches the K point from the M point. On the other hand, when n is the sum of multiples of 3 and 2, the allowed wave vector approaches the K point from the Γ point. Along these two different directions to the K point, we can clearly see the anisotropy of phonon band in Figure 2(a). The anisotropic phonon band structure, different from the linear dispersion of electronic band structure, leads to “three” kinds of diameter dependences of phononic bandgaps. As the diameters of CNTs become large, two kinds of allowed wave vectors from the M and Γ points to the K point become so small enough to ignore the anisotropy of phonon bands of graphene around the K point and then the magnitudes of phononic bandgaps become the same. In the phonon bands of graphene close to the K point in Figures 2(b) and 2(c), we see that the Dirac’s cone near the K point is isotropic, while the cone becomes distorted far from the K point. This leads to the diameter dependences of phononic

bandgaps to change from “three” kinds in the small n to two kinds in the large n .

In Figure 3, we see that dots deviate from cross points for small n with small diameters. For instance, when n is the multiple of 3, there are no bandgaps in cross points, while small phononic bandgaps appear in dots, which are directly calculated from the phonon bands. The difference of phononic bandgaps between two methods is also seen for the electronic bandgap calculation [11]. Tight-binding calculations of electronic band structure for $(n, 0)$ zigzag CNTs when n is the multiple of 3 exhibit narrow bandgaps due to the nonorthogonality conditions of the atomic orbitals, and displacement of the atomic points where bonding and antibonding π bands are degenerate. Namely, the difference between two methods is caused by the curvature of CNTs.

As the diameter of CNT becomes large, the effects become less important and the phononic bandgaps of CNTs with large diameter is explained in terms of the phonon band structure of graphene. In this respect, the deviation of two methods reveals the crossover from one-dimensional to two-dimensional characteristics. Let us see two special diameters for this crossover. First, we consider the optimized interatomic distance. For CNTs with small diameters, the distances between carbon atoms become longer than that of graphene. We find that, for $n > 16$ with the diameter of 1.3 nm, the distance of carbon atoms in CNTs agree with that of graphene, showing the crossover from tube like to sheet like. Second, a more minor point, CNTs have specific phonon dispersion relations close to the Γ point where acoustic phonon branches have special properties with zero frequencies. For one-dimensional material, it is known that phonon bands have four acoustic phonon branches, while only three acoustic phonon branches exist for two- and three-dimensional materials. We find that CNTs with $n > 35$ have only three acoustic phonons. This leads to the small deviation of phononic bandgaps of CNTs with diameters larger than about 3 nm in the zone-folding method as is seen in Figure 3. These show that, for CNTs which have diameter smaller than 1.3 nm, phonon bandgaps must be calculated directly from the phonon bands of CNTs.

To summarize, we study the phononic bandgap of CNTs. We find that the condition of chirality of CNTs which have finite phononic bandgaps is almost the same as that of the electronic bandgap case. This is due to the fact that phonon band of graphene has only two bands close to the K point at specific energy around 150 meV, while electronic band structure of graphene has only two bands around the K point at the Fermi level. Diameter dependence of phononic bandgaps is, however, quite different. We find that phononic bandgap has “three” kinds of diameter dependence, different from the electronic bandgap which has only two kinds. This difference is caused by the anisotropy of the Dirac’s cone around the K point of graphene. While the Dirac’s cone is isotropic close to the K point for phonon bands of graphene, it becomes distorted away from the K point. This changes the dependences of phononic bandgaps from three kinds for small diameter to two kinds for large diameter. Due to the curvature of CNTs at small diameter, phononic bandgaps differ with two calculating methods: direct calculation for

CNTs and zone-folding method for graphene, for which we need the direct one. As the diameter becomes large, curvature effects become less important and the difference becomes small. We find that we need the direct phonon dispersion calculation for diameter smaller than 1.3 nm and that the zone-folding method becomes reliable for diameter larger than 3 nm. This is regarded as the dimensional crossover from one- to two-dimensional characteristics in phononic bandgaps.

Acknowledgment

This work is supported in part by a Grant-in-Aid for Scientific Research from the Ministry of Education, Culture, Sports, Science and Technology of Japan.

References

- [1] A. V. Akimov, Y. Tanaka, A. B. Pevtsov et al., “Hypersonic modulation of light in three-dimensional photonic and phononic band-gap materials,” *Physical Review Letters*, vol. 101, no. 3, Article ID 033902, 2008.
- [2] C. W. Chang, D. Okawa, H. Garcia, A. Manjumdar, and A. Zettl, “Nanotube phonon waveguide,” *Physical Review Letters*, vol. 99, no. 4, Article ID 045901, 4 pages, 2007.
- [3] W. Choi, S. Hong, J. T. Abrahamson et al., “Chemically driven carbon-nanotube-guided thermopower waves,” *Nature Materials*, vol. 9, no. 5, pp. 423–429, 2010.
- [4] M. Maldovan, “Narrow low-frequency spectrum and heat management by thermocrystals,” *Physical Review Letters*, vol. 110, no. 2, Article ID 025902, 5 pages, 2013.
- [5] T. P. M. Alegre, A. Safavi-Naeini, M. Winger, and O. Painter, “Quasi-two-dimensional optomechanical crystals with a complete phononic bandgap,” *Optics Express*, vol. 19, no. 6, pp. 5658–5669, 2011.
- [6] O. Sigmund and J. S. Jensen, “Systematic design of phononic band-gap materials and structures by topology optimization,” *Philosophical Transactions of the Royal Society A*, vol. 361, no. 1806, pp. 1001–1019, 2003.
- [7] G. A. Gazonas, D. S. Weile, R. Wildman, and A. Mohan, “Genetic algorithm optimization of phononic bandgap structures,” *International Journal of Solids and Structures*, vol. 43, no. 18-19, pp. 5851–5866, 2006.
- [8] T. Gorishnyy, C. K. Ullal, M. Maldovan, G. Fytas, and E. L. Thomas, “Hypersonic phononic crystals,” *Physical Review Letters*, vol. 94, no. 11, Article ID 115501, 4 pages, 2005.
- [9] W. Cheng, J. Wang, U. Jonas, G. Fytas, and N. Stefanou, “Observation and tuning of hypersonic bandgaps in colloidal crystals,” *Nature Materials*, vol. 5, no. 10, pp. 830–836, 2006.
- [10] S. Iijima, “Helical microtubules of graphitic carbon,” *Nature*, vol. 354, no. 6348, pp. 56–58, 1991.
- [11] N. Hamada, S.-I. Sawada, and A. Oshiyama, “New one-dimensional conductors: graphitic microtubules,” *Physical Review Letters*, vol. 68, no. 10, pp. 1579–1581, 1992.
- [12] R. Saito, M. Fujita, G. Dresselhaus, and M. S. Dresselhaus, “Electronic structure of chiral graphene tubules,” *Applied Physics Letters*, vol. 60, no. 18, pp. 2204–2206, 1992.
- [13] D. W. Brenner, “Empirical potential for hydrocarbons for use in simulating the chemical vapor deposition of diamond films,” *Physical Review B*, vol. 42, no. 15, pp. 9458–9471, 1990.
- [14] K. Yamamoto, H. Ishii, N. Kobayashi, and K. Hirose, “Effects of vacancy defects on thermal conduction of silicon nanowire: nonequilibrium green’s function approach,” *Applied Physics Express*, vol. 4, Article ID 085001, 3 pages, 2011.
- [15] R. Saito, G. Dresselhaus, and M. S. Dresselhaus, *Physical Properties of Carbon Nanotubes*, chapter 9, Imperial College Press, London, UK, 1998.

Research Article

Heat Transfer between an Individual Carbon Nanotube and Gas Environment in a Wide Knudsen Number Regime

Hai-Dong Wang,¹ Jin-Hui Liu,¹ Xing Zhang,¹ Tian-Yi Li,² Ru-Fan Zhang,³ and Fei Wei³

¹ Key Laboratory for Thermal Science and Power Engineering of Ministry of Education, Department of Engineering Mechanics, Tsinghua University, Beijing 100084, China

² Department of Physics and Tsinghua-Foxconn Nanotechnology Research Center, Tsinghua University, Beijing 100084, China

³ Beijing Key Laboratory of Green Chemical Reaction Engineering and Technology, Department of Chemical Engineering, Tsinghua University, Beijing 100084, China

Correspondence should be addressed to Xing Zhang; x-zhang@tsinghua.edu.cn

Received 14 March 2013; Accepted 20 May 2013

Academic Editor: Teng Li

Copyright © 2013 Hai-Dong Wang et al. This is an open access article distributed under the Creative Commons Attribution License, which permits unrestricted use, distribution, and reproduction in any medium, provided the original work is properly cited.

Applications of carbon nanotube (CNT) and graphene in thermal management have recently attracted significant attention. However, the lack of efficient prediction formula for heat transfer coefficient between nanomaterials and gas environment limits the further development of this technique. In this work, a kinetic model has been established to predict the heat transfer coefficient of an individual CNT in gas environment. The heat dissipation around the CNT is governed by molecular collisions, and outside the collision layer, the heat conduction is dominant. At nanoscales, the natural convection can be neglected. In order to describe the intermolecular collisions around the CNT quantitatively, a correction factor $1/24$ is introduced and agrees well with the experimental observation. The prediction of the present model is in good agreement with our experimental results in free molecular regime. Further, a maximum heat transfer coefficient occurs at a critical diameter of several nanometers, providing guidelines on the practical design of CNT-based heat spreaders.

1. Introduction

As the scale of electronic devices continuously decreases to nanometers, the power density increases to a very high level; for example, an individual microprocessor operating at a low GHz frequency has a typical power density of 100 Wcm^{-2} [1]. Meanwhile, the waste heat at this high generation rate has to be dissipated efficiently in a limited space; otherwise, the resulting local high temperature may cause thermal failure of the device and highly reduce its lifetime. Hence, the thermal management at nanoscales has become a critical issue and attracted much attention. Recently, the carbon nanotube (CNT), nanowires, and graphene have been found to be the promising materials to remove the waste heat from nanoelectronic devices due to their super high thermal conductivities [2–5]. At two-dimensional scales, the graphene has important applications as heat spreaders and thermal interfacial materials [6–8]. Meanwhile, the CNT can be designed into a one-dimensional heat spreader connecting

the hotspot with high power density and the heat sinks. These new techniques have potential applications in many areas, such as nanoelectromechanical systems [9], gas sensors [10], field emitters [11], and nanowire-based lasers [12, 13]. Since all the nanodevices will be used in the air environment, the study of heat transfer between the nanomaterials and surrounding air forms the foundation of the practical design of nano heat spreaders.

Heat transfer across the interface between macroscale solid and gas environment is well understood, where many experimental data and empirical formulas are available. However, as the characteristic size scales down to nanometers, it becomes a challenging task to determine the heat transfer coefficient (HTC) of nanomaterials quantitatively. In the experimental study, the commonly used resistance thermometer or thermocouples at macroscales are no longer applicable, and a noncontact measurement should be performed at the nanometer level in order to avoid the uncertainty of temperature measurement at interfaces. Recently,

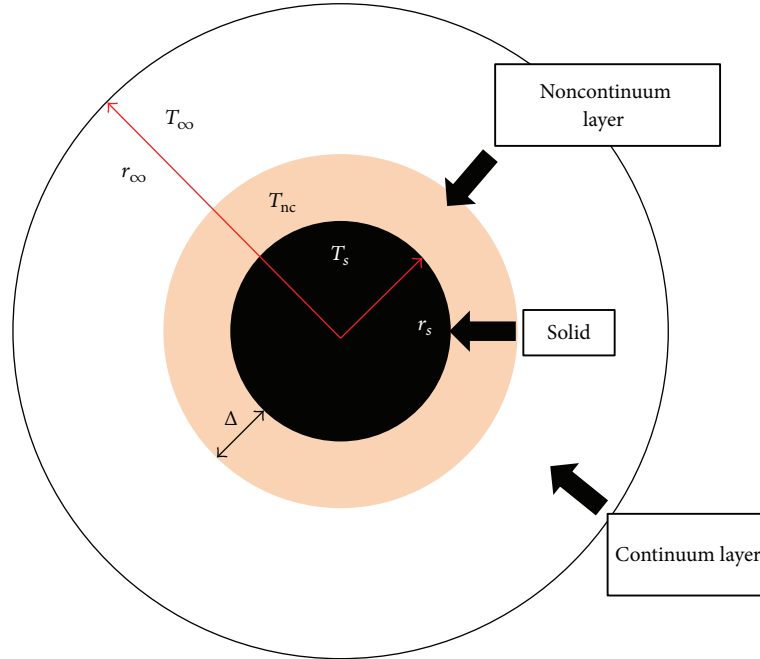


FIGURE 1: Schematic diagram of the two-layer model.

a noncontact technique of micro-Raman spectroscopy has been utilized to measure the thermal properties of CNT and graphene [9, 10, 14–16]. In this technique, a focused laser is used to heat the sample locally and the temperature response can be measured simultaneously from the downshifted G-band frequency. Combining with electrical measurement, both the optical absorption and thermal conductivity of an individual CNT can be obtained [16]. While this technique has the potential to provide both thermal conductivity and HTC of an individual CNT, the presented experimental data are still too few to conclude a convincing variation trend of the thermal property on a single parameter of CNT, like its length, diameter, or chirality.

In the theoretical study, no quantitative theoretical model has been fully developed to predict the HTC between an individual CNT and gas environment. Some molecular dynamics (MD) simulations of CNT-air interfacial thermal conductance have been reported and give a result of about $1.0 \times 10^5 \text{ Wm}^{-2} \text{ K}^{-1}$ [17]. The associated thermal resistance is equivalent to the resistance of about 250 nm thick layer of air. Because of the high surface to volume ratios, the heat dissipation from an individual CNT to the gas environment becomes increasingly important compared with that at macroscales [5]. The heat dissipated across the CNT-air interface is more than 50% for a 2.04 nm, 5 μm long suspended CNT [18], and this fraction will approach 100% for CNTs longer than 60 μm [19]. Hence, the heat dissipation to the air environment can be exploited as an effective way for cooling CNT associated devices [20]. It is particularly important to develop an accurate prediction model for the HTC of individual CNT or nanowire, benefiting the practical thermal design of efficient heat spreaders at nanoscales. On the other hand, from CNT to nanowire, the characteristic diameter of HTC changes

from several nanometers to hundreds of nanometers, ranging from the free molecular regime to the transition regime. The development of a unified theoretical model also has important academic significance.

In this work, a theoretical model of heat transfer across the CNT-gas interface has been established based on the kinetic theory. It demonstrates that a critical diameter exists at several nanometers for a maximum HTC of $1.08 \times 10^5 \text{ Wm}^{-2} \text{ K}^{-1}$. The theoretical prediction agrees well with our experimental results in the free molecular regime [19].

2. Two-Layer Model of Heat Transfer

Fuchs proposed a general physical model to estimate the heat transfer between the gas environment and isolated particle at submicroscales [21, 22]. In this model, the whole space is separated into two layers: the layer around the particle with a thickness comparable to the mean free path (MFP) of molecules and the outside layer where the continuum theory is applicable. A schematic diagram of this two-layer model is shown in Figure 1.

Figure 1 shows the two-layer model for a spherical particle. The black circle in the center represents the solid part, around which a thin layer is the noncontinuum layer with a thickness of Δ . T_s , T_{nc} , and T_∞ are the temperatures at the solid surface and at the interface of noncontinuum layer and of surrounding gas, respectively. r_s and r_∞ are the radii of solid particle and outer continuum layer when $T = T_\infty$, respectively. In this model, the heat transfer from the solid surface to the outer gas environment is finished in two steps: (1) energy exchange between the solid surface and gas molecules by collisions in the noncontinuum layer; (2) heat dissipation in the outer continuum layer. In Fuchs' model,

the first step heat transfer is described by molecular kinetics and the second step is described by means of continuum theory. Following this model, a governing equation for the HTC between the nanoparticles and surrounding gas is given as [23]

$$h = \frac{Q}{4\pi r_s^2 (T_s - T_\infty)} = \frac{\lambda f_{\text{ncr}} (\xi + \gamma)}{l [f_{\text{ncr}} \xi^2 + \beta (\xi + \gamma)]}, \quad (1)$$

where h , Q , λ , and l are the heat coefficient, heat dissipated into the gas environment, thermal conductivity of gas, and molecular MFP, respectively; $\xi = r_s/l$ is the dimensionless radius, and $\gamma = \Delta/l$ is the dimensionless thickness of inner layer. $f_{\text{ncr}} = \xi[1 + \xi e^\xi \text{Ei}(-\xi)]$ is the correction factor in the noncontinuum layer, where $\text{Ei}(x)$ is the exponential integral of x . β is the correction factor for molecular collisions.

Based on (1), the Nusselt number Nu can be summarized as

$$\text{Nu} = \frac{2r_s h}{\lambda} = \frac{2f_{\text{ncr}} \xi (\xi + \gamma)}{f_{\text{ncr}} \xi^2 + \beta (\xi + \gamma)}. \quad (2)$$

This two-layer model is capable of predicting the HTC of particle with a diameter ranging from nanometers to micrometers, and the corresponding Knudsen number Kn is from 0.01 to 10. However, some questions still remain to limit the prediction accuracy: (1) an exact equivalent particle radius is needed for a good prediction, which is usually hard to get for aerosolized nanoparticles; (2) the molecular motion inside the inner layer is considered to be collisionless and there is no transition layer between the two layers in Figure 1 [24]. Ignoring the interactions between molecules may cause prediction uncertainty. Reference [23] takes into account the intermolecular collisions by changing the inner layer thickness and this thickness is assumed to increase as the particle diameter increases. But the accurate inner layer thickness is difficult to evaluate in practical applications.

In this work, we developed a prediction formula for the HTC of an individual CNT based on the two-layer model. The physical model shown in Figure 1 is applicable using a cylindrical coordinate system instead. The noncontinuum layer is adjacent to the CNT surface, where the kinetic theory is applied. The outside continuum layer is concentric with the CNT and the noncontinuum layer, where the continuum theory is applied. In the noncontinuum layer, the average velocity of molecules is given as [25]

$$\bar{v} = 2 \left(\frac{2k_B T}{\pi m} \right)^{1/2}, \quad (3)$$

where k_B and m are the Boltzmann constant and mass of a molecule, respectively. In a cylindrical coordinate system, the number of molecules moving towards the solid surface with an incident angle θ is given as

$$N = n r d\theta dr dx \frac{\cos \theta ds}{2\pi r L}, \quad (4)$$

where n , r , L , and ds are the molecular number density, radius, CNT length, and area element, respectively. Using

the classical Maxwell distribution function, the fraction of molecules with a velocity between v and dv is given as

$$N_{dv} = 4\pi \left(\frac{m}{2\pi k_B T} \right)^{3/2} v^2 \exp \left(-\frac{mv^2}{2k_B T} \right) dv. \quad (5)$$

The molecular impact flux on the solid surface is given as [23]

$$\begin{aligned} \psi &= \frac{2mn}{\pi^2 k_B T l} \int_0^\infty \left(\frac{r_s}{r_s + \Delta} \right)^2 \exp \left(\frac{-\Delta}{l} \right) d\Delta \\ &\times \int_0^\infty v^2 \exp \left(-\frac{mv^2}{2k_B T} \right) dv \\ &= \frac{\bar{v}n}{2\pi} \xi [1 + \xi e^\xi \text{Ei}(-\xi)] = \frac{\bar{v}n}{2\pi} f_{\text{ncr}}. \end{aligned} \quad (6)$$

The dissipated energy Q at the wire surface can be described as

$$Q = \psi S \alpha_f C_v m (T_s - T_{\text{nc}}). \quad (7)$$

Substituting the integrated result of ψ into (7), one can get

$$Q = 2\alpha_f d L n C_v m f_{\text{ncr}} \sqrt{\frac{k_B T}{2\pi m}} (T_s - T_{\text{nc}}), \quad (8)$$

where S , α_f , C_v , T_s , T_{nc} , and d are the wire surface, accommodation coefficient, specific heat capacity at constant volume, solid surface temperature, noncontinuum layer temperature, and diameter of CNT, respectively.

According to the kinetic theory of gas, the thermal conductivity is given as [26]

$$\lambda = \frac{2\beta'}{\pi} \frac{\bar{v}n}{4} C_v m l = \beta n C_v m l \sqrt{\frac{k_B T}{2\pi m}}, \quad (9)$$

where l is the molecular MFP and β is the correction factor representing the effect of intermolecular collisions. The constant $2/\pi$ is caused by the different geometric coordinates of cylinder and sphere. Combining (8) and (9), the heat flux from the CNT surface to the noncontinuum layer is derived as

$$q_{s-\text{nc}} = \alpha_f \frac{\lambda f_{\text{ncr}}}{\beta l} (T_s - T_{\text{nc}}). \quad (10)$$

Figure 2 shows a schematic diagram of molecular collisions around an individual CNT. Because the diameter of CNT is much smaller than the molecular MFP, the probability of molecules colliding with CNT decreases as the diameter decreases. In this case, the surrounding gas appears to be rarefied for the CNT. As shown in Figure 2, the CNT is "covered" by a layer of molecules with a thickness of molecular MFP, referred to as the noncontinuum layer. Out of this layer, the gas is continuous and the collision cross-section is given as $\sigma = \pi l^2$. To consider the probability that a molecule appears in the volume of CNT with a diameter of d , the cross-section is given as $\sigma_{\text{CNT}} = 0.25\pi d^2$. $\sigma_{\text{CNT}}/\sigma$ equals zero as the diameter approaches zero, and it equals

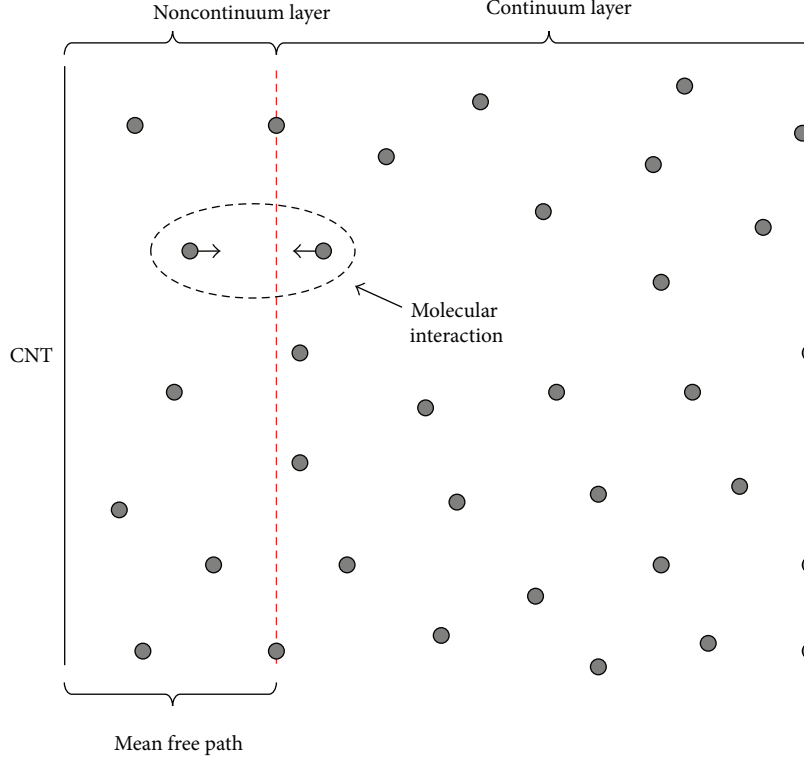


FIGURE 2: Schematic diagram of molecular collision model.

unity as the radius of CNT approaches the molecular MFP. The integration average value of $\sigma_{\text{CNT}}/\sigma$ from zero to l equals $1/3$. On the other hand, the reflected molecules from the CNT surface will collide with the other incident molecules within the layer of MFP, and the molecular interaction will decrease the collision probability. If every reflected molecule collides with the incoming one, that gives a limiting value of $1/2$ for each direction. In a three-dimensional space, this fraction is $1/8$. As a result, the correction factor β can be estimated as about $1/24$.

In the continuum layer, the heat flux caused by heat conduction from radius r_1 to radius r_2 is $q = (\lambda/r_s)\Delta T / \ln(r_2/r_1)$, where r_s is the solid wire radius. The heat conductance $q/\Delta T$ is inversely proportional to the radius r_s . When $r_w = 2\ \mu\text{m}$, the HTC of natural convection is about $3.4 \times 10^3\ \text{Wm}^{-2}\ \text{K}^{-1}$ [26, 27], while the heat conductance $q/\Delta T$ is about $1.4 \times 10^4\ \text{Wm}^{-2}\ \text{K}^{-1}$, and the most heat is dissipated by conduction. As the radius r_s decreases to submicrometers, the Grashof number Gr decreases rapidly below 1×10^{-7} in the third power of radius, implying that the buoyancy force is negligible compared with the viscous force and the heat conduction becomes the only dominant way. Governed by the one-dimensional heat conduction equation in cylindrical coordinates, the heat flux from the noncontinuum layer to the gas environment is given as

$$q_{\text{nc}-\infty} = \frac{\lambda}{r_s + \Delta} \left(\frac{T_{\text{nc}} - T_{\infty}}{\ln(n_r(r_s + r_0)/(r_s + \Delta))} \right), \quad (11)$$

where T_{∞} is the environment temperature and $r_{\infty} = n_r(r_w + r_0)$ is the radius when $T = T_{\infty}$. Imposing the continuity

condition on heat flux at the interface between noncontinuum layer and continuum layer, the temperature T_{nc} is given as

$$T_{\text{nc}} = T_s - \left[1 + \frac{f_{\text{ncr}}}{\beta l} (r_s + \Delta) \ln \left(\frac{r_{\infty}}{r_s + \Delta} \right) \right]^{-1} (T_s - T_{\infty}). \quad (12)$$

Hence, we derived the HTC h as

$$h = \frac{Q}{\pi d L (T_s - T_{\infty})} = \frac{(2/\pi) \alpha_f n C_v m f_{\text{ncr}} \sqrt{k_B T / 2\pi m}}{1 + (f_{\text{ncr}}/\beta l) (r_s + \Delta) \ln(n_r((r_s + r_0)/(r_s + \Delta)))}. \quad (13)$$

3. Results and Discussion

In order to verify the accuracy of the present theoretical model, we measured the HTCs of several single-walled CNTs (SWCNTs) using a Raman spectroscopy technique [19]. The experimental data and theoretical predictions are compared in Figure 3.

As shown in Figure 3, the experimental data (red circles) match quite well the present model (solid curve) in a diameter range from 0.97 nm to 1.47 nm. Meanwhile, the literature data of microwires agree well with the present model as well [26]. When the accommodation coefficient α_f equals unity, the maximum value of h is given as [28]

$$h_{\text{max}} = \frac{5}{8} n u k_B = 1.1 \times 10^5\ \text{Wm}^{-2}\ \text{K}^{-1}, \quad (14)$$

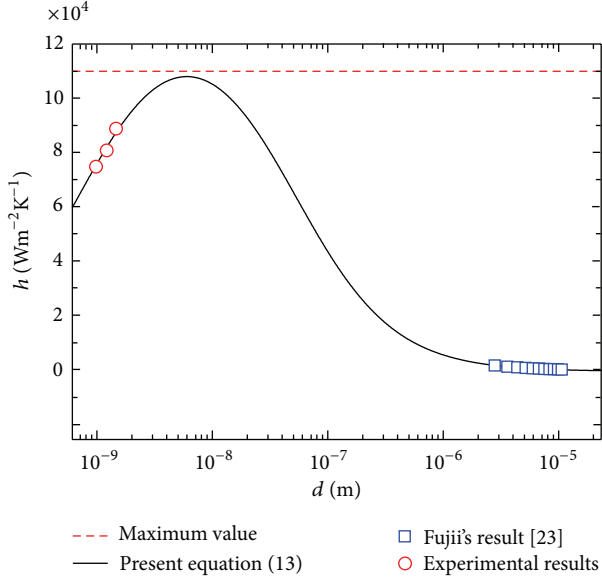


FIGURE 3: Comparison between the experimental data and theoretical prediction. The red dash line is the maximum value given by the kinetic theory.

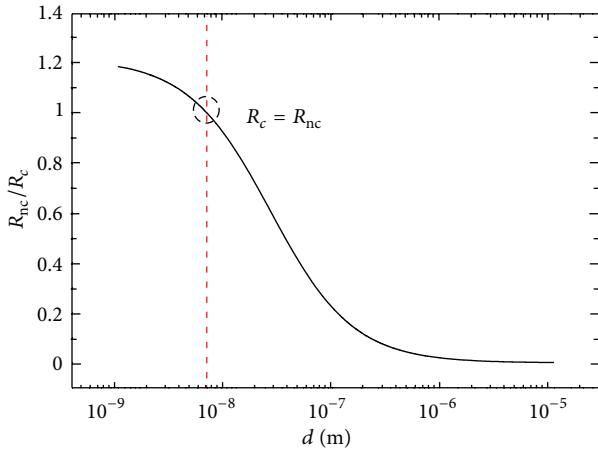


FIGURE 4: Ratio between the thermal resistances of noncontinuum and continuum layers plotted with respect to the diameter. The red dash line marks the critical diameter when $R_{nc} = R_c$.

where $u = (3k_B T/m)^{0.5}$ is the root mean square velocity. The maximum value predicted by (13) is $1.08 \times 10^5 \text{ Wm}^{-2} \text{ K}^{-1}$, consistent with the prediction of (14). The best fitted parameters for the calculation result of Figure 3 are $\alpha_f = 1$, $\beta = 0.04$, $n_r = 100$, and $r_0 = 0.4l$. As mentioned previously, the correction factor β can be calculated as

$$\beta = \frac{1}{8} \int_0^{2l} \frac{\sigma}{\sigma_{CNT}} dx = \frac{1}{8} \int_0^{2l} \frac{\pi x^2}{4\pi l^2} dx = \frac{1}{24} \approx 0.04, \quad (15)$$

and the best fitted value is consistent with the theoretical prediction, showing a good accuracy of the present model.

Figure 4 shows the ratio between the thermal resistances of noncontinuum layer and continuum layer, that is, R_{nc}

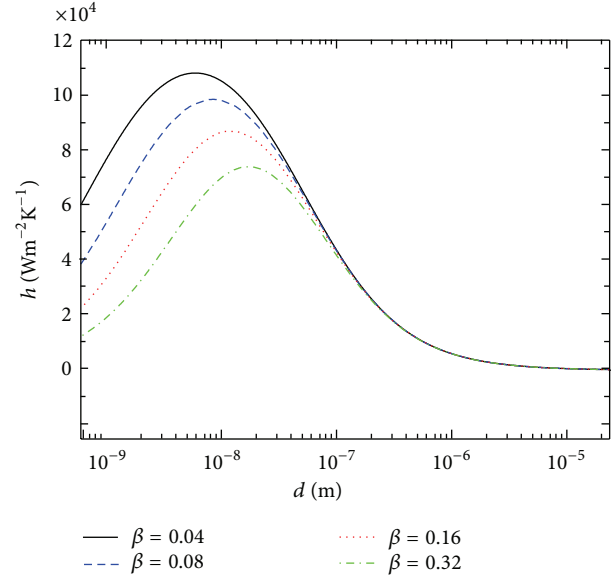


FIGURE 5: The effect of molecular interactions on the HTC.

and R_c , respectively. Here, the previous thermal resistance is calculated as $R_{nc} = l/\lambda$, where the thermal conductivity λ is calculated by (9) containing the correction factor β . The latter thermal resistance is calculated as $R_c = (r_{\infty}/\lambda_{\text{air}}) \ln [r_{\infty}/(r_s + l)]$, where the thermal conductivity of air λ_{air} is used. It is seen in Figure 4 that the continuum layer contributes to the most thermal resistance when the diameter is at micrometers; in this case, the noncontinuum layer around the thin wire can be totally neglected. However, as the diameter decreases, the resistance R_{nc} becomes more and more important and the difference between R_{nc} and R_c decreases rapidly below 100 nm. At a critical diameter of about 5 nm, R_{nc} equals R_c and a maximum HTC value occurs as shown in Figure 3. When the diameter drops below the critical value, R_{nc} becomes larger than R_c and the HTC decreases as well. As a result, the existence of a maximum HTC is caused by the competition between R_{nc} and R_c .

Figure 5 shows the HTC predicted by (13) with a correction factor β changing from 0.04 to 0.32. For a given temperature difference $T_s - T_{nc}$, the dissipated heat Q is proportional to the molecular number density n based on (8). As the correction factor β increases, the probability of intermolecular collisions inside the noncontinuum layer increases and the effective molecular density decreases. Thus the dissipated heat Q decreases and HTC h decreases as well. Changing the factor β only affects the HTC with a diameter below 100 nm, and the results of thick wires remain unchanged.

Based on (13), a dimensionless Nusselt number Nu is given as

$$Nu = \frac{hd}{\lambda} = \frac{4\alpha_f f_{ncr} \xi / \pi}{\beta + f_{ncr} (\xi + \Delta/l) \ln (n_r ((\xi + r_0/l) / (\xi + \Delta/l)))}. \quad (16)$$

The calculation results of (16) are given in Figure 6 as follows.

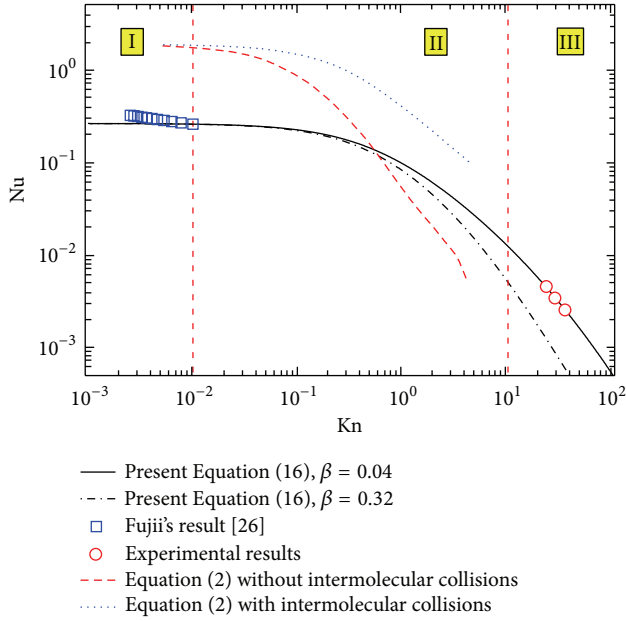


FIGURE 6: Nusselt number plotted with respect to Knudsen's number, and different values of factor β are used for calculation. The regimes I, II, and III are the continuum regime, transition regime, and free molecular regime, respectively.

In Figure 6, the black solid and dash-dot curves are the prediction results of the present model for CNTs. The red dash curve and blue dot curve are the prediction results for nanoparticles, where the previous one takes into account the intermolecular collisions while the latter one does not [23]. Equation (2) relates the molecular interaction with the thickness of noncontinuum layer, and the increasing thickness decreases the dissipated heat at the particle surface. Similarly in the present model, as the CNT diameter increases, more molecules are reflected from the solid surface and collide with other molecules and the correction factor β increases. Using gas dynamics, the exact value of β can be estimated.

Figure 6 can be divided into three regimes, that is, the continuum regime ($Kn < 10^{-2}$), transition regime ($10^{-2} < Kn < 10$), and free molecular regime ($Kn > 10$), respectively. In the continuum regime, the continuum theory is applicable and the thermal resistance induced by the molecular collisions at the solid surface is negligible. As the diameter decreases to the transition regime, the molecular interactions become more significant and reduce the Nu number accordingly. Finally in the free molecular regime, the intermolecular interactions within the MFP layer play a dominant role and decide the HTC. The present model given in (13) and (16) has been proved valid by the experiments in both free molecular and continuum regimes, while the experimental data in the transition regime are still lacking. In our future work, the HTC in a wide Kn number from 0.01 to 100 will be measured.

4. Summary

- (1) So far, there is no efficient theoretical model proposed to predict the HTC between an individual CNT

and gas environment. In this work, a quantitative model has been established to predict HTC, and the prediction of the present model is in good agreement with the experimental data in both free molecular and continuum regimes.

- (2) The present model demonstrates that the natural convection can be neglected in the continuum layer outside the CNT, where the heat conduction plays a dominant role.
- (3) In the previous models for nanoparticles, it is difficult to evaluate the effect of intermolecular collisions on HTC around the solid surface. In the present model, the intermolecular effect can be quantitatively calculated using a correction factor β , and the analytical value is consistent with the experimental observation.
- (4) It is predicted by the present model that a maximum HTC exists in the transition regime, corresponding to a critical diameter at several nanometers. Similar to the concept of critical diameter of thermal insulation layer, the critical diameter here accounts for the dividing line of relative importance between the thermal resistances of noncontinuum layer and continuum layer. In practical applications, the performance of CNT-based heat spreader can be improved by choosing the critical diameters.

Acknowledgments

The authors would like to acknowledge the great help and support from Professor Zeng-Yuan Guo. The main idea of this work is derived from the discussion with Guo. This work is financially supported by the National Natural Science Foundation of China (Grant nos. 51076080 and 51136001), China Postdoctoral Science Foundation funded project, and Tsinghua University Initiative Scientific Research Program.

References

- [1] E. Pop, "Energy dissipation and transport in nanoscale devices," *Nano Research*, vol. 3, no. 3, pp. 147–169, 2010.
- [2] S. Chen, A. L. Moore, W. Cai et al., "Raman measurements of thermal transport in suspended monolayer graphene of variable sizes in vacuum and gaseous environments," *ACS Nano*, vol. 5, no. 1, pp. 321–328, 2011.
- [3] P. Kim, L. Shi, A. Majumdar, and P. L. McEuen, "Thermal transport measurements of individual multiwalled nanotubes," *Physical Review Letters*, vol. 87, no. 21, Article ID 215502, 4 pages, 2001.
- [4] S. V. Rotkin, V. Perebeinos, A. G. Petrov, and P. Avouris, "An essential mechanism of heat dissipation in carbon nanotube electronics," *Nano Letters*, vol. 9, no. 5, pp. 1850–1855, 2009.
- [5] C. Cheng, W. Fan, J. Cao et al., "Heat transfer across the interface between nanoscale solids and gas," *ACS Nano*, vol. 5, no. 12, pp. 10102–10107, 2011.
- [6] A. A. Balandin, "Thermal properties of graphene and nanostructured carbon materials," *Nature Materials*, vol. 10, no. 8, pp. 569–581, 2011.
- [7] K. M. F. Shahil and A. A. Balandin, "Thermal properties of graphene and multilayer graphene: applications in thermal

- interface materials,” *Solid State Communications*, vol. 152, no. 15, pp. 1331–1340, 2012.
- [8] D. L. Nika and A. A. Balandin, “Two-dimensional phonon transport in graphene,” *Journal of Physics: Condensed Matter*, vol. 24, no. 23, Article ID 233203, 2012.
- [9] R. H. Blick and M. Grifoni, “Focus on nano-electromechanical systems,” *New Journal of Physics*, vol. 7, pp. 1367–2630, 2005.
- [10] E. Strelcov, Y. Lilach, and A. Kolmakov, “Gas sensor based on metal-insulator transition in VO₂ nanowire thermistor,” *Nano Letters*, vol. 9, no. 6, pp. 2322–2326, 2009.
- [11] J. She, Z. Xiao, Y. Yang et al., “Correlation between resistance and field emission performance of individual ZnO one-dimensional nanostructures,” *ACS Nano*, vol. 2, no. 10, pp. 2015–2022, 2008.
- [12] M. H. Huang, S. Mao, H. Feick et al., “Room-temperature ultraviolet nanowire nanolasers,” *Science*, vol. 292, no. 5523, pp. 1897–1899, 2001.
- [13] L. K. van Vugt, S. Ruhle, and D. Vanmaekelbergh, “Phase-correlated nondirectional laser emission from the end facets of a ZnO nanowire,” *Nano Letters*, vol. 6, no. 12, pp. 2707–2711, 2006.
- [14] V. V. Deshpande, S. Hsieh, A. W. Bushmaker, M. Bockrath, and S. B. Cronin, “Spatially resolved temperature measurements of electrically heated carbon nanotubes,” *Physical Review Letters*, vol. 102, no. 10, Article ID 105501, 4 pages, 2009.
- [15] A. A. Balandin, S. Ghosh, W. Bao et al., “Superior thermal conductivity of single-layer graphene,” *Nano Letters*, vol. 8, no. 3, pp. 902–907, 2008.
- [16] I. Hsu, M. T. Pettes, A. Bushmaker, M. Aykol, L. Shi, and S. B. Cronin, “Optical absorption and thermal transport of individual suspended carbon nanotube bundles,” *Nano Letters*, vol. 9, no. 2, pp. 590–594, 2009.
- [17] M. Hu, S. Shenogin, P. Keblinski, and N. Raravikar, “Thermal energy exchange between carbon nanotube and air,” *Applied Physics Letters*, vol. 90, no. 23, Article ID 231905, 3 pages, 2007.
- [18] I. Hsu, M. T. Pettes, M. Aykol, L. Shi, and S. B. Cronin, “The effect of gas environment on electrical heating in suspended carbon nanotubes,” *Journal of Applied Physics*, vol. 108, no. 8, Article ID 084307, 4 pages, 2010.
- [19] H. D. Wang, L. J. Hui, Z. Y. Guo et al., “Thermal transport across the interface between a suspended single-wall carbon nanotube and air,” *Nanoscale and Microscale Thermophysical Engineering*. In press.
- [20] A. Beskok and G. E. Karniadakis, “A model for flows in channels, pipes, and ducts at micro and nano scales,” *Microscale Thermophysical Engineering*, vol. 3, no. 1, pp. 43–77, 1999.
- [21] N. A. Fuchs, “On the stationary charge distribution on aerosol particles in a bipolar ionic atmosphere,” *Geofisica Pura e Applicata*, vol. 56, no. 1, pp. 185–193, 1963.
- [22] N. A. Fuchs, *The Mechanics of Aerosols*, Dover, New York, NY, USA, 1989.
- [23] H. H. Klein, J. Karni, R. Ben-Zvi, and R. Bertocchi, “Heat transfer in a directly irradiated solar receiver/reactor for solid-gas reactions,” *Solar Energy*, vol. 81, no. 10, pp. 1227–1239, 2007.
- [24] A. V. Filippov and D. E. Rosner, “Energy transfer between an aerosol particle and gas at high temperature ratios in the Knudsen transition regime,” *International Journal of Heat and Mass Transfer*, vol. 43, no. 1, pp. 127–138, 2000.
- [25] J. E. A. John, *Gas Dynamics*, Allyn and Bacon, Boston, Mass, USA, 1933.
- [26] T. Fujii, M. Fujii, and T. Honda, “Theoretical and experimental studies of the free convection around a long horizontal thin wire in air,” in *Proceedings of the 7th International Heat Transfer Conference*, vol. 2, pp. 311–316, Munich, Germany, 1982.
- [27] X. Zhang, S. Fujiwara, Z. Qi, and M. Fujii, “Natural convection effect on transient short-hot-wire method,” *Journal of the Japanese Society of Microgravity Applications*, vol. 16, pp. 129–135, 1999.
- [28] I. K. Hsu, M. T. Pettes, M. Aykol et al., “Direct observation of heat dissipation in individual suspended carbon nanotubes using a two-laser technique,” *Journal of Applied Physics*, vol. 110, no. 4, Article ID 044328, 5 pages, 2011.

Research Article

Embedding Effect on the Mechanical Stability of Pressurised Carbon Nanotubes

Motohiro Sato,¹ Hisao Taira,^{1,2} Tetsuro Ikeda,¹ and Hiroyuki Shima³

¹ Division of Engineering and Policy for Sustainable Environment, Faculty of Engineering, Hokkaido University, Sapporo 060-8628, Japan

² Department of Physics, Faculty of Science, Hokkaido University, Sapporo 060-0810, Japan

³ Department of Environmental Sciences & Interdisciplinary Graduate School of Medicine and Engineering, University of Yamanashi, 4-4-37 Takeda, Kofu, Yamanashi 400-8510, Japan

Correspondence should be addressed to Hiroyuki Shima; hshima@yamanashi.ac.jp

Received 6 March 2013; Revised 15 April 2013; Accepted 26 April 2013

Academic Editor: Teng Li

Copyright © 2013 Motohiro Sato et al. This is an open access article distributed under the Creative Commons Attribution License, which permits unrestricted use, distribution, and reproduction in any medium, provided the original work is properly cited.

We elaborate on the cross-sectional deformation of carbon nanotubes embedded into a self-contracting host medium. The continuum elastic approach is used to formulate the mechanical energy of both the embedded nanotubes and the self-contracting outer medium with finite thickness. Our formula allows us to evaluate the critical radial pressure applied on the interface between the embedded nanotube and the outer contracting medium as well as the deformation mode that arises immediately above the critical pressure. An interesting mechanical implication of the embedding effect, that is, the power-law dependence of the critical pressure on the elastic modulus of the medium, is deduced by the theoretical approach established.

1. Introduction

The salient structural feature of a carbon nanotube is its self-repairing behaviour that arises under high-energy beam irradiation [1, 2]. When the kinetic energy transferred from the incident beam to the constituent carbon atoms is sufficiently large, the atoms are pushed away from the original equilibrium positions, leaving vacancies in the host hexagonal lattice [3, 4]. In typical solids, such irradiation-induced vacancies survive without curing as time passes. However, this is not the case in carbon nanotubes; the removal of carbon atoms from the purely hexagonal lattice leads to a local reconstruction that acts to maintain its coherent network structure with cylindrical geometry. For this reason, carbon nanotubes are often referred to as self-repairing (or self-healing) materials [5–7].

This self-repairing nature provides beneficial effects for manipulating the carbon nanotube morphology, especially when combined with heat treatment. For instance, fine-tuning of electron beam irradiation makes it possible to synthesize multiwall carbon nanotubes (MWNTs) with reduced interwall spacings [8]; the spontaneous shrinkage in the

radial direction is a result of the knock-on collision of carbon atoms followed by annealing reconstruction of the vacancies. This experimental finding implies that when the outermost carbon walls of an MWNT are eroded selectively by irradiation, the self-contraction of the outermost walls exerts high pressure on the encapsulated, undamaged innermost walls [9–11]. Application of high pressure may then trigger a novel class of cross-sectional transformations of the inner walls [12], similar to the case of pristine (irradiation-free) MWNTs under hydrostatic pressure [13, 14]. Another class of radial contraction has been observed in MWNTs synthesized in the presence of nitrogen [15]. The yielded nanotubes showed polygon-shaped cross-sections rather than ordinary circular ones, a phenomenon that is partly attributed to the interwall thermal contraction upon cooling, as verified numerically by molecular dynamics simulations [16].

From a nanoengineering perspective, the tunability of cross-sectional geometry may be useful for developing nanofluidic [17–19] or nanoelectrochemical devices [20] based on carbon nanotubes, because both utilize the hollow cavity within the innermost tube. A very interesting issue from an academic viewpoint is the effect of the core tube

deformation on the physicochemical properties of intercalated molecules confined in the hollow cavity. It is indeed known that various types of intercalated molecules can fill the innermost hollow cavities of nanotubes [18] and exhibit intriguing behaviours that are distinct from their macroscopic counterparts [21–23]. These distinct behaviours originate from the similarity between the intermolecular spacings and the linear dimension of the nanoscale compartment. Therefore, cross-sectional deformation that breaks cylindrical symmetry will provide a clue to improving the performance of nanotube-based devices.

In this paper, we establish the continuum elastic approach that describes the cross-sectional deformation of carbon nanotubes surrounded by a self-contracting host medium. The mechanical energy of both the pressurized nanotubes and the contracting medium with finite thickness are formulated using thin-shell theory. The obtained formula allows us to evaluate the critical radial pressure applied on the interface between the inner nanotube and the outer medium. Our numerical calculations have unveiled a power-law dependence of the critical pressure on the elastic modulus of the medium that is independent of the medium thickness.

2. Methodology

2.1. Relevant Energy Components. Figure 1 illustrates the self-contraction process of MWNTs subjected to high-energetic beam irradiation. Under irradiation, the induced beam kicks off a portion of carbon atoms at outer walls, causing vacancies followed by spontaneous shrinkage as marked by color in Figure 1(b). Even during the outer-walls self-contraction, the inner walls remain undamaged by irradiation, and thus they tend to keep their initial tube radii. As a result, the contracting outerwalls exert a high pressure, designated by p , on the inner undamaged walls (see Figure 1). A possible consequence of the radiation-induced high-pressure application is a circumferentially wrinkling structure, called radial corrugation [13], in the inner undamaged walls embedded in the eroded region, as examined later in an approximation based on the thin-shell theory.

The stable cross-sectional shape of the embedded tube is obtained by minimizing its mechanical energy U per unit axial length [13] as

$$U = U_D + U_I + U_m + \Omega. \quad (1)$$

The first term $U_D = \sum_{i=1}^N U_D^{(i)}$ with the definition

$$U_D^{(i)} = \frac{r_i}{2} \left(\frac{C}{1-\nu^2} \int_0^{2\pi} \mathcal{F}_i^2 d\theta + D \int_0^{2\pi} \mathcal{B}_i^2 d\theta \right) \quad (2)$$

represents the deformation energy of the embedded nanotubes. \mathcal{F}_i and \mathcal{B}_i are, respectively, in-plane and bending-induced strains of the i th wall, and θ is the circumferential coordinate. For (2), we supposed that each i th wall had a radius r_i prior to cross-sectional deformation and that the deformation caused a displacement $\mathbf{x}_i = (u_i, v_i)$ of a volume element of the i th wall at (r_i, θ) in the polar coordinate

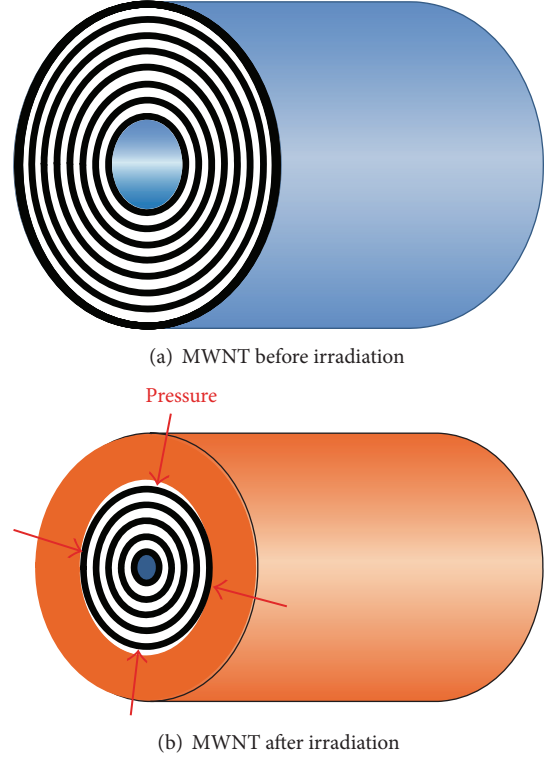


FIGURE 1: Schematics of the pressurized carbon nanotubes. (a) A pristine MWNT prior to high-energy beam irradiation. (b) An irradiated MWNT whose outermost carbon walls contract radially because of the self-repairing property of the eroded region (indicated in orange).

representation. The two strain terms \mathcal{F}_i and \mathcal{B}_i are described in terms of the displacement components by [14]

$$\mathcal{F}_i = \frac{u_i + \partial_\theta v_i}{r_i} + \frac{1}{2} \left(\frac{\partial_\theta u_i - v_i}{r_i} \right)^2, \quad \mathcal{B}_i = -\frac{\partial_\theta^2 u_i - \partial_\theta v_i}{r_i^2}, \quad (3)$$

where $\partial_\theta = \partial/\partial\theta$.

For quantitative discussions, the elastic coefficients C and D need to be carefully determined. In conventional thin-shell theory for macroscopic objects, C and D are related to the Young's modulus E of the wall and its thickness h as

$$C = Eh, \quad D = \frac{Eh^3}{12(1-\nu^2)} \quad \text{for macroscopic shells.} \quad (4)$$

However, for carbon nanotubes, the macroscopic relations for C and D noted earlier fail because there is no unique way of defining the thickness of the graphene wall [24]. Thus, the values of C and D should be evaluated *ab initio* from direct measurements or computations of carbon sheets, without reference to the macroscopic relations. In actual calculations, we substitute $C = 345$ nN/nm, $D = 0.238$ nN-nm for carbon nanotubes, and $\nu = 0.149$ from prior work [25] based on the density functional theory.

The second term, $U_I = \sum_{i,j=i\pm 1} U_I^{(i,j)}$, in (1) accounts for the van der Waals (vdW) interaction energy, which

determines the equilibrium distance between adjacent concentric walls. Thus far, several continuum models for the vdW interactions have been proposed. Expressions for the wall-wall interaction proposed in [26] were based on the surface integration of the vdW force and its derivative over the cylindrical walls, while disregarding the vectorial nature of the force. The significance of the vectorial nature of the force was addressed in [27], where analytical expressions for the wall-wall interaction were obtained by considering only the component of the vdW force normal to the wall. In accordance with the result of [27], we define the interaction energy by

$$U_I^{(i,j)} = \frac{c_{ij}(r_i + r_j)}{4} \int_0^{2\pi} (u_i - u_j)^2 d\theta, \quad (5)$$

where the coefficients c_{ij} are derived through a harmonic approximation of the interwall force [28] associated with the vdW intermolecular potential

$$V(r) = 4\alpha \left[\left(\frac{\beta}{r} \right)^{12} - \left(\frac{\beta}{r} \right)^6 \right] \quad (6)$$

with the definitions of $\alpha = 2.39$ meV and $\beta = 0.3415$ nm the same as those in [29]. Equation (5) takes into account correctly the normal-to-wall component of vdW forces, and it is valid for infinitesimal deformation, which we address in the present work.

The final term Ω in (1) is the negative of the work done by p during cross-sectional deformation; it can be written as [13]

$$\Omega = p \int_0^{2\pi} \left(r_N u_N + \frac{u_N^2 + v_N^2 - v_N \partial_\theta u_N + u_N \partial_\theta v_N}{2} \right) d\theta. \quad (7)$$

Note that all three terms are functions of $u_i(p, \theta)$ and $v_i(p, \theta)$ of the i th wall under p .

The remaining term, U_m , in (1) is the elastic energy of the eroded medium surrounding the inner part of the nanotubes. To derive it, we assume that the medium has finite thickness of $r_m - r_N$, where r_m is the outmost radius of the cylinder-shaped surrounding medium and r_N is the outmost tube radius of the embedded nanotube. In addition, the medium is assumed to be homogeneous and isotropic with Young's modulus E_m and Poisson's ratio ν_m . The validity of the latter assumption depends on the following two effects of irradiation on the mechanical stiffness of MWNTs. Irradiation reduces the axial stiffness because it creates vacancies [30, 31], and it simultaneously enhances the radial stiffness, owing to the production of covalent bonding between adjacent walls [32]. The possible value of E_m ranges from 100 GPa (for amorphous carbon) [33, 34] to much less. An explicit form of U_m is presented in the next section.

2.2. Corrugation Mode Analysis. Our objectives are to determine (i) the optimal displacements u_i and v_i that minimize U under a given value of p and (ii) the critical pressure p_c above which the circular cross section of the embedded

nanotube is elastically deformed into a noncircular one. These are accomplished by decomposing the displacement $u_i(p, \theta)$ just after buckling as follows:

$$u_i(p, \theta) = u_i^{(0)}(p) + \delta u_i(\theta). \quad (8)$$

In (8), the term $u_i^{(0)}(p) \propto p$ describes a uniform radial contraction at $p < p_c$, at which the cross section remains circular and thus the displacement is independent of θ . The other term $\delta u_i(\theta)$ describes a deformed (noncircular) cross-section observed immediately above p_c . Note that the superscript (0) attached to $u_i^{(0)}(p)$ differentiates it from the θ -dependent displacement $u_i(p, \theta)$ observed at $p > p_c$. As to $v_i(p, \theta)$, we can write

$$v_i(p, \theta) = \delta v_i(\theta), \quad (9)$$

because no circumferential displacement arises at $p < p_c$ (i.e., $v_i^{(0)}(p) \equiv 0$).

Applying the variation method to U with respect to u_i and v_i , we obtain a system of $2N$ linear differential equations with regard to $\delta u_i(\theta)$ and $\delta v_i(\theta)$. To derive the $2N$ linear differential equations, quadratic or cubic terms in δu_i and δv_i are omitted since we consider elastic deformation with sufficiently small displacements. In addition, the terms consisting only of $u_i^{(0)}$ and p are also omitted; the sum of such terms should be equal to zero since $u_i^{(0)}$ represents an equilibrium circular cross-section under p . In fact, the function form of $u_i^{(0)}(p)$ is determined by the fact that the sum of those terms equals zero. The differential equations can be solved using the Fourier series expansions

$$\delta u_i(\theta) = \sum_{n=1}^{\infty} \delta \bar{\mu}_i^{(n)} \cos n\theta, \quad \delta v_i(\theta) = \sum_{n=1}^{\infty} \delta \bar{\nu}_i^{(n)} \sin n\theta, \quad (10)$$

wherein we took into account that δu_i , δv_i , and their derivatives are periodic in θ . Substituting the expansions into the differential equations results in the matrix equation $\mathbf{M}\mathbf{u} = \mathbf{0}$; the vector \mathbf{u} consists of $\delta \bar{\mu}_i^{(n)}$ and $\delta \bar{\nu}_i^{(n)}$ with all possible i and n , and the matrix \mathbf{M} involves one variable p and other material parameters. It should be noted that, due to the orthogonality of $\cos n\theta$ and $\sin n\theta$, the matrix \mathbf{M} can be expressed by a block diagonal matrix of the form

$$\mathbf{M} = \mathbf{M}_{n=1} \oplus \mathbf{M}_{n=2} \oplus \cdots \quad (11)$$

Here, $\mathbf{M}_{n=k}$ for arbitrary integer k is a $2N \times 2N$ submatrix that satisfies $\mathbf{M}_{n=k} \mathbf{u}_{n=k} = \mathbf{0}$, where $\mathbf{u}_{n=k}$ is a $2N$ -column vector composed of $\delta \bar{\mu}_i^{(k)}$ and $\delta \bar{\nu}_i^{(k)}$. As a result, the secular equation $\det(\mathbf{M}) = 0$ is rewritten by

$$\det(\mathbf{M}_{n=1}) \det(\mathbf{M}_{n=2}) \cdots = 0. \quad (12)$$

Solving (12) with respect to p , we obtain a sequence of discrete values of p . Among these values, the minimum one serves as the critical pressure p_c that is associated with a specific integer k . From the definition, the p_c associated with a specific k allows only $\delta \bar{\mu}_i$ ($n = k$) and $\delta \bar{\nu}_i$ ($n = k$) be finite, but it requires $\delta \bar{\mu}_i$ ($n \neq k$) $\equiv 0$ and $\delta \bar{\nu}_i$ ($n \neq k$) $\equiv 0$. Immediately

above p_c , therefore, the cross section of embedded nanotubes becomes radially deformed as described by

$$u_i(\theta) = u_i^{(0)}(p_c) + \delta \bar{u}_i^{(k)} \cos k\theta, \quad v_i(\theta) = \delta \bar{v}_i^{(k)} \sin k\theta, \quad (13)$$

where the value of k is uniquely determined by the one-to-one relation between k and p_c .

3. Mechanical Energy of the Embedding Medium

3.1. Total Energy Cost. In polar coordinates, the radial and circumferential components of normal stress in the medium are denoted by σ_r and σ_θ , respectively, and the shear stress is denoted by $\tau_{r\theta}$; all three quantities are functions of r and θ . Then, U_m is determined by σ_r and $\tau_{r\theta}$ at $r = r_N$ as

$$U_m = U_m^{(0)} + \Delta U_m^{(n)}, \quad (14)$$

$$U_m^{(0)} = \frac{r_N}{2} \int_0^{2\pi} \sigma_r^{(0)} \Big|_{r=r_N} u_N^{(0)} d\theta, \quad (15)$$

$$\Delta U_m^{(n)} = \frac{r_N}{2} \int_0^{2\pi} \left(\sigma_r^{(n)} \Big|_{r=r_N} \delta u_N + \tau_{r\theta}^{(n)} \Big|_{r=r_N} \delta v_N \right) d\theta, \quad (16)$$

where δu_N and δv_N describe the corrugation amplitudes of the outermost wall of the embedded nanotube; see (10). The superscripts (0) and (n) indicate the quantities corresponding to uniform contraction and radial corrugation, respectively. In other words, $U_m^{(0)}$ represents the energy required for uniform radial contraction of the surrounding medium keeping in contact with the embedded nanotube, and ΔU_m represents the energy required for radial corrugation with mode index n .

3.2. Stress-Strain-Displacement Relation. The mechanics of an elastic medium is governed by the stress function ϕ , which satisfies the so-called compatibility equation [35]

$$\left(\partial_r^2 + r^{-1} \partial_r + r^{-2} \partial_\theta^2 \right) \phi(r, \theta) = 0, \quad (17)$$

where $\partial_r = \partial/\partial r$ and $\partial_\theta = \partial/\partial \theta$. Once ϕ is obtained, we can deduce the stress components as follows:

$$\begin{aligned} \sigma_r &= \left(r^{-1} \partial_r + r^{-2} \partial_\theta^2 \right) \phi, & \sigma_\theta &= \partial_r^2 \phi, \\ \tau_{r\theta} &= \partial_r \left(r^{-1} \partial_\theta \right) \phi. \end{aligned} \quad (18)$$

By definition, the strain components ε_r , ε_θ , and $\gamma_{r\theta}$ are given by the matrix form

$$\begin{bmatrix} \varepsilon_r \\ \varepsilon_\theta \\ \gamma_{r\theta} \end{bmatrix} = \mathbf{G} \begin{bmatrix} \sigma_r \\ \sigma_\theta \\ \tau_{r\theta} \end{bmatrix} = \begin{bmatrix} \partial_r & 0 \\ r^{-1} & r^{-1} \partial_\theta \\ r^{-1} \partial_\theta & \partial_r - r^{-1} \end{bmatrix} \begin{bmatrix} u \\ v \end{bmatrix}, \quad (19)$$

$$\mathbf{G} = \frac{1}{E_m} \begin{bmatrix} 1 - \nu_m^2 & -\nu_m(1 + \nu_m) & 0 \\ -\nu_m(1 + \nu_m) & 1 - \nu_m^2 & 0 \\ 0 & 0 & 2(1 + \nu_m) \end{bmatrix}, \quad (20)$$

where $u = u(r, \theta)$ and $v = v(r, \theta)$ are, respectively, the radial and circumferential displacements of a volume element in the elastic medium.

The general solution of (17) is given by

$$\phi(r, \theta) = \sum_{n=0}^{\infty} \phi_n(r, \theta) = \sum_{n=0}^{\infty} [f_n(r) \cos n\theta + g_n(r) \sin n\theta]. \quad (21)$$

The zeroth component ϕ_0 represents a uniform contraction of the circular cross section, thus corresponding to the energy $U_m^{(0)}$ that we have introduced in (15). The first one, ϕ_1 , implies a rigid-body translation, which is irrelevant to our consideration. Other components, ϕ_n for $n \geq 2$, describe radial corrugations with mode index n , thus providing the energy $\Delta U_m^{(n)}$ given by (16). In the following, we set [36]

$$f_0 = a_0 \log r + c_0 r^2, \quad (22)$$

$$f_n = a_n r^{-n} + b_n r^{2-n} + c_n r^{2+n} + d_n r^n, \quad (n \geq 2)$$

in order to obtain physically relevant solutions of σ_r , σ_θ , and $\tau_{r\theta}$ that decay with increasing r . Without loss of generality, we set $g_n \equiv 0$ in (21) according to our assumption of cosine-type radial displacement $\delta u_i(\theta)$; see (10). We emphasize that the hypothesized solution forms of f_0 and $f_{n \geq 2}$ differ from those in our earlier work [12]; in the present study, we introduce the positive power terms of r in (22) to take into account correctly the boundary condition at $r = r_m$, whereas these terms were omitted in [12].

3.3. Energy Cost under Uniform Contraction. We now evaluate the explicit form of the energy $U_m^{(0)}$. It results from the uniform contraction of the medium described by the r -dependent medium displacement $u^{(0)}(r)$. The elastic nature of the embedding medium assures that

$$\sigma_r^{(0)}(r) = \kappa(r) u^{(0)}(r) \quad (23)$$

with the r -dependent stiffness coefficient $\kappa(r)$. In addition, complete contact at the interface of the medium and the embedded nanotube implies

$$u^{(0)}(r_N) = u_N^{(0)}. \quad (24)$$

Hence, the previous expression of $U_m^{(0)}$, given in (15), can be rewritten as

$$U_m^{(0)} = \frac{\kappa_0}{2} \int_0^{2\pi} \{u_N^{(0)}\}^2 r_N d\theta \quad \text{with } \kappa_0 \equiv \kappa(r_N). \quad (25)$$

The remaining task is, therefore, to represent κ_0 in terms of already-known material parameters such as E_m , ν_m , r_m , and r_N .

To accomplish this task, we consider a specific solution of (17) that has the form $\phi = \phi_0$, and then we substitute it back into (18) to obtain

$$\sigma_r^{(0)} = a_0 r^{-2} + 2c_0, \quad \sigma_\theta^{(0)} = -a_0 r^{-2} + 2c_0, \quad (26)$$

and $\tau_{r\theta}^{(0)} = 0$. The coefficients a_0 and c_0 are determined by imposing the boundary conditions of $\sigma_r^{(0)}$ at $r = r_N$ and $r = r_m$ as follows:

$$a_0 r_N^{-2} + 2c_0 = p, \quad a_0 r_m^{-2} + 2c_0 = 0. \quad (27)$$

Eliminating a_0 and c_0 from (27), we have

$$\begin{aligned} \sigma_r^{(0)}(r) &= \frac{r_N^2 p}{r_m^2 - r_N^2} \left(\frac{r_m^2}{r^2} - 1 \right), \\ \sigma_\theta^{(0)}(r) &= \frac{-r_N^2 p}{r_m^2 - r_N^2} \left(\frac{r_m^2}{r^2} + 1 \right). \end{aligned} \quad (28)$$

The obtained $\sigma_r^{(0)}(r)$ and $\sigma_\theta^{(0)}(r)$ lead to the displacements

$$u^{(0)}(r) = -\frac{1 + \nu_m}{E_m} \cdot \frac{r_N^2 p}{r_m^2 - r_N^2} \left[(1 - 2\nu_m)r + \frac{r_m^2}{r} \right] \quad (29)$$

and $v^{(0)}(r) = 0$ at the medium region ($r_N < r < r_m$), as confirmed by (19). By comparing (23), (28), and (29), we conclude that

$$\kappa_0 = -\frac{E_m}{(1 + \nu_m)} \cdot \left(\frac{r_m^2}{r_N^2} - 1 \right) \cdot \left[(1 - 2\nu_m)r_N + \frac{r_m^2}{r_N} \right]^{-1}. \quad (30)$$

3.4. Energy Cost under Radial Corrugation. Next, we consider the energy $\Delta U_m^{(n)}$ ($n \geq 2$) that corresponds to the radial corrugation of the n th order. A similar procedure to the case of $n = 0$ yields

$$\begin{aligned} \sigma_r^{(n)}(r, \theta) &= \left\{ -n(n+1)a_n r^{-2} - (n-1)(n+2)b_n \right\} r^{-n} \cos n\theta \\ &\quad + \left\{ -n(n-1)d_n r^{-2} - (n+1)(n-2)c_n \right\} r^n \cos n\theta, \\ \sigma_\theta^{(n)}(r, \theta) &= \left\{ n(n+1)a_n r^{-2} + (n-1)(n-2)b_n \right\} r^{-n} \cos n\theta \\ &\quad + \left\{ n(n-1)d_n r^{-2} + (n+1)(n+2)c_n \right\} r^n \cos n\theta, \\ \tau_{r\theta}^{(n)}(r, \theta) &= \left\{ n(n+1)a_n r^{-2} + n(n-1)b_n \right\} r^{-n} \sin n\theta \\ &\quad - \left\{ n(n-1)d_n r^{-2} + n(n+1)c_n \right\} r^n \sin n\theta, \end{aligned} \quad (31)$$

leading to the results

$$\begin{aligned} u^{(n)}(r, \theta) &= \frac{(1 + \nu_m)}{E_m} \left(na_n r^{-2} + \xi_+ b_n \right) r^{1-n} \cos n\theta \\ &\quad - \frac{(1 + \nu_m)}{E_m} \left(nd_n r^{-2} + \xi_- c_n \right) r^{1+n} \cos n\theta, \end{aligned} \quad (32)$$

$$\begin{aligned} v^{(n)}(r, \theta) &= \frac{(1 + \nu_m)}{E_m} \left(na_n r^{-2} + \eta_- b_n \right) r^{1-n} \sin n\theta \\ &\quad + \frac{(1 + \nu_m)}{E_m} \left(nd_n r^{-2} + \eta_+ c_n \right) r^{1+n} \sin n\theta, \end{aligned} \quad (33)$$

with $\xi_\pm = n \pm 2(1 - 2\nu_m)$ and $\eta_\pm = n \pm 4(1 - \nu_m)$. Of the four coefficients a_n , b_n , c_n , and d_n involved in the previous equations, two of them are eliminated by considering the boundary conditions $\sigma_r^{(n)}(r_N, \theta) \equiv 0$ and $\tau_{r\theta}^{(n)}(r_N, \theta) \equiv 0$.

Owing to the complete contact condition, we have

$$u^{(n)}(r_N, \theta) = \delta \bar{\mu}_N^{(n)} \cos n\theta, \quad v^{(n)}(r_N, \theta) = \delta \bar{\nu}_N^{(n)} \sin n\theta. \quad (34)$$

Besides, the elastic nature of the medium at the contact interface implies the relations

$$\begin{aligned} \sigma_r^{(n)} \Big|_{r=r_N} &= \left[\kappa_1 \delta \bar{\mu}_N^{(n)} + \kappa_2 \delta \bar{\nu}_N^{(n)} \right] \cos n\theta, \\ \tau_{r\theta}^{(n)} \Big|_{r=r_N} &= \left[\kappa_2 \delta \bar{\mu}_N^{(n)} + \kappa_1 \delta \bar{\nu}_N^{(n)} \right] \sin n\theta. \end{aligned} \quad (35)$$

From (35), the stiffness coefficients are given by

$$\kappa_1 = \frac{\sigma_r^{(n)} \Big|_{r=r_N, \delta \bar{\mu}_N^{(n)}=1, \delta \bar{\nu}_N^{(n)}=0}}{\cos n\theta}, \quad \kappa_2 = \frac{\sigma_r^{(n)} \Big|_{r=r_N, \delta \bar{\mu}_N^{(n)}=0, \delta \bar{\nu}_N^{(n)}=1}}{\cos n\theta}. \quad (36)$$

Note that a set of two normalization conditions of

$$\left\{ \delta \bar{\mu}_N^{(n)} = 1, \delta \bar{\nu}_N^{(n)} = 0 \right\}, \quad \left\{ \delta \bar{\mu}_N^{(n)} = 0, \delta \bar{\nu}_N^{(n)} = 1 \right\}, \quad (37)$$

which is indicated by (36), allows us to describe the two remaining undetermined coefficients, from among a_n , b_n , c_n , and d_n , in terms of materials parameters such as E_m , ν_m , and r_m ; see the statement immediately below (33). Hence, κ_1 and κ_2 derived as mentioned are those expressed by already-known parameters, though the explicit forms are not shown here to save space. Eventually, we obtain $\Delta U_m^{(n)}$ by substituting the results into (16).

4. Results and Discussions

Figure 2 shows the critical pressure p_c required for the cross-sectional deformation of embedded carbon nanotubes. Different types of curves in the plots (dashed, dashed-dotted, and solid) correspond to different values of Young's modulus ratio E_m/E , where $E = 1$ TPa is assumed to be the nanotube's modulus. We found that, independent of the E_m/E value, the p_c curves are upward convex as functions of the medium

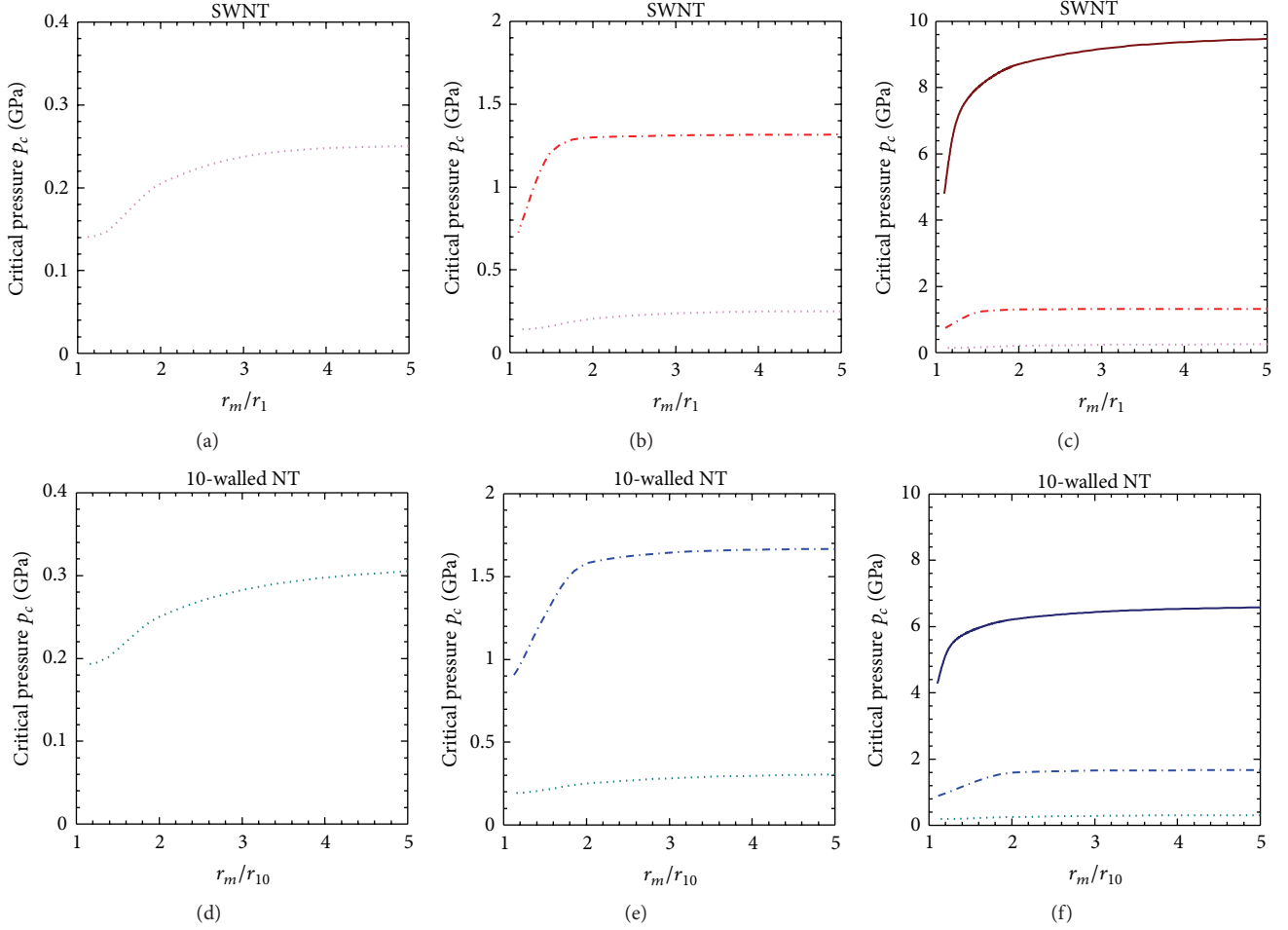


FIGURE 2: Critical pressure p_c for cross-sectional deformation of embedded carbon nanotubes. Monotonic increases with r_m/r_N , the ratio between the radii of the medium (r_m) and the outermost tube (r_N), are observed regardless of the Young's modulus ratio E_m/E between the elastic medium (E_m) and the carbon nanotubes (E): $E_m/E = 10^{-3}$ (dashed curves), $E_m/E = 10^{-2}$ (dash-dotted curves), and $E_m/E = 10^{-1}$ (solid curve).

radius r_m in units of r_N . The growth of p_c is rapid for $r_m/r_N < 2$, and then, it saturates for larger r_m/r_N . The rapid growth in p_c indicates a “hardening effect” caused by the surrounding medium, that is, an enhancement in the radial stiffness of the embedded nanotube by encapsulation. This hardening effect disappears with a further increase in r_m/r_N ; the results imply that the surrounding medium with thickness $r_m > 5r_N$ no longer enhances the hardening effect and thus can be identified as a medium with infinitely large thickness ($r_m \rightarrow \infty$), which is the case considered in our earlier work [12].

Figure 3 provides the index of radial deformation modes observed immediately above p_c . Successive transformation of deformation modes with increasing medium thickness r_m was confirmed, as a result of the fact that the energy required to deform the surrounding medium needed to be responsible for determining the stable corrugation pattern of the embedded nanotube. Again, we found that the mode variation disappears for $r_m/r_N > 3$, and a larger value of n arises for a higher modulus ratio E_m/E . The nonmonotonic variance in the corrugation mode n observed within $1 < r_m/r_N < 2$ is what can be clarified for the first time by the

present work; it is applicable to the condition $r_m \sim r_N$, which lay beyond the scope of our earlier work [12].

Figure 4 shows the p_c dependence on the modulus ratio (E_m/E), where the radius ratio $\alpha \equiv r_m/r_N$ is fixed to be $\alpha = 1.1$ or 5.0 . For every choice of α and N , the p_c curves in this plot obey a power law represented by

$$p_c \propto \left(\frac{E_m}{E}\right)^\beta \quad \text{with } \beta \approx \frac{2}{3}. \quad (38)$$

We have confirmed that the power-law behaviour holds for any values of α and N within the ranges of $1.1 < \alpha < 5$ and $1 < N < 10$, respectively. Recall here that, for $\alpha > 5$, p_c becomes almost constant even with increasing α . These facts lead to the conjecture that the power law described by (38) is universal to all embedded nanotubes, at least under the numerical conditions that we have addressed. The power law of p_c represented by (38) is an interesting manifestation of the embedding effect of nanotubes into an elastic medium.

It is worthy to note that the two-third power law of p_c has been also proposed for the buckling of macroscopic “tunnels”

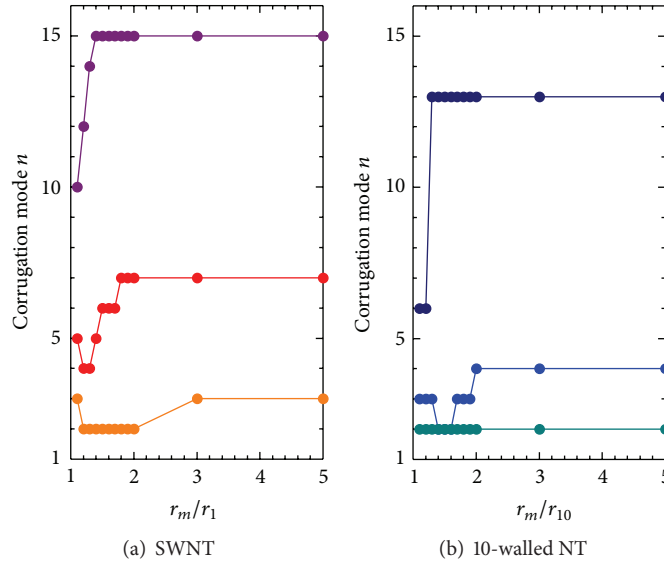


FIGURE 3: Mode index n of the radial corrugation observed in the embedded nanotubes. The modulus ratio is set to $E_m/E = 10^{-3}, 10^{-2}$, and 10^{-1} from the bottom to the top.

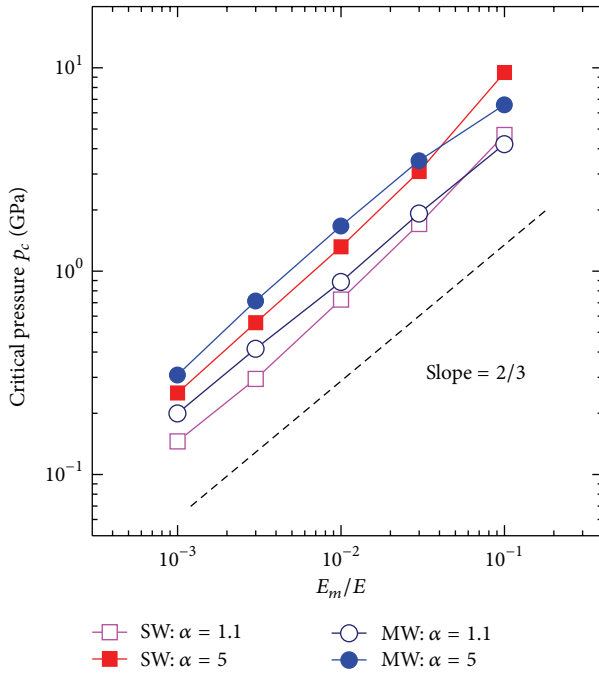


FIGURE 4: Double logarithm plot of the critical pressure p_c as a function of the Young's modulus ratio E_m/E between the elastic medium (E_m) and the nanotubes (E). The parameter $\alpha \equiv r_m/r_N$ represents the ratio of the medium radius r_m to the outermost tube radius r_N , where $N = 1$ for single-walled nanotubes and $N = 10$ for MWNTs. For all the parameter values chosen, the two-third power law of p_c given by (38) is observed.

embedded in an infinite soft ground [36]. The radial collapse of tunnel liners, which is one of the major civil engineering disasters, was analysed to reveal a closed form of p_c ; several

approximations led to the conclusion of a power-law of p_c similar to (38), though an infinitely large medium and only the case of one cylindrical shell (i.e., $N = 1$) are hypothesized. In this context, our results suggest that the approximation theory proposed for macroscopic tunnels [36] is valid for nanoscopic cylinders, even though they consist of more than one concentric walls.

The previous discussion may pose a further question: does the power law of p_c hold true for macroscopic counterparts of “many”-walled nanotubes? In fact, macroscaled pipe-in-pipe structures (i.e., a pipe inserted inside another pipe) are known to be an efficient design solution for subsea-pipeline developments in deep water [37, 38], wherein buckling resistance to large amounts of external hydrostatic pressure is a key structural design requirement. Addressing these problems is expected to shed light on the development of multiple-cylindrical structures from multidisciplinary viewpoints and will be considered in our future work.

5. Conclusion

We have demonstrated a continuum elastic approach that describes the cross-sectional deformation of carbon nanotubes surrounded by a self-contracting host medium. The approach enables quantitative discussions of the critical pressure for radial corrugation and the stable corrugation mode of the nanotube surrounded by the contracting medium. Numerical calculations based on the established theory revealed the power-law dependence of the critical pressure on the elastic modulus of the medium, which is independent of the medium thickness. Further studies are expected to shed light on other mechanical properties of embedded nanotubes and to suggest applications based on their unique cross-sectional deformations.

Acknowledgments

This work was supported by JSPS KAKENHI (Grant nos. 24686096, 11J03636, 22760058, and 25390147). One of the authors (H. Shima) appreciates the financial support provided by the Asahi Glass Foundation.

References

- [1] H. Shima and M. Sato, *Elastic and Plastic Buckling of Carbon Nanotubes*, Pan Stanford Publishing, Singapore, 1st edition, 2013.
- [2] H. Shima, "Buckling of carbon nanotubes: a state of the art review," *Materials*, vol. 5, no. 1, pp. 47–84, 2012.
- [3] Z. Osváth, G. Vértesy, L. Tapasztó et al., "Atomically resolved STM images of carbon nanotube defects produced by Ar⁺ irradiation," *Physical Review B*, vol. 72, no. 4, Article ID 045429, 6 pages, 2005.
- [4] A. V. Krasheninnikov and K. Nordlund, "Ion and electron irradiation-induced effects in nanostructured materials," *Journal of Applied Physics*, vol. 107, no. 7, Article ID 071301, 2010.
- [5] P. M. Ajayan, V. Ravikumar, and J. C. Charlier, "Surface reconstructions and dimensional changes in single-walled carbon nanotubes," *Physical Review Letters*, vol. 81, no. 7, pp. 1437–1440, 1998.
- [6] F. Ding, K. Jiao, Y. Lin, and B. I. Yakobson, "How evaporating carbon nanotubes retain their perfection?" *Nano Letters*, vol. 7, no. 3, pp. 681–684, 2007.
- [7] F. Börrnert, S. Gorantla, A. Bachmatiuk et al., "In situ observations of self-repairing single-walled carbon nanotubes," *Physical Review B*, vol. 81, no. 20, Article ID 201401, 4 pages, 2010.
- [8] L. Sun, F. Banhart, A. V. Krasheninnikov, J. A. Rodríguez-Manzo, M. Terrones, and P. M. Ajayan, "Carbon nanotubes as high-pressure cylinders and nanoextruders," *Science*, vol. 312, no. 5777, pp. 1199–1202, 2006.
- [9] Y. Guo and W. Guo, "Reassembly of single-walled carbon nanotubes into hybrid multilayered nanostructures inside nanotube extruders," *Physical Review B*, vol. 76, no. 4, Article ID 045404, 2007.
- [10] Z. Xu, L. Wang, and Q. Zheng, "Enhanced mechanical properties of prestressed multi-walled carbon nanotubes," *Small*, vol. 4, no. 6, pp. 733–737, 2008.
- [11] S. H. Yang, L. L. Feng, and F. Feng, "Torsional behaviour of carbon nanotubes with abnormal interlayer distances," *Journal of Physics D*, vol. 42, no. 5, Article ID 055414, 5 pages, 2009.
- [12] H. Shima, M. Sato, K. Iiboshi, S. Ghosh, and M. Arroyo, "Diverse corrugation pattern in radially shrinking carbon nanotubes," *Physical Review B*, vol. 82, no. 8, Article ID 085401, 2010.
- [13] H. Shima and M. Sato, "Multiple radial corrugations in multi-walled carbon nanotubes under pressure," *Nanotechnology*, vol. 19, no. 49, Article ID 495705, 2008.
- [14] H. Shima and M. Sato, "Pressure-induced structural transitions in multi-walled carbon nanotubes," *Physica Status Solidi (A)*, vol. 206, no. 10, pp. 2228–2233, 2009.
- [15] C. Ducati, K. Koziol, S. Friedrichs et al., "Crystallographic order in multi-walled carbon nanotubes synthesized in the presence of nitrogen," *Small*, vol. 2, no. 6, pp. 774–784, 2006.
- [16] X. Huang, W. Liang, and S. Zhang, "Radial corrugations of multi-walled carbon nanotubes driven by inter-wall nonbonding interactions," *Nanoscale Research Letters*, vol. 6, no. 1, article 53, 6 pages, 2011.
- [17] M. Majumder, N. Chopra, R. Andrews, and B. J. Hinds, "Nanoscale hydrodynamics: enhanced flow in carbon nanotubes," *Nature*, vol. 438, no. 7064, p. 44, 2005.
- [18] A. Noy, H. G. Park, F. Fornasiero, J. K. Holt, C. P. Grigoropoulos, and O. Bakajin, "Nanofluidics in carbon nanotubes," *Nano Today*, vol. 2, no. 6, pp. 22–29, 2007.
- [19] M. Whitby and N. Quirke, "Fluid flow in carbon nanotubes and nanopipes," *Nature Nanotechnology*, vol. 2, no. 2, pp. 87–94, 2007.
- [20] E. Frackowiak and F. Béguin, "Electrochemical storage of energy in carbon nanotubes and nanostructured carbons," *Carbon*, vol. 40, no. 10, pp. 1775–1787, 2002.
- [21] C.-K. Yang, J. Zhao, and J. P. Lu, "Magnetism of transition-metal/carbon-nanotube hybrid structures," *Physical Review Letters*, vol. 90, no. 25, Article ID 257203, 4 pages, 2003.
- [22] Y. Maniwa, K. Matsuda, H. Yakuno et al., "Water-filled single-wall carbon nanotubes as molecular nanovalves," *Nature Materials*, vol. 6, no. 2, pp. 135–141, 2007.
- [23] H. Shima and H. Yoshioka, "Electronic spectral shift of oxygen-filled (6,6) carbon nanotubes," *Chemical Physics Letters*, vol. 513, no. 4–6, pp. 224–228, 2011.
- [24] S. S. Gupta, F. G. Bosco, and R. C. Batra, "Wall thickness and elastic moduli of single-walled carbon nanotubes from frequencies of axial, torsional and inextensional modes of vibration," *Computational Materials Science*, vol. 47, no. 4, pp. 1049–1059, 2010.
- [25] K. N. Kudin, G. E. Scuseria, and B. I. Yakobson, "C₂F, BN, and C nanoshell elasticity from *ab initio* computations," *Physical Review B*, vol. 64, no. 23, Article ID 235406, 10 pages, 2001.
- [26] X. Q. He, S. Kitipornchai, and K. M. Liew, "Buckling analysis of multi-walled carbon nanotubes: a continuum model accounting for van der Waals interaction," *Journal of the Mechanics and Physics of Solids*, vol. 53, no. 2, pp. 303–326, 2005.
- [27] W. B. Lu, B. Liu, J. Wu et al., "Continuum modeling of van der Waals interactions between carbon nanotube walls," *Applied Physics Letters*, vol. 94, no. 10, Article ID 101917, 3 pages, 2009.
- [28] H. Shima, S. Ghosh, M. Arroyo, K. Iiboshi, and M. Sato, "Thin-shell theory based analysis of radially pressurized multiwalled carbon nanotubes," *Computational Materials Science*, vol. 52, no. 1, pp. 90–94, 2012.
- [29] L. A. Girifalco, M. Hodak, and R. S. Lee, "Carbon nanotubes, buckyballs, ropes, and a universal graphitic potential," *Physical Review B*, vol. 62, no. 19, pp. 13104–13110, 2000.
- [30] M. Sammalkorpi, A. Krasheninnikov, A. Kuronen, K. Nordlund, and K. Kaski, "Mechanical properties of carbon nanotubes with vacancies and related defects," *Physical Review B*, vol. 70, no. 24, Article ID 245416, 8 pages, 2005.
- [31] N. M. Pugno, "Young's modulus reduction of defective nanotubes," *Applied Physics Letters*, vol. 90, no. 4, Article ID 043106, 3 pages, 2007.
- [32] A. V. Krasheninnikov and F. Banhart, "Engineering of nanostructured carbon materials with electron or ion beams," *Nature Materials*, vol. 6, no. 10, pp. 723–733, 2007.
- [33] S. Okada, T. Mukawa, R. Kobayashi et al., "Comparison of Young's modulus dependency on beam accelerating voltage between electron-beam- and focused ion-beam-induced chemical vapor deposition pillars," *Japanese Journal of Applied Physics Part 1*, vol. 45, no. 6 B, pp. 5556–5559, 2006.
- [34] A. Champi, A. S. Ferlauto, F. Alvarez, S. R. P. Silva, and F. C. Marques, "On the elastic constants of amorphous carbon nitride," *Diamond and Related Materials*, vol. 17, no. 11, pp. 1850–1852, 2008.

- [35] S. R. Timoshenko and J. N. Goodier, *Theory of Elasticity*, McGraw-Hill, 3rd edition, 1970.
- [36] J. G. A. Croll, "Buckling of cylindrical tunnel liners," *Journal of Engineering Mechanics*, vol. 127, no. 4, pp. 333–341, 2001.
- [37] M. Sato and M. H. Patel, "Exact and simplified estimations for elastic buckling pressures of structural pipe-in-pipe cross sections under external hydrostatic pressure," *Journal of Marine Science and Technology*, vol. 12, no. 4, pp. 251–262, 2007.
- [38] M. Sato, M. H. Patel, and F. Trarieux, "Static displacement and elastic buckling characteristics of structural pipe-in-pipe cross-sections," *Structural Engineering and Mechanics*, vol. 30, no. 3, pp. 263–278, 2008.

Research Article

Classic and Quantum Capacitances in Bernal Bilayer and Trilayer Graphene Field Effect Transistor

Hatef Sadeghi,¹ Daniel T. H. Lai,¹ Jean-Michel Redoute,² and Aladin Zayegh¹

¹The TEPS Research Group, College of Engineering and Science, Footscray Park Campus, Victoria University, Melbourne, VIC 3011, Australia

²Department of Electrical and Computer Systems Engineering, Monash University, Melbourne, VIC 3800, Australia

Correspondence should be addressed to Hatef Sadeghi; hatef.sadeghi@live.vu.edu.au

Received 9 November 2012; Accepted 26 March 2013

Academic Editor: Nadya Mason

Copyright © 2013 Hatef Sadeghi et al. This is an open access article distributed under the Creative Commons Attribution License, which permits unrestricted use, distribution, and reproduction in any medium, provided the original work is properly cited.

Our focus in this study is on characterizing the capacitance voltage (C-V) behavior of Bernal stacking bilayer graphene (BG) and trilayer graphene (TG) as the channel of FET devices. The analytical models of quantum capacitance (QC) of BG and TG are presented. Although QC is smaller than the classic capacitance in conventional devices, its contribution to the total metal oxide semiconductor capacitor in graphene-based FET devices becomes significant in the nanoscale. Our calculation shows that QC increases with gate voltage in both BG and TG and decreases with temperature with some fluctuations. However, in bilayer graphene the fluctuation is higher due to its tunable band structure with external electric fields. In similar temperature and size, QC in metal oxide BG is higher than metal oxide TG configuration. Moreover, in both BG and TG, total capacitance is more affected by classic capacitance as the distance between gate electrode and channel increases. However, QC is more dominant when the channel becomes thinner into the nanoscale, and therefore we mostly deal with quantum capacitance in top gate in contrast with bottom gate that the classic capacitance is dominant.

1. Introduction

As the fundamental miniaturization limits of integrated metal oxide (MOS) processes are being approached, the conventional path of scaling integrated processes, obeying Moore's law and correspondingly leading to smaller gate lengths and oxide thicknesses, is no longer meeting the performance and power consumption requirements [1]. Robert Dennard's scaling theory, published almost four decades ago, summarized how transistor and corresponding circuit parameter change when these are being scaled under ideal conditions, where K is the unitless scaling constant [2, 3]. Amongst these circuit parameters, reducing the thickness of the gate oxide has been a key contributor to scaling improvements. The resulting oxide capacitance between the gate electrode and the inverted channel is given by [4]: $C_{ox} = \epsilon_{ox}WL/t_{ox}$, where W is the effective width, L is the effective length, t_{ox} is the thickness of the gate oxide, and ϵ_{ox} is the permittivity of the gate insulator. The importance of a high oxide capacitance is illustrated by means of the drain current to gate-source voltage square law

relationship for a MOS transistor biased in saturation, namely, [5]; $I_d = \mu C_{ox}W(V_{gs} - V_t)^2/2L$ illustrates that increasing the oxide capacitance increases the transistor drain current for a given overdrive voltage.

Dennard's scaling theory predicted a scaling of K in the gate oxide capacitance between each process node, explained by the fact that W , L , and t_{ox} scale with K . Current integrated technologies use oxide thicknesses which are a few atomic layers thick, and as a result, they do not follow Dennard's theory regarding transistor density, performance, and power consumption. New materials, processes, and device architectures are continuously being researched so as to overcome current technological barriers. As an example, Intel's 65 nm process node transistors use a silicon dioxide with a thickness of 1.2 nm [6]; Intel's 22 nm process features a high- K and metal gate technology and manages to reduce the gate oxide thickness to 0.9 nm [7]. In future semiconductor technology, thinner material with a higher dielectric constant is expected to be used as gate insulators in MOS structures [8]. However, the gate capacitance of a MOS structure with a finite density of

states cannot be described properly by the oxide capacitance alone [9]. In nanoscale devices with strongly coupled gates, the quantum capacitance (QC) as high as hundreds of attofarads could be obtained due to a low density of states in the channel [10]. For these two reasons studying the quantum capacitance in new materials for future electronic devices is very important particularly when it becomes a dominant source of capacitance.

Graphene is a two-dimensional (2D) honeycomb lattice of an atomic layer of carbon. Exciting electronic, thermal, and photoelectronic properties of graphene as a two dimensional electron gas (2DEG) has attracted a huge scientific interest in recent years. After the discovery of graphene [11] the studies on electronic properties of this material are dramatically increased and some studies tuned toward the characterizing the multilayer of this material. Further investigation on bilayer and trilayer graphene shows that each of these materials shows different behavior rather than monolayer graphene [12, 13]. Linear band structure in monolayer graphene changes to quadratic with tunable gap in Bernal bilayer graphene (BG) and tunable band overlap in trilayer graphene (TG). This leads to different electronic structure in mono-, bi- and trilayer graphene.

Graphene has an extraordinary mobility (200 times higher than in silicon), amazing current-handling capability (ten times higher than copper), very high thermal conductivity, and a long mean free path [14]. Graphene could be stacked in different forms but the only stable structure of BG is in Bernal or *AB* stacking structure. In addition, TG could be realized in two different forms: *ABA* (Bernal) and *ABC* [15, 16]. The common hexagonal structure found in graphite is Bernal stacking (*ABA*) [17]. From a geometrical point of view, *AB* BG and *ABA* TG have the same stacking configuration. Although the only geometrical difference between those is an additional graphene layer in TG, the effect of this additional layer in quantum capacitance of the system might be interesting point which has not been explored yet. Figure 1 demonstrates the Bernal stacking structure of BG (Figure 1(a)) and TG (Figure 1(b)) which come in to our focus through this paper.

The quantum capacitance of epitaxial and exfoliated single-layer graphene as well as nanoribbon has been investigated from both theoretical and experimental perspectives. Recently, Xu, et al. reported a mathematical description for monolayer graphene QC which is in good agreement with the experiment [18]. A V-shape dependence of QC versus gate voltage in monolayer graphene was observed [8, 10, 19–25]. However, fluctuation in QC of single layer graphene nanoribbon with van Hove singularities has been reported which is due to a gap in its band structure [26–30]. Also experiments show that multilayer graphene nanoribbons exhibit larger capacitance than their few-layer and single-layer graphene [31, 32]. To the best of our knowledge from the body of the literature, theoretical QC in bilayer and trilayer graphene has not been investigated yet.

Here, we present the mathematical model of capacitance where intrinsic *AB* bilayer graphene or *ABA* Trilayer graphene is used as channel of FET devices in low energy regime with respect to classical (electrostatic) and quantum aspects. Their behavior under different gate voltage as well as

temperature dependence will be studied. We show that although there is not the experimental evidence reported in the body of literature for C-V characteristic of BG and TG, this model shows good agreement with a reported DFT simulation for BG [33]. In addition, the behavior of quantum capacitance in BG and TG will be compared and discussed, and finally the effect of the distance between the center of the channel and the gate electrodes (top and bottom) on total capacitance will be argued.

2. Band Structure

The starting point for understanding the electronic structure of bilayer and trilayer graphene is obtaining their band structure. The gap between the valence and conduction bands can be varied by external perpendicular electric field in BGs though it varies the overlap between the valence and conduction bands in TGs [34]. The spectra of full tight-binding Hamiltonian of Bernal stacked BGs and TGs [35–38] give their electronic structure. In the absence of an electric field, the band structure of *ABA* TG is a combination of monolayer and bilayer graphene band structures. Using perturbation theory [39], (1) and (2) represent the band structures (*E-k* relation) of the BGs [35] and TGs [36], respectively, in the presence of applied external perpendicular electric field:

$$E_{\text{BG}}^{\pm}(k) = \pm\Delta \mp \alpha_{\text{BG}}|k|^2 \pm \beta_{\text{BG}}|k|^4, \quad (1)$$

$$E_{\text{TG}}^{\pm}(k) = \pm\alpha_{\text{TG}}|k| \mp \beta_{\text{TG}}|k|^3, \quad (2)$$

where $\alpha_{\text{BG}} = v_g v_F^2 / t_{\perp\text{BG}}^2$, $\beta_{\text{BG}} = v_F^4 / v_g t_{\perp\text{BG}}^2$, $\alpha_{\text{TG}} = \sqrt{2}\Delta v_F / t_{\perp\text{TG}}$, and $\beta_{\text{TG}} = \sqrt{2}v_F^3 / \Delta t_{\perp\text{TG}}$ in which the upper layer and lower layers are at potential $\pm\Delta = qv_g/2$ and the middle layer in TG is at zero potential. The Fermi velocity is $v_F = \sqrt{3}\gamma_0 a / 2\hbar \approx 10^6$ m/s [38], where hopping between π orbitals located at nearest neighbor atoms is $\gamma_0 (\approx 3.1$ eV) [40]. In addition, the interlayer hopping energy values for BGs and TGs are $t_{\perp\text{BG}} \approx 0.39$ eV and $t_{\perp\text{TG}} \approx 0.44$ eV, respectively [41].

3. Capacitance Model

One way to determine device performance is measuring I-V (current-voltage) and C-V (capacitance-voltage) characteristics which would be helpful to understand fundamental electronic properties of the devices such as density of states (DOS), band energy, mobility, and conductance and that is why the capacitance is an important parameter [42]. In conventional MOSFETs, we usually deal with only the classic capacitance. However, device miniaturization to nanoscale has started to make QC comparable with electrostatic capacitance in channel. For instance, in carbon nanotube both classic and quantum capacitances are in the range of 1–10 pF/cm [43, 44]. Figure 1 shows the approximate circuited representation of a MOS capacitor including classic and quantum capacitors.

Electrostatic capacitance ($C_{\text{ox}} = 2C_{\text{in}}$) per unit area is proportional to the effective dielectric constant (ϵ) divided by

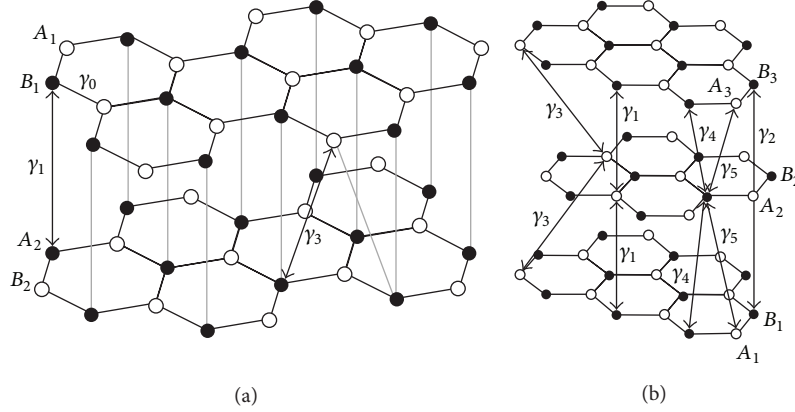


FIGURE 1: Configuration of (a) AB (Bernal) BG with $A_1 B_1 A_2 B_2$ unit cell and in plain hopping ($\gamma_0 = 3.14$ eV) and interlayer hopping ($\gamma_1 = 0.35$ eV); (b) ABA (Bernal) TG with $A_1 B_1 A_2 B_2 A_3 B_3$ unit cell and interlayer hopping ($\gamma_1 = 0.44$ eV).

distance between two plates (d) as $C_{in} = \epsilon/d$. The channel capacitance can be expressed by the series combination of classic and QC (Figure 2) as $C = C_{ox}C_q(C_{ox} + C_q)^{-1}$ [45]. For a double gate BGFET or TGFET with 285 nm SiO_2 insulator region where $\epsilon = 4$ [46], electrostatic capacitance could be easily obtained.

Carrier concentration in a band is achieved by integrating the Fermi-Dirac distribution function over energy band as $n = \int D(E)f_F(E)dE$, where $D(E)$ and $f_F(E) = (1 + \exp((E - E_F)/k_B T))^{-1}$ are available energy states (density of states) and Fermi-Dirac distribution function, respectively. Derivatives k over the energy $D(E) = 2\pi k dk/dE$ with respect to E - k relation of Bernal BG and TG (1) and (2) indicate the density of states as $D_{BG}(E) = 2\pi(4\beta_{BG}k^2 - 2\alpha_{BG})^{-1}$ for Bernal stacking BG and $D_{TG}(E) = 2\pi k(\alpha_{TG} - 3\beta_{TG}k^2)^{-1}$ for Bernal stacking TG. Employing the quadratic and Cardano's solutions for quadratic and cubic equations [47], the momentum (k) can be obtained from E - k relations of both Bernal stacking BG and TG. Averaged density of states over a few $k_B T$ around Fermi level indicates the quantum capacitance ($C_q(E) = q^2 \int dE D(E)F_T(E)$), where ($F_T(E) = df(E)/dE$) is a thermal broadening function [45]. Therefore, by substituting $D_{BG}(E)$ and $D_{TG}(E)$ into the QC mathematical expression ($C_q(E)$), the quantum capacitance of BGs and TGs could be obtained as follows:

$$C_{qBG} = \frac{WLq^2}{4\pi^2} \times \int_0^{+\infty} \frac{2\pi e^{(E-E_F)/k_B T} dE}{k_B T (4\beta_{BG} (|A \pm B|) - 2\alpha_{BG}) (1 + e^{(E-E_F)/k_B T})}, \quad (3)$$

$$C_{qTG} = \frac{WLq^2}{4\pi^2} \times \int_0^{+\infty} (2\pi e^{(E-E_F)/k_B T} |\sqrt[3]{C+D} + \sqrt[3]{C-D}| dE)$$

$$\times (k_B T (\alpha_{TG} - 3\beta_{TG} (|\sqrt[3]{C+D} + \sqrt[3]{C-D}|)^2) \times (1 + e^{(E-E_F)/k_B T}))^{-1}, \quad (4)$$

where $A = -\alpha_{BG}/2\beta_{BG}$, $B = 0.5\sqrt{A^2/4 - 4(E - \Delta)/\beta_{BG}}$, $C = -E/2\beta_{TG}$, and $D = \sqrt{(-\alpha_{TG}/3\beta_{TG})^3 + (E/2\beta_{TG})^2}$. By changing the variables as $x = (E - \Delta)/k_B T$ and $\eta = (E_F - \Delta)/k_B T$, (3) and (4) could be readily written as

$$C_{qBG} = \frac{WLq^2}{2\pi} \int_0^{vg} \frac{e^{x-\eta} dx}{(4\beta_{BG} (|A \pm B'|) - 2\alpha_{BG}) (1 + e^{x-\eta})}, \quad (5)$$

$$C_{qTG} = \frac{WLq^2}{2\pi} \times \int_0^{vg} (e^{x-\eta} |\sqrt[3]{C'+D'} + \sqrt[3]{C'-D'}| dx) \times \left((\alpha_{TG} - 3\beta_{TG} (|\sqrt[3]{C'+D'} + \sqrt[3]{C'-D'}|)^2) \times (1 + e^{x-\eta}) \right)^{-1}, \quad (6)$$

where $A = -\alpha_{BG}/2\beta_{BG}$, $B' = 0.5\sqrt{A^2/4 - 4(xk_B T)/\beta_{BG}}$, $C' = -(xk_B T + \Delta)/2\beta_{TG}$, and $D' = \sqrt{(-\alpha_{TG}/3\beta_{TG})^3 + ((xk_B T + \Delta)/2\beta_{TG})^2}$. Equations (5) and (6) express QC in AB BG and ABA TG where they are used as channels in FET devices.

Recently, experimental work has been done to determine QC in TG-metal Schottky contact [48] as well as a DFT-based simulation to determine QC on Bernal BG [33]. QC is expected to be increased by gate voltage with some fluctuation. Fiori and Iannaccone showed by DFT-based simulation calculation that QC is increased by gate voltage

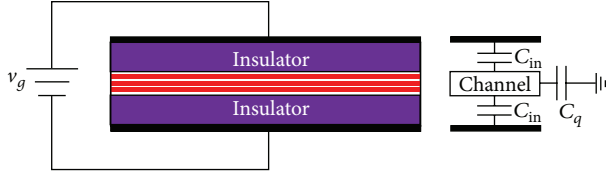


FIGURE 2: Circuited representation of metal oxide bi-/trilayer graphene capacitor.

($[-0.15, 0.15]$ V) around Fermi level in Bernal BGFET which our analytical model shows good agreement with as well. However, they reported in a low range of gate voltage. Here not only we present the analytical model of a BG QC, which not considered yet; to the best of our knowledge, there is no detailed work (theoretical or experimental) reported in the existing body of literature on Bernal TG quantum capacitance. It is apparent that the presented single band approximation model applicable for a proper range of the gate voltages. However, for very high gate voltages, a modified model which takes the multiband effect [37] into account is needed.

Our calculation result shows that around the neutrality point (Fermi level which is set to zero here) QC is increased for both BG and TG as shown in Figure 3. Figure 3(a) shows QC of BG in different temperatures. Fluctuations in the graph could be explained by the behavior of the density of states versus electric field as quantum capacitance is proportional to density of states. In addition, minimum QC decreases with increasing temperature. However, QC increases with higher rate in lower temperatures and that is why although QC is lower around neutrality point for higher temperature, the graph predicts higher peaks in lower temperature for similar gate voltages as shown in Figure 3(a). As demonstrated in Figure 3(b), QC of TG is increased by gate voltage with smoother fluctuation rather than BG. Here also temperature decreases QC. However, temperature much affects BG rather than TG in neutrality point as shown in Figures 3(a) and 3(b). Figure 3(c) shows QC of BG and TG versus gate voltage in similar temperature ($T = 50$ K). Comparing QC on BG and TG, it is apparent that QC in BG is higher than TG specifically at the neutrality point which is more dominant in transport. In the case of biased bilayer graphene, a band gap opens and QC similar to the density of states exhibits van Hove singularities. But in TG where it is semimetal, the gap does not exist and then we expect to observe gate voltage QC dependence without fluctuation.

Figure 4 shows the comparison between classic and quantum capacitances in BG and TG as well as effect of the gating region size in total capacitance. Figures 4(a) and 4(b) show the quantum and classic capacitance of BG and TG in two different temperatures ($T = 10, 50$ K) in a device with $d = 285$ nm and SiO_2 dielectric. With this condition where classic capacitance is higher than QC, the contribution of the QC in total capacitance is higher. Meaning that for a device with similar size, the effect of the QC should be considered. Moreover, comparing Figures 4(a) and 4(b) reveals that although the classic capacitance contribution in total capacitance is very small, the effect of the classic capacitance on total

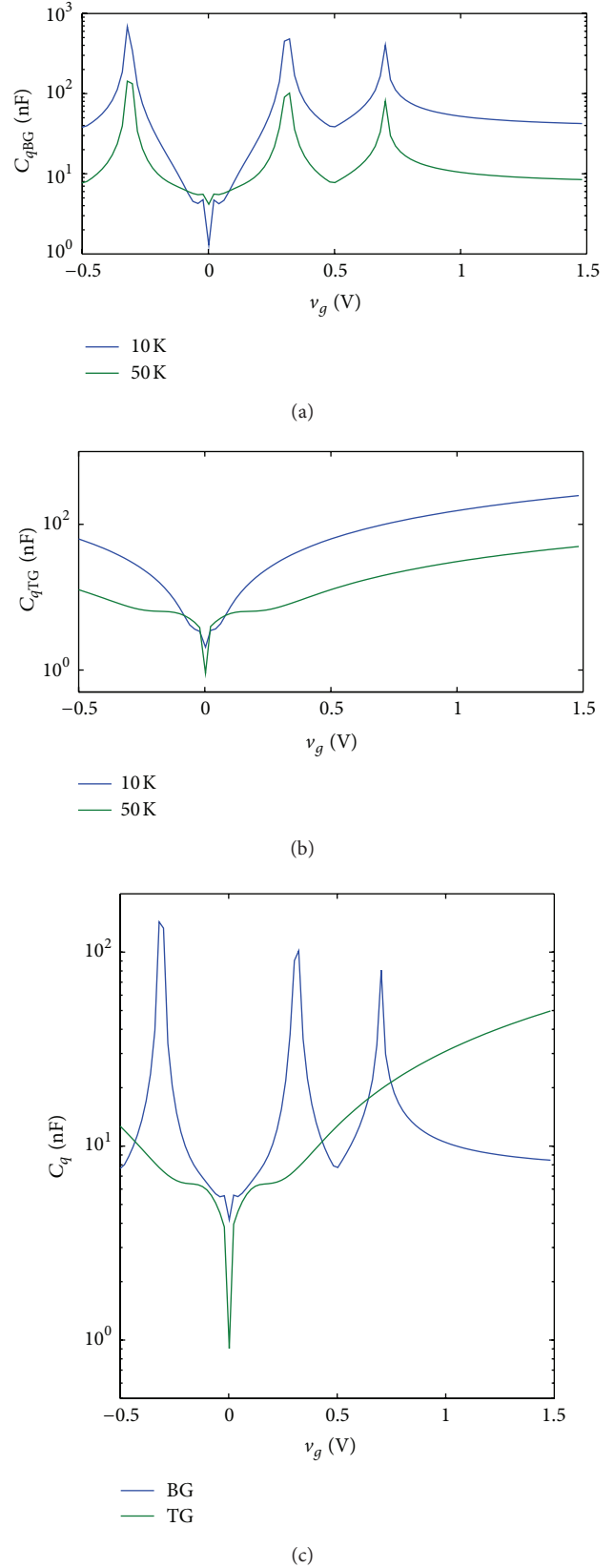


FIGURE 3: Quantum capacitance versus gate voltage around Fermi energy (a) in AB bilayer graphene in different temperature based on (4), (b) in ABA trilayer graphene in different temperatures based on (5), and (c) comparison between Bernal AB and TG in $T = 50$ K.

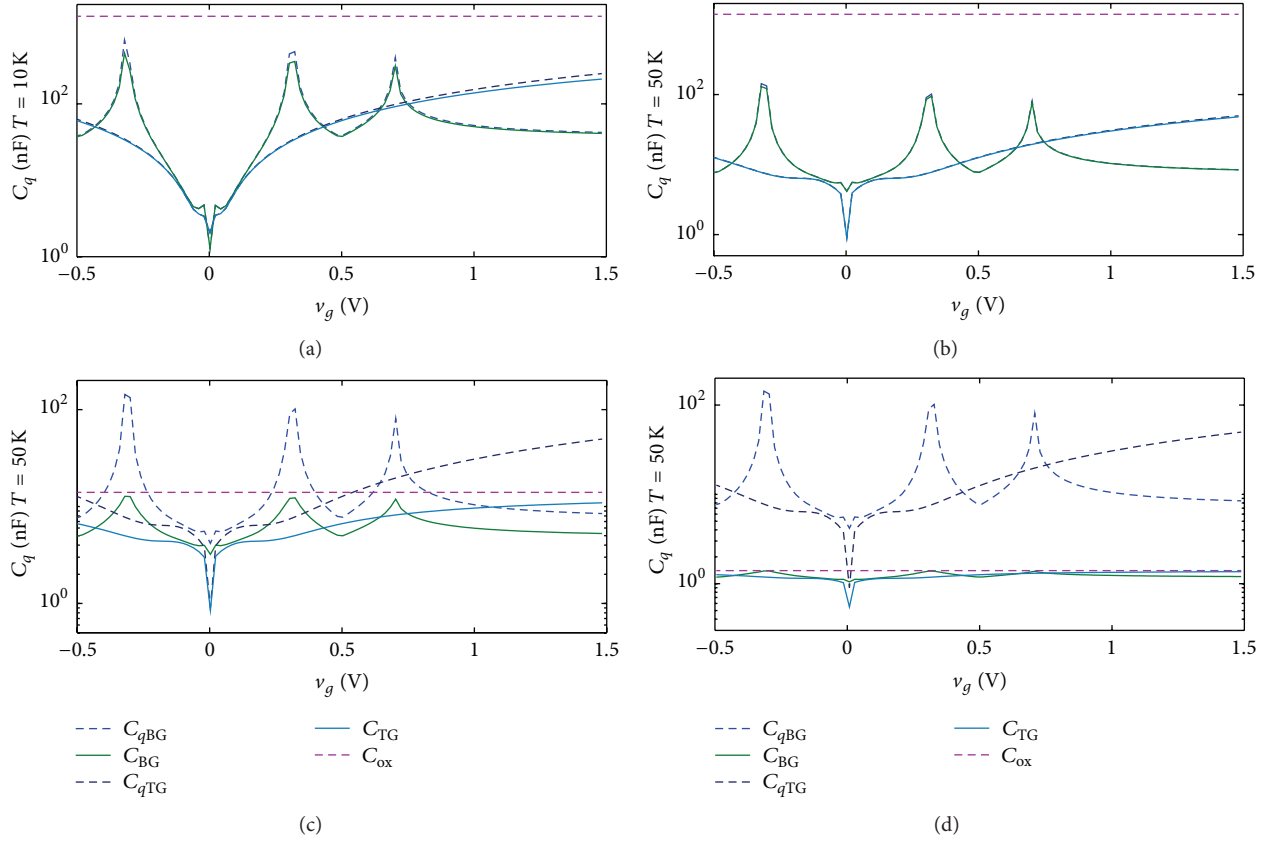


FIGURE 4: Total (dark and light green solid lines), quantum (dark and light blue dashed lines), and classic (purple dashed lines) capacitances in BG and TG for (a) $T = 10$ K and $d = 285$ nm; (b) $T = 50$ K and $d = 285$ nm; (c) $T = 50$ K and $d = 28.5$ μ m; (d) $T = 50$ K and $d = 285$ μ m.

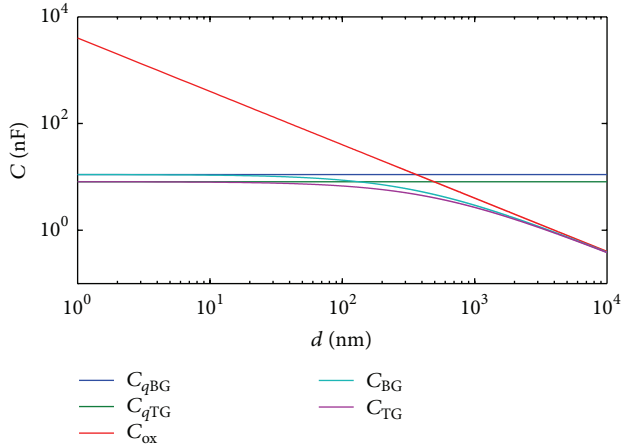


FIGURE 5: Total, quantum, and classic capacitances in BG and TG at room temperature.

capacitance is higher in lower temperature. We generate Figures 4(c) and 4(d) with the same device (SiO_2 dielectric) but with higher d ($d = 28.5$ μ m in Figure 4(c) and $d = 285$ μ m in Figure 4(d)). It is apparent that the total capacitance is more affected by classic capacitance in Figure 4(c), and its contribution becomes major where we increase d as shown in

Figure 4(d). This is important since we usually have higher dielectric in bottom gate rather than upper gate in double gate devices. Therefore, we could conclude that in upper gate the QC leads the total capacitance rather than bottom gate where classic capacitance is dominant for BGFET and TGFET.

Figure 5 shows total, quantum, and classic capacitances in BG and TG at room temperature. Figure 5 clearly confirms that for the channels with d (distance between two plates) less than about 200 nm, classical capacitance does not affect total capacitance in both BG and TG. However, classical capacitance becomes dominant for greater d . Advances in chip fabrication technology which yields capability of fabricating nanoscale devices would reach very small devices, which would induce thinner top gate oxide in FET structures. As shown in Figure 5, device fabrication should be concerned about only quantum capacitance for very thin (less than 100 nm) gate oxide devices. This research could be continued in the different directions such as studying the second stable stacking of TG (ABC) and comparing with current ABA TG QC model, looking at higher energy regime and studying unclean structures such as doped or defected channels.

4. Conclusion

Each of BG and TG when applied as channel in FET devices shows different behavior compared to each other and

monolayer graphene. Rather than a linear band structure as observed in monolayer graphene, the band gap could be tuned in BG and band overlap could be varied in TG. These differences lead us to expect different behavior of these materials. Measuring the QC in the MOS configuration, has been a question for years. Although there is not any experimental result reporting QC in BG and TG, a method has recently been proposed to measure this in monolayer graphene which shows V-shape relation with gate voltage. In this study, our focus was on characterizing the capacitance voltage behavior of Bernal stacking BG and TG from theoretical point of view. Analytical quantum capacitance model of BG and TG was presented in low energy limit. Although the quantum capacitance is not considerable in conventional devices, our result clearly shows that it is dominant in BG- and TG-based devices specifically when the dielectric thickness is in nanometer range. Our calculation shows that quantum capacitances in both BG and TG increase with gate voltage and decrease with temperature with some fluctuation. However, in bilayer graphene the fluctuation is higher due to its band structure. In similar condition, the quantum capacitance in BG metal oxide is higher than TG metal oxide. Moreover, higher distance between gate electrode and channel leads total capacitance in both BG and TG to be more affected by classic capacitance. On the contrary, the quantum capacitance becomes dominant where the dielectric thickness is lower, for example, top gate. However, the experimental observation of the quantum capacitance in BG and TG needs to be addressed.

Acknowledgment

The authors acknowledge Victoria University Postgraduate Research Office for their support and providing the necessary environment for this research.

References

- [1] S. I. Association, *International Technology Roadmap for Semiconductors (ITRS)*, 2011.
- [2] R. H. Dennard, F. H. Gaensslen, H. N. Yu, V. L. Rideout, E. Bassous, and A. R. LeBlanc, "Design of ion-implanted MOSFET's with very small physical dimensions," *IEEE Journal of Solid-State Circuits*, vol. 9, no. 5, pp. 256–268, 1974.
- [3] H. Iwai, "CMOS technology—year 2010 and beyond," *IEEE Journal of Solid-State Circuits*, vol. 34, no. 3, pp. 357–366, 1999.
- [4] Y. Tsividis, *Mixed Analog-Digital VLSI Devices and Technology*, World Scientific Publishing Company Incorporated, 2002.
- [5] W. M. C. Sansen, *Analog Design Essentials*, vol. 289, Springer, Berlin, Germany, 2006.
- [6] P. Bai, C. Auth, S. Balakrishnan et al., "A 65nm logic technology featuring 35 nm gate lengths, enhanced channel strain, 8 Cu interconnect layers, low-k ILD and 0.57 μm^2 SRAM cell," in *Proceedings of the Electron Devices Meeting, IEDM Technical Digest. IEEE International*, pp. 657–660, December 2004.
- [7] C. Auth, C. Allen, A. Blattner et al., "A 22 nm high performance and low-power CMOS technology featuring fully-depleted tri-gate transistors, self-aligned contacts and high density MIM capacitors," in *Symposium on VLSI Technology (VLSIT '12)*, pp. 131–132, 2012.
- [8] J. Xia, F. Chen, J. Li, and N. Tao, "Measurement of the quantum capacitance of graphene," *Nature Nanotechnology*, vol. 4, no. 8, pp. 505–509, 2009.
- [9] S. A. Thiele, J. A. Schaefer, and F. Schwierz, "Modeling of graphene metal-oxide-semiconductor field-effect transistors with gapless large-area graphene channels," *Journal of Applied Physics*, vol. 107, no. 9, Article ID 094505, 2010.
- [10] A. Hazeghi, J. A. Sulpizio, G. Diankov, D. Goldhaber-Gordon, and H. S. P. Wong, "An integrated capacitance bridge for high-resolution, wide temperature range quantum capacitance measurements," *Review of Scientific Instruments*, vol. 82, no. 5, Article ID 053904, 2011.
- [11] K. S. Novoselov, A. K. Geim, S. V. Morozov et al., "Two-dimensional gas of massless Dirac fermions in graphene," *Nature*, vol. 438, no. 7065, pp. 197–200, 2005.
- [12] Y. B. Zhang, T. T. Tang, C. Girit et al., "Direct observation of a widely tunable bandgap in bilayer graphene," *Nature*, vol. 459, no. 7248, pp. 820–823, 2009.
- [13] M. F. Craciun, S. Russo, M. Yamamoto, J. B. Oostinga, A. F. Morpurgo, and S. Tarucha, "Trilayer graphene is a semimetal with a gate-tunable band overlap," *Nature Nanotechnology*, vol. 4, no. 6, pp. 383–388, 2009.
- [14] H. Sadeghi, J.-M. Redoute, D. T. H. Lai, M. T. Ahmadi, and R. Ismail, "A review on: carbon based materials as on-chip interconnects," in *Proceedings of the SPIE Smart Nano-Micro Materials and Devices*, Melbourne, Australia, December 2011.
- [15] H. Sadeghi, M. T. Ahmadi, S. M. Mousavi, M. H. Ghadir, and A. R. Ismail, "Channel conductance of ABA stacking trilayer graphene nanoribbon field effect transistor," *Modern Physics Letters B*, vol. 26, no. 8, Article ID 1250047, 10 pages, 2012.
- [16] H. Sadeghi, M. T. Ahmadi, B. I. Ishak, S. M. Mousavi, and A. R. Ismail, "Ballistic conductance model of Bilayer Graphene Nanoribbon (BGN)," *Journal of Computational and Theoretical Nanoscience*, vol. 8, pp. 1993–1998, 2011.
- [17] H. Lipson and A. R. Stokes, "The structure of graphite," *Proceedings of the Royal Society of London A. Mathematical and Physical Sciences*, vol. 181, no. 984, pp. 101–105, 1942.
- [18] H. Xu, Z. Zhang, and L.-M. Peng, "Measurements and microscopic model of quantum capacitance in graphene," *Applied Physics Letters*, vol. 98, no. 13, Article ID 133122, 2011.
- [19] S. Thiele and F. Schwierz, "Modeling of the steady state characteristics of large-area graphene field-effect transistors," *Journal of Applied Physics*, vol. 110, no. 3, Article ID 034506, 7 pages, 2011.
- [20] M. D. Stoller, C. W. Magnuson, Y. Zhu et al., "Interfacial capacitance of single layer graphene," *Energy & Environmental Science*, vol. 4, pp. 4685–4689, 2011.
- [21] M. Begliarbekov, S. Strauf, and C. P. Search, "Quantum inductance and high frequency oscillators in graphene nanoribbons," *Nanotechnology*, vol. 22, no. 16, Article ID 165203, 2011.
- [22] J. L. Xia, F. Chen, J. L. Tedesco et al., "The transport and quantum capacitance properties of epitaxial graphene," *Applied Physics Letters*, vol. 96, no. 16, Article ID 162101, 2010.
- [23] L. A. Ponomarenko, R. Yang, R. V. Gorbachev et al., "Density of states and zero landau level probed through capacitance of graphene," *Physical Review Letters*, vol. 105, no. 13, Article ID 136801, 2010.
- [24] S. Sonde, F. Giannazzo, V. Raineri, and E. Rimini, "Dielectric thickness dependence of capacitive behavior in graphene deposited on silicon dioxide," *Journal of Vacuum Science and Technology B*, vol. 27, no. 2, pp. 868–873, 2009.

- [25] S. Dröscher, P. Roulleau, F. Molitor et al., “Quantum capacitance and density of states of graphene,” *Applied Physics Letters*, vol. 96, no. 15, Article ID 152104, 2010.
- [26] G. S. Kliros, “Modeling of carrier density and quantum capacitance in graphene nanoribbon FETs,” in *Proceedings of the International Conference on Microelectronics (ICM '10)*, pp. 236–239, December 2010.
- [27] J. Guo, Y. Yoon, and Y. Ouyang, “Gate electrostatics and quantum capacitance of graphene nanoribbons,” *Nano Letters*, vol. 7, no. 7, pp. 1935–1940, 2007.
- [28] A. A. Shylau, J. W. Klos, and I. V. Zozoulenko, “Capacitance of graphene nanoribbons,” *Physical Review B*, vol. 80, no. 20, 9 pages, 2009.
- [29] Y. Ouyang, Y. Yoon, and J. Guo, “Edge chemistry engineering of graphene nanoribbon transistors: a computational study,” in *Proceedings of the IEEE International Electron Devices Meeting (IEDM '08)*, December 2008.
- [30] T. Fang, A. Konar, H. Xing, and D. Jena, “Carrier statistics and quantum capacitance of graphene sheets and ribbons,” *Applied Physics Letters*, vol. 91, no. 9, Article ID 092109, 2007.
- [31] M. S. Goh and M. Pumera, “Multilayer graphene nanoribbons exhibit larger capacitance than their few-layer and single-layer graphene counterparts,” *Electrochemistry Communications*, vol. 12, no. 10, pp. 1375–1377, 2010.
- [32] A. Misra, H. Kalita, M. Waikar et al., “Multilayer graphene as charge storage layer in floating gate flash memory,” in *Proceedings of the 4th IEEE International Memory Workshop (IMW '12)*, pp. 1–4, 2012.
- [33] G. Fiori and G. Iannaccone, “Ultralow-voltage bilayer graphene tunnel FET,” *IEEE Electron Device Letters*, vol. 30, no. 10, pp. 1096–1098, 2009.
- [34] A. A. Avetisyan, B. Partoens, and F. M. Peeters, “Electric-field control of the band gap and Fermi energy in graphene multilayers by top and back gates,” *Physical Review B*, vol. 80, no. 19, Article ID 195401, 2009.
- [35] E. V. Castro, K. S. Novoselov, S. V. Morozov et al., “Electronic properties of a biased graphene bilayer,” *Journal of Physics Condensed Matter*, vol. 22, no. 17, Article ID 175503, 2010.
- [36] F. Guinea, A. H. Castro Neto, and N. M. R. Peres, “Electronic states and Landau levels in graphene stacks,” *Physical Review B*, vol. 73, no. 24, Article ID 245426, 2006.
- [37] B. Partoens and F. M. Peeters, “From graphene to graphite: electronic structure around the K point,” *Physical Review B*, vol. 74, no. 7, Article ID 075404, 2006.
- [38] A. A. Avetisyan, B. Partoens, and F. M. Peeters, “Stacking order dependent electric field tuning of the band gap in graphene multilayers,” *Physical Review B*, vol. 81, no. 11, Article ID 115432, 2010.
- [39] T. Kat, *Perturbation Theory for Linear Operators*, vol. 132, Springer, 1995.
- [40] K. F. Mak, J. Shan, and T. F. Heinz, “Electronic structure of few-layer graphene: experimental demonstration of strong dependence on stacking sequence,” *Physical Review Letters*, vol. 104, no. 17, Article ID 176404, 2010.
- [41] A. Bostwick, J. McChesney, T. Ohta, E. Rotenberg, T. Seyller, and K. Horn, “Experimental studies of the electronic structure of graphene,” *Progress in Surface Science*, vol. 84, no. 11–12, pp. 380–413, 2009.
- [42] D. L. John, L. C. Castro, and D. L. Pulfrey, “Quantum capacitance in nanoscale device modeling,” *Journal of Applied Physics*, vol. 96, no. 9, pp. 5180–5184, 2004.
- [43] S. Ilani, L. A. K. Donev, M. Kindermann, and P. L. McEuen, “Measurement of the quantum capacitance of interacting electrons in carbon nanotubes,” *Nature Physics*, vol. 2, no. 10, pp. 687–691, 2006.
- [44] M. T. Ahmadi, J. F. Webb, N. A. Amin et al., “Carbon nanotube capacitance model in the degenerate and the non-degenerate regimes,” in *Presented at the 4th Global Conference on Power Control and Optimization (PCO '10)*, Sarawak, Malaysia, 2011.
- [45] S. Datta, *Quantum Transport: Atom to Transistor*, Cambridge University Press, 2005.
- [46] S. Russo, M. F. Craciun, M. Yamamoto, S. Tarucha, and A. F. Morpurgo, “Double-gated graphene-based devices,” *New Journal of Physics*, vol. 11, Article ID 095018, 2009.
- [47] G. Cardano and T. R. Witmer, *Ars Magna or the Rules of Algebra*, Dover, 1993.
- [48] S. Tongay, T. Schumann, X. Miao, B. R. Appleton, and A. F. Hebard, “Tuning Schottky diodes at the many-layer-graphene/semiconductor interface by doping,” *Carbon*, vol. 49, no. 6, pp. 2033–2038, 2011.